



Veröffentlichungen der DGK

Ausschuss Geodäsie der Bayerischen Akademie der Wissenschaften

Reihe C

Dissertationen

Heft Nr. 874

Hani Dbouk

**Alternative Integrity Measures Based on Interval Analysis and
Set Theory**

München 2021

Verlag der Bayerischen Akademie der Wissenschaften

ISSN 0065-5325

ISBN 978-3-7696-5286-4

Diese Arbeit ist gleichzeitig veröffentlicht in:
Wissenschaftliche Arbeiten der Fachrichtung Geodäsie und Geoinformatik der Leibniz
Universität Hannover
ISSN 0174-1454, Nr. 370, Hannover 2021



Veröffentlichungen der DGK

Ausschuss Geodäsie der Bayerischen Akademie der Wissenschaften

Reihe C

Dissertationen

Heft Nr. 874

Alternative Integrity Measures Based on Interval Analysis and Set Theory

Von der Fakultät für Bauingenieurwesen und Geodäsie
der Gottfried Wilhelm Leibniz Universität Hannover

zur Erlangung des Grades

Doktor-Ingenieur (Dr.-Ing.)

genehmigte Dissertation

Vorgelegt von

M.Sc. Hani Dbouk

Geboren am 08.03.1984 in Deir Ames, Libanon

München 2021

Verlag der Bayerischen Akademie der Wissenschaften

ISSN 0065-5325

ISBN 978-3-7696-5286-4

Diese Arbeit ist gleichzeitig veröffentlicht in:
Wissenschaftliche Arbeiten der Fachrichtung Geodäsie und Geoinformatik der Leibniz Universität Hannover
ISSN 0174-1454, Nr. 370, Hannover 2021

Adresse der DGK:



Ausschuss Geodäsie der Bayerischen Akademie der Wissenschaften (DGK)

Alfons-Goppel-Straße 11 • D – 80 539 München
Telefon +49 – 331 – 288 1685 • Telefax +49 – 331 – 288 1759
E-Mail post@dgk.badw.de • <http://www.dgk.badw.de>

Prüfungskommission:

Vorsitzender: Prof. Dr.-Ing. Habil. Monika Sester

Referent: Prof. Dr.-Ing. Steffen Schön

Korreferenten: Prof. Dr. Mathieu Joerger (VT Virginia)
Prof. Dr.-Ing. Claus Brenner

Tag der mündlichen Prüfung: 30.10.2020

© 2021 Bayerische Akademie der Wissenschaften, München

Alle Rechte vorbehalten. Ohne Genehmigung der Herausgeber ist es auch nicht gestattet,
die Veröffentlichung oder Teile daraus auf photomechanischem Wege (Photokopie, Mikrokopie) zu vervielfältigen

Abstract

Confidence domains for Global Navigation Satellite Systems (GNSSs) positioning and consistency measures of the observations are of great importance for any navigation system, especially for safety-critical applications. Integrity of GNSS applies to a variety of highly demanding tasks, like e.g., precision landing approaches. Consequently, the quality and trust that we put into navigation solutions must be extremely high: Integrity measures this performance, i.e. the ability of the navigation system to timely warn the user when error thresholds, the so-called alert limits are transgressed. Integrity for aviation applications can be provided by ground-based augmented systems or satellite-based augmented systems, which are highly complex and expensive systems. An alternative is Receiver Autonomous Integrity Monitoring (RAIM), which evaluates the integrity risk (IR) inside the GNSS receiver itself. The IR evaluation is necessary when designing a navigation system to meet the predefined integrity requirements. Currently, there is a big interest in developing RAIM algorithms, especially for autonomous driving applications. The IR evaluation involves both assessing the fault detection and exclusion capability and quantifying the impact of undetected faults on the position estimation. There is a variety of RAIM algorithms based on statistical hypothesis tests acting on the measurement or position domain. The residual-based and solution separation RAIMs have gained more interest than the other has and they have been widely implemented over the last three decades. In the past years, new integrity approaches were proposed based on interval mathematics namely set inversion and least-squares.

This thesis presents a newly developed deterministic bounding method based on convex optimization. In this deterministic bounding method, the observation interval bounds (OIBs) are applied to the observation equations that represent constraints for the parameters that have to be satisfied. As a result, a convex polytope is obtained. Consistency measures are obtained by comparing the non-regular polytope with a regular polytope (zonotope) computed solely from OIB and the current geometry. In this thesis, a primal-dual polytope algorithm is used to estimate all possible solutions. The obtained polytope represents exactly the feasible region of the positioning solution. The developed method guarantees the internal reliability that is presented by the minimum detectable bias. Besides, fault detection and exclusion algorithms based on the polytope consistency measures are developed. In addition, a guaranteed protection level is developed that corresponds to a one-relaxed zonotope. Our newly developed polytopic method will be investigated in all aspects and compared to the above-mentioned RAIM algorithms showing the benefits and the drawbacks of each method. To perform all the above-mentioned interval-based methods the observation interval bounds need to be estimated. Three main methods could be used to determine the OIBs, which will be investigated: a probabilistic approach with predefined IR, sensitivity analysis of the correction models, and expert knowledge.

This work provides the theoretical framework, the mathematical properties, and the geometrical interpretation of the polytope concerning the positioning problem. A study of the form and orientation of the polytope w.r.t. line-of-sights, number of satellites in view, and random observation errors, as well as biases, is conducted. Also, a simulation study of a simple but didactic positioning system for better understanding the geometry of the polytopes and its relation to the navigation geometry is performed. Moreover, an intensive Monte Carlo simulation to study the newly developed RAIM algorithm is performed. Then, real GPS pseudo-range observations from a kinematic test drive will be analyzed, and a comparison between different RAIM algorithms are performed in terms of precision, accuracy, internal reliability, integrity, continuity, and availability.

Keywords: GNSS, RAIM, Reliability, Integrity, Interval analysis, Set theory

Kurzfassung

Für jedes Ortungsproblem mittels Globalen Navigationssatellitensystemen GNSS sind Konfidenzbereiche sowie Konsistenzmaße für zugehörige Beobachtungen von erheblicher Bedeutung. Sogar in besonderem Maße, wenn es sich um sicherheitskritische Anwendungen handelt, wie zum Beispiel Präzisionslandungsanflüge. Dementsprechend müssen die Qualität und das Vertrauen, welches in die Navigationslösung gesetzt wird, extrem hoch sein. Die Integrität misst die Leistungsfähigkeit, d.h. die Fähigkeit des Navigationssystems, den Benutzer rechtzeitig zu warnen, wenn Fehlergrenzwerte, die sogenannten Alarmgrenzen, überschritten werden. Die Integrität für Luftfahrtanwendungen kann durch Bodenbasiertes Ergänzungssysteme bzw. Satellitenbasiertes Ergänzungssysteme gewährleistet werden. Jedoch sind hochkomplexe und kostenintensive Systeme hierfür notwendig. Eine Alternative ist die empfängerautonome Integritätsüberwachung (RAIM), bei der das Integritätsrisiko direkt im GNSS-Empfänger bestimmt und bewertet wird. Gegenwärtig besteht ein großes Interesse an der Weiterentwicklung von RAIM-Algorithmen, insbesondere für Anwendungen im Bereich des autonomen Fahrens. Die Beurteilung des Integritätsrisikos (IR) umfasst sowohl die Fähigkeit der Fehlererkennung- und deren Ausschluss, als auch die Quantifizierung der Auswirkungen unerkannter Fehler. Eine Vielzahl von acsraim-Algorithmen basiert auf statistischen Hypothesentests, die auf der Beobachtungs- oder Positionsebene operieren. Insbesondere residuenbasierte Verfahren und Solution-Separation-Verfahren sind in den letzten drei Dekaden entwickelt und umfangreich eingesetzt worden. Neue Integritätsansätze vergangener Jahre basieren zunehmend auf der Intervallmathematik: die Mengeninversion und die Ausgleichung nach kleinsten Quadraten.

Diese Dissertation präsentiert eine neue deterministische Begrenzungsmethode basierend auf dem Konzept der konvexen Optimierung. Bei dieser Methode werden zunächst die Intervallgrenzen der Beobachtungen (OIBs) festgelegt und auf die Beobachtungsgleichungen angewendet. Die so gesetzten Bedingungen führen einen Zwang auf die unbekanntenen Parameter ein. Das Ergebnis ist ein nicht-reguläres Polytop. Ein Konsistenzmaß erhält man durch den Vergleich des nicht-regulären Polytops mit einem regulären Polytop (Zonotop), das sich ausschließlich aus OIB und der aktuellen Geometrie berechnet. In dieser Arbeit wird der Primal-Dual-Polytop-Algorithmus verwendet, um alle vorhandenen Lösungsmöglichkeiten abzuschätzen. Das resultierende Polytop repräsentiert exakt alle möglichen Zonen einer Positionslösung. Die entwickelte Methode garantiert die interne Zuverlässigkeit. Diese ist durch den minimal-feststellbaren Fehler repräsentiert. Auf Basis der Konsistenzmaße wurde ein Fehlererkennung- und Ausschlussalgorithmus entwickelt. Darüber hinaus wird ein garantiertes Sicherheitsmaß entwickelt, das einem one-relaxed Zonotop entspricht. Der innovative Polytop-basierte Ansatz ist zur Bewertung und Qualitätsanalyse gegenüber den aktuell wissenschaftlich anerkannten und verfügbaren RAIM-Algorithmen einer kritischen Analyse unterzogen worden. Die Schätzung von Beobachtungsintervallgrenzen ist zur Durchführung aller oben genannten intervallbasierten Methoden erforderlich. Dazu werden drei Verfahren eingesetzt: ein probabilistischer Ansatz mit vordefinierter IR, eine Sensitivitätsanalyse der Korrekturmodelle und Expertenwissen.

Diese Arbeit liefert die theoretischen Grundlagen, die mathematischen Eigenschaften und die geometrische Interpretation des Polytops im Bezug zu einem klassischen Ortungsproblem. Es werden zusätzlich Form und Orientierung der Polytope in Bezug auf die Sichtlinie, die Anzahl an sichtbaren Satelliten und zufällige sowie systematische Beobachtungsfehler studiert. Um die Geometrie der Polytope und ihre Beziehung zur Geometrie besser verstehen zu können, wurde eine Simulationsstudie eines einfachen aber didaktischen Positionierungssystems durchgeführt. Anhand umfangreicher Monte-Carlo-Studien werden die neu entwickelten Konsistenzmaße untersucht. Abschließend werden reale GPS-Daten aus einer kinematischen Trajektorie evaluiert und ein Vergleich zwischen verschiedenen RAIM-Algorithmen bezüglich Präzision, Genauigkeit, interner Zuverlässigkeit, Integrität, Kontinuität und Verfügbarkeit durchgeführt.

Schlagwörter: GNSS, RAIM, Verlässlichkeit, Integrität, Intervallanalyse, Mengenlehre

Acronyms

AL	Alert Limit
ARAIM	Advanced Receiver Autonomous Integrity Monitoring
APV	Approach with Vertical Guidance
AWN	Additive White Noise
BDS	BeiDou Navigation Satellite System
CS	Commercial Service
CDMA	Code-Division Multiple Access
CDMA	Code-Division Multiple Access
CV	Critical Value
DoD	Department of Defense
DoF	Degree of Freedom
DOP	Dilution of Precision
ECEF	Earth-Centred Earth-Fixed
ECIF	Earth Centred Inertial Frame
EGNOS	European Geostationary Navigation Overlay System
ENU	East, North, Up
ESA	European Space Agency
FDMA	Frequency Division Multiple Access
FD	Fault Detection
FDE	Fault Detection and Exclusion
GAGAN	GPS Aided Geo Augmented Navigation
GDOP	Geometrical Dilution of Precision
GEAS	GNSS Evolutionary Architecture Study
GLONASS	Globalnaja Nawigazionnaja Sputnikowaja Sistema
GNSS	Global Navigation Satellite System
GBAS	Ground-Based Augmentation System
GPS	Global Positioning System
HAV	Highly Automated Vehicles
HDOP	Horizontal Dilution of Precision
HMI	Hazardous Misleading Information
HPL	Horizontal Protection Level
ICAO	International Civil Aviation Organization
IELSA	Interval Extension of Least-Squares Adjustment
IGS	International GNSS Service
IMU	Inertial Measurement Unit

INS	Inertial Navigation System
IR	Integrity Risk
IRNSS/NavIC	Indian Regional Navigation Satellite System/Navigation Indian Constellation
ITS	Intelligent Transport Systems
LOS	Line-of-Sights
LP	Linear Programming
LS	Least-Squares
LSA	Least-Squares Adjustment
MDB	Minimum Detectable Bias
MEO	Medium Earth Orbit
MIB	Minimum Identifiable Bias
MGEX	Multi-GNSS Experiment
MSAS	Multi-functional Satellite Augmentation System
NCXPDF	Non-Central Chi Square Probability Density Function
NDB	Non-Detectable Biases
NPA	Non-Precision Approach
OIB	Observation Interval Bound
OMC	Observed-Minus-Computed
OS	Open Service
PDF	Probability Density Function
PDP	Primal-Dual Polytope
PE	Position Error
PFA	Probability of False alarm
PGT	Polytope Global Test
PL	Protection Level
PLT	Polytope Local Test
PMD	Probability of Missed Detection
PMDB	Polytopal Minimum Detectable Bias
PNT	Positioning, Navigation and Timing
PMI	Probability of Misleading Information
PPP	Precise Point Positioning
PRN	Pseudo-Random Noise
PRS	Public Regulated Service
QZSS	Quasi-Zenith Satellite System
RAIM	Receiver Autonomous Integrity Monitoring
RB	Residual-Based
SAE	Society of Automotive Engineers
SBAS	Satellite-Based Augmentation System
SDCM	System for Differential Correction and Monitoring
SIVIA	Set Inversion Via Interval Analysis
SIS	Signal in Space

SNAS	Satellite Navigation Augmentation System
SNR	Signal to Noise Ratio
SPP	Single Point Position
SS	Solution Separation
STEC	Slant Total Electron Content
TTA	Time to Alert
TEC	Total Electron Content
ToA	Time of Arrival
US	United States
VDOP	Vertical Dilution of Precision
VPL	Vertical Protection Level
WAAS	Wide Area Augmentation System
WGN	White Gaussian Noise
XSPDF	Chi-Square Probability Density Function
ZMDB	Zonotopal Minimum Detectable Bias

Table of contents

1	Introduction	1
1.1	Motivation	1
1.2	Objective & Research Questions	3
1.3	Outline of the Thesis	3
2	Related Work and Theory	5
2.1	GNSS Positioning	5
2.1.1	GNSS Constellations	5
2.1.2	Position Estimation	6
2.1.3	Measurement Errors in GPS Measurements	8
2.2	Reliability	11
2.3	Integrity	13
2.3.1	Conventional RAIM	13
2.3.2	Advanced RAIM	14
2.3.3	Augmentation Systems	15
2.3.4	Derivation of Conventional RAIM	15
2.3.5	Protection Level	24
2.4	Interval Mathematics	26
2.4.1	Basic Interval Mathematical Operations	27
2.4.2	Interval Vectors and Matrices	28
2.4.3	Interval Functions	28
2.4.4	Set Inversion via Interval Analysis	29
2.4.5	Contractors	30
2.4.6	Application of Interval Analysis to Navigation	32
2.5	Determination of Observation Interval Bounds	33
2.5.1	Probabilistic Approaches with a Priori Integrity Risk	33
2.5.2	Sensitivity Analysis of the Measurement Correction	34
2.5.2.1	Concept	34
2.5.2.2	Klobuchar Ionospheric Model	35
2.5.2.3	Saastamoinen Tropospheric Model	36
2.5.3	Expert Knowledge and Desired Size of the Bounding Zone	37
3	Integrity Approaches Based on Interval Mathematics and Set Theory	39
3.1	Interval Extension of Least-Squares Adjustment	39
3.2	Set Inversion Via Interval Analysis	41
3.3	Linear Programming Bounding Method	43
3.4	Developed Method Based on Primal-Dual Polytope and Intervals	45
3.4.1	Polytopes and Zonotopes	47
3.4.2	Formulation and Methodology	49
3.4.3	Interpretation of Bounding Zones and Related Consistency Measures	51
3.4.4	Minimum Detectable Bias Definition	58
3.4.5	Integrity Measures Via Zonotopes and Polytopes	61
4	Performance Analysis of the Developed Methods by Monte Carlo Simulations	67
4.1	Introduction	67

4.2	Characterization of a Nominal Behavior	67
4.3	Proposal to Select the Critical Value of the Polytope Tests	71
4.4	Impact of Biases	72
4.4.1	Introductory Example	72
4.4.2	Impact of Different Biased Satellites and Observation Interval Bounds	73
4.4.3	Impact of Different Biased Satellites and Satellite Geometry	73
4.5	Analysis of the Polytope Global and Local Tests	77
4.5.1	General Proceeding	77
4.5.2	Critical Detection Scenarios - Correlated Satellites	82
4.5.3	Critical Detection Scenarios - Bad Geometry	85
4.6	Probabilistic Test Statistic Results	85
4.6.1	Results of Probabilistic Test Statistics	85
4.7	Comparison Between Probabilistic Tests and Polytopal Test	87
4.7.1	Good Satellite Geometry	87
4.7.2	Bad Satellite Geometry	88
4.8	Analysis of Protection Levels	90
4.8.1	Zonotopal Horizontal and Vertical Protection Levels	90
4.8.2	Statistical Based Horizontal and Vertical Protection Level	92
5	Real Data Analysis	95
5.1	Introduction	95
5.2	Positioning Analysis	96
5.2.1	Results from Scenario 1 - Urban Area	96
5.2.2	Results from Scenario 2 - Semi-Urban Area	99
5.3	Fault Detection and Exclusion	103
5.4	Minimum Detectable Bias	105
5.5	Protection Level	107
6	Conclusions and Outlook	111
	Bibliography	126
	Acknowledgments	127
	Curriculum Vitae	129

1 Introduction

1.1 Motivation

Global Navigation Satellite Systems (GNSSs) play an important role in today's life, especially in Positioning, Navigation and Timing (PNT) applications. In addition to the classical geodetic applications, like surveying, telecommunication networks, power plant optimization, fleet management, railway, and financial transaction benefit from GNSS-based services. Moreover, GNSS-based navigation is moving toward critical applications, like e.g., aviation, maritime, and autonomous driving cars. Reliable confidence domains and integrity measures for positioning and navigation with GNSS are of great importance for any navigation system, especially for safety-critical applications. Integrity measures the trust of the performance and the correctness of the information delivered by any navigation system. The performance of any navigation system is characterized by four factors: accuracy, integrity, continuity, and availability. When we are dealing with safety-critical applications, integrity is the most important factor in system performance. We could have the best accuracy and the solution could be continuously available at any time, but without valid information about system integrity, we cannot rely on this system.

There are different methods to provide integrity information about GNSS. The most used methods are the Satellite-Based Augmentation Systems (SBASs) (Ventura-Traveset et al., 2006; Enge and Van Dierendonck, 1996) and the Ground-Based Augmentation Systems (GBASs), (Felux et al., 2013). These solutions are very powerful and can provide timely corrections and integrity information to the user. The drawbacks of these integrity systems are their very complex and expensive infrastructure and costly maintenance.

Another method to provide integrity information is a computation inside the user's GNSS receiver itself using redundant observations. This method is called RAIM. There are several algorithms to compute integrity information using RAIM for the positioning solution. The main requirement for RAIM is having redundancy in the observations. For the GNSS position solution, we need at least five measurements to detect a fault or satellite anomaly and six measurements to isolate, i.e., identify, the faulty measurement. Most of the existing RAIM algorithms assume that there is only one faulty measurement at a time. There exist Advanced Receiver Autonomous Integrity Monitoring (ARAIM) algorithms that deal with multiple-faults at the same time. However, Multiple Fault RAIM algorithms are time-consuming since many alternative hypotheses must be computed and it is not easy to reach the time to alert specification in safety-critical applications such as landing approaches in civil aviation.

Integrity definition is somewhat vague and needs further specification. This is achieved by means of the concepts of Alert Limit (AL), Integrity Risk (IR), Protection Level (PL) and Time to Alert (TTA), FAA (2008); Tossaint et al. (2014); Speidel et al. (2013):

- Alert Limit: The alert limit for a given parameter (i.e., position) is the error tolerance not to be exceeded without issuing an alert.
- Time to Alert: The maximum allowable time elapsed from the start of the navigation system being out of tolerance until the equipment announces the alert.
- Integrity Risk: Probability of the position error exceeds the AL.
- Protection Level: Statistical error bound on the absolute position error PE with a probability smaller than or equal to the integrity risk that the PE exceeds the error bound.

The above-mentioned definitions are acquainted from DoD/DHS (2008). A GNSS integrity concept has been firstly developed and formalized in the aviation field for Safety-of-Life (SoL) applications ICAO (2006); RTCA (2006). It depends on the phase of operation of flight, different requirements assigned in

terms of accuracy, integrity, continuity, and availability, where integrity is assigned in terms of IR, AL, and TTA.

Table 1.1 exhibits the required navigation performance for each phase of civilian flights. These requirements have been endorsed by the International Civil Aviation Organization (ICAO). Due to the increase in civil aviation worldwide and the limitation of traditional air traffic control systems to manage the demand for airspace capacity, ICAO promotes more research and new methods to make recommendations for the future development of navigation systems for civil aviation Ochieng et al. (2003).

In addition to GNSS integrity in civil aviation, GNSS integrity is gaining a lot of interest in the transportation fields e.g., railways and autonomous cars, especially in the urban areas, Joerger and Spenko (2017); SEA (2018). New requirements will be defined for each application. In particular, autonomous driving cars are on their way, having specific integrity requirements and a lot of interest is spotting on the ARAIM techniques, since GBAS and SBAS will not be sufficient for such an application. In autonomous driving the GNSS stand-alone solution is not enough and needs to be integrated with a different sensor such as Inertial Measurement Unit (IMU), lidar, radar, cameras, odometer, and so on. However, the integrity of the GNSS solution is of great importance since GNSS receiver is the only sensor that can provide a geo-referenced position solution. As in aviation, where the performance requirements are defined by ICAO, the definitions for terms related to driving automation system for on-road motor vehicles are defined by the international Society of Automotive Engineers (SAE), Reid et al. (2019). Six different levels of driving automation have been defined from no automation to full automation. Depending on the level of driving automation, specific integrity requirements will be defined. Some of the self-driving cars are already under test and all automotive companies around the globe show a big interest in autonomous driving cars. The integrity of the GNSS solution is one of the most important factors to achieve the requirement of autonomous cars due to the complexity of the environment and lack of infrastructures. Very low integrity risk will be on-demand and even a guaranteed navigation solution. Due to this huge interest in the integrity of the navigation solution, it is worth doing research in this field, improving existing methods and algorithms, or developing new methods that can overcome the shortcoming of the existing methods and thus provide high integrity solutions and guaranteed solutions if possible.

Table 1.1: GNSS Aviation Operational Performance Requirements. (H) denotes the horizontal requirement and (V) denotes the vertical requirement

Operation	Accuracy (95%)	Integrity Risk 1-Integrity Risk	Alert Limit	Time to Alert	Continuity	Availability
Oceanic	3.7 km	$1-10^{-7}/h$	7.5 km	300 s	$1-10^{-4}/h$ to $1-10^{-8}/h$	0.99 to 0.99999
En-route	3.7 km	$1-10^{-7}/h$	3.7 km	300 s	$1-10^{-4}/h$ to $1-10^{-8}/h$	0.99 to 0.99999
Terminal	0.74 km	$1-10^{-7}/h$	1.85 km	15 s	$1-10^{-4}/h$ to $1-10^{-8}/h$	0.99 to 0.99999
NPA	220 m	$1-2 \times 10^{-7}/h$	556 m	10 s	$1-10^{-4}/h$ to $1-10^{-8}/h$	0.99 to 0.99999
APVI	16 m	$1-2 \times 10^{-7}/$ any approach	40 m (H) 50 m (V)	10 s	$1-8 \times 10^{-6}/$ 15sec	0.99 to 0.99999
APVII	16 m	$1-2 \times 10^{-7}/$ any approach	40 m (H) 20 m (V)	6 s	$1-8 \times 10^{-6}/$ 15sec	0.99 to 0.99999
Cat.I	16 m	$1-2 \times 10^{-7}/$ any approach	40 m (H)	6 s	$1-8 \times 10^{-6}/$ 15 s	0.99 to 0.99999
Cat.II	6.9 m	$1-10^{-9}/15$ s	17.3 m (H) 5.3 m (V)	1 s	$1-4 \times 10^{-6}/$ 15 s	0.99 to 0.99999
Cat.III	6.9 m	$1-10^{-9}/15$ s	15.5 m (H)	1 s	$1-2 \times 10^{-6}/$ 30 s (H) $1-2 \times 10^{-6}/$ 15 s (V)	0.99 to 0.99999
		5.3 m (H)	5.3 m (H)			

There exists a variety of RAIM techniques for determining integrity based on self-consistency checks on receiver measurements. These techniques can be divided into two categories

- Snapshot technique: RAIM uses the current measurement to provide integrity measures.
- Filtering or Averaging technique: RAIM uses the previous and present measurements to provide integrity measures.

Both of the above-mentioned techniques assume that the measurements are affected by White Gaussian Noise (WGN) errors and treat the problem purely stochastically. The traditional RAIM techniques have their limitations and they are based on hypothesis testing. For instance, the wrong assumption on the distribution of the residuals could provide misleading information. Hypothesis testing is based on pre-defined Probability of False alarm (PFA) and Probability of Missed Detection (PMD).

Alternative methods based on interval analysis and set theory have been developed in the last decade. The three main methods are Interval Extension of Least-Squares Adjustment (IELSA), zonotope interval extension of least-squares, and Set Inversion Via Interval Analysis (SIVIA). Robust SIVIA is used to compute the three-dimensional bounded zone in real-time. This new approach differs significantly from the usual Gaussian error model since the satellite positions and the pseudo-ranges measurements are represented by intervals bounding the true value with particular confidence. Interval analysis community claims that interval mathematical computations are rigorous and guaranteed, see Tucker (2011). There are few applications of interval analysis on GNSS and it worth invest in those methods and see what kind of information we could extract and if all the interval computation is guaranteed.

1.2 Objective & Research Questions

The focus of this thesis is on developing alternative integrity approaches based on interval analysis and set theory. The two main RAIM techniques which are widely implemented in GNSS applications, i.e. Residual-Based (RB) and Solution Separation (SS) RAIMs will be investigated and compared two the interval-based methods in simulated scenarios and in real Global Positioning System (GPS) data.

The objective of this thesis is to investigate the most used probabilistic hypothesis testing techniques in RAIM applications. As well as, investigate the already existing interval-based methods and develop our own method based on interval mathematics and set theory for integrity monitoring. The focus is on the consistency measures, fault detection and exclusion FDE, and derivation of the protection level PL. Apart from that, the interval-based method is known to provide a guaranteed solution under some assumptions. The objective here is to see if it is possible to have a guaranteed solution and integrity measures. Which information can be 100 % guaranteed and which information can be guaranteed to a certain confidence level.

1.3 Outline of the Thesis

This thesis is dealing with different GNSS integrity methods based on probabilistic hypothesis testing, pure interval mathematics, and combined interval and set theory. Accordingly, the structure of this thesis is as follows.

Chapter 2 explains the fundamental of the GNSS positioning and navigation from the system level to the user level including the estimation process with least-squares adjustment and its related parameters. Then, an overview of reliability and integrity measures of the GNSS positioning and related work is given. In addition, I will categorize existing RAIM methods in the literature and categorized them according to the writer. Then, the two main RAIM approaches RB and SS that are based on probabilistic hypothesis testing are explained in detail with an overview of the testing procedure especially when the test has a χ^2 -distribution. Finally, an overview and basics of interval arithmetic are provided.

Then, the main contribution of this thesis is in chapter 3. First, the interval-based methods namely interval extension of least-squares adjustment IELSA and set inversion via interval analysis SIVIA are introduced

and compared in a simulated scenario. In addition to these two methods, a new method based on linear programming LP and interval analysis is developed during this work and introduced. This method provides the basic idea of our newly developed integrity monitoring method. Then, an integrity monitoring method based on interval analysis and set theory is developed and explained in detail from the transformation of the navigation problem to the convex optimization problem to the derivation of each parameter related to the integrity monitoring. This method provides a polytope as bounding zone and feasible solution of the GNSS positioning and a zonotope confidence domain and protection level. In addition, newly developed consistency measures, minimum detectable bias MDB, FDE, and protection level are explained in detail.

To assess the capabilities of our developed method and compare it to classical used statistic methods of residual-based integrity monitoring and solution separation, an intensive Monte Carlo simulation is performed in chapter 4. In this simulation, different scenarios with different navigation geometry are taken from real GPS measurements and analyzed. Then, in chapter 5 two real test drives in the city of Hanover, Germany is analyzed in terms of positioning accuracy, reliability, integrity, continuity, and availability for all methods.

Finally, a conclusion of this work and the most important findings are presented and an outlook for future work and possible research areas and improvements are proposed in chapter 6.

2 Related Work and Theory

In this chapter, I addressed the concept of positioning and navigation by GNSS, so the reader can have sufficient information on how does the GNSS work. Then, the GNSS related concepts of reliability and integrity will be addressed. Then I will explain the so-called RAIM and categorize the existing algorithms. Afterward, I introduce the basics of interval analysis from a computational point of view and its application to GNSS.

2.1 GNSS Positioning

2.1.1 GNSS Constellations

The first operational GNSS is the GPS, originally NAVSTAR GPS. It is a satellite-based radio navigation system developed by the United States (US) government, particularly by the Department of Defense (DoD) in 1973, and operated by the United States Air Force. The first GPS prototype satellite launched in 1978, and the system was fully operational in 1993 with 24 satellites. It is a military system. However, in the 1980s the US government provided GPS services to the civilians with selective availability. Selective availability is an intentional degradation introduced to the civil GPS signals for security reasons, which was canceled in 2000.

Nowadays, the first and some of the second generation of GPS satellites (Block I, Block II, and Block IIA) are out of use, and the current constellation consists of mixed of modernized satellites (Block IIR and Block IIF), which are 33 operational satellites, Renfro et al. (2018). All GPS satellite signals are broadcast at three frequencies, 1575.42 MHz (L1), 1227.60 MHz (L2), and 1176.45 MHz (L5) DoD/DHS (2020). L5 has been used for secure and robust radio navigation for safety-critical applications, such as aircraft precision approach guidance. The GPS satellite signals use the so-called Code-Division Multiple Access (CDMA) spread spectrum technique, where low bit-rate data is encoded with a high rate Pseudo-Random Noise (PRN) sequence, which is different for each satellite. The civilian code for coarse/acquisition (C/A) transmits data at 1.023 million chips per second, and the precise military P-code transmits at 10.23 million chips per second. The L1 carrier is modulated by both the C/A and P codes, while the L2 carrier is only modulated by the P-code. The GPS satellites block IIIA (L3 signal) broadcast signal at a frequency of 1.38105 GHz only to ground stations. This data is used by the US Nuclear Detonation and Detection System to detect, locate, and report nuclear detonations in the Earth's atmosphere and near space. All GPS blocks together form the so-called GPS space segment which is controlled by the ground segment, Spilker et al. (1996); Meurer and Antreich (2017); Directorate (2019); ICD (2019).

The GPS ground segment consists of a network of ground stations: a master station that monitors and sends commands to all satellites via eleven ground antennas and sixteen monitoring sites, an alternative master control station, four dedicated antennas, and six dedicated monitoring stations. The user segment comprises hundreds of thousands of US military users and millions of civil users around the world. GPS or GNSS users have a very wide range of applications from positioning, timing, and navigation to geodetic and cartographic applications. Nowadays, GPS is used almost in every type of application, i.e. sports, fleet management, cellular telephony, power plants, surveying, tectonics, telematics, clocks synchronization, autonomous vehicles, robotics, and many others. GPS receivers come in different varieties, from devices integrated into cars, phones, and watches, to dedicated device timing and geodetic receivers.

After the development of the GPS, the Russian started developing their own GNSS military system in 1976. The Russian Globalnaja Nawigazionnaja Sputnikowaja Sistema (GLONASS) is developed by the Academician M. F. Reshetnev's State Unitary Enterprise of Applied Mechanics and multiple subcontractors.

GLONASS is composed of 24 operational satellites arranged in three equally-spaced orbital planes. Instead of CDMA, GLONASS uses the so-called FDMA technique, where all satellites transmit the same PRN codes on a specific frequency to each satellite. These frequency bands are: 1602.0–1615.5 MHz for L1 and 1246.0–1256.5 MHz for L2. The new satellite generation (GLONASS-K) use CDMA to transmit signals on a third frequency band around 1204.704 MHz for better interoperability with other GNSSs, Russian Space Systems (2016).

The first civil GNSS was jointly initiated by the European Commission, the European Space Agency (ESA) and the European GNSS Agency under the name Galileo in the 1990s. The motivations behind developing a civil GNSS are the continued dependence on other country navigation systems i.e., GPS and GLONASS, and the fact the previous systems are military and cannot be relied on, especially in safety-critical applications. Currently, there are 22 operational satellites and two satellites under test, while the final system will contain 30 satellites and is expected to be fully operational by 2025, European-Union (2018); EGSA (2020).

Galileo provides an Open Service (OS) and free services like a Commercial Service (CS) and a Public Regulated Service (PRS). The OS signals use the same carrier frequencies as GPS L1 and L5 while CS and PRS transmits a signal called E6 at 1278.75MHz. Galileo provides higher accuracy and precision than the other GNSS due to its complex signal structure which will assort beside the authentication a high level of reliability, integrity, and continuity, Beidleman (2005); Wu et al. (2020). The Galileo signal equal to GPS L5 is called E5a at 1176.45MHz is complemented by the E5b signal at 1207.14 MHz, forming the wide-band signal E5a+b called alternative binary offset carrier (AltBOC) at 1191.795MHz which, among others, provides better multi-path mitigation, Ries et al. (2003).

China also started its GNSS system in 2000, which was called BeiDou Navigation Satellite System (BDS) and consists of two separate satellite constellations. This system is known as BDS-1 and it was decommissioned at the end of 2012. However, the second generation of BDS was already under development since 2011 and this system was known as COMPASS or BDS-2 with ten operational satellites in the Asia-Pacific region at that time. For global coverage, China starts to build the 3rd generation BDS system BDS-3 in 2015. Nowadays, BDS is fully operational with 49 satellites in orbits where 44 satellites are operational and five satellites are not included in the operational orbital constellation, IACPNT (2020). It is claimed that BDS-3 will provide millimeter-level accuracy with post-processing Li (2016); Liu et al. (2014). BDS-3 satellites broadcast signals at the same frequency bands as the other GNSS for interoperable reasons. Besides these four GNSS, there are two regional satellite navigation systems, the Japanese QZSS and the IRNSS/NavIC in India.

Despite all these GNSS which enable multi-constellation processing, this thesis will deal only with GPS code measurements and simulated measurements, since we are developing a new concept of reliability and integrity measures. The new concept can be applied to any GNSS or multi-GNSS observations, but for the sake of simplicity and validity, we will restrict ourselves to GPS observations when we use real data.

2.1.2 Position Estimation

The principle of the position, navigation, and timing PNT in any GNSS is based on measuring the Time of Arrival (ToA) of the satellite signals. A GNSS receiver measures the difference between the transmitted and received signals. The GPS satellites are equipped with atomic clocks and these clocks are synchronized at nanosecond level to GPS time. For GPS, the ground segment monitors all the satellites and synchronizes all of them to the common time scale, the so-called GPS time scale. The correction to GPS time is sent to the receiver via the navigation message using polynomial clock correction coefficients. Contrary, receivers are equipped with inexpensive quartz oscillators and their time is not synchronized to the GPS time scale. So, the user must estimate the fourth parameter besides the 3D position which is the common receiver clock bias δ_A . Multiplying the flight time τ_A^j by the speed of light (c) gives a code measurement usually called pseudo-range measurements. There are two other types of GNSS measurements, the carrier phase, and the Doppler shift. Carrier phase measurements are more precise than the code measurements and the Doppler shift is used to determine independently the velocity. However, in this thesis, we are interested in a GNSS integrity concept more than the precision, so only the code measurements will be used.

The code pseudo-ranges observation equation (2.1), i.e., the functional model for satellite j and station A in an Earth-Centred Earth-Fixed (ECEF) coordinate system, reads

$$PR_A^j(t) = \sqrt{(x_j(t - \tau_A^j) - x_A(t))^2 + (y_j(t - \tau_A^j) - y_A(t))^2 + (z_j(t - \tau_A^j) - z_A(t))^2} + c(\delta_A(t) - \delta_j(t - \tau_A^j)) + I_A^j(t) + T_A^j(t) + M_A^j(t) + w(t), \quad (2.1)$$

where, t is the epoch of reception, $t - \tau_A^j$ the transmission time, both in GPS time scale, τ_A^j the signal travel time, x, y , and z are the coordinates in an ECEF coordinate system, c denotes the speed of light, δ_j satellite clock offset, $I_A^j(t)$ and $T_A^j(t)$ denote the ionospheric and tropospheric delays, respectively, $M_A^j(t)$ is the multipath error and w contain the remaining errors.

There are models and techniques to compensate for each error source, cf. Parkinson et al. (1996); Teunissen and Montenbruck (2017). Subsequently, the corrected observations (OMC) $\Delta l = PR - corrections$ can be computed. The error sources will be discussed in detail in the next section.

The solution of the navigation equation has to be computed. At least four satellites in view are needed to estimate the receiver position and the metric receiver clock offset b_A . If we have more than four satellites in view the system is overdetermined and better estimation can be achieved. If we denote m as a number of satellites in view or the number of available observation, we get the following system of equations:

$$\begin{cases} \Delta l_A^1(t) &= \sqrt{(x_1(t - \tau_A^1) - x_A(t))^2 + (y_1(t - \tau_A^1) - y_A(t))^2 + (z_1(t - \tau_A^1) - z_A(t))^2} + b_A \\ \Delta l_A^2(t) &= \sqrt{(x_2(t - \tau_A^2) - x_A(t))^2 + (y_2(t - \tau_A^2) - y_A(t))^2 + (z_2(t - \tau_A^2) - z_A(t))^2} + b_A \\ \Delta l_A^3(t) &= \sqrt{(x_3(t - \tau_A^3) - x_A(t))^2 + (y_3(t - \tau_A^3) - y_A(t))^2 + (z_3(t - \tau_A^3) - z_A(t))^2} + b_A \\ &\vdots \\ &\vdots \\ &\vdots \\ \Delta l_A^m(t) &= \sqrt{(x_m(t - \tau_A^m) - x_A(t))^2 + (y_m(t - \tau_A^m) - y_A(t))^2 + (z_m(t - \tau_A^m) - z_A(t))^2} + b_A. \end{cases} \quad (2.2)$$

We have to solve this for the station (receiver) position (x_A, y_A, z_A) and its clock offset b_A . There are many ways to solve this system of equations. First of all, the equations are non-linear and most of the methods to solve this system need a linearization. Most receivers and post-processing algorithms are based on Least-Squares (LS) adjustment, which could be sequential, iterative, or recursive, i.e. Kalman filtering, Kalman (1960). There exist other methods that can solve non-linear equations directly without any linearization, but these methods are computationally expensive. Since most of the RAIM algorithms for GNSS standalone solutions are related to LS adjustment, the focus of this thesis is on LS and related RAIM.

Linearizing equation (2.2) via Taylor expansion at some initial values \mathbf{x}_0 , we get the over-determined system of linearized observation equations at every epoch:

$$\Delta \mathbf{l} = \mathbf{A} \Delta \mathbf{x}, \quad (2.3)$$

where $\Delta \mathbf{l}$ denotes the $m \times 1$ vector of Observed-Minus-Computed (OMC) values, \mathbf{A} the $m \times 4$ design matrix containing the partial derivatives w.r.t. the parameters, and $\Delta \mathbf{x}$ the 4×1 vector of parameter corrections to be estimated and added to \mathbf{x}_0 .

$$\Delta \hat{\mathbf{x}} = (\mathbf{A}^T \mathbf{W} \mathbf{A})^{-1} \mathbf{A}^T \mathbf{W} \Delta \mathbf{l}. \quad (2.4)$$

In general, the weighted least-squares principle is applied to obtain best estimates (2.4), Koch (1999); Teunissen (2006), where the observations are weighted depending on the satellite elevation angle El . The stochastic model of the adjustment, which account for the random behavior, allows different weighting,

$$\mathbf{C}_{ll} = \sigma_0^2 \mathbf{Q}_{ll} = \sigma_0^2 \mathbf{W}^{-1}, \quad (2.5)$$

where \mathbf{C}_{ll} is the $(m \times m)$ variance-covariance matrix, σ_0^2 is the prior variance factor and \mathbf{Q}_{ll} is the co-factor matrix whose inverse is the weight matrix \mathbf{W} .

A typical weighting matrix could read: $\mathbf{W} = \text{diag}(\sin^2(El))$, thus taking into account potentially larger deviations at low elevation angles. Other weighting criteria depends on the Signal to Noise Ratio (SNR) or in case of carrier phase measurements depends on signal power to noise ratio $\frac{C}{N_0}$, Luo et al. (2014); Tay and Marais (2013).

Now, the so-called normal equation matrix \mathbf{N} is introduced for the sake of consolidation of all parameters and to be consistent with most of the literature on LS and stochastic models.

$$\Delta\hat{\mathbf{x}} = (\mathbf{A}^T \mathbf{W} \mathbf{A})^{-1} \mathbf{A}^T \mathbf{W} \Delta\mathbf{l} = \mathbf{N}^{-1} \mathbf{n}. \quad (2.6)$$

Then, the co-factor matrix of the estimated parameters $\Delta\hat{\mathbf{x}}$ is the inverse of the normal equation matrix \mathbf{N} :

$$\mathbf{Q}_{\hat{\mathbf{x}}\hat{\mathbf{x}}} = \mathbf{N}^{-1} = (\mathbf{A}^T \mathbf{W} \mathbf{A})^{-1}. \quad (2.7)$$

In addition, the residuals $\hat{\mathbf{v}}$ and their corresponding co-factor matrix $\mathbf{Q}_{\hat{\mathbf{v}}\hat{\mathbf{v}}}$ and the *a posteriori* variance factor $\hat{\sigma}_0^2$ can be computed in the following:

$$\hat{\mathbf{v}} = \mathbf{A} \Delta\hat{\mathbf{x}} - \Delta\mathbf{l} \quad (2.8)$$

$$\mathbf{Q}_{\hat{\mathbf{v}}\hat{\mathbf{v}}} = \mathbf{Q}_{ll} - \mathbf{A} \mathbf{Q}_{\hat{\mathbf{x}}\hat{\mathbf{x}}} \mathbf{A}^T \quad (2.9)$$

$$\hat{\sigma}_0^2 = \frac{\hat{\mathbf{v}}^T \mathbf{W} \hat{\mathbf{v}}}{m - u}. \quad (2.10)$$

The latter three quantities reflect the relationship between the parameters and the observations. They are essential quantities to evaluate the reliability and integrity of the estimation process and the navigation solution, i.e. they can be used to validate the assumptions that have been made on the functional and stochastic model. Usually, the residuals are assumed to have a *Gaussian* distribution which leads to the χ^2 -distribution of the *a posteriori* variance, equation (2.10). The *Fisher* distribution is the result of the division of two χ^2 -distribution. Later on, the residuals and the *a posteriori* variance factor will be used and discussed in hypothesis testing applied on GNSS and compared to other techniques and parameters.

The so-called error ellipse or confidence ellipse can be derived from the co-factor matrix as:

$$\begin{cases} a_1 = \sigma_0 \sqrt{\lambda_1} \sqrt{\kappa} \\ a_2 = \sigma_0 \sqrt{\lambda_2} \sqrt{\kappa}, \end{cases} \quad (2.11)$$

where a_1 and a_2 are the semi-major and semi-minor axes of the error ellipse, respectively, λ_1 and λ_2 are the maximum and minimum eigenvalues of the co-factor matrix of the estimates, respectively, and κ is a scalar factor representing the confidence level computed from χ^2 -distribution with desired confidence and Degree of Freedom (DoF) equal to 2 in the 2D case. The χ^2 -distribution is a result of the assumption that the observation error has a *Gaussian* distribution.

2.1.3 Measurement Errors in GPS Measurements

The signal travel time or the propagation time between the satellite and the receiver is estimated by measuring the time difference between a local replica of the C/A code and the received Signal in Space (SIS). There are three different cases of error sources that depend on several factors:

1. At system level:

- Selective Availability (off since May 1st, 2000)
- Errors in the information uploaded by the GNSS ground segments to the satellites, e.g. orbits, ephemeris, clock parameters, etc.

2. Errors occurring during the path of signal from the satellite to the receiver:

- Ionosphere effects
- Troposphere effects

3. Errors at receiver level:

- Receiver noise
- Multipaths, interference signals, jamming, etc.

Errors at the System Level

The first type of errors comes from the GNSS space and ground segments, such as orbits and ephemeris. There are three different types of products provided by the International GNSS Service (IGS) that can be used instead of the navigation message. These products are named Ultra-rapid, Rapid, and final. The Ultra-Rapid is divided into two products: the Ultra-Rapid predicted products that are available in real-time and near real-time use and the Ultra-Rapid observed products which have a latency between three to nine hours. The IGS rapid and final products have a latency between 17 to 41 hours and eleven to 17 days, respectively. The final product is very useful for post-processing applications since it provides very accurate and precise information. These products are provided by analysis centers having different IGS stations around the globe, Griffiths and Ray (2009); Dach and Jean (2013); Griffiths (2019).

Since nowadays multi-GNSS constellations are available and new challenges arise, especially in high precision applications, the IGS initiated the Multi-GNSS Experiment (MGEX) Experiment in 2011, which is today referred to as IGS Multi-GNSS Pilot Project. MGEX products provide the three main biases the user needs to estimate when using multi-GNSS constellations. These biases are differential code biases, inter-system biases, and carrier phase biases, Montenbruck and Hauschild (2013).

The navigation message contains corrections for ephemeris and clock errors and estimates of the accuracy of the atomic clock. They are based on predictions and may not indicate the actual clock's current state. These problems tend to be very small but may add up to a few meters of inaccuracy. Moreover, the satellite clock drift is affected by the relativistic effect, e.g., GPS the satellite clock frequency is adjusted so that the frequency observed by the user at sea level has the nominal value. The user has to take into account a relativistic periodical effect due to the eccentricity of the satellite orbit, Mingyu and Jeongrae (2015); ICD (2019). At Medium Earth Orbit (MEO) orbital height, half of the error is due to the periodic change in the speed of the satellite relative to the Earth Centred Inertial Frame (ECIF). The other half is caused by the satellite's periodic change in its gravitational potential.

Signal Path Errors

The GNSS satellites are around 20.000 km, 19.100 km, and 23.222 km away from the Earth for GPS, GLONASS, and Galileo orbits, respectively. All GNSS systems transmit radio electromagnetic waves at frequencies between 1146 MHz to 1610 MHz. During the path of the radio electromagnetic waves from the satellites to the Earth's surface, they move through different layers of the atmosphere. There are two layers of the atmosphere that mainly affect the GNSS signals, which are the troposphere and ionosphere.

Troposphere The troposphere is the lowest layer of the atmosphere which contains most of the clouds, rain, and snow. It contains 75% of the atmosphere's mass and 99% of the water vapor, Hofmann-Wellenhof et al. (2008). The average height of the troposphere is around 13 km which varies between 6 km in the polar regions and 18 km in the tropics, Crutzen and Zimmermann (1991). Levering up from the Earth's surface, the temperature of the troposphere decreases about $6.5^\circ / \text{km}$, but the decreasing rate varies from one region to another and from day to night, Witold (2012).

The tropospheric is a non-dispersive medium for GNSS signals which means that refraction is independent of the signal's frequency, the code and carrier phase measurements are affected by the same delay. The electromagnetic signals are affected by the neutral atoms and molecules in the troposphere. The amount of tropospheric delay depends on the temperature, pressure, humidity along the signal path between the satellite and receiver antennas location and in agreement with:

$$\mathbf{T}_A^j = \int_j^A (n - 1) dl, \quad (2.12)$$

where n is the refractive index of air and l represents a line distance. The effect is divided into two main parts: hydrostatic, the dry gases (primarily, N_2 and O_2), and the wet gases, i.e., water vapor components.

$$N = 10^{-6}(n - 1) = N_{dry} + N_{wet}, \quad (2.13)$$

where N is the refractivity. The wet and the dry part of the refractivity have different effects on the GNSS signals. The wet delay is due to the water vapor which depends on the weather conditions. It is relatively small (decimeter level) but it can vary randomly and very fast, so it is not easy to be modeled. Instead, the dry component depends on the local atmospheric pressures and temperature which is very stable and can vary very slowly. It is also easy to measure and predict the variations based on pressure and temperature variations. However, the error due to this component is quite big and varies from 2 to 10 meters between zenith and 10° elevation, respectively.

The effects are called tropospheric delay or tropospheric refraction. The tropospheric delay is minimum (about 2 m) at the zenith direction, and it increases with the increase of the zenith angle of the Line-of-Sights (LOS) to the satellite. At a low elevation angle, i.e., few degrees, the tropospheric delay of the GNSS signal could reach 25 meters. Therefore, the tropospheric effect is an important error source in precise GNSS applications.

There are different models for the tropospheric delay applied in the GNSS community such as the *Hopfield* model, Hopfield (1969, 1971) or the *Saastamoinen* model Saastamoinen (1972, 1973). The atmospheric correction for troposphere in radio ranging is given by equation (2.14)

$$\delta_{s_0} = \beta_1 \frac{(1 + \beta_2 \cos^2(\theta) + \beta_3 H)}{\cos(z)} \left[p + \frac{\beta_4}{T} e + \beta_5 e - B \tan^2(z) \right] + \delta_r, \quad (2.14)$$

where δ_{s_0} is the range correction, p is the total barometric pressure, e is the water vapor partial pressure, T is the absolute temperature in degree Kelvin, B and δ_r are correction quantities, $\beta_1, \beta_2, \dots, \beta_5$ are constants, and z is the apparent zenith distance which can be determined from true zenith distance Z of the satellite by the formula $z = Z - \delta_z$ where

$$\delta_z = \frac{\alpha_1}{T} \tan(Z) (p + \frac{\alpha_2}{T} e) - \alpha_3 \tan(Z) (\tan^2(Z) + 1) \frac{P}{1000}, \quad (2.15)$$

where α_1, α_2 and α_3 are constant coefficients.

Later on, a sensitivity analysis will be performed on this model to determine the observation interval bounds of the tropospheric delay.

Ionosphere The ionosphere layer is the uppermost part of the Earth's atmosphere, from 60 km to 1.000 km, approximately. It is called ionosphere because the atoms present in this layer are ionized by solar radiation resulting in free electrons and ions. The ionosphere as a whole is electrically neutral. The GNSS electromagnetic signals alter its speed when it passes through the ionosphere and the variation of the signal speed depends on the electron density. The GNSS signals are affected by the negatively charged electrons in different ways. The effect on the code measurements is different from the effects on the carrier phase measurements, where phase measurements are affected by advancement, i.e., a negative delay, while the code measurements are influenced by positive group delay, Langley (2011); Klobuchar (1987).

Since the ionosphere is a dispersive medium, the delays of the GNSS signals depend on their frequencies, equation (2.16). The differences $I_{ph,f}$ and $I_{gr,f}$ are called the phase and code ionospheric refraction and, the integral is defined as the Slant Total Electron Content (STEC), equation (2.17).

$$I_p = \frac{40.3 \cdot (STEC)}{f^2}, \quad (2.16)$$

where f is the frequency of the electromagnetic signal,

$$STEC = \int N_e(l) dl, \quad (2.17)$$

where N_e is the electron density in the ionosphere layer.

Thanks to the frequency dependence, 99.9% of the ionospheric effect on GNSS signals can be removed using a combination of two signals at two different frequencies, the so-called ionosphere-free linear combination (see equation (2.18) phase measurements and equation (2.19) code measurements) for dual-frequency receivers, Odijk (2003); Hofmann-Wellenhof et al. (2008). The differences between using single frequency

receiver and dual-frequency receiver for Precise Point Positioning (PPP) are highlighted in Van Der Marel and De Bakker (2012)

$$\phi_{Iono-free} = \frac{f_1^2 \cdot \phi_{L1} - f_2^2 \cdot \phi_{L2}}{f_1^2 - f_2^2} \quad (2.18)$$

$$PR_{Iono-free} = \frac{f_1^2 \cdot PR_1 - f_2^2 \cdot PR_2}{f_1^2 - f_2^2}. \quad (2.19)$$

The ionosphere-free linear combination eliminates the systematic errors due to the ionosphere but it increases the measurement noises by a factor of three. To compensate for the ionospheric effect for single-frequency receivers, the ionospheric prediction model has to be applied. The models are not very accurate and can remove around half to two-thirds of the error. Different GNSSs use different models, e.g. GPS use the *Klobuchar* ionospheric model while Galileo use the *NeQuick* model that is presented in, Nava et al. (2008). In this thesis, we will focus on the *Klobuchar* model that is presented in Klobuchar (1987), since we are going to use GPS measurements in our experimental data. The *Klobuchar* ionospheric model (equation 2.20) will be used to correct the GPS code measurements and sensitivity analysis will be performed on this model to derive physically meaningful interval bounds.

$$I_{L1} = \begin{cases} \left[5 \cdot 10^{-9} + \sum_{n=1}^4 \alpha_n \phi_m^n \cdot \left(1 - \frac{X_I^2}{2} + \frac{X_I^4}{24} \right) \right] \cdot M_f & ; |X_I| \leq 1.57 \\ 5 \cdot 10^{-9} \cdot M_f & ; |X_I| \geq 1.57, \end{cases} \quad (2.20)$$

where M_f is the mapping function of the satellite elevation angle, ϕ_m^n is the geomagnetic latitude, $X_I = \frac{2\pi(t-50400)}{\sum_{n=0}^3 \beta_n \phi_m^n}$, α_n and β_n are the coefficients provided by the GPS navigation message.

Errors at the Receiver Level

At the receiver level, different types of errors can occur. The receiver noise depends on the receiver itself since electronic devices have different types of noise and sometimes different items from the same equipment could suffer from different noise. Usually, the receiver noise is treated as white noise, Misra and Enge (2011). Another very important error at the receiver level is the multipath due to the reflection of the signals by some obstacle, such as the wall of a building. This reflection makes the path of the signal from the satellites to the receiver's antenna a little bit longer and also can deteriorate the signal power as discussed in Tranquilla and Carr (1990); Wells et al. (1987); Van Nee (1992). Using a high-end antenna can improve and minimize the multipath error, e.g. reduce the signals coming from low elevation angles. In this work, we focus on the GNSS applications in urban areas where the multipath is very high, so we consider the multipath error as an outlier. Other errors at receiver level are interference of other electromagnetic signals, jamming, and spoofing, Humphreys et al. (2008); Nicola et al. (2010); Motella et al. (2010); Borio et al. (2016); Berardo et al. (2016). However, jamming and spoofing will not be the type of biases that are discussed in this work.

2.2 Reliability

Reliability indicates the ability of the system to detect faulty measurements and exclude them. Usually, for any navigation system and depending on the application, different requirements are demanded in terms of reliability and integrity. The algorithms should be designed in such a way as to achieve those requirements and to be able to warn the user at a specific time if the integrity of the system is violated. The reliability of a navigation system or any theoretical and practical development in the area of statistic and stochastic processes is one of the most important parameters. Back in the 1960s, the quality of geodetic networks was measured concerning the accuracy and the reliability of the results. Reliability concepts were introduced by Baarda (1967, 1968) to detect gross errors in geodetic network measurements. This approach is known as the data snooping technique. The concept of reliability continues to be developed with time and introduced to different applications especially, in geodetic one Teunissen (1985); De Jong and Teunissen (2000). Later

on, it has been introduced to the Monte Carlo methods by Lehmann and Scheffler (2011) applied on geodetic networks.

Since data snooping is based on hypothesis testing, the main issue is to have redundant measurements. In the case of GNSS applications, we need four satellites in view to estimate the receiver position and its clock offset. To detect biases or faulty measurements, we need one more, i.e., five satellites in view. To exclude the faulty measurements, we need one more satellite, i.e., six satellites in view. This is due to the need for redundancy in the test statistic which should be at least one or more for the detection and two or more for the isolation. Since in the isolation process different sets of the measurements have to be tested separately, the redundancy in the total measurements should be two, so that the redundancy in the separate sets is one. Once the requirement of at least six satellites is achieved, fault detection and exclusion could be implemented in various ways. Reliability is divided into two separate parts.

Internal reliability is defined as the ability to detect outliers in the observations, which is quantified the minimum detectable observation errors in the geodetic network. This is identical to the so-called Minimum Detectable Bias (MDB) in the hypothesis test statistic and RAIM algorithms, Teunissen (1998). Assuming normally distributed observation errors, the non-centrality parameter depends on the chosen probability of false alarm (the significance level) and the detection power (test quality) that separates the hypothesis H_0 : the case of no-fault from the faulty case (alternative hypothesis H_1), Teunissen (2006). In general, an overall model test or global test is preceding the individual outlier test:

$$T_{gl} = \frac{\hat{\mathbf{v}}^T \mathbf{W} \hat{\mathbf{v}}}{\sigma_0^2} : \begin{cases} F_{(m-4, \infty)} | H_0 \\ F_{(m-4, \infty, \lambda_0)} | H_1, \end{cases} \quad (2.21)$$

where σ_0^2 is the prior variance factor, $\hat{\mathbf{v}}$ is the vector of estimated residuals, \mathbf{W} is the weight matrix, and λ_0 is the non-centrality parameter of the *Fisher* distribution. The global test statistics T_{gl} follows a Fisher F -distribution of $f = m - 4$ degrees of freedom in the fault-free case H_0 and a non-central F -distribution in the faulty case. This test can be transformed into a χ^2 distribution by taking into account only the nominator ($\hat{\mathbf{v}}^T \mathbf{W} \hat{\mathbf{v}}$). The redundancy number has a χ^2 distribution under the assumption that the vector of residuals $\hat{\mathbf{v}}$ normally distributed.

In the perspective of the LS adjustment and the residual-based RB test statistic, equation (2.21), the most common MDB is derived from hypothesis testing of individual outliers in observations:

$$\text{MDB}_i = \nabla_i = \frac{\sigma_0}{w_i} \cdot \sqrt{\frac{\lambda_0}{q_{v_i v_i}}} \quad (2.22)$$

where w_i is the weight of the i -th observation which depends on the elevation angle, $q_{v_i v_i}$ is the estimated co-factor of the i -th observation's residual, the non-centrality parameters λ_0 of the *Normal*-distribution is a function of PFA, PMD and the DoF. The probabilities of error and the non-centrality parameters λ_0 must be adjusted, e.g. by the so-called β -method, see Baarda (1968); Teunissen (2006).

In the above test equation (2.21), there is a single alternative hypothesis, so that the MDB is equivalent to the Minimum Identifiable Bias (MIB). The MIB is the minimum bias that can be isolated when the global test failed, i.e. a bias is detected. The test statistic could be constructed with multiple alternative hypotheses, i.e., one alternative for each measurement and in this way the MDB is not equivalent anymore to the MIB and the expression ($\text{MIB} \geq \text{MDB}$) holds, Imperato et al. (2019). However, the MDB of the multi-alternative hypotheses is smaller than or equal to the MDB of a single hypothesis. So, for single alternative hypothesis holds ($\text{MDB} = \text{MIB}$), while for multiple alternative hypotheses the MDB decreases at the cost of increasing the MIB.

External reliability is defined as the impact of undetected observation errors on the estimated parameters. The effect of undetected observation errors smaller than MDB on the estimated parameters is given in the following equation:

$$\nabla_{\mathbf{x}_i} = (\mathbf{A}^T \mathbf{W} \mathbf{A})^{-1} \mathbf{A}^T \mathbf{W} \mathbf{C}_i \nabla_i, \quad (2.23)$$

where \mathbf{C}_i is a selection vector of $m \times 1$ dimension and with zero entries everywhere except the i -th entry which is equal to one, corresponding to single MDB in the i -th observation. This shows the effect of the MDB of the i -th observation on the whole vector of estimated parameters.

2.3 Integrity

Integrity is the measure of the trust that can be set in the correctness of the information provided by any navigation system. Integrity contains the capability of the system to warn the user at a specific time in case the system does not provide the required performance. For each application with specified IR and AL, the system should provide integrity with these specifications, where the PL does not exceed the AL and in case it is exceeded, the system can notify the user with the TTA. In the GNSS field, there are a large number of methods and techniques to deliver integrity measures such as: GBAS, SBAS, and various RAIM algorithms.

Integrity in the navigation solution is troubled by the errors and biases which could be due to different stages in the navigation system. The GNSS anomalies and biases could arise from receiver level, system-level such as Signal in Space errors, and signal propagation, or from its augmentation system if in use for some application. Since anomalies and biases could occur at different stages, the integrity could be monitored at different stages, i.e. at user level via RAIM algorithms, or at GNSS control segment, or via augmentation systems such as GBAS and SBAS. A literature review of GNSS integrity is presented in Zhu et al. (2018).

The interest in GNSS integrity monitoring is increasing over time since more safety and liability critical applications are depending on GNSS integrity. First, GNSS integrity was mostly related to aviation applications, Ochieng et al. (2003), then its spread in maritime Porretta et al. (2016); Zalewski (2019) and railway applications, EGSA (2015); Stallo et al. (2019). In the past few years, the interest in autonomous driving cars is increasing, and a new integrity monitoring technique is needed, and an especially self-dependent system like RAIM. In the following, we will provide an overview of the integrity methods and try to classify them by different categories depending on the algorithm's concepts.

The algorithms can be classified with respect to the level of autonomy, i.e., whether they are fully self-autonomous or they depend on other systems and on the ability to detect and exclude a single fault or multiple faults. There are integrity monitoring algorithms that depending on other navigation systems that provide them some integrity information or other information that will be used to compute the integrity information, e.g., corrections provided by the geostationary satellites to the user Ventura-Traveset et al. (2006). Usually, the augmented systems in which those integrity algorithms are used, provide higher performance to the user simply by the fact that the parameters represent the current environment more realistically. Fully receiver-autonomous algorithms need to make very conservative assumptions about their conditions which decreases their performance.

The conventional RAIM algorithms are fully self-autonomous and they use only the receiver measurements to compute integrity information without any support from an external party. In addition, conventional RAIM is capable to detect and exclude single fault. On the contrary, ARAIM algorithms are sustained by external reference monitoring networks that send the needed information to the user and they are multi-faults algorithms. Likewise, the augmentation systems algorithms such as GBAS and SBAS are provided by information from external sources. For example, SBAS is fed with information continuously by ground control network stations (monitoring and reference stations). An overview of integrity algorithms is illustrated in Figure 2.1. Note that this discrimination or categorization reflects the author's view and it is similar to the categorization in Mink (2016). There is no official categorization of the integrity monitoring in GNSS application. However, we would like to categorize them in order to focus on one category for the rest of this thesis, i.e. the conventional RAIM.

2.3.1 Conventional RAIM

The conventional RAIM algorithms have full receiver autonomous integrity monitoring capability without any external information. Usually, conventional RAIM executes a consistency check of the observations and compute a protection level PL with predefined integrity parameters, i.e. PFA, PMD, and IR. If the consistency check fails, the algorithms try to identify the faulty observation and remove it from the position computations. In case the detection and isolation of the fault do not match the integrity requirements, i.e. AL, TTA, and IR, the algorithm decides to disregard the positioning solution and raises an integrity flag.

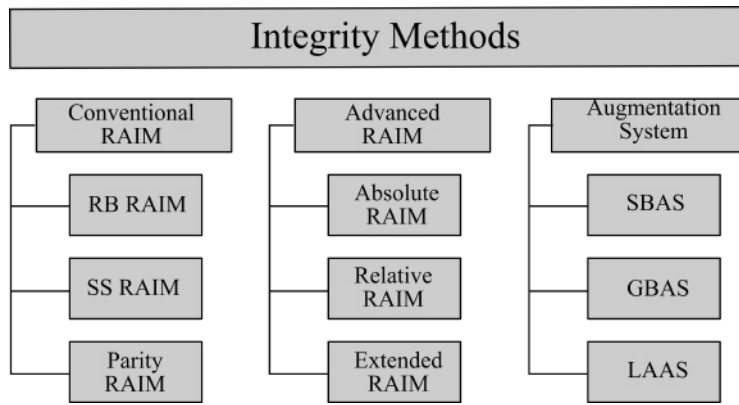


Figure 2.1: Overview of Integrity Methods

There are different algorithms in the conventional RAIM category and the most used algorithms are listed in figure 2.1. The three main conventional algorithms are RB RAIM, SS RAIM, and parity RAIM. These three RAIM algorithms are all extensions of the least-squares LS estimation. The residual-based RAIM can be performed in different ways such as in parity space (Brown (1997)) and range comparison (Lee (1986)) which are equivalent according to Brown (1992). Both residual-based and parity RAIM perform inconsistency check in the observation domain. On the contrary, solution separation RAIM performs inconsistency check in the position domain directly, Brown and McBurney (1988); Joerger et al. (2016a,b). A comparison between residual-based, parity space and solution separation is conducted in Joerger et al. (2013, 2014). There is a very large number of algorithms and for the purpose of this thesis we cannot cover all of them. Sometimes the same algorithms are named differently, for example residual-based could be called χ^2 RAIM since the test statistic is assumed to have a χ^2 -distribution. A χ^2 test applied on GNSS and INS is done in Sturza (1988), a comparison with fixed and variable threshold algorithms is done in Sturza and Brown (1990), A χ^2 test applied on GPS and Galileo code observations is performed in Belabbas and Gass (2005), an analysis of the performance of different conventional RAIM algorithms applied on GPS after the selective availability set to zero is presented in Murphy and Harris (2008). Other conventional RAIM is used for specific applications such as vertical guidance in Martineau et al. (2009), and for electronic toll in Salós et al. (2013), and implementation of iterative RAIM in software receiver, Rakipi et al. (2015). The derivation of residual-based, parity space and solution separation RAIM will be discussed in details in the section 2.3.4. The conventional RAIM is of our interest more than other types of integrity monitoring approaches and our developed method falls in this category. It can be extended to ARAIM, but it is a new development in the integrity monitoring and needs to be well finalized before being extended to ARAIM.

Already existing RAIM algorithms and our developed algorithm that will be studied in this thesis belong to this category. Other algorithms are not studied in detail due to unfair comparison since they depend on external entities.

2.3.2 Advanced RAIM

Advanced Receiver Autonomous Integrity Monitoring is a new development of conventional RAIM and focuses on the vertical guidance, Blanch et al. (2010a). It improves enormously the horizontal performance. It is based on multi-constellations for better navigation geometry and redundancy as well as on multi-frequencies to overcome the problem of the ionospheric delay. Using multi constellations GNSS, the assumption of one fault at a time is no more valid, so ARAIM has to be a multi-faults algorithm (Blanch et al. (2014)). However, the increased number of satellites in view has a large positive impact on positioning performance. In addition to the satellite failures, ARAIM has to detect the effect of a whole single constellation, i.e., the so-called constellation-wide failures.

As conventional RAIM algorithms have a wide range of different techniques, likewise, ARAIM also has a wide range of techniques such as solution separation and χ^2 ARAIM, Joerger and Pervan (2014, 2016). The most used algorithm is based on solution separation technique, Blanch et al. (2007).

The GNSS Evolutionary Architecture Study (GEAS) panel supports the development of ARAIM algorithms, GEAS (2010). There are 3 different main methods that have been identified under the ARAIM category which make use of an independent reference ground network that computes respective data and which is sent to the user:

- Absolute RAIM technique, Blanch et al. (2010b).
- Relative RAIM technique, Gratton et al. (2010); Lee (2011).
- Extended RAIM technique, Feng et al. (2009); Hewitson and Wang (2010); Jokinen et al. (2012).

Some of these algorithms are called carrier phase RAIM since they are based on the carrier phase observations. However, there is no such categorization of RAIM, and we try to categorize all RAIM and ARAIM algorithms depending on the capability of the number of faults that can be detected and the use of external aiding systems.

2.3.3 Augmentation Systems

Augmentation of GNSS is a technique used to enhance the performance of the navigation system in terms of accuracy, reliability, integrity, continuity, and availability. This is done by integrating external information computed by external ground stations or satellites into the computation of navigation solution and their related parameters. SBAS make use of ground station observations to create a correction message which will be sent via up-link to geostationary satellites and send back to the users as differential signals. The main advantage of SBAS is that it can support a very large area. For example, Wide Area Augmentation System (WAAS) is the American SBAS that is developed to augment the GPS and it is available in the region of North America, while the European SBAS, i.e, European Geostationary Navigation Overlay System (EGNOS) is available in Europe and North Africa.

There are other SBAS such as the Japanese augmentation system Multi-functional Satellite Augmentation System (MSAS), the Indian augmentation system GPS Aided Geo Augmented Navigation (GAGAN), the Chinese augmentation system Satellite Navigation Augmentation System (SNAS), the Russian augmentation system System for Differential Correction and Monitoring (SDCM) which has global coverage.

The GBAS is a local augmentation system that provides differential corrections and integrity information for a small coverage area and is usually used near airports. Reference stations inside the airport and near it measure the GNSS deviations and compute corrections which will be broadcast to the users.

2.3.4 Derivation of Conventional RAIM

Due to the increased liability and safety-critical application in GNSS especially in the Intelligent Transport Systems (ITS) and aviation, there is a need for integrity monitoring to cover the whole Earth. Research started looking for integrity monitoring at the receiver level in the 1980's Parkinson and Axelrad (1987); Sturza (1988); Parkinson and Axelrad (1988). In the last three decades, researchers in GNSS navigation, especially in railway, car, maritime, and aviation showed more interest in integrity monitoring Lee (2007); Binjammaz et al. (2013); Joerger et al. (2016b,a); Wörner et al. (2016); Reid et al. (2019). This increase of interest is due to the increasing number of available satellites in view as a result of the full deployment of GLONASS and the development of Galileo and BDS besides the already existing GPS system. The reason behind that is the fact that the main requirement of any RAIM algorithm is the redundancy in the observations. Redundancy is achieved by having more satellites in view. In addition to that, the interest increases because of automated applications such as HAV which needs an embedded integrity measures system.

The GNSS integrity is mainly based on probability and hypothesis testing theory. Since the most used algorithms in parameter estimation such as LS and Kalman filtering are based on probabilistic distribution assumptions, it makes sense to continue in this manner. Also, integrity is defined by the probability of hazardous situations and the probability of misleading information PMI. Moreover, the hypothesis testing procedures are based on two main probabilistic parameters which are PFA and PMD. PFA is defined as

the significance of the test statistic and as the probability of type I error. PMD is known as the power of the test statistic and the probability of type II error. In addition, the integrity parameters AL, TTA, PL, and IR are defined by probabilistic means. The integrity of any navigation system is defined by the performance as a function of all the above-mentioned parameters and probabilities. For instance, in aviation and depending on the flight stage (the en-route or landing approach), the integrity requirements are different, and different integrity systems are used. RAIM is used during en-route approach while it could not match the requirements for the landing approach where a more sophisticated system is used, e.g. GBAS. The integrity requirements in aviation are discussed in RTCA (2006).

The conventional RAIM algorithms or FDE algorithms can be divided into two categories: performing the FDE in the measurements domain or in the state domain. For each domain there exists different algorithm, so each category can be divided into subcategories. The division depends on the design of the test statistic itself. For example, in the measurement domain there are many different algorithm designs and in particular range comparison, least-squares residual, slope, and parity. Also in the state domain or position domain, there are many different ways to design the test statistic which falls under solution separation RAIM. In particular, the test could be designed to check specific states or to check all the states together (full state). In the following, the two main categories of integrity monitoring using conventional RAIM will be discussed separately in detail. The differences and the similarities will be explained emphasizing the advantages and the drawbacks of each method.

Two principal approaches for integrity monitoring in the observation domain are widely studied and implemented in the literature. The first one is the residual-based approach and the second one is the parity space approach which is also based on the residuals, but the computation of the test statistic is done in the parity space.

In general, the main issue of an RAIM algorithm is the evaluation of the IR which can be expressed in a probabilistic way by the probability of Hazardous Misleading Information (HMI). The HMI is declaring the system available while the Position Error (PE) exceeds the alert limit. Let m be the number of GNSS measurements so that we have m satellites in view. Any measurement could be faulty or fault-free. Let us consider H_i to be the faulty hypothesis corresponding to the i -th measurement and H_0 the fault-free hypothesis. The total number of faulty hypotheses H_i of multiple simultaneous measurement faults is 2^m . Following the law of probabilities, the integrity measures and the availability is expressed as:

$$P(HMI) = \sum_{i=0}^{2^m-1} P(HMI | H_i) P(H_i) < I_{REQ} \quad (2.24)$$

where I_{REQ} is the integrity risk requirement.

Let us now consider PE to be the error in the estimated state, i.e., error in East, North, Up (ENU) local geodetic coordinates or XYZ in a ECEF coordinate system plus the receiver clock offset. As well, let T be the test statistic of the navigation system. The probability of HMI given a hypothesis test statistic H_i , is the joint probability of the PE to be larger than the AL while the test statistic T stays lower than a detection threshold, i.e., the Critical Value (CV), Joerger et al. (2012). Given a hypothesis test statistic H_i , the probability of HMI is:

$$P(HMI | H_i) = P(|PE| > AL, |T| < CV | H_i) \quad (2.25)$$

Next, the residual-based test statistic T is derived from the residual vector and parity vector in the observation domain. Additionally, the test statistic is also derived from the state domain, i.e., position domain.

Measurement Model

The general case of the measurement model in the LS estimator and RAIM detector with m measurements in an u dimensional state space can be addressed in the following measurement equation:

$$\Delta \mathbf{l} = \mathbf{A} \Delta \mathbf{x} + \boldsymbol{\varepsilon} + \mathbf{f}, \quad (2.26)$$

where \mathbf{l} is the $m \times 1$ measurement vector. But in our case it is the OMC vector as explained in section *Position Estimation*, \mathbf{A} is the $m \times u$ design matrix as defined in section 2.1.2, \mathbf{x} is the $u \times 1$ state vector, $\boldsymbol{\varepsilon}$ is the $m \times 1$ measurement noise vector, and \mathbf{f} is the $m \times 1$ fault vector.

Residual-Based Approach

Let us consider the single satellite fault model at the i -th satellite. Then, the failure of the i -th measurement is modeled by $\mathbf{f} = \mathbf{f}_i$, where \mathbf{f}_i is $m \times 1$ vector with the i -th element has some value f and zeros elsewhere.

If $\mathbf{f} = 0$ (fault-free measurements), then, the measurement equation reads:

$$\Delta \mathbf{l} = \mathbf{A} \Delta \mathbf{x} + \varepsilon. \quad (2.27)$$

As discussed before, in order to detect faults in the observations we need to have redundancy so that the condition $m - u > 1$ must holds. Let us assume we are in the faulty hypothesis H_i , the best estimator of the fault vector in the residual-based test statistic can be determined by Teunissen (2006); Bakker et al. (2009):

$$\mathbf{f}_i = \mathbf{c}_i^T \mathbf{W} \hat{\mathbf{v}} \hat{=} [0, 0, \frac{v_i}{w_i}, 0, \dots, 0]^T \quad (2.28)$$

where \mathbf{W} is the weight matrix, $\hat{\mathbf{v}}$ is the vector of residuals, equation (2.8), and \mathbf{c}_i is a vector with zeros except one at the i -th entry. If $i = 3$ and $m = 8$, then $\mathbf{c}_i^T = [0 \ 0 \ 1 \ 0 \ 0 \ 0 \ 0 \ 0]$.

Assuming that the observation errors are zero-mean with a *Gaussian* distribution, implies that \mathbf{f}_i is also normally distributed in the fault-free mode. Then, the test statistic in equation (2.29) has a *Chi-Square* distribution $\chi^2(m - u, 0)$.

$$T_{rb_m} = \left(\mathbf{f}_i^T (\mathbf{c}_i^T \mathbf{W} \mathbf{Q}_{\hat{\mathbf{v}}} \mathbf{W} \mathbf{c}_i)^{-1} \mathbf{f}_i \right) \quad (2.29)$$

The above test statistic can be reduced to the test statistic in equation (2.30), in case a single fault is assumed in the observations, Teunissen and Kleusberg (1998).

$$T_{rb_s} = (\hat{\mathbf{v}}^T \mathbf{Q}_{\hat{\mathbf{v}}}^{-1} \hat{\mathbf{v}}) \quad (2.30)$$

The hypothesis test statistic is constructed as:

$$T_{rb} = (\hat{\mathbf{v}}^T \mathbf{W} \hat{\mathbf{v}}) : \begin{cases} H_0 \sim \chi^2_{(m-u, 0)} \\ H_i \sim \chi^2_{(m-u, \lambda)} \end{cases} \quad (2.31)$$

equivalently, the χ^2 test could be performed using *Fisher* distribution as:

$$T_{rb} = \frac{(\hat{\mathbf{v}}^T \mathbf{W} \hat{\mathbf{v}})}{m - u} : \begin{cases} H_0 \sim F_{(m-u, \infty)} \\ H_i \sim F_{(m-u, \infty, \lambda)} \end{cases} \quad (2.32)$$

Since the two tests are equivalent, the χ^2 test will be used from now on. To perform such a test statistic, a significance level (α) which also means PFA of the test and the power of the test ($1 - \beta$) which means that β is the PMD requirement and should be set in advance. Sometimes, α is called type I error and β is called type II error, Teunissen (2006). Significance level α together with the DoF defines the point of the tail of the χ^2 distribution of errors at which to place the CV. For instance, civil aviation integrity requirements allocate the PFA between 10^{-4} and 10^{-7} depending on particular stage of flight. The purpose of setting very small PFA is to keep the probability of HMI and so the IR extremely low. Table 1.1 depicts the aviation performance requirements for all operational phases. However, α and β have a big impact on the non-centrality parameter λ , which has the main contribution in the MDB computation. This impact will be discussed in the following sections. Figure 2.2 depicts an example of the central Chi-Square Probability Density Function (XSPDF) and Non-Central Chi Square Probability Density Function (NCXPDF) and a computed CV for $\alpha = 0.01$, $\beta = 0.01$ and DoF = 12.

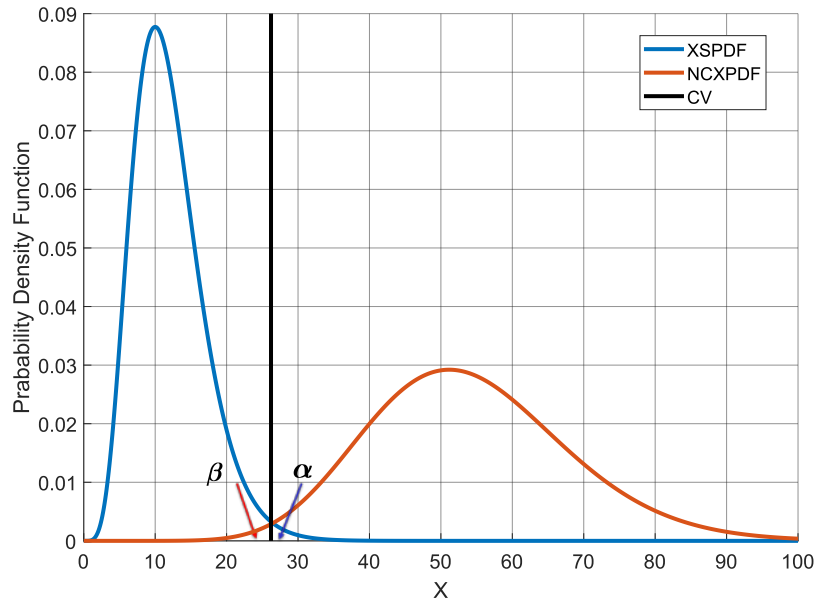


Figure 2.2: Example of XSPDF, NCXPDF and its computed CV with $\alpha = 0.01$, $\beta = 0.01$, and DoF = 12.

The non-centrality parameter λ is the distance between the central and non-central χ^2 -distribution, i.e., the distance between H_0 and H_i . Once the main parameter (α and β) of the test statistic is chosen, the non-centrality parameter can be computed. The computation of the non-centrality parameter is done by adjusting the two distributions. First we compute the CV using the inverse of the XSPDF at the defined level of significant, then the inverse of the NCXPDF is adjusted to the CV and the detection power $1 - \beta$. The adjustment process means the computation of the non-centrality parameter λ .

Parity Space Approach

The test statistic for GNSS can be constructed in different ways. If the test is assumed to have a χ^2 distribution, its behavior is as discussed above. The test can be assumed to have a *Fisher* distribution but the way it behaves will not change. These two distributions have been always used in GNSS RAIM algorithms due to the experience knowledge in this field where the residuals are always assumed to be *Gaussian* distribution.

The residual-based test statistic can also be performed in the parity space as explained in Sturza (1988); Joerger et al. (2013). To do so, an $(m - u) \times 1$ parity vector \mathbf{p} has to be constructed. The LS estimate of the state vector in equation (2.4) can be rewritten as:

$$\Delta \hat{\mathbf{x}} = \mathbf{S} \Delta \mathbf{l}. \quad (2.33)$$

where $\mathbf{S} = (\mathbf{A}^T \mathbf{W} \mathbf{A})^{-1} \mathbf{A}^T \mathbf{W}$ is the $(u \times m)$ generalized left inverse of the design matrix \mathbf{A} . The generalized inverse matrix can also be written as $\mathbf{S} = (\mathbf{A}^T \mathbf{A})^{-1} \mathbf{A}^T$ in case no weight is applied on the observations. The matrix \mathbf{S} serves as a transformation from the measurement space to the state space.

Suppose that the design matrix \mathbf{A} has rank u , then a $((m - u) \times m)$ parity space matrix \mathbf{P} has the following properties: $\text{Rank}(\mathbf{P}) = m - u$, $\mathbf{P} \mathbf{P}^T = \mathbf{I}$, and $\mathbf{P} \mathbf{A} = \mathbf{0}$, where \mathbf{I} is $(m - u \times m - u)$ identity matrix. The parity space matrix \mathbf{P} spans the null space of matrix \mathbf{A} . To compute the matrix \mathbf{P} , an Orthogonal-triangular decomposition of the matrix \mathbf{A} has to be computed. The Orthogonal-triangular decomposition of \mathbf{A} produces two matrices \mathbf{Q} and \mathbf{R} so that, \mathbf{Q} is $(m \times m)$ and \mathbf{R} is upper triangular $(m \times u)$ so that $\mathbf{A} = \mathbf{Q} \mathbf{R}$. Then, \mathbf{P} is the transpose of the concatenated matrix $(m, (m - u))$ \mathbf{Q}_c which is the last $m - u$ columns of \mathbf{Q} . The rows of matrix \mathbf{P} are orthogonal unit basis vectors for the parity space. Then, the parity vector \mathbf{p} can be computed as follows:

$$\mathbf{p} = \mathbf{P} \Delta \mathbf{l} = \mathbf{P} (\boldsymbol{\varepsilon} + \mathbf{f}) \quad (2.34)$$

The parity vector \mathbf{p} is independent of the state vector $\Delta \mathbf{x}$ considering the fact that $\mathbf{P} \mathbf{A} = \mathbf{0}$. The parity vector \mathbf{p} is assumed to be normally distributed with the following expectation value $E\{\cdot\}$ and dispersion $D\{\cdot\}$ or

covariance:

$$E\{\mathbf{p}\} = \mathbf{P}\mathbf{f} \quad (2.35)$$

$$D\{\mathbf{p}\} = \sigma_0^2 \mathbf{I}_{m-u} \quad (2.36)$$

Now, in order to go from the measurement space to the parity and state space, a $m \times m$ matrix \mathbf{H} is constructed as follows:

$$\mathbf{H} = \begin{bmatrix} \mathbf{S} \\ \dots \\ \mathbf{P} \end{bmatrix} \quad (2.37)$$

This matrix divides the m dimensional measurement space into two subspaces: an u dimensional state space and an $(m-u)$ dimensional parity space. The inverse \mathbf{H}^{-1} produce the inverse linear transformation from the state and party states to the measurements space, which enables us to transform the parity vector \mathbf{p} to the measurements space:

$$\mathbf{f} = \mathbf{H}^{-1} \begin{bmatrix} \mathbf{0} \\ \mathbf{p} \end{bmatrix} = [\mathbf{A} \mid \mathbf{P}^T] \begin{bmatrix} \mathbf{0} \\ \mathbf{p} \end{bmatrix}, \quad (2.38)$$

where vector $u \times 1$ of zeros is concatenated with the vector \mathbf{p} which represents the state space. The fault vector \mathbf{f} can be computed directly from the measurement vector $\Delta\mathbf{l}$ as:

$$\mathbf{f} = \mathbf{P}^T \mathbf{P} \Delta\mathbf{l}, \quad (2.39)$$

equivalently,

$$\mathbf{f} = (\mathbf{I} - \mathbf{A}\mathbf{S}) \Delta\mathbf{l}. \quad (2.40)$$

The matrix $\mathbf{M} = \mathbf{P}^T \mathbf{P} = \mathbf{I} - \mathbf{A}\mathbf{S}$ is $(m \times m)$ and has a rank $m-u$ and can be either derived from the parity space or the mathematical model. Hence, the fault vector \mathbf{f} is characterized by:

$$E\{\mathbf{f}\} = \mathbf{M}\boldsymbol{\delta} \quad (2.41)$$

$$D\{\mathbf{f}\} = \sigma_0^2 \mathbf{M}, \quad (2.42)$$

where $\boldsymbol{\delta}$ is a vector of biases and each entry represent a bias in corresponding observation, i.e. δ_i corresponds to the i -th observation.

Once the parity vector is computed and the assumption on the distribution has been made, the hypothesis test statistic can be constructed as follows:

$$T_{ps} = \frac{(\mathbf{p}^T \mathbf{p})}{\sigma_0^2} : \begin{cases} H_0 \sim \chi^2_{(m-u, 0)} \\ H_i \sim \chi^2_{(m-u, \lambda)} \end{cases} \quad (2.43)$$

To perform this test, a decision variable D is computed as $D = \mathbf{p}^T \mathbf{p}$ and checked against the CV. As discussed before, the CV depends on the PFA or α and the on the redundancy number $m-u$. The test is as follows:

$$if \begin{cases} D < CV \implies H_0 \\ D > CV \implies H_i \end{cases} \quad (2.44)$$

To compute the CV, the PFA α has to be set in advance. Then

$$CV = \chi^2_{(\alpha, m-u, 0)}^{-1}, \quad (2.45)$$

where, χ^2^{-1} is the inverse of the χ^2 distribution function. If the test failed, the identification of the faulty measurements is performed. The parity vector is assumed to be zero i.e., $\mathbf{p} = \mathbf{0}$ (all entries are zeros) if there is no fault. Instead, the i -th entry is equal to some value δ_i if the i -th measurement is faulty. In practice, the party vector \mathbf{p} will not be zero but has some small values near zero if there is no fault or it will contain one large entry if there is one fault. So, to isolate the faulty measurement the isolation vector (\mathbf{I}_{pp}) is computed as follows:

$$\mathbf{I}_{pp} = \mathbf{p} \odot \mathbf{p}, \quad (2.46)$$

where \odot denote pairwise multiplication of vectors. The maximum entry of the vector \mathbf{I}_{pp} corresponds to the faulty measurement.

Furthermore, the MDB of the test has to be computed in order to have full reliability and integrity information. To do so, the power of the test $1 - \beta$ has to be chosen. Then, the non-centrality parameter λ which depends also on the level of significance α can be estimated and so the MDB. When the test is assumed to be in H_i it follows a non-central χ^2 distribution with non-centrality parameter λ . To compute λ , non-central χ^2 inverse cumulative distribution function is adjusted to meet the CV and the PMD $1 - \beta$.

The non-centrality parameter λ_i for i -th observation can be also computed as follows:

$$\lambda_i = \frac{\mathbf{p}_i^2}{\sigma_0^2} \mathbf{M}_{ii} \hat{=} \frac{v_i^2}{\sigma_0^2} (pq_{vv})_i, \quad (2.47)$$

This computation of λ depends on α , on the observations and on the statistical and mathematical model, but does not depend on the PMD $1 - \beta$. In fact, once λ is computed, the PMD can also be computed from the non-central χ^2 probability function as:

$$\text{PMD} = \frac{1}{m} \sum_{i=0}^m P \left(\frac{\text{CV}}{\sigma_0^2} \mid m - u, \lambda_i \right) \quad (2.48)$$

In general, the PMD is defined in the integrity requirements for each application and it is fixed to a constant number and should not be computed for each observation. That's why the non-central χ^2 inverse cumulative distribution function is adjusted to meet the computed CV and the specified PMD $1 - \beta$. Following this computation procedures, the MDB for each observation can be derived for equation (2.47) as

$$\nabla_{ps_i} = \sqrt{\frac{\lambda_i \sigma_0^2}{\mathbf{M}_{ii}}}. \quad (2.49)$$

Equivalently, to the parity test T_{ps} , the test statistic could be constructed from the fault vector \mathbf{f} as:

$$T_{ff} = \frac{(\mathbf{f}^T \mathbf{f})}{\sigma_0^2} : \begin{cases} H_0 \sim \chi^2_{(m-u, 0)} \\ H_i \sim \chi^2_{(m-u, \lambda)} \end{cases}, \quad (2.50)$$

since the decision variable $D = \mathbf{p}^T \mathbf{p}$ is equivalent to $D = \mathbf{f}^T \mathbf{f}$.

The parity space is similar to the so-called conditional least-squares in Teunissen (1995).

Solution Separation Approach

Similar to the above test statistics that are performed in the observation domain, the test statistic can also be performed in the state domain, i.e., for GNSS in the position and time domain. The so-called solution separation test statistics are very popular in literature, Joerger et al. (2016b,a); Blanch et al. (2013); Joerger et al. (2013). A comparison study between the SS and residual-based RAIM is done in Joerger et al. (2014). The particularity of SS test statistic is that it could be performed on a single state, set of states, or on the full state. For instance, if we are interested in the horizontal position, the SS test could be performed only on the east-north state in the local topocentric ENU coordinate system. Performing the test on a specific state decreases the computational load. However, in this thesis, the focus will be on the full state SS test since the other test statistic cannot be separated.

The error of the LS state estimate in equation (2.26) is defined as:

$$\mathbf{e} = \Delta \hat{\mathbf{x}} - \Delta \mathbf{x} = \mathbf{S}(\boldsymbol{\varepsilon} + \mathbf{f}). \quad (2.51)$$

The errors of the estimates \mathbf{e} is unknown. Similar to the residual vector, it is assumed to have a *Gaussian* distribution with:

$$\text{E}\{\mathbf{e}\} = \mathbf{S}\mathbf{f}, \quad (2.52)$$

$$D\{\mathbf{e}\} = \mathbf{Q}_{\hat{\mathbf{x}}\hat{\mathbf{x}}}. \quad (2.53)$$

The above error \mathbf{e} (the difference between the estimated solution and true solution) is assumed to be biased since it contains all the observation, i.e., $\Delta\hat{\mathbf{x}}$ is the LS solution computed from using all observations. To identify the faulty observation, all the subset solutions have to be computed as follows:

$$\Delta\hat{\mathbf{x}}_i = \mathbf{S}_i \Delta\mathbf{l}_i, \quad \text{for } i = 1, \dots, m \quad (2.54)$$

where, $\Delta\hat{\mathbf{x}}_i$ is LS solution derived from $(m-1)$ observations, i.e., all observations except the i -th one. Similarly, $\mathbf{S}_i = ((\mathbf{A}_i^T \mathbf{W}_i \mathbf{A}_i)^{-1} \mathbf{A}_i^T \mathbf{W}_i)$, where the matrix \mathbf{A}_i and \mathbf{W}_i are constructed excluding the i -th observation. Similar operation can be done using a matrix partition of the design matrix \mathbf{A} , see Joerger et al. (2013). Assuming $\Delta\hat{\mathbf{x}}_i$ is the estimate of the fault free subset, then the error vector is defined as:

$$\mathbf{e}_i = \Delta\hat{\mathbf{x}}_i - \Delta\mathbf{x} = \mathbf{S}_i \boldsymbol{\varepsilon}_i. \quad (2.55)$$

The errors of the fault-free estimates are assumed to have a *Gaussian* distribution with:

$$E\{\mathbf{e}_i\} = 0, \quad (2.56)$$

$$D\{\mathbf{e}_i\} = \mathbf{Q}_{\hat{\mathbf{x}}\hat{\mathbf{x}}_i}. \quad (2.57)$$

The solution separation

$$\mathbf{x}_{ss} = \Delta\hat{\mathbf{x}}_i - \Delta\hat{\mathbf{x}} = \mathbf{e} - \mathbf{e}_i = \mathbf{S}_{\mathbf{x}_{ss}} \Delta\mathbf{l}, \quad (2.58)$$

where $\mathbf{S}_{\mathbf{x}_{ss}} = \mathbf{S}_0 - \mathbf{S}_i$. The full state SS utilizes the full vector \mathbf{x}_{ss} while the residual-based test is a scalar value. So to have fair comparison the weighted norm of the full state vector \mathbf{x}_{ss} is used. The weighted norm is defined as the pseudo-inverse of covariance matrix of the SS. The SS covariance matrix has rank deficiency equal to the number of faults n and can be defined as:

$$\mathbf{Q}_{ss} = \mathbf{Q}_{\hat{\mathbf{x}}\hat{\mathbf{x}}_i} - \mathbf{Q}_{\hat{\mathbf{x}}\hat{\mathbf{x}}}. \quad (2.59)$$

The pseudo-inverse \mathbf{Q}_{ss}^+ can be computed using the singular value decomposition of the covariance matrix \mathbf{Q}_{ss} . Then the SS test statistic is defined as:

$$T_{ss} = \mathbf{x}_{ss}^T \mathbf{Q}_{ss}^+ \mathbf{x}_{ss} : \begin{cases} H_0 \sim \chi^2(n, 0) \\ H_i \sim \chi^2(n, \lambda_{ss}), \end{cases} \quad (2.60)$$

where the non-centrality parameter λ_{ss} of the SS test is defined as:

$$\lambda_{ss} = \mathbf{f}_{ss}^T \mathbf{S}_{\mathbf{x}_{ss}}^T \mathbf{Q}_{ss}^+ \mathbf{S}_{\mathbf{x}_{ss}} \mathbf{f}_{ss}. \quad (2.61)$$

The non-centrality parameter λ_{ss} can be computed in a similar way as for the residual-based test statistic, the MDB of the SS test statistic (T_{ss}) can be derived as:

$$\nabla_{ss_i} = \sqrt{\frac{\lambda_{ss}}{\mathbf{c}_i^T \mathbf{S}_{\mathbf{x}_{ss}}^T \mathbf{Q}_{ss}^+ \mathbf{S}_{\mathbf{x}_{ss}} \mathbf{c}_i}}, \quad (2.62)$$

where \mathbf{c}_i is a vector with zeros except one at the i^{th} entry corresponding to the tested measurement.

The solution separation MDB (∇_{ss_i}) is expected to be smaller than the MDBs (∇_{rb_i} and ∇_{ps_i}) derived from the residual biased or parity space test statistics T_{rb} and T_{ps} , respectively. The reason behind that is that the matrix \mathbf{Q}_{ss} is rank deficient which will decrease the redundancy number (n) by the number of assumed faulty measurements. As it was seen before for smaller DoF the CV and the non-centrality parameter of the χ^2 distribution will be smaller. As a consequence, smaller non-centrality parameter will provide smaller MDB.

For a better comparison between solution separation and residual-based test statistics, the solution separation can be presented in the parity space. We will address this comparison in the single fault hypothesis. However, solution separation is defined in the state domain so it is not straight forward to derive the relation

between the test statistic T_{ss} defined in equation (2.60) and the parity vector \mathbf{p} defined in equation (2.34). The derivation of the solution separation test statistic can be found in Joerger et al. (2014). The unit vector of the fault lines in SS is defined as:

$$\mathbf{u}_i = \frac{\mathbf{P}\mathbf{c}_i}{\sqrt{\mathbf{c}_i^T \mathbf{P}^T \mathbf{P} \mathbf{c}_i}}. \quad (2.63)$$

In multi-fault hypotheses, the vector \mathbf{c}_i will become a matrix with one in the test observation entries and zeros elsewhere. The above equation (2.63) is restricted to a single fault, so in this way the $\mathbf{P}\mathbf{c}_i$ becomes the i^{th} column of the parity matrix \mathbf{P} . Then, the SS tests T_{ss_i} are the projection of the parity vector on their corresponding fault lines as:

$$\mathbf{T}_{ss_i} = \mathbf{x}_{ss_i}^T \mathbf{Q}_{ss_i}^+ \mathbf{x}_{ss_i} = \mathbf{u}_i^T \mathbf{p} \quad (2.64)$$

To illustrate both residual-based and SS test statistics in the parity space, an example in 2D state and four observation is performed. Figure (2.3) shows the LOS of all transmitters in view. The navigation geometry in terms of GDOP is very good ($\text{GDOP} = 1.07$). Additive white noise is introduced to the observation ($\mu = 0$, $\sigma = 1$) and bias = 8 m is introduced to the 2nd observation. Having 4 transmitters i.e., four observation in 2D state estimation provides the parity space ($m - u = 4 - 2 = 2$) in 2D which is convenient for illustration. Assuming a single fault, the fault vector \mathbf{f} expresses four single observation faults which corresponds to four faulty hypothesis H_i as follows:

$$\mathbf{f} = \begin{bmatrix} f_1 \\ 0 \\ 0 \\ 0 \end{bmatrix} \text{ or } \mathbf{f} = \begin{bmatrix} 0 \\ f_2 \\ 0 \\ 0 \end{bmatrix} \text{ or } \mathbf{f} = \begin{bmatrix} 0 \\ 0 \\ f_3 \\ 0 \end{bmatrix} \text{ or } \mathbf{f} = \begin{bmatrix} 0 \\ 0 \\ 0 \\ f_4 \end{bmatrix}, \quad (2.65)$$

where, f_1, f_2, f_3 and f_4 are the unknown fault magnitudes which can vary from $-\infty$ to ∞ .

Figure (2.4) depict both test statistics from residual-based and SS in parity space which are represented in equations (2.43 and 2.60), respectively. The residual-based test in parity space T_{ps} is represented by the norm of the parity vector \mathbf{p} while the SS test is represented by the projection of the parity vector \mathbf{p} onto the fault lines in parity space, equation (2.63). T_1, T_2, T_3 and T_4 are the SS test for observation 1, 2, 3, and 4, respectively. In this specific example, T_2 and T_3 are almost equal due to the geometry of the fault lines in the parity space, so the bias in 2nd observation could be swapped by the 3rd observation. If the line faults are well distributed, this problem will not happen. Similar examples are presented in Potter and Suman (1977); Joerger et al. (2014), where the parity fault lines are uniformly distributed with a more simplified scenario. Also, the fault isolation in the residual-based approach will be difficult because the parity vector lies between fault lines 2 and 3. However, for better evaluation, the worst-case scenario has to be evaluated for both methods utilizing the probability of HMI under the hypothesis H_i :

$$P(|\mathbf{e}| > \text{AL}, |T| < \text{CV} | H_i) \leq P(|\mathbf{e}| > \text{AL}, |T| < \text{CV} | \bar{\mathbf{f}}_i), \quad (2.66)$$

where vector $\bar{\mathbf{f}}_i$ is the worst-case fault vector of \mathbf{f} which maximizes the integrity risk under the fault hypothesis. Since the estimated error \mathbf{e} in LS and the test statistic of both methods T_{ss} and T_{rb} are statistically

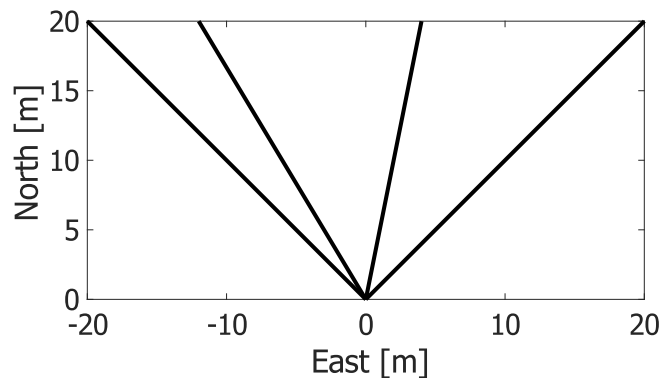


Figure 2.3: LOS of the transmitters in east north directions.

independent, the above equation can be written as:

$$P(|\mathbf{e}| > \text{AL}, | \bar{\mathbf{f}}_i) P(|T| < \text{CV} | \bar{\mathbf{f}}_i). \quad (2.67)$$

The above probability of missed detection under H_i is directly applied on the residual-based test statistic T_{rb} as: $P(|T_{rb}| < \text{CV}_{rb} | \bar{\mathbf{f}}_i)$, while in SS test statistic the probability of miss detection under H_i is a joint probability of all individual test and can be represented as:

$$P(|T_1| < \text{CV}_1 \cap |T_2| < \text{CV}_2 \cap |T_3| < \text{CV}_3 \cap |T_4| < \text{CV}_4 | \bar{\mathbf{f}}_i). \quad (2.68)$$

The correlation between individual SS test statistics T_{ss_i} can be expressed by the angles between corresponding fault lines in the parity space. If the lines are perpendicular, then there is no correlation, and as the angle decreases the correlation increases. For instance, figure (2.4) shows high correlation between T_2 and T_3 while T_1 and T_3 are almost non-correlated. However, the direction of the parity vector is also correlated with the fault line in the same way. Since the parity vector lies between the fault lines u_2 and u_3 , it becomes difficult to separate between the fault vector \mathbf{f}_2 and \mathbf{f}_3 , while the fault lines u_1 and u_4 are also highly negatively correlated but the parity vector is weakly correlated to them, so it is easy to differentiate between the fault vectors \mathbf{f}_1 and \mathbf{f}_4 .

Due to the correlation between the fault lines in parity space, equation (2.68) is not valid anymore. However, the detection bounds of both tests T_{sp} and T_{ss_i} can be derived from equation (2.64) and (2.43), where the boundaries of the SS test is a zonotope and the boundaries of residual-based is a circle in 2D or hypersphere in a higher dimension. If the parity vector \mathbf{p} is inside the bounding zone, then the test passes. Otherwise the test failed and the bias is detected. In the above example, all the SS test statistics T_{ss_i} have the same values, but in general, they could have different values depending on the rank deficiency of the pseudo-inverse \mathbf{Q}_{ss}^+ . Moreover, the residual-based boundary (circle) is bigger than the SS boundary (zonotope), i.e., SS test can detect faults lower than the fault that could be detected by the residual-based test. In other words ∇_{ss_i} is smaller than ∇_{ps_i} for same chosen PFA and PMD. This effect is due to the fact that, DoF of the residual-based test statistic is $(m - u)$ is always bigger than the DoF of the SS test n number of faulty measurement, since a number of faulty measurements should satisfy the condition $m - n \geq u$. As we have seen before, when DoF increases the CV of the test will increase and as a consequence the non-centrality parameter λ will increase, i.e., the MDB will increase despite the type of test statistic. In this example DoF for residual-based and SS tests are equal to 2 and 1, respectively.

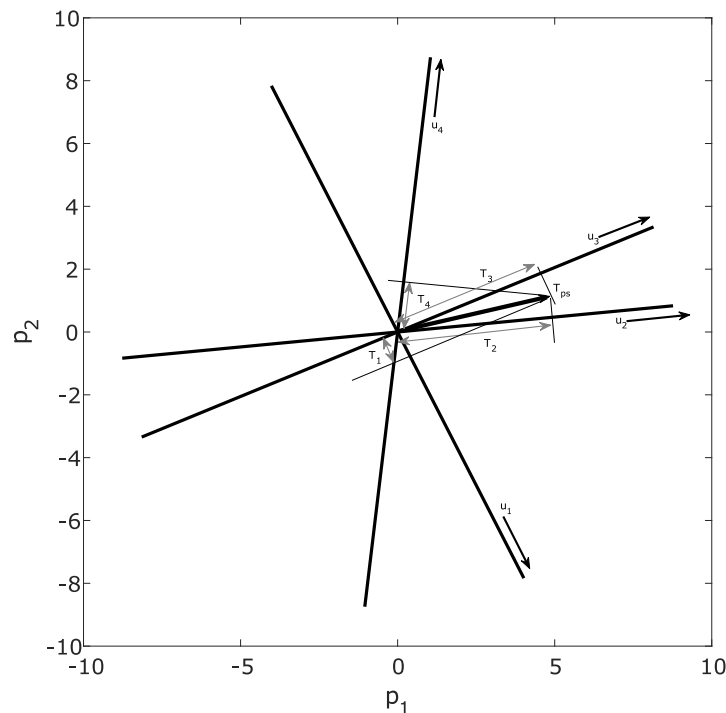


Figure 2.4: Detection test statistic for residual base (T_{ps}) and SS (T_{ss}) in Parity Space.

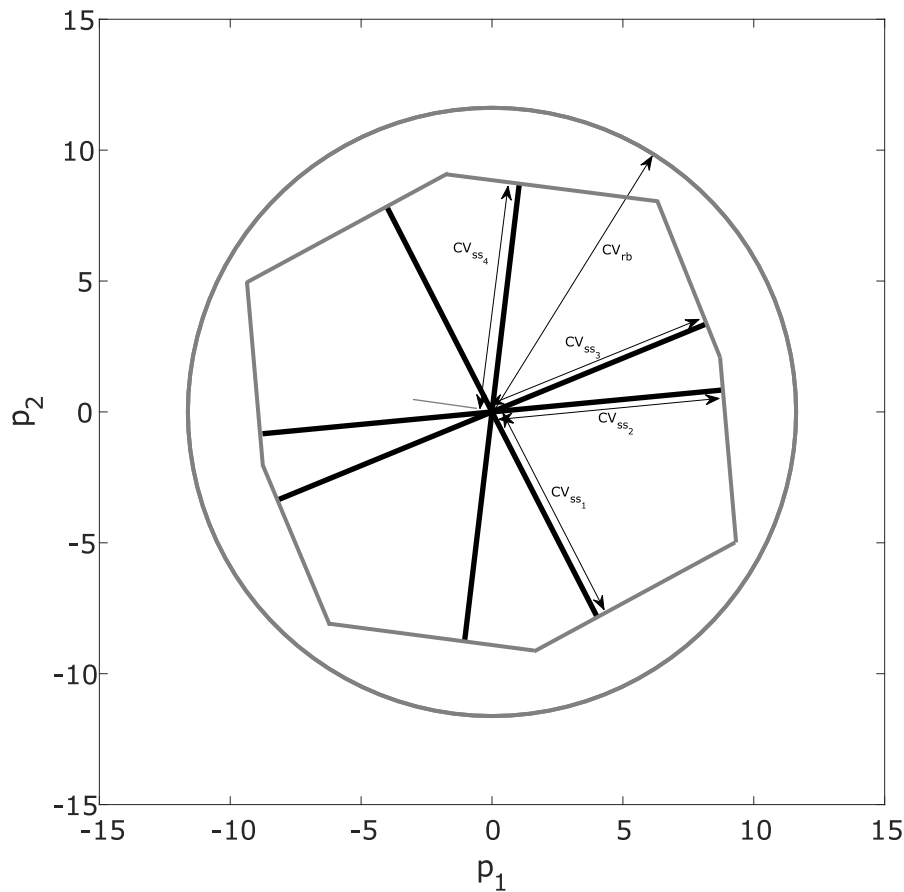


Figure 2.5: Boundaries of the detection test statistic for residual base (circle) and SS (polygon) in Parity Space.

2.3.5 Protection Level

Definition

The Protection Level is bound with specified IR on the actual position error which has to be computed in real time and checked against the AL. So the system availability is evaluated by means of PL not by the actual position error. In this way, the probability that the position error surpasses the AL is above the specified IR. Protection levels are usually divided into two parts: Horizontal Protection Level (HPL) and Vertical Protection Level (VPL). HPL is a bound on the horizontal position error expressed by a radius of a circle with a specified probability requirement, i.e., PFA and PMD. As well as the VPL is a bound on the vertical position error. Combining the HPL and the VPL provide a cylinder as a full PL. The PL should be computed in a way to guarantee that the probability of PE not to exceed the PL is smaller than the IR.

One of the most useful tools to analyze the integrity events as a function of PL, PE and AL is the so-called Stanford Diagram, Tossaint et al. (2006). Figure 2.6 illustrates the Stanford Diagram and all possible integrity events. There are six different integrity events that could happen depending on the relation between PL, PE and AL. The three upper regions in the Stanford Diagram represent the system unavailable status since the PL is greater than the AL. In those cases, the navigation system could not provide the integrity requirement, and the system can alert the user to abort the mission, even though the situation ($AL < PL < PE$) provides misleading information. The misleading operation is when the computed PL does not contain the true solution, i.e., ($PL < PE$). Then, there are two operational modes where the system will not warn the user to abort its mission since it has been misleading. However, if the PE does not exceed the AL, the system is safe even though it is misleading. Instead, if the PE exceeds the AL the system is not safe anymore and it is in hazardous operation mode. The nominal operation mode is what we would like to have always where all required conditions are achieved ($PE < PL < AL$).

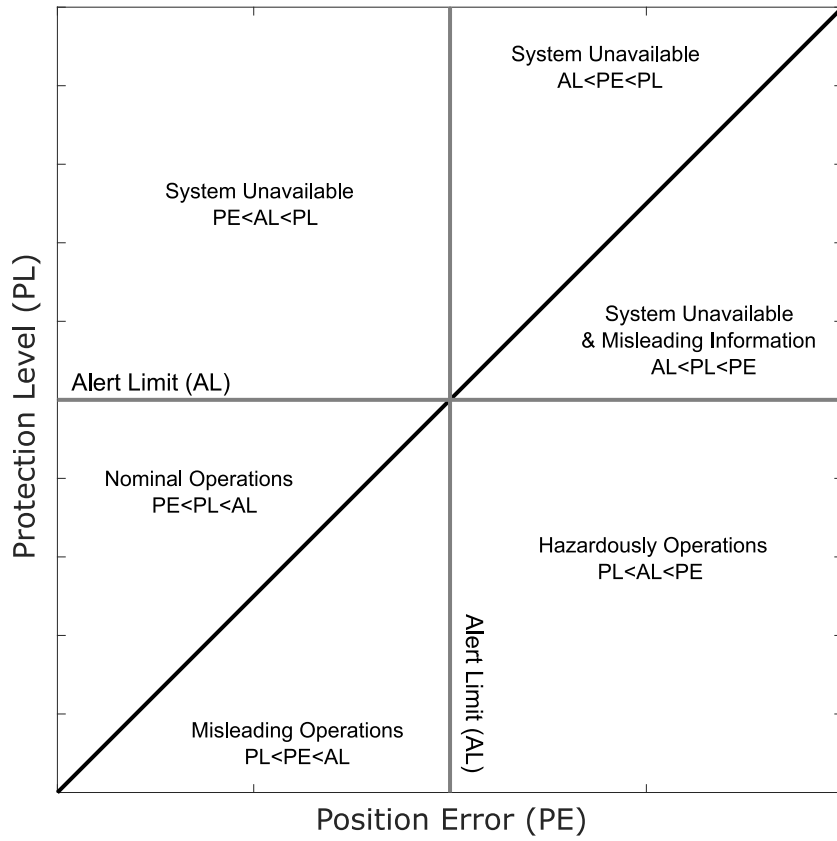


Figure 2.6: Stanford Diagram: a tool to evaluate different operational situation.

Derivation

To finalize the integrity measures, the PL of the estimated states must be derived, in our case for the position estimate. Depending on the test statistic used in deriving the integrity measures, the PL is computed. In case of LS estimation combined with residual-based test statistic, the most used PL is derived from the co-factor matrix $\mathbf{Q}_{\hat{x}\hat{x}}$ as following:

$$\text{HPL} = \kappa_H \sigma_0 \sqrt{\frac{q_{nn} + q_{ee}}{2} + \sqrt{\left(\frac{q_{nn} - q_{ee}}{2}\right)^2} + q_{ne}^2} = \kappa_H \sigma_0 \sqrt{\lambda_{\max}}, \quad (2.69)$$

$$\text{VPL} = \kappa_V \sigma_0 \sqrt{q_{uu}}, \quad (2.70)$$

where q_{nn} , q_{ee} , q_{uu} , and q_{ne} are the co-factors of the north, east, and up coordinates, respectively, λ_{\max} is the maximum eigenvalue of the co-factor sub matrix of the horizontal positions. The co-factor matrix $\mathbf{Q}_{\hat{x}\hat{x}}$ derived in equation (2.7) is in ECEF coordinate system and needs to be transferred to the local tropocentric coordinate system ENU in order to compute the protection levels in equations (2.69 and 2.70). The scale factors κ_H and κ_V can be computed from the assumption of the error distribution (here *Gaussian* in 1D and *Rayleigh* in 2D, i.e. χ^2 with 2 DoF) and the IR requirements RTCA (2006) EGSA (2015). Assuming that the error has a *Gaussian* distribution, the IR which is the probability that the PE exceeds the PL can be computed as:

$$\text{IR} = P_{ex} = 2 \int_{\text{PL}}^{\infty} f_G(\varepsilon) d\varepsilon, \quad (2.71)$$

where f_G is the Probability Density Function (PDF) of the *Gaussian* distribution. The factor 2 is to take into account both tails of the *Gaussian* distribution. P_{ex} is the probability of the PE to be outside the PL. Assuming σ_0 is the standard deviation of the *Gaussian* distribution, equation (2.71) can be computed in a

closed form as:

$$\text{IR} = P_{ex} = \text{erfc} \left(\frac{PL}{\sqrt{2\sigma_0^2}} \right), \quad (2.72)$$

where erfc is the complementary error function of the *Gaussian* distribution. Equation (2.72) can be solved as:

$$PL = \sqrt{2\sigma_0^2} \cdot \text{erfc}^{-1}(P_{ex}) = \kappa \cdot \sigma_0. \quad (2.73)$$

Then, the scale factor can be computed in advance with the desired IR as:

$$\kappa = \sqrt{2} \cdot \text{erfc}^{-1}(P_{ex}) = \sqrt{2} \cdot \text{erfc}^{-1}(\text{IR}). \quad (2.74)$$

This means the PL contains the true position with probability equal to $1 - P_{ex}$, i.e., $1 - \text{IR}$.

In SS test statistic the PL can be derived for each state alone. Moreover, each fault mode has its PL, so the protection level has a zonotopal shape similar to the bounding zone of the test statistic discussed in the previous section. The PL of each mode is defined as:

$$PL_i = |\mathbf{x}_{\text{ss}_i}| + CV_i, \quad (2.75)$$

where, PL_i is the protection level for the i^{th} fault mode for all states. The PL can also be derived for each state alone such as: VPL, see Blanch et al. (2007) and HPL, see Brenner (1996).

Then, the maximum of all bounds is considered as the PL for all fault modes as:

$$PL = \max(|\mathbf{x}_{\text{ss}_i}| + CV_i), \quad (2.76)$$

to separate the HPL and the VPL, the solution set can be projected on a horizontal plane for the HPL and the vertical component can be separated by the projection of the solution on the vertical plane. Another way is to separate the states from the beginning of the SS algorithm, for instance, if we are interested in vertical position and VPL the matrix \mathbf{S}_{ss} have to be multiplied by the vector $[0 \ 0 \ 1 \ 0]$, assuming that the 3^{rd} state represents the vertical or up state.

2.4 Interval Mathematics

The idea of using interval computation is first introduced in Young (1931). One of the first books in interval analysis theory is Moore (1966) and some other books that describe the basic operations and computation in interval mathematics are Alefeld and Herzberger (1983); Moore et al. (2009). A more advanced reference to interval analysis and its application in different engineering fields is Jaulin et al. (2001). Interval analysis and interval computation are special cases of computation on sets, and set theory provides the foundations for interval analysis. There are two main categories of set operations: First, the operations that are meaningful only in the context of set theory such as intersection, union, Cartesian products, and the second types are the operations that deal with real numbers, vectors, and matrices as an extension of the elementary arithmetic.

A small introduction of interval elements and interval computation is necessary for the understanding of the thesis. An interval is a closed set of a real numbers denoted by $[a, \bar{a}]$, such that:

$$[a] = [a, \bar{a}] = \{x \in \mathbb{R}^n \mid a \leq x \leq \bar{a}\}, \quad (2.77)$$

where a indicates the lower bound and \bar{a} the upper bound of the interval $[a]$. The square bracket $[]$ are used to denote interval throughout this dissertation. \mathbb{R}^n is the set of real number with dimension n , in equation (2.77), $n = 1$. This is the most used interval representation in the interval community. Another equivalent representation of the interval is expressed by its midpoint a_m and radius a_r using the following transformation:

$$a_m = \frac{\bar{a} + a}{2}, \quad a_r = \frac{\bar{a} - a}{2}, \quad (2.78)$$

thence,

$$[a] = \langle a_m, a_r \rangle, \quad a_m \in \mathbb{R}, \quad a_r \in \mathbb{R}^+. \quad (2.79)$$

2.4.1 Basic Interval Mathematical Operations

The interval arithmetic operations are defined by the application of the corresponding real operations to all elements of the intervals. We will follow the interval arithmetic operations as defined in Jaulin et al. (2001). The general interval arithmetic operator \mathcal{O} is defined as:

$$[a] \mathcal{O} [b] = \{x \mathcal{O} y \mid x \in [a], y \in [b]\}, \quad (2.80)$$

where the operator \mathcal{O} belongs to the set of all interval operators such as, $\{+, -, \cdot, \div, \cup, \cap, \max, \min, \dots\}$.

In this section, a few examples of the basics of interval arithmetic operation are introduced. In general, performing interval operations uses only the upper and lower bound of the intervals. The following interval operation rules hold:

$$[a] + [b] = [\underline{a} + \underline{b}, \bar{a} + \bar{b}], \quad (2.81)$$

$$[a] - [b] = [\underline{a} - \bar{b}, \bar{a} - \underline{b}], \quad (2.82)$$

$$[a] \cdot [b] = [\min\{\underline{a}\underline{b}, \underline{a}\bar{b}, \bar{a}\underline{b}, \bar{a}\bar{b}\}, \max\{\underline{a}\underline{b}, \underline{a}\bar{b}, \bar{a}\underline{b}, \bar{a}\bar{b}\}]. \quad (2.83)$$

For division, it is more complicated due to the fact that zero could belong to the denominator. To simplify the process lets define the $\left[\frac{1}{b}\right]$ as:

$$\begin{aligned} \frac{1}{[b]} &= \emptyset, & \text{if } [b] &= [0, 0] \\ &= \left[\frac{1}{\bar{b}}, \frac{1}{\underline{b}}\right], & \text{if } 0 &\notin [b] \\ &= \left[\frac{1}{\bar{b}}, \infty\right[, & \text{if } \underline{b} &= 0 \ \& \ \bar{b} > 0 \\ &= \left]-\infty, \frac{1}{\underline{b}}\right], & \text{if } \underline{b} < 0 \ \& \ \bar{b} = 0 \\ &= \left]-\infty, \infty\right[, & \text{if } \underline{b} < 0 \ \& \ \bar{b} > 0, \end{aligned} \quad (2.84)$$

Then the interval division defined as:

$$\frac{[a]}{[b]} = [a] \cdot \left[\frac{1}{[b]}\right], \quad (2.85)$$

where \emptyset represents an empty set. Some examples of the basic interval computations:

$$\begin{aligned} [-2, 5] + [1, 4] &= [-1, 9] \\ [-1, 6] - [4, 9] &= [-10, 2] \\ [-1, 4] \cdot [2, 6] &= [-6, 24] \\ \frac{[-3, 6]}{[3, 5]} &= [-1, 2] \end{aligned} \quad (2.86)$$

From these examples, we can see that the nature of interval computation tends to over-bound the solution, and the intervals keep increasing if more computations are performed. Inclusion functions and contractors can be used to overcome this problem. Those will be explained later on.

Moreover, the operation that is purely related to set theory is also performed on interval analysis. Let us consider two sets \mathbb{X} and \mathbb{Y} , then their intersection, union, and Cartesian products are defined as:

$$\mathbb{X} \cap \mathbb{Y} \triangleq \{x \mid x \in \mathbb{X} \ \& \ x \in \mathbb{Y}\}, \quad (2.87)$$

$$\mathbb{X} \cup \mathbb{Y} \triangleq \{x \mid x \in \mathbb{X} \ \parallel \ x \in \mathbb{Y}\}, \quad (2.88)$$

$$\mathbb{X} \times \mathbb{Y} \triangleq \{(x, y) \mid x \in \mathbb{X} \ \& \ y \in \mathbb{Y}\}, \quad (2.89)$$

where \triangleq is an equal by definition and the symbol \parallel means *or*.

2.4.2 Interval Vectors and Matrices

The interval multiplication of two intervals gives a new interval in the same dimension as we have seen in equation (2.83). Instead, the *Cartesian* product of two or more intervals produces an interval box, i.e., interval vector and not just an interval. If $[\mathbf{x}]$ is a *Cartesian* product of n interval, then $[\mathbf{x}]$ is a subset of \mathbb{R}^n . The interval vector is then written as:

$$[\mathbf{x}] = [x_1] \times [x_2] \times \dots \times [x_n], \quad \text{where } [x_i] = [\underline{x}_i, \bar{x}_i], \quad i = 1, \dots, n. \quad (2.90)$$

The projection of the interval vector $[\mathbf{x}]$ on the i^{th} axis is the component $[x_i]$. The interval vector is n -dimensional parallelepipeds with axes aligned to the coordinate axes. Figure (2.7) depicts an example for $n = 2$, with $[\mathbf{x}] = [x_1] \times [x_2]$.

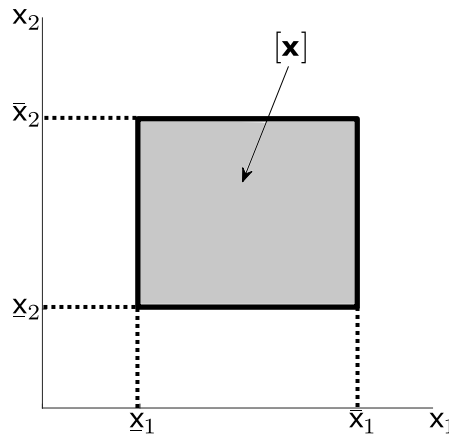


Figure 2.7: Interval box $[\mathbf{x}]$ of \mathbb{R}^n

In the same way that the notion of the interval can be generalized to vectors, we can define interval matrices, where each matrix element is an interval. The classical calculations of linear algebra can thus be applied on intervals, which allows, for example, to take into account the linearization error by defining a matrix uncertain. The use of interval matrices also makes it possible to take account of the precision of the numerical representation in numerical calculations, to solve badly conditioned problems, Deif (1991, 2012).

2.4.3 Interval Functions

Real arithmetic and calculus include functions as well as interval analysis, handles also interval functions. The elementary interval functions represented an interval in terms of upper and lower bounds. For instance, for any non-empty interval $[x]$:

$$[f]([x]) = [f(\underline{x}), f(\bar{x})]. \quad (2.91)$$

This definition of interval function can be applied directly to monotonic functions, such as *exp* and *log*, i.e., $[exp]([x]) = [exp(\underline{x}), exp(\bar{x})]$. However, for non-monotonic functions, the interval counterpart function is much more complicated, so that for each function a specific algorithms has to be performed. For example $[sin]([0, \pi]) \neq [sin(0), sin(\pi)] = [0, 0]$, instead it must be equal to $[0, 1]$. It corresponds to the factual range of the function inside the interval $[x]$. For more information about the interval functions and their algorithms, the reader is referred to Jaulin et al. (2001).

These rules applied to interval functions are derived from real arithmetic, so we can consider interval arithmetic as an extension of real arithmetic. For instance, the image of an interval $[x]$ by a function f is:

$$f([x]) = \{f(x) \mid x \in [x]\}. \quad (2.92)$$

Other types of sets are extended from the real arithmetic, such as functions that map one domain to another and inverse function. These types of functions are the basis of the so-called *Contractor* and the set inversion.

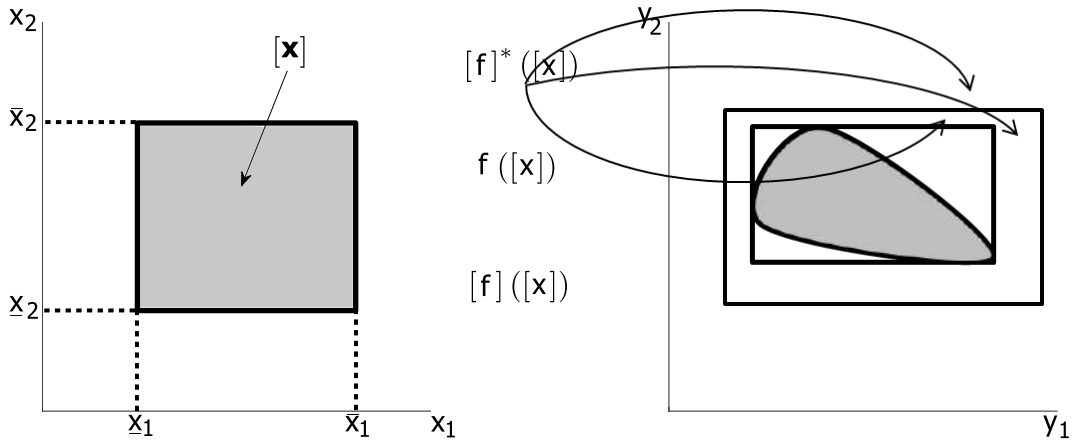


Figure 2.8: Images of an interval box by a function f and two of its inclusion functions $[f]$ and $[f]^*$, where $[f]^*$ is the minimum inclusion function.

Contractor programming and SIVIA will be used later on in the parameter estimation. Let us consider two sets \mathbb{X} and \mathbb{Y} and a function $f : \mathbb{X} \rightarrow \mathbb{Y}$. If $\mathbb{X}_1 \subset \mathbb{X}$, then the image of \mathbb{X}_1 by the function f is

$$f(\mathbb{X}_1) \triangleq \{f(x) \mid x \in \mathbb{X}_1\}, \quad (2.93)$$

and if $\mathbb{Y}_1 \subset \mathbb{Y}$, then the reciprocal image of \mathbb{Y}_1 by f is

$$f^{-1}(\mathbb{Y}_1) \triangleq \{x \in \mathbb{X}_1 \mid f(x) \in \mathbb{Y}_1\}, \quad (2.94)$$

The interval inclusion function $[f]$ from \mathbb{R}^n to \mathbb{R}^m , is an inclusion function of f if

$$\forall [\mathbf{x}] \in \mathbb{R}^n, f([\mathbf{x}]) \subset [f]([\mathbf{x}]) \quad (2.95)$$

The image of a box by a function is in general not a box, but an arbitrary shape. In general, no exact representation exists that permits it to easily handle the whole image of a box by a function. So, the interval inclusion function is used to return a box that contains the image of an interval. The smallest enclosure interval box is provided by the minimum inclusion function. The interval function in equation (2.95), is an example of a generic inclusion function for all functions f .

One of the main motivations of interval analysis is to provide, for a large class of functions f , inclusion functions that can be evaluated reasonably fast and not overestimate the factual range. The function f could be of different type, e.g., polynomial, logarithmic, or differential equations. In most of the cases it is possible to find a minimum inclusion function which has the property: $\forall [\mathbf{x}]$, it is the smallest box that include $f([\mathbf{x}])$. For every function there exist infinite number of inclusion functions, but the minimum inclusion function is unique. Moreover, an image of the function $f([\mathbf{x}])$ may have any shape, i.e. it could be convex or non-convex shape, or it could be discontinuous (two or more separate sets). In any case an inclusion function $[f]$ of f provides an interval box guaranteed to contain the image of f . Figure (2.8) illustrates an example of the generic inclusion function $[f]$ and the minimum inclusion function $[f]^*$ of the function f .

2.4.4 Set Inversion via Interval Analysis

Consider any subset \mathbb{Y} of \mathbb{R}^m , then the set inversion of any non-linear function f from \mathbb{R}^n to \mathbb{R}^m is characterized by

$$\mathbb{X} = \{\mathbf{x} \in \mathbb{R}^n \mid f(\mathbf{x}) \in \mathbb{Y}\} = f^{-1}(\mathbb{Y}) \quad (2.96)$$

In order to obtain the set solution \mathbb{X} , the so-called SIVIA algorithm is used, Jaulin and Walter (1993b,a); Jaulin (2009). The SIVIA algorithm computes the solution set \mathbb{X} and its inner and outer sub-pavings as.

$$\underline{\mathbb{X}} \subset \mathbb{X} \subset \bar{\mathbb{X}} \quad (2.97)$$

The outer sub-paving $\overline{\mathbb{X}}$ is an uncertain set solution, i.e., they could be an inverse image of a subset \mathbb{Y} or not. The most probable situation is that parts of the sub-paving sets are the inverse image of \mathbb{Y} and parts are not. Usually, these are the union of very small boxes at the boundaries of the solution set \mathbb{X} . In the SIVIA algorithm a threshold has to be set in advance, which will determine the maximum width of the interval boxes in the sub-paving. Sub-paving computations are explained in Kieffer et al. (2001).

The SIVIA algorithm can handle any non-linear function, but it needs to start with a large initial box $[\mathbf{x}]_0$ which is guaranteed to contain the outer sub-paving sets $\overline{\mathbb{X}}$. The SIVIA algorithm is divided into four operations starting from the initial box as follows:

- If $[f]([\mathbf{x}])$ intersects with \mathbb{Y} , but is not entirely in \mathbb{Y} , then $[\mathbb{Y}]$ may contain a part of the solution set and another part is not a solution. Then, this has to be checked w.r.t. the predefined precision parameter ε and if its width is greater than a ε , then it should be bisected and the test should be recursively applied to these newly generated boxes.
- If $[f]([\mathbf{x}])$ does not intersect with \mathbb{Y} , then $[\mathbf{x}]$ does not belong to the solution set \mathbb{X} and can be discarded from the solution list. The list started with one box $[\mathbf{x}]_0$.
- If $[f]([\mathbf{x}])$ is a subset of \mathbb{Y} , then $[\mathbf{x}]$ belongs to the solution set \mathbb{X} and has to be saved in the solution set.
- The last step is similar to the first step but in case the width of the box is less than the predefined precision parameter ε , then it is stored in the non-certain set, i.e. the outer sub-paver.

These four steps are repeated recursively until the list of boxes is empty. The final guaranteed solution is the union of all boxes stored in \mathbb{X} . The uncertain solution is the union of all boxes stored in $\overline{\mathbb{X}}$, and all the discarded intervals are guaranteed to be not a solution.

2.4.5 Contractors

To characterize a set \mathbb{X} as a subset of \mathbb{R}^n or to find a solution set via inverse interval functions, the bisection algorithms such as in SIVIA bisect the boxes in all directions (usually bisect the width of the box) and become inefficient. The width of an interval box is the largest interval of the box. Interval methods can still be useful for post-processing applications but not for real-time applications. To overcome this problem contraction programming can be used instead of bisection, Chabert and Jaulin (2009). Very few bisections could be used at the end of the computation. An operator $C_{\mathbb{X}} : \mathbb{R}^n \rightarrow \mathbb{R}^n$ said to be a contractor for a set $\mathbb{X} \in \mathbb{R}^n$ if the following conditions hold:

$$\forall [\mathbf{x}] \in \mathbb{R}^n : \begin{cases} C_{\mathbb{X}}([\mathbf{x}]) \subset [\mathbf{x}] & \text{(contractancy)} \\ C_{\mathbb{X}}([\mathbf{x}]) \cap \mathbb{X} = [\mathbf{x}] \cap \mathbb{X} & \text{(completeness)}. \end{cases} \quad (2.98)$$

Some algebraic properties of contractor are:

- Union: $(C_1 \cup C_2)([\mathbf{x}]) \triangleq [C_1([\mathbf{x}]) \cup C_2([\mathbf{x}])]$.
- Intersection: $(C_1 \cap C_2)([\mathbf{x}]) \triangleq C_1([\mathbf{x}]) \cap C_2([\mathbf{x}])$
- Composition: $(C_1 \circ C_2)([\mathbf{x}]) \triangleq C_1(C_2([\mathbf{x}]))$
- Repetition: $C^\infty \triangleq C_1 \circ C_2 \circ C_3 \dots$

These are the most important properties of the contractors and when any algorithm is developed based on contractor programming they should be taken into account. Contractor programming is a type of *constraint satisfaction* programming that aims to solve a constraint satisfaction problem. To perform or project a constraint is to compute the smallest intervals which contain all consistent values. Here, we give some examples of primitive contractors which are the building blocks of a bigger contractor or final one. For

instance, the primitive addition contractor C_+ of the constraint $[z] = [x] + [y]$ is constructed as:

$$C_+([z] = [x] + [y]) \begin{cases} [z] := [z] \cap ([x] + [y]) \\ [x] := [x] \cap ([z] - [y]) \\ [y] := [y] \cap ([z] - [x]) \end{cases} \quad (2.99)$$

Multiplication contractor C of constraint $[z] = [x] \cdot [y]$ is constructed as :

$$C([z] = [x] \cdot [y]) \begin{cases} [z] := [z] \cap ([x] \cdot [y]) \\ [x] := [x] \cap \left([z] \cdot \frac{1}{[y]} \right) \\ [y] := [y] \cap \left([z] \cdot \frac{1}{[x]} \right) \end{cases} \quad (2.100)$$

The contractor C_{\exp} associated to the constraint $([y] = \exp[x])$ is constructed as:

$$C_{\exp}([y] = \exp[x]) \begin{cases} [y] := [y] \cap \exp([x]) \\ [x] := [x] \cap \log([y]) \end{cases} \quad (2.101)$$

The contractor should be iteratively performed until no contraction can be done on any interval or until some predefined limit of contraction is reached in order to save computation time. Here are some numerical example of the above contractor. Let $[x] = [-\infty, 8]$, $[y] = [-\infty, 2]$ and $[z] = [4, \infty]$, then $C_+([z] = [x] + [y])$ is

$$\begin{aligned} [z] = [x] + [y] &\implies [z] \in [4, \infty] \cap ([-\infty, 8] + [-\infty, 2]) = [4, \infty] \cap [-\infty, 10] = [4, 10], \\ [x] = [z] - [y] &\implies [x] \in [-\infty, 8] \cap ([4, \infty] - [-\infty, 2]) = [-\infty, 8] \cap [2, \infty] = [2, 8], \\ [y] = [z] - [x] &\implies [y] \in [-\infty, 2] \cap ([4, \infty] - [-\infty, 8]) = [-\infty, 2] \cap [-4, \infty] = [-4, 2]. \end{aligned} \quad (2.102)$$

As a result, the interval $[z]$, $[x]$ and $[y]$ have been contracted from $[4, \infty]$, $[-\infty, 8]$ and $[-\infty, 2]$ to $[4, 10]$, $[2, 8]$ and $[-4, 2]$, respectively. If we apply the same contractor C_+ on the constraint $([z] = [x] + [y])$ one more time it will not contract any interval anymore. However, in real application the main contractor is a compound contractor and it contains different primitive contractors. So iterative contraction will be able to contract the same intervals again due to consecutively application of different primitive contractor. A compound contractor can be decomposed into primitive contractors. Suppose we have a compound contractor $C_c([x] + \cos([x] \cdot [y]) \geq 0)$ for $[x] = [-1, 1]$ and $[y] = [-1, 1]$, then C_c can be decomposed as:

$$\begin{aligned} C([a] = [x] \cdot [y]) \\ C_{\cos}([b] = \cos([a])) \\ C_+([c] = [x] + [b]). \end{aligned} \quad (2.103)$$

The intervals $[x]$ and $[y]$ are already defined and we need to initialize the new intervals $[a]$, $[b]$ and $[c]$. Since there is no knowledge about the intervals $[a]$ and $[b]$ we have to initialise them as $[-\infty, \infty]$ while the interval $[c]$ has to be positive from the constrain $([c] = [x] + [b] \geq 0)$ so it could initialised as $[0, \infty]$. The three contractors C , C_{\cos} and C_+ will be repeated consecutively until no more significant contraction can happen.

One of the most efficient ways of constructing complex or compound contractor decomposition algorithms is the so-called *Forward-Backward Contractor*. Suppose we want to build a contractor for the following set:

$$\mathbb{S} = \{([x_1] + [x_2]) \cdot [x_3] \in [1, 4]\} \quad (2.104)$$

The *Forward-Backward Contractor* of set \mathbb{S} , $C_{\mathbb{S}}$ can be derived from the so-called binary tree, see figure (2.9). The interval variables $[x_1]$, $[x_2]$ and $[x_3]$ belong to the leaf of the tree. The last primitive contractor, here associated with the operator \cap , is the root of the tree. The forward contraction is going from the leaf to the root and the backward contracting is the way back, i.e., from the root to the leaf. First, new interval variables (here a and b) have to be introduced into the nodes of the leaf. These new variables are corresponding to the following constraints:

$$\begin{cases} [a] = [x_1] + [x_2] \\ [b] = [a] \cdot [x_3] \\ c \in [1, 4] \end{cases} \quad (2.105)$$

Then the *Forward-Backward Contractor* $C_{\mathbb{S}}$ can be constructed as follows:

$$\text{Forward} \begin{cases} [a] = [x_1] + [x_2] \\ [b] = [a] \cdot [x_3] \\ c \in [1, 4] \end{cases} \quad \text{Backward} \begin{cases} [a] = [a] \cap \frac{[b]}{[x_3]} \\ [x_3] = [x_3] \cap \frac{[b]}{[a]} \\ [x_1] = [x_1] \cap [a] - [x_2] \\ [x_2] = [x_2] \cap [a] - [x_1] \end{cases} \quad (2.106)$$

Initial intervals have to be assigned to the input intervals $[x_1]$, $[x_1]$ and $[x_1]$. If we have no information about how large this interval could be we can start from infinity intervals, i.e., very large intervals guaranteed to contain the solution set. Then a few iterations of the contractor can reach the smallest solution set.

2.4.6 Application of Interval Analysis to Navigation

The first application of interval analysis related to GNSS starts in late 1970 especially in the adjustment theory in the geodetic applications, Schmitt (1977). The conventional computation of interval analysis is first used in GNSS related applications. Later on, conventional interval computation is used in the LS adjustment for GNSS positioning and computation of reliable confidence domain in terms in interval boxes and zonotopes (Kutterer, 1994; Schön and Kutterer, 2001; Schön, 2002; Schön and Kutterer, 2005b, 2006). More integrity reliability-related orientation using interval analysis to overcome the intensive Monte Carlo simulation is done in Schön (2016). The derivation of IELSA and its extension to zonotope will be discussed in section (3.1). Afterword, those methods will be compared to the probabilistic approaches and our developed method furthermore, interval computation introduced to the Kalman filtering in a general way Chen et al. (1997), and then application of interval Kalman filter used in GNSS positioning, Jiang et al. (2016).

Least-squares adjustment and interval Kalman filter using conventional interval computation provide a bounding box of the parameter state. As discussed early in this section, to overcome the overestimation problem of the interval computation different methods such as sub-paving, SIVIA and interval contractors have been developed. These methods were initially used in the control theory and robotics applications, Jaulin et al. (2000); Jaulin (2009); Le Bars et al. (2018); Rauh et al. (2015, 2006), also compared to the Kalman filtering methods in Ashokaraj et al. (2004); Nicola and Jaulin (2018). Contractor programming and SIVIA are also applied on GNSS position to provide integrity bounding zone in form of an interval box, Drevelle and Bonnifait (2009). The same method has then been applied on GNSS positioning with height aided from digital elevation model, Drevelle and Bonnifait (2011). Moreover, this method is also integrated into a 3D map for GNSS positioning in an urban environment in the scope of autonomous driving Drevelle and Bonnifait (2013). SIVIA algorithm applied on the code GNSS measurements will be discussed in details in section 3.2.

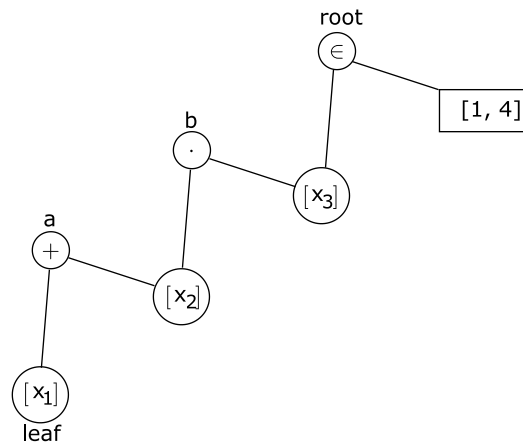


Figure 2.9: Binary tree of the set $\mathbb{S} = \{([x_1] + [x_2]) \cdot [x_3] \in [1, 4]\}$.

2.5 Determination of Observation Interval Bounds

One of the most important issues using interval analysis is the determination of the interval bound. In this thesis, we are interested in the interval bounds applied to GNSS observation. Depending on the interval method, the interval bound could be applied in different ways. Some methods like IELSA apply the whole interval bound on the observation directly, SIVIA method applies interval bounds on the observations and the satellite positions. However, there are different ways to determine the interval bounds depending on user objectives. For instance, assuming the observation errors having a *Gaussian* distribution model, interval bounds could be derived with specific predefined IR. The OIB could be chosen arbitrarily and depends on the desired range of the bounding zone since the area of the bounding zone depends strictly on the OIB regardless of the applied interval method. Moreover, the MDB depends on the OIB, so many considerations have to be taken into account when we chose the interval bound. Lastly, the interval bound for GNSS observation could be derived in a physically meaningful way using sensitivity analysis, Schön and Kutterer (2005a). Sensitivity analysis derived interval bound for each applied correction model on the observation, such as *Klobuchar* ionospheric model. Then all the intervals are summed up to determine the final interval bounds.

The main issue in using interval analysis for parameter estimation and optimization is to get proper interval error bounds on the observations. For GNSS the target parameters are the receiver antenna coordinates and the receiver clock offset. Due to remaining systematic errors i.e. ephemeris, tropospheric and ionospheric delays, multipath, corrections must be applied to the observations for valuable parameter estimation. However, these corrections are sometimes far from being perfect, e.g. it is known that applying the broadcast ionospheric model typically reduces 50 % of the actual effect. Thus, in addition to the random noise, remaining systematic persist and should be treated adequately. Different approaches can be distinguished for the derivation of observation interval bounds. In the following, each approach will be discussed separately.

2.5.1 Probabilistic Approaches with a Priori Integrity Risk

In this orientation of interval study, the remaining errors in GNSS observations are supposed to be mutually independent *Gaussian* distributed variables $\sim N(0, \sigma^2)$. Using interval mathematics, a confidence domain of the estimated position is computed with a priori integrity risk. A priori integrity risk computation associated with the computed confidence domain is of great importance for reliable navigation. In this manner, the risk that the computed confidence domain does not contain the true solution depends only on the measurement error. To compute a confidence domain with a given integrity risk, an appropriate setting of the error bound on the pseudo-range measurement is done as follows, Drevelle and Bonnifait (2011).

Let c_p being the confidence in all pseudo-range measurement error bounds, i.e.

$$c_p = P(l_i \in [l_i]) = \int_a^b f_l(\varepsilon) d\varepsilon, \quad (2.107)$$

where l_i represent the pseudo-range measurement, $[l_i] = [l_i + a, l_i + b]$ interval bound on the i^{th} measurement, P stands for probability, and f_l is the probability density function of the measurement error assuming that n_t is the number of measurements that are included in their corresponding interval bounds. Then, the probability that n_t is the number of true measurements out of m measurements can be computed by the binomial law as:

$$P(n_t) = \frac{m!}{n_t!(m-n_t)!} c_p^{n_t} (1-c_p)^{m-n_t}. \quad (2.108)$$

So that the probability of having all the measurements consistent with their corresponding interval bounds is:

$$P(n_{all}) = c_p^m (1-c_p). \quad (2.109)$$

The computed interval confidence domain $[\mathbf{X}(t)]$ is guaranteed to be consistent with the true position $\mathbf{x}(t)$, i.e., the true position is inside the confidence interval if all observation interval bounds are consistent with the true error. However, the observation interval bounds will be consistent with the true observation errors

with the specified IR under the assumption that GNSS observations are mutually independent *Gaussian* distributed $\sim N(0, \sigma^2)$. So we get

$$[l_{all}] \in [l_{all} + a, l_{all} + b] \implies \mathbf{x}(t) \in [\mathbf{X}(t)] \quad (2.110)$$

Which leads to

$$\begin{cases} P(\mathbf{x}(t) \in [\mathbf{X}(t)]) \geq P([l_{all}] \in [l_{all} + a, l_{all} + b]) \\ \implies P(\mathbf{x}(t) \notin [\mathbf{X}(t)]) \leq 1 - P([l_{all}] \in [l_{all} + a, l_{all} + b]) \\ \implies \text{IR} \leq 1 - P(n_{all}) \\ \implies \text{IR} \leq 1 - c_p^m (1 - c_p). \end{cases} \quad (2.111)$$

Under the assumption that GNSS observations are mutually independent *Gaussian* distributed $\sim N(0, \sigma^2)$, the OIBs of each pseudo-range measurement can be computed in terms of the confidence c_p for a given IR as follows:

$$[l_i] = [l_i - \alpha\sigma, l_i + \alpha\sigma], \quad (2.112)$$

$$\alpha = \phi\left(1 - \frac{c_p}{2}\right), \quad (2.113)$$

where ϕ is the cumulative distribution probability function of the *Gaussian* distribution.

The confidence interval $[\mathbf{X}(t)]$ will contain the true position $\mathbf{x}(t)$ with the specified integrity risk IR. However, if the assumption that GNSS observations are mutually independent *Gaussian* distributed does not hold or some biases were present in the observation, the confidence interval will be violated and may not contain the true position anymore. To overcome this problem further testing on the estimation process has to be done to ensure that there are no outliers in the observations.

2.5.2 Sensitivity Analysis of the Measurement Correction

The sensitivity analysis of each correction model gives a solid and physical meaningful interval bound on each model's errors. Besides, it allows us to see the effect of each model parameter on the model itself. It also permits us to bound the systematic errors and not just random noise. In case a random noise is presented in the observation, the bounding interval can be chosen with the desired confidence level. For example, a *Gaussian* noise can be bounded with interval radius equal to $3 \cdot \sigma$ for 99.7 % confidence level. So, sensitivity analysis is a useful tool to assess the systematic errors of each correction model and gives an insightful analysis of each model parameter.

2.5.2.1 Concept

In this approach, OIBs in form of intervals with lower and upper bounds are applied to the OMC values $\Delta \mathbf{l}$ to assess the remaining observation uncertainty. A sensitivity analysis w.r.t influence parameters can be performed on the observation equation (2.1) to derive observation intervals, Schön and Kutterer (2006). Each corrected model in equation (2.1) is checked w.r.t influence parameters whose values are known at some precision level. Usually, there are both systematic and random effects. Equation (2.114) shows the dependencies of the total differential D_i^j of equation (2.1) w.r.t. the influence parameters.

$$D_A^j = \frac{\partial \rho_A^j}{\partial \mathbf{s}} \mathbf{d}\mathbf{s} + \frac{\partial I_A^j}{\partial \mathbf{s}} \mathbf{d}\mathbf{s} + \frac{\partial T_A^j}{\partial \mathbf{s}} \mathbf{d}\mathbf{s} + \dots = \mathbf{F} \mathbf{d}\mathbf{s} \quad (2.114)$$

where ρ_A^j denotes the euclidean distance, the $(n_{infl} \times 1)$ vector \mathbf{s} is the set of influence parameters and $\mathbf{d}\mathbf{s}$ is their uncertainty. The remaining errors are enclosed by an error bound equal to 1σ where, σ equals the typical observation error of 1% of the chip or wavelength, i.e. $\sim 1m$. \mathbf{F} is a matrix containing the partial derivatives. The interval radius $\Delta_{A,r}^j$ is defined as

$$\Delta_A^j = \left| \frac{\partial PR_A^j}{\partial \mathbf{s}} \right| \mathbf{d}\mathbf{s} = |\mathbf{F}| \mathbf{d}\mathbf{s}, \quad (2.115)$$

where the symbol $|\cdot|$ is the absolute values applied to each matrix element. We assume, that the error bounds are symmetric and centered at the actual value of the corrected observations ΔI_A^j , so the interval observation is as follows:

$$[\Delta I_A^j] = [\Delta I_A^j - \Delta_A^j, \Delta I_A^j + \Delta_A^j] \quad (2.116)$$

Next, an exemplary sensitivity analysis has been conducted on the *Saastamoinen* Saastamoinen (1973) tropospheric model (equation (2.14) and (2.15)) and the *Klobuchar* (Klobuchar (1987)) ionospheric model in order to derive physically meaningful interval bounds.

2.5.2.2 Klobuchar Ionospheric Model

The *Klobuchar* ionospheric model was introduced earlier in equation (2.20). The influence parameters of the *Klobuchar* ionospheric model considered here are α_n , β_n , and D_c . Figure 2.10 shows the ionospheric delays and their interval radius for two simulated satellites with different elevation angles and times of the day.

Figure 2.10a depicts the ionospheric delay and its interval radius of a satellite raising from 15° to 90° elevation along the whole day while figure 2.10b depicts the ionospheric delay and its interval radius of a satellite fixed at 90° elevation. Figure 2.10c depicts ionospheric delay and its interval radius of a satellite raising from 15° to 90° elevation at a fixed time (midday) of the day. Depending on the elevation angle and on the time of day, the ionospheric delay could vary between 10 m to 1.5 m while its interval radius varies from 0.15 m to 5.3 m. The ionospheric interval radius in figure 2.10 is obtained with the values in Table 2.1 which shows the uncertainty values $\mathbf{ds} = [d\alpha, d\beta]$ of the α and β parameters of *Klobuchar* ionospheric model while the parameter D_c has $0.5 \cdot 10^{-8}$ as uncertainty. These uncertainty values correspond to 0.5 uncertainty in the last digit of each influence parameter, where α and β parameters are taken from the navigation message.

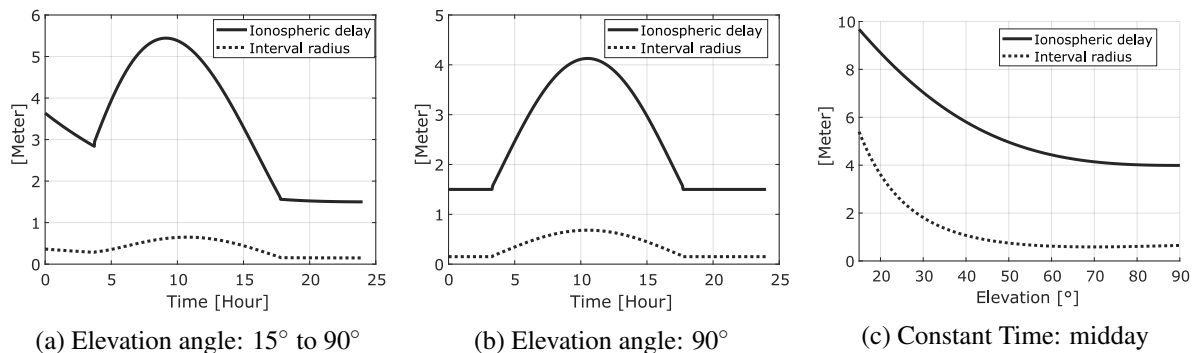


Figure 2.10: Resulting observation corrections of *Klobuchar* ionospheric model and its interval radii: (a) Satellite raising from 15° to 90° elevation during one complete day. (b) Constant elevation = 90° for complete day. (c) Fixed time at mid day and varying the elevation angle from 15° to 90° .

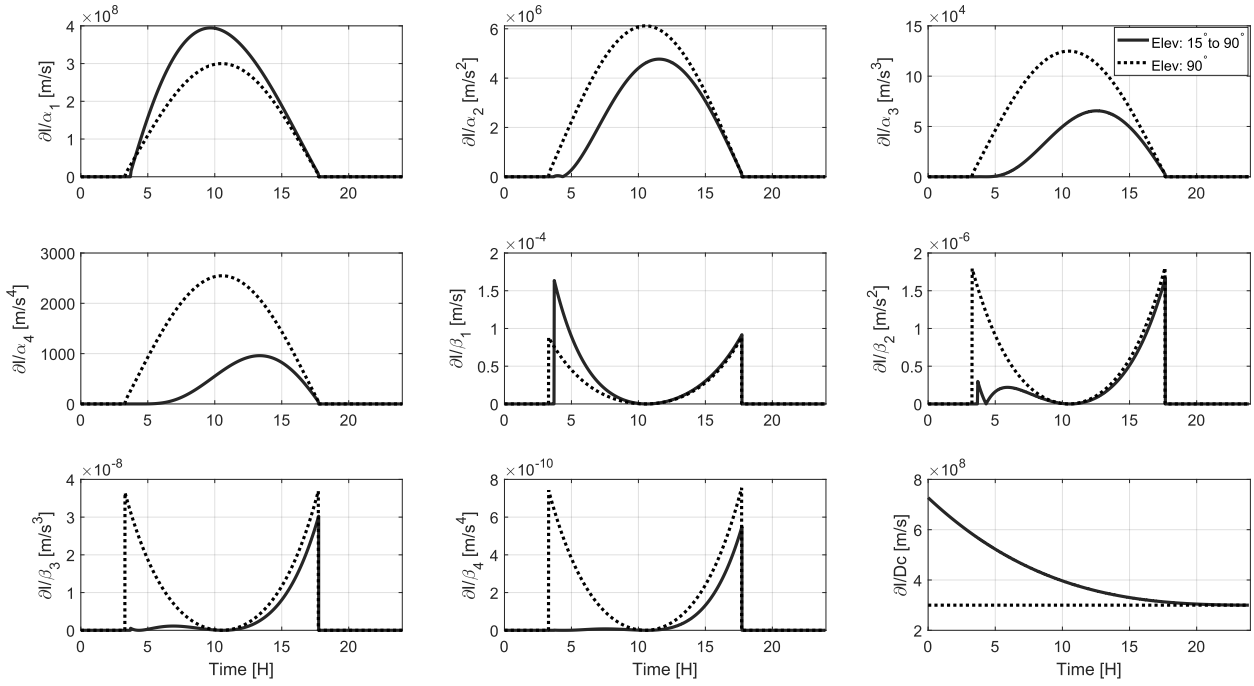


Figure 2.11: Partial derivatives (F) of *Klobuchar* ionospheric model w.r.t. the model influence parameters. Solid lines: satellite raising from 15° to 90° elevation, and dot lines: constant elevation = 90° .

Table 2.1: Assumed uncertainty values of the influence parameters of *Klobuchar* ionospheric model.

	α_1, β_1	α_2, β_2	α_3, β_3	α_4, β_4
$d\alpha$	$0.5 \cdot 10^{-9}$	$0.5 \cdot 10^{-8}$	$0.5 \cdot 10^{-8}$	$0.5 \cdot 10^{-7}$
$d\beta$	$0.5 \cdot 10^{-5}$	$0.5 \cdot 10^{-5}$	$0.5 \cdot 10^{-5}$	$0.5 \cdot 10^{-6}$

Figure 2.11 represents the partial derivatives (F) of two satellites (one at 90° elevation (dot line) and the other raising from 15° to 90° elevation (solid line)) of the ionospheric delay w.r.t. the model parameters α_n, β_n and $D_c = 5$ ns. The influence parameters α_n have the biggest effect, especially α_1 and α_2 notice that the axes label is different for different plots in figure 2.11. Moreover, the symmetry behavior of the partial derivatives depends on the elevation angle, where the raising satellite shows low or no symmetry while the satellite at a fixed elevation shows high symmetry.

The values of \mathbf{ds} have been roughly estimated by analyzing the partial derivatives \mathbf{F} , but more investigation of the uncertainty of each parameter needs to be done. Also, depending on where the influence parameters come from different imprecision values can be used. For example GPS satellites broadcast the parameters of the *Klobuchar* ionospheric model while other agencies also provide these parameters with different precision, like CODE-analysis center (CODE (2017)).

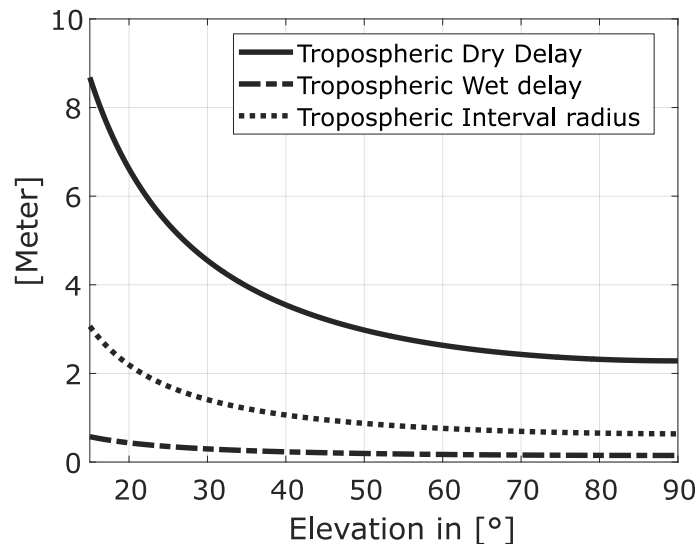
2.5.2.3 Saastamoinen Tropospheric Model

The atmospheric correction for troposphere in radio ranging is given by equation (2.14) and the related apparent zenith distance which can be determined from true zenith distance Z of the satellite by the formula $z = Z - \delta_z$ from equation (2.15) in section 2.1.3. All influence parameters involved in the dry and wet tropospheric distance correction as described in Saastamoinen (1973) with the same notation are given in Table 2.2 with their uncertainty. Also in this model, the uncertainty is 0.5 of the last digit of each influence parameter.

Figure 2.13 depicts the partial derivative of the tropospheric *Saastamoinen* model w.r.t. the model influence parameters for a simulated satellite raising from 15° to 90° elevation angle keep the time constant at midday.

Table 2.2: Assumed uncertainty of the influence parameters of *Saastamoinen* tropospheric model.

Influence parameter	Uncertainty
dT : Surface temperature	$0.5 \cdot 10^{-4}$
dP : Total surface pressure	$0.5 \cdot 10^{-4}$
de : Partial water vapor pressure	$0.5 \cdot 10^{-4}$
$d\alpha_1$: constant= $16''$	$0.5 \cdot 10^{-3}$
$d\alpha_2$: constant= 4800	$0.5 \cdot 10^{-4}$
$d\alpha_3$: constant= $0''.07$	$0.5 \cdot 10^{-3}$
$d\beta_1$: constant= 0.002277	$0.5 \cdot 10^{-6}$
$d\beta_2$: constant= 0.0026	$0.5 \cdot 10^{-4}$
$d\beta_3$: constant= 0.00028	$0.5 \cdot 10^{-5}$
$d\beta_4$: constant= 1255	$0.5 \cdot 10^{-4}$
$d\beta_5$: constant= 0.05	$0.5 \cdot 10^{-2}$
$d\delta_r$	$0.5 \cdot 10^{-4}$
$d\phi$: station latitude	$0.5 \cdot 10^{-4}$
dh : station height above see level	$0.5 \cdot 10^{-4}$
dZ_d : true zenith distance	$0.5 \cdot 10^{-4}$

Figure 2.12: Tropospheric dry and wet delay and their total interval radius for a satellite raising from 15° to 90° elevation angle at mid day.

We choose midday since this time has the biggest effect on the model for the whole day. All parameter partial derivatives show similar behaviors in terms of elevation angle except the partial derivatives of δ_r has a constant value for different elevation angles. Some parameters have a small influence on the model e.g., α_2 while other parameters have a very large influence on the model, and a small uncertainty in those parameters can cause a large error in the model, e.g., α_3 , β_1 and β_2 . However, those parameters have small constant values (see table 2.2) which reduce their effects on the model.

2.5.3 Expert Knowledge and Desired Size of the Bounding Zone

In addition to the probabilistic approaches and sensitivity analysis for the observation interval bounds determination, expert knowledge and desired size of bounding zones can be used to set a OIB. Depending on the interval method used in the estimation process and our knowledge of the observation, interval bounds can be chosen properly. For instance, if the bonding must not exceed one meter in each direction from the point position, it makes sense to set the observation interval bound to one meter or less. However, it is not that simple, due to the nature of the interval computations and its tendency of increasing with the interval oper-

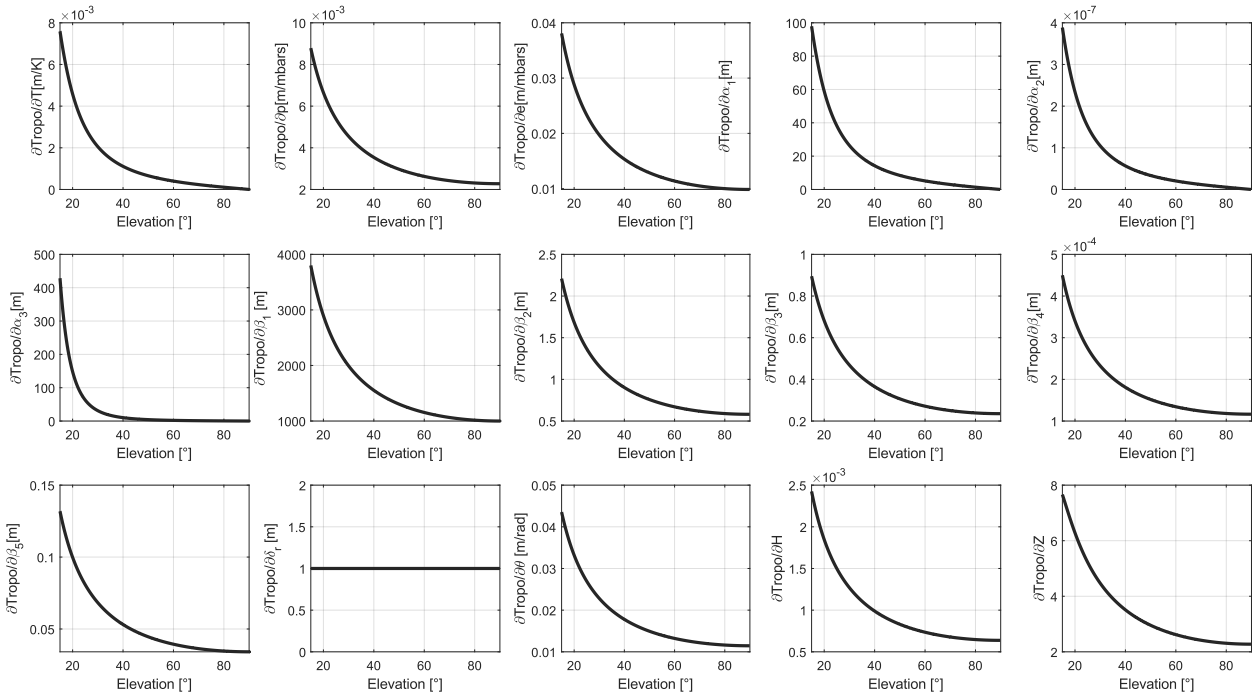


Figure 2.13: Partial derivatives (F) of the tropospheric *Saastamoinen* model w.r.t. the model influence parameters for a satellite raising from 15° to 90° elevation angle at midday.

ation a ratio of one to one between observation interval and desired bounding zone may not be appropriate. So, the user has to understate the nature of the method in use and the quality and type of observation in order to properly set the interval bounds. For instance, the SIVIA method with contractor programming tends to decrease the bounding zone w.r.t. the observation interval bound while using only conventional interval arithmetic tends to increase the bounding zone w.r.t. the observation interval bound. Moreover, depending on the measurement type, different magnitudes and types of error can occur. For example, the multipath error in the carrier phase measurement is different from the multipath error in the code measurements. The maximum carrier phase multipath error can be obtained from the wavelength of the signal, e.g., the phase error equivalent to a range error of 4.8 cm for the phase measurements of the 1.57542 GHz L1 GPS signal, Georgiadou et al. (1988). So that, in the case of carrier phase measurements, a guaranteed interval bound can be put on the multipath error of the simple geometry. On the other hand, the maximum error in the range that can be induced by the multipath of the GPS code measurement is 1.5 times the length of a chip, i.e., it is more often a few meters. So, also here it depends on the code observation in use (C/A or P-code), and different OIBs can be set on the multipath. Not only the type of code affect the error induced by the multipath but also the GPS receiver itself and especially the type of correlator embedded in it. For instance, the narrow correlator can mitigate the multipath error more than the wide correlator, Misra and Enge (2011).

In addition to the size of the bounding zone, the reliability, integrity, continuity, and availability of the navigation solution heavily depend on the applied observation interval bounds. The user has to take into consideration all those factors.

Furthermore, the geometry of the navigation problem has large effects on the bounding zone and other reliability and integrity parameters. Notably, GNSS positioning in an open area is quite different from the GNSS positioning in an urban area where the geometry of the navigation problem varies so often and the observation interval bounds have different coincidences and outcome on the bounding zone.

3 Integrity Approaches Based on Interval Mathematics and Set Theory

Supplementary to the probabilistic approaches of integrity monitoring, new approaches based on interval analysis are developed in the last decade. An extension of the least-squares adjustment using interval analysis is presented in Schön and Kutterer (2006) that can provide an interval box or zonotope as a confidence region for the point position determined by LSA. Besides that, a pure interval approach based on interval computation and contractors is presented in Drevelle and Bonnifait (2009, 2013). This method called set inversion via interval analysis SIVIA provides a set of interval boxes as a solution set of the positioning solution and did not has a single point position. A comparison of these approaches is done in Dbouk and Schön (2018). However, due to the dependence of the integrity monitoring on the probabilities, a full integrity monitoring via interval analysis somehow vague and not straightforward is to be defined. Next, I will discuss briefly the two interval existing approaches and present the newly developed approach based on interval mathematics and set theory which provides the same reliability, integrity, and continuity information as the probabilistic approaches, such as confidence regions, consistency measures, minimum detectable bias, fault detection and exclusion, and protection level.

3.1 Interval Extension of Least-Squares Adjustment

Interval extension of Least-squares adjustment (IELSA) is an extension of the traditional least-squares adjustment LSA which is used to estimate the unknown parameters, i.e. typically the coordinates and the receiver clock offset of the GPS receiver, Schön and Kutterer (2005b). This method is simple and straightforward. The observation interval bounds are applied to the OMC, so $\Delta\mathbf{l}$ becomes $[\Delta\mathbf{l} - \mathbf{\Delta}, \Delta\mathbf{l} + \mathbf{\Delta}]$ where $\mathbf{\Delta}$ is the vector interval radii of the observations. We assume symmetric intervals so that the midpoint of the interval vector is the actual OMC $\Delta\mathbf{l}$. The vector of interval radii $\mathbf{\Delta}$ express the OIBs. The interval extension of LSA, i.e., IELSA read:

$$[d\hat{\mathbf{x}}] = (\mathbf{A}^T \mathbf{W} \mathbf{A})^{-1} \mathbf{A}^T \mathbf{W} [\Delta\mathbf{l} - \mathbf{\Delta}, \Delta\mathbf{l} + \mathbf{\Delta}], \quad (3.1)$$

where the midpoint of the interval box $[d\hat{\mathbf{x}}]$ is the actual estimate by the traditional LSA and the radii of the interval box $[d\hat{\mathbf{x}}]$ represent the uncertainty of the estimated parameter which is the propagation of the applied uncertainty on the observation i.e., the observation interval bound. Due to the nature of the conventional interval computation, which tends to increases the computed intervals with each iteration of the computation, the interval box solution is an overestimation of the uncertainty.

Equation (3.1) can be split into two parts by considering the midpoint and the radius of the observation interval separately. Therefore,

$$d\hat{\mathbf{x}}_m = (\mathbf{A}^T \mathbf{W} \mathbf{A})^{-1} \mathbf{A}^T \mathbf{W} \Delta\mathbf{l}, \quad (3.2)$$

and

$$d\hat{\mathbf{x}}_r = |(\mathbf{A}^T \mathbf{W} \mathbf{A})^{-1} \mathbf{A}^T \mathbf{W}| \mathbf{\Delta}, \quad (3.3)$$

where equation (3.2) is the usual LSA which provide the single point position in GPS positioning and equation (3.3) propagate the interval uncertainty from the observation domain to the parameter domain. A full derivation of the IELSA can be found in Schön and Kutterer (2003, 2005b).

The solution and the algorithm of IELSA have the following properties:

- The midpoint of the interval box $[d\hat{\mathbf{x}}]$ is the same solution as the traditional LSA.

- This interval box is centered on the estimated point position and its faces are always parallel to the coordinate axes which are not the perfect representation of the uncertainty especially in terms of directions, not magnitudes. Thus, it varies when rotating the coordinate system, which means that the uncertainty of the coordinates varies depending on the orientation of the coordinate frame.
- The factual range of the coordinate vector is overestimated by the interval box and describing the uncertainty measures by this box is thus pessimistic.

The main problem of the IELSA is that the interval extension is not closed with respect to linear mappings, such as the traditional LS algorithm. Therefore, to overcome the two drawbacks of the IELSA, zonotopes can be used since the factual range of the coordinates is the zonotope given by:

$$\begin{aligned}
\mathbb{Z} = \mathbb{Z}(\mathbf{K}) &:= \mathbf{K}C_n + \mathbf{z}_0 \\
&= \{\mathbf{K}\mathbf{w} + \mathbf{z}_0 \mid \mathbf{w} \in C_n\} \\
&= \left\{ \mathbf{z} \in \mathbb{R}^u \mid \mathbf{z} = \mathbf{z}_0 + \sum_{i=1}^n w_i \mathbf{K}_i, -1 \leq w_i \leq 1 \right\},
\end{aligned} \tag{3.4}$$

where $\mathbb{Z} \subseteq \mathbb{R}^u$ is a zonotope and an image of a hypercube under an affine projection, \mathbf{K} is an $u \times n$ matrix and C_n is n -dimensional hypercube defined as:

$$C_n = \{\mathbf{w} \in \mathbb{R}^n \mid -1 \leq w_i \leq 1, i = 1, \dots, n\} \tag{3.5}$$

Figure 3.1 illustrates the affine projection of a hypercube which gives a zonotope. The above construction and definition of the zonotope have been presented in Ziegler (1995). The zonotope can also be defined and constructed by a *Minkowski* sum of n segments Epstein (1995); Ziegler (1995); Kühn (1998).

Zonotopes determine the impact of the remaining systematic errors in the observations on the estimated parameters. Zonotopes has the following special properties:

- Each zonotope is a convex regular polytope which is symmetric with respect to its center \mathbf{z}_0 .
- A zonotope does not change its shape when it rotates in the coordinate system and the affine projection of the zonotope is also a zonotope with lower dimension.
- The geometry of the navigation problem affects the point uncertainty, and thus the shape of the zonotope. Similarly, error ellipses in the probabilistic approaches indicate the directions of the minimum and maximum uncertainty.
- For the non-overdetermined positioning problem, the edges of the zonotope are perpendicular to the LOS of the measurements. The uncertainty is minimal if the LOS are perpendicular, and maximal when the angle between LOS tends to 0° or 180° .
- The distance between two parallel edges is twice the systematic of the corresponding observations.
- The number of edges is proportional to the number of measurements and as the number of measurements increases the zonotope tends to get rounded.

Figure 3.2 depicts an example of the IELSA interval box and zonotope solution of a simulated scenario with six well distributed static transmitters 2D. The zonotope confidence domain of the IELSA is the largest zonotope confined by the interval box where always some of the zonotope vertexes lay on the interval box edges. The orientation of the zonotopes changes w.r.t. the LOS which reflects the uncertainty in all directions and the quality of the navigation geometry. Instead, the interval box has a fixed orientation with edges parallel to the coordinate axes of the frame system. However, the zonotope is still an overestimation of the confidence domain and represents the precision of the navigation geometry and the impact of the remaining systematic errors in the observations without taking into account the overall observation errors.

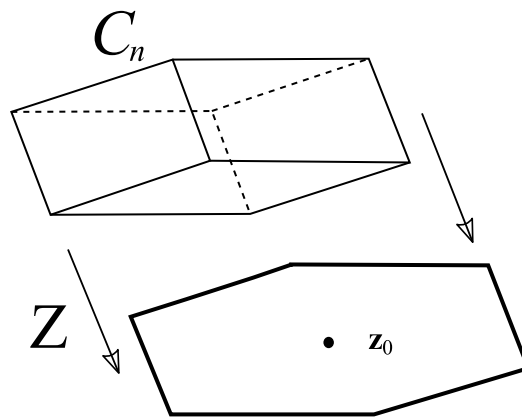


Figure 3.1: Construction of zonotope by affine projection of a hypercube, Schön and Kutterer (2005b).

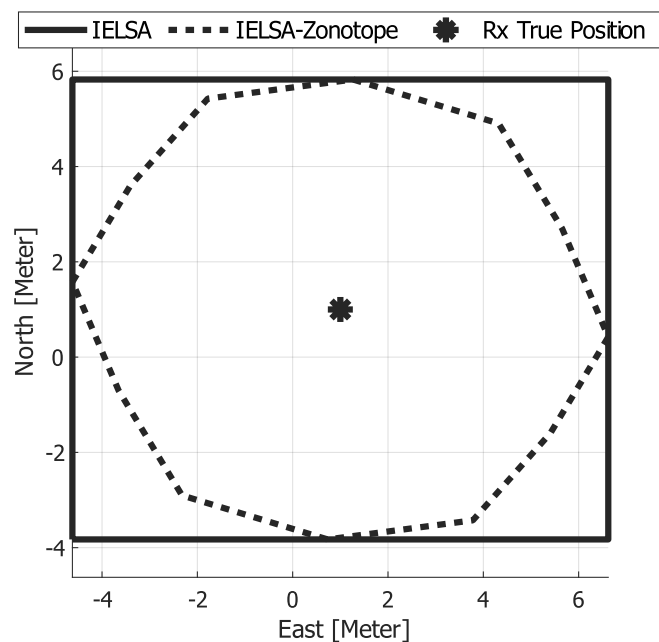


Figure 3.2: Interval box solution of IELSA (black solid line), its factual zonoztope range (black dot line), and the true position (black asterisk).

3.2 Set Inversion Via Interval Analysis

Set Inversion Via Interval Analysis (SIVIA) is applied to solve positioning problems using contraction and bisection, Drevelle and Bonnifait (2011, 2013). This approach differs from the probabilistic approaches such as LS and Kalman filtering where most of the time the observation errors are modeled as *Gaussian* distribution with zero mean and some variances Parkinson and Enge (1996). In SIVIA, the satellite positions and the observations are represented by intervals. Also, the initial solution set of the estimates, i.e., receiver position and clock offset is a very large interval box guaranteed to contain the true solution. The initial box could also be an infinity interval box that can be easily contracted to a small box in few iterations. SIVIA solve the non-linear navigation equation directly without any linearization, which is needed in most of the probabilistic approaches. Each observation acts as a constraint which is represented in the case of pseudo-range measurement by the natural inclusion function for the observation equation:

$$[f_m]([\mathbf{x}]) = \sqrt{([x_s^r] - [x_A])^2 + ([y_s^r] - [y_A])^2 + ([z_s^r] - [z_A])^2} + [b_A] = \Delta I \quad (3.6)$$

The natural inclusion function for f_m is minimum since each variable is involved only once in its expression Jaulin et al. (2001). The inclusion function is obtained by replacing each operator of f_m by its interval

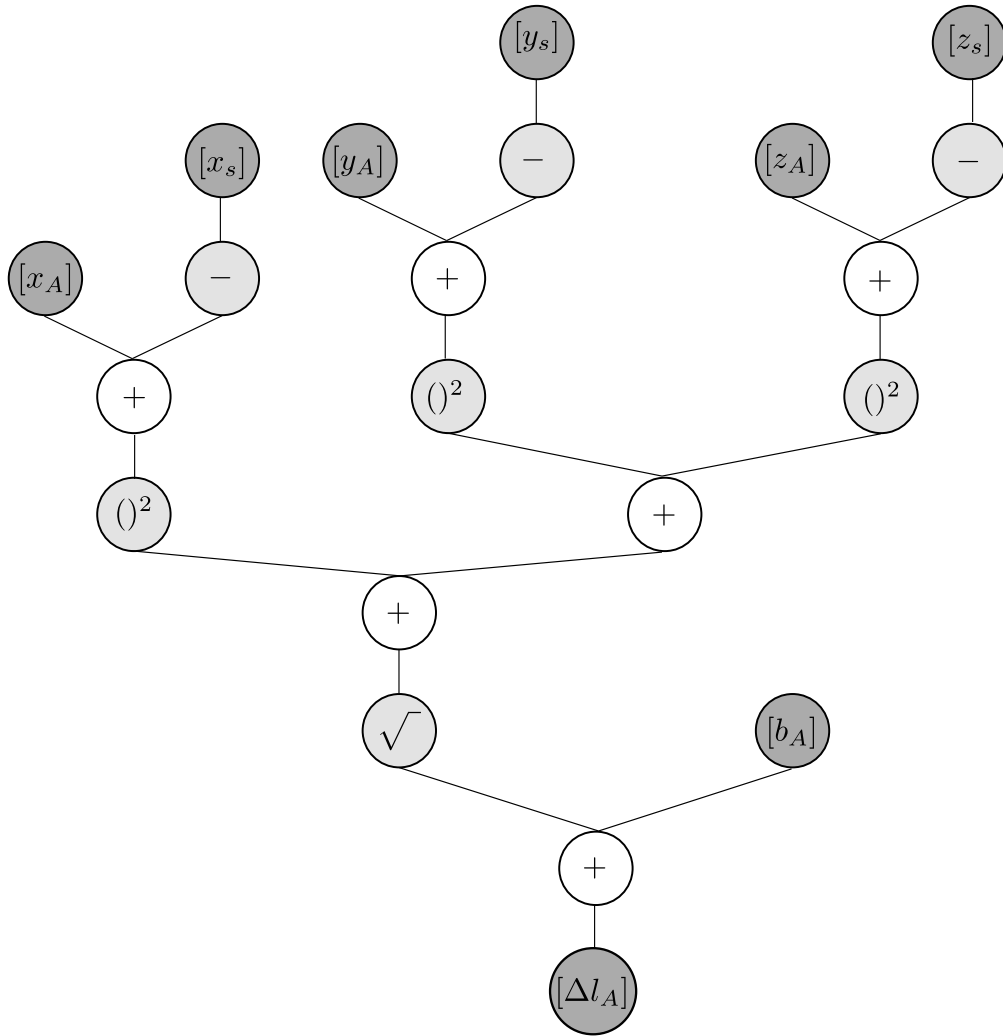


Figure 3.3: Elementary constraints decomposition of GNSS pseudo-range measurement inclusion function.

extension. A forward-backward contractor of the inclusion function can be built using constraint propagation. The fall-climb algorithm is used to propagate constraints in an optimal way as described in section 2.4.5. This algorithm is suitable since the decomposition of the elementary constraints does not contain any cycle, figure 3.3. The forward contraction starts from the leaf and goes down to the root of the tree. After that, a backward contraction was carried out climbing the tree from the root up to the leaves. During the propagation when a binary operator is encountered, contraction is done on its two operands.

Each measurement provides a contracted box of an initial very big box. The final solution is the intersection of all contracted boxes. If one of the measurements is biased, the solution will be the empty set. The so-called q-relaxed solver can be used to tolerate q biased measurements, Jaulin et al. (1996). For example, the 1-relaxed solution is guaranteed to contain the true solution in the presence of 1 biased measurement at a time.

The SIVIA algorithm applied in this work is different from the usual SIVIA approaches. Usually, the initial box is bisected and every new box is checked to be a solution, not a solution or part of it is solution and part is not, i.e., need to be bisected again. Then, a predefined precision parameter has to be assigned for those boxes that still need a bisection as described in section 2.4.4. For a small predefined precision parameter, a very large number of bisections will be needed which is time-consuming.

In this work, the initial box is bisected into small boxes, and then each box is used as an initial box for SIVIA. The final solution for each measurement is the union hull of all contracted boxes, and the final solution of SIVIA is the intersection between the boxes from all measurements. Figure 3.4, depicts an example of SIVIA solution compared to the IELSA interval box and its zonotope extension. The SIVIA solution is the union hull of all the small boxes indicates in black. The transmitters configuration used in this

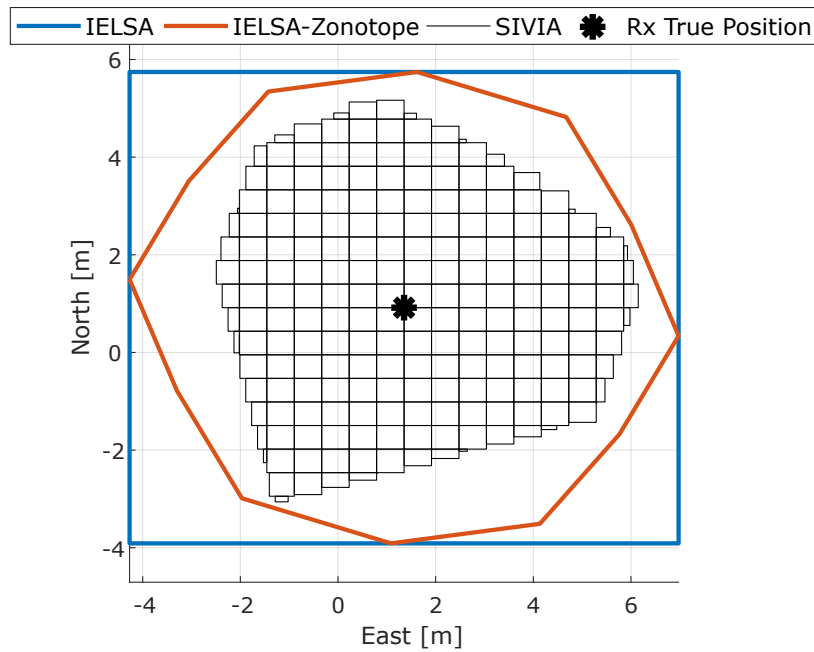


Figure 3.4: SIVIA solution as union hull of the black boxes compared to the results from IELSA (both interval box and zonotope).

example and the observations are the same as for the other methods examples, cf. Figure 3.4. Moreover, the same observation interval bounds are applied on all methods, but in the SIVIA case part of the observation interval goes to the observation itself and the other part goes to the transmitter positions. Since in this example the transmitter positions are considered perfectly known, $\frac{1}{10}$ of the total interval bound is applied to the transmitter position.

In conclusion, SIVIA bounding zone provides a smaller and more realistic bounding zone than the IELSA but it is computationally expensive while IELSA is quite fast and suitable for real data applications.

3.3 Linear Programming Bounding Method

Linear Programming (LP) problems consist of a linear objective function and a system of linear equalities and inequalities called constraints. This system of equation (equalities and inequalities) represent a system of constraint equations that represent a convex polytope as a feasible region. The barycenter of the polytope can be considered a point position as an initial estimate. An objective function has to be optimized (minimize or maximize) on those constraints, Luenberger et al. (1984). The general matrix form of LP problem is:

$$\max \{ \mathbf{c}^T \mathbf{x} \mid \mathbf{A} \mathbf{x} \leq \mathbf{b} \wedge \mathbf{x} \geq 0 \}, \quad (3.7)$$

where \mathbf{c} and \mathbf{b} are vectors, \mathbf{A} is a matrix and \mathbf{x} represent the parameters to be estimated. The LP problem consists of three parts: $\mathbf{c}^T \mathbf{x}$ represent the linear function to be maximized, $\mathbf{A} \mathbf{x} \leq \mathbf{b}$ system of inequalities represent the constraints problem, and $\mathbf{x} \geq 0$ represent the non negative variables.

Applying the observation interval bounds on both sides of the OMC of the over-determined system of linearized observation equations (2.3), we get a system of inequalities to represent the constraint problems. Only the constraint equations are enough and in our case, they are as follows:

$$\begin{cases} \mathbf{A} \Delta \mathbf{x} \leq \Delta \mathbf{l} + \Delta \\ -\mathbf{A} \Delta \mathbf{x} \leq -\Delta \mathbf{l} + \Delta. \end{cases} \quad (3.8)$$

Now we need to set up the objective functions. Each objective function will provide a minimal point solution that will be a vertex point of the polytope or will lie on the plane of the polytope solution that is perpendicular to the objective function direction. In a 2D navigation problem, we evaluate these constraints in 16 objective

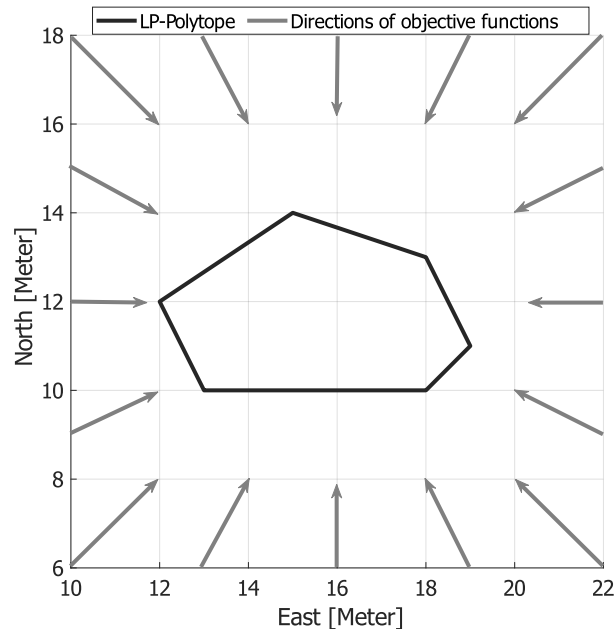


Figure 3.5: Normal vectors of objective functions (grey arrow) and Linear Programming feasible region (black polytope).

functions constructed from a linear combination of the state vector. The objective functions are a set of straight lines equally rotated by 22.5° which define the degree of detail of the results. Figure 3.5, shows the directions of the normal vectors representing the objective functions in grey and an example of the polytope feasible region of those objective functions in black. These normal vectors are the directions where the LP solver acts. In the end, there is a set of 16 LP problems to be solved. Each one gives a point solution that minimizes the related objective function under the constraints. More objective functions can be constructed by rotating a straight line from 0 to 2π . For the 2D case and taken the typical number of observations (6 - 10) into account, we found 16 objective functions being enough since the consecutive functions provide the same vertex. Some vertices will be duplicated depending on the satellite geometry. When there are two or more satellites nearby, the same vertex will appear more than once. Moreover, when the uncertainty is large in the direction of a polytope angle bisector, the related vertices will be a solution of more than one objective function, mainly two or three consecutive objective functions. For a 3D GNSS navigation problem, we use 36 objective functions since we have more variables to be determined. In 3D positioning, the objective functions are represented by plane equations as a linear combination of the state vector.

Figure (3.6) depicts the polytope LP solution superimposed with the IELSA interval box, IELSA zonotope and the interval boxes of SIVIA solution from the same example represented in figure 3.4. We can see the polytope is enclosed by the IELSA zonotope and the polytope is not regular or symmetric, i.e., it does not have opposite parallel edges and even number of vertices. If the observation is perfect, i.e., there are no errors in the observation, the polytope will be regular. The set solution of SIVIA is very similar to the polytope solution of the LP where a linear fitting of the SIVIA interval boxes edges could provide a very similar polytope to the LP polytope.

There are some special properties of the LP polytopes feasible region:

- The edges of the polytope are perpendicular to the LOS.
- The polytope represents all possible solutions to the navigation problem. Random and systematic errors are combined in the observation interval or explicit assumptions about the random error distribution are not made.
- LP polytope is convex and the affine projection of 3D polytope (polyhedron) onto a plane spanned by two coordinate axes is a 2D convex polytope (polygon)

- The surface/volume is minimum if the LOSs are perpendicular. Maximum uncertainty is in the direction of one of the two bisectors of the polytope angles, i.e., in the bisector of the angle between LOSs.

The LP polytope provides a smaller and more realistic uncertainty domain for the navigation solution than the IELSA interval box, zonotope and the SIVIA solution. However, in real GNSS scenario where the parameters to be estimates are at least 4, a higher number of the objective functions are needed and this will be computationally expensive and not suitable for real-time applications.

The LP polytope solution was developed during the research period of this thesis and it was the basis of the newly developed method for the GNSS position and computation of related parameters especially uncertainty and integrity parameters. Moreover, LP polytope can be used to detect and exclude biases from the observation, but we will leave the explanation to the newly developed methods which are also based on polytopes and zonotopes but using convex optimization problem instead of linear programming to compute the polytopes and the zonotopes.

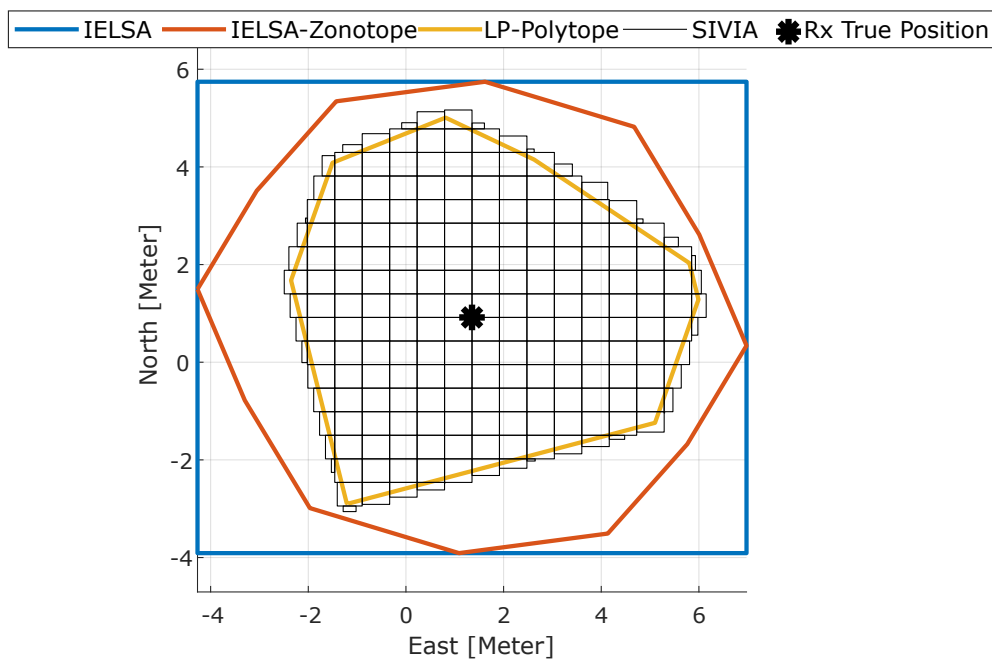


Figure 3.6: Interval box solution of IELSA (black solid line), its factual range as zonotope (black dot line), and the true position (black asterisk).

3.4 Developed Method Based on Primal-Dual Polytope and Intervals

This section is the main contribution of this thesis to the research topic reliability and integrity of GNSS. The navigation problem is transformed into a special case of the convex optimization problem in terms of polygons. The accuracy, reliability, integrity, and continuity information are developed and computed in a completely different way from the traditional approaches. This method provides a polytope feasible region of the navigation problem, barycenter of the polytope as a point position, a zonotope confidence region, a new consistency measures concept, reliability information in terms of minimum detectable bias, integrity information in terms of fault detection and identification, and finally a guaranteed protection level in a shape of a zonotope.

Interval analysis and polygons have been used in the optimization process for a wide range of applications such as robotics, control theory, and positioning, Blesa et al. (2011); Mahato et al. (2020); Voges and Wagner (2018). Interval analysis is a relatively new type of mathematical analysis that exploits the mathematical operation of intervals themselves and not of numbers as in calculus. On the other side, polygons are at the core of elementary geometry and computational geometry. In 2D, elementary geometry connects a finite

number of straight-line segments to produce a closed polygon, while computational geometry is dedicated to the study of algorithms that can compute geometrical shapes, such as polygons. Interval analysis, polygons, elementary geometry, and computational geometry are all different types of mathematical fields. Each of them is a broad branch of mathematics. We will not go into each field in depth since it is not the purpose of this thesis. We will combine these mathematical fields and make use of them in GNSS positioning and integrity monitoring. To do so, interval bounds are introduced to the GNSS observation and bounding zones in the shape of polygons are computed as feasible regions of the navigation problem. The basics of this method and preliminary results are presented in Dbouk and Schön (2019, 2020). The Primal-Dual Polytope (PDP) algorithm will be used to compute the polygons which are mainly polytopes and zonotopes. PDP is an algorithm in the field of computational geometry, in particular, algorithms to solve vertex enumeration problem of hyper-plane polytopes, figure 3.7 and 3.11.

Combining different mathematical fields, a polygon feasible solution can be achieved in GNSS positioning. Utilizing the properties of different types of polygons especially zonotopes and polytopes, consistency check and integrity monitoring can be derived. Figure (3.7) depicts the three main situations that can happen in GNSS-based positioning using interval observation bounds and polygons.

Figure 3.7a shows an example of error-free GNSS observations which leads to a nominal polytope solution, i.e., zonotope which is a regular polytope. This can be used as a reference polytope. Regular polytopes have an even number of vertices, angles, and edges, where opposite edges are of equal length and parallel. Zonotopes can be either achieved by error-free observations or using only the OIBs and the satellite's geometry. The determination of the zonotopes will be explained later on in section 3.4.2 and section 3.4.3.

Figure 3.7b presents the actual situation of the GNSS observations that contain random noise. These noisy observations induce a deformation in the nominal polytope which leads to a non-regular polytope solution. This deformation affects the number of vertices and edges in the polytope. The number of edges and vertices may stay the same as in the non-deformed case, i.e., zonotope or decreases if the observations are more and more inconsistent. The barycenter of the polytope can be considered as a representative location for the Single Point Position (SPP).

In Figure 3.7a and 3.7b, the black dot is the true position and the grey dot is the estimated position i.e., the barycenter of the polytope. In case (a) where we have a zonotope bounding zone i.e., error-free observations, the true and estimated position coincides as expected, while in the second case (b) the estimated position is shifted from the true position due to the deformation in the polytope. This effect will be enlightened in section 3.4.3.

In case an outlier occurs in one of the observations, the solution set is empty, which means there is no common intersection between all pairs of interval observation bounds. Figure 3.7c depicts this situation when we have an outlier in one of the observations. There are different intersection zones between different pairs of interval observation bounds but no common intersection zone. This pair of interval observation bounds is the so-called slab in the convex optimization community, Boyd and Vandenberghe (2004). Figure 3.7c illustrates this situation, but in fact, the solution will be just an empty set i.e., no numbers in the solution. When the solution is an empty set, this means an outlier is detected and needs to be identified and excluded.

Based on these three main situations of the bounding zone, a single point position (SPP), confidence domain of the SPP, MDB, FDE, PL and other positioning, accuracy, reliability and integrity information will developed in this chapter. It is worth mentioning that the illustration of these situations is done in 2-dimensions. The real GNSS data will be at least in 4-dimensions in the case of one constellation such as GPS, where the polygons could not be graphically represented. In the higher dimension case, hyper-planes will bound the polytope, in addition to the edges and vertices. The behavior of the planes is similar to the edge behavior in 2D. Both edges and planes are the hyper-planes in 2-D and 3-D, respectively.

The motivation behind this study is finding a new way to derive integrity measures with guaranteed information, minimizing internal and external reliability, and IR. Due to the nature of interval mathematics and convex optimization, most of the information will be guaranteed once the observation intervals are defined. The one that could not be guaranteed will have a confidence level as the probabilistic approaches.

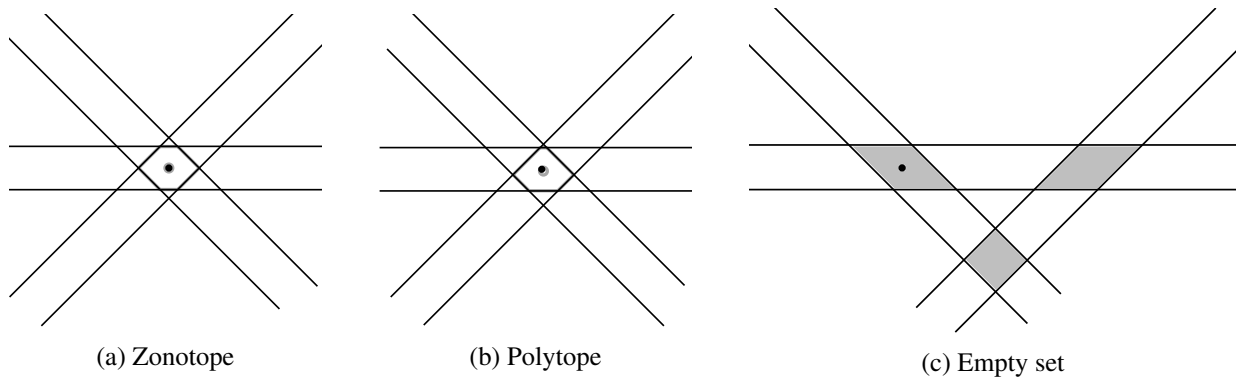


Figure 3.7: Main 3 geometric situations where error bounds are intersecting: (a) error-free observations lead to a nominal polytope, i.e., zonotope, (b) noisy observations lead to a general polytope, and (c) bias in one observation leads to an empty set.

3.4.1 Polytopes and Zonotopes

Following Boyd and Vandenberghe (2004), a polyhedron is defined as the solution set of a finite number of linear equalities and inequalities

$$\mathbb{P} = \{\mathbf{x} | \mathbf{n}_i^T \mathbf{x} \leq u_i, i = 1, \dots, m, \quad \mathbf{c}_i^T \mathbf{x} = d_i, i = 1, \dots, p\}, \quad (3.9)$$

where \mathbf{x} is the solution set, \mathbf{n}_i is the vector of inequality coefficients, \mathbf{c}_i is the vector of equality coefficients, m and p are the numbers of inequalities and equalities, respectively. The polyhedron can also be defined as the convex hull of a finite number of points which represent its vertices

$$\mathbb{P} = \text{conv}(\mathbf{v}_0, \mathbf{v}_1, \dots, \mathbf{v}_m) = \{\theta_0 \mathbf{v}_0, \theta_1 \mathbf{v}_1, \dots, \theta_m \mathbf{v}_m | \theta \geq \mathbf{0}, \mathbf{1}^T \theta = \mathbf{1}\}, \quad (3.10)$$

where \mathbf{v} represents the polytope vertices and θ is the coefficients of the inequality when projecting the hyper-planes on the normalized hyper-cube. A polyhedron is the intersection of a finite number of half-spaces and hyperplanes. In this thesis, we will follow the convention of calling a bounded polyhedron a polytope. Zonotopes or parallelotopes are special polytopes with specific geometrical properties, e.g. pairs of edges have the same length and are parallel. Good references for zonotopes and their uses in uncertainty estimation are Ziegler (1995); Schön and Kutterer (2005a).

A hyperplane is a set of the following form:

$$\mathbb{X} = \{\mathbf{x} \in \mathbb{R}^n | \mathbf{a}^T \mathbf{x} = b\}, \quad (3.11)$$

where $\mathbf{a} \in \mathbb{R}^n$, $\mathbf{a} \neq \mathbf{0}$, $b \in \mathbb{R}$ and n is the dimension of the hyper-plane. The analytical description of the hyperplane is the solution set of the linear equations between the components of \mathbf{x} . The geometrical description of the hyperplane $\mathbf{x} \in \mathbb{R}^n | \mathbf{a}^T \mathbf{x} = b$ can be depicted as the set of points with a constant inner product to a given vector \mathbf{a} or can be interpreted as a hyperplane with the normal vector \mathbf{a} , where the constant value b determines the offset of the hyperplane from the origin. The hyperplane can also be expressed as in equation (3.12) for a better understanding of its geometrical interpretation.

$$\mathbb{X} = \{\mathbf{x} \in \mathbb{R}^n | \mathbf{a}^T (\mathbf{x} - \mathbf{x}_0) = 0\}, \quad (3.12)$$

where \mathbf{x}_0 is an arbitrary but fixed point on the hyperplane. This geometrical interpretation will be used in the following sections to understand the behavior of the convex optimization problem and how the zonotopes and polytopes are constructed. Figure 3.8 illustrates the geometrical interpretation of the hyperplane orthogonal to the vector \mathbf{a} with an offset b

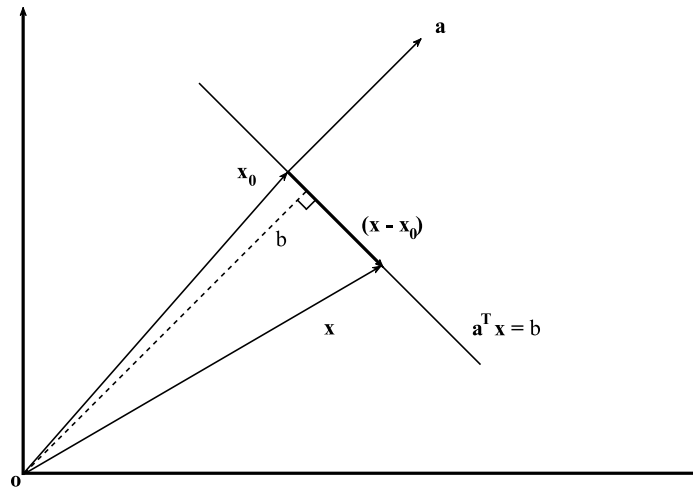


Figure 3.8: Hyperplane $\mathbf{a}^T \mathbf{x} = b$ in \mathbb{R}^2 , with normal vector \mathbf{a} , a point \mathbf{x}_0 in the hyperplane and scalar orthogonal distance b from the origin to the hyperplane. For any vector \mathbf{x} from the origin to any point on the hyperplane, the vector $(\mathbf{x} - \mathbf{x}_0)$ (shown as the darker arrow) is orthogonal to \mathbf{a} .

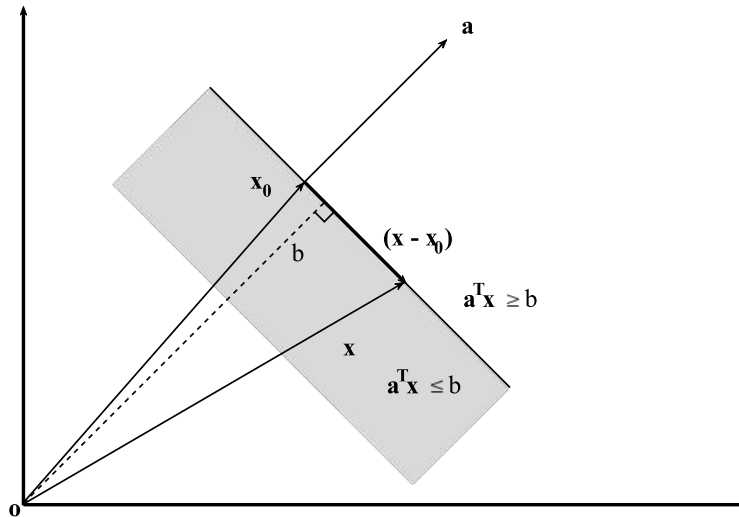


Figure 3.9: Hyperplane $\mathbf{a}^T \mathbf{x} = b$ in \mathbb{R}^2 separating \mathbb{R}^2 into two half-spaces. The half-space $\mathbf{a}^T \mathbf{x} \leq b$ indicated by the shaded area is in the opposite direction of the normal vector \mathbf{a} . The half-space indicated by $\mathbf{a}^T \mathbf{x} \geq b$ (opposite to the shaded area) is in the direction of the normal vector \mathbf{a} .

A hyperplane divides the space into two hyper-spaces or half-spaces. Figure 3.9 depicts the one half-space (shaded area) defined by the constraint $\mathbf{a}^T \mathbf{x} \leq b$.

Two parallel hyperplanes form a slab. Taking the hyper-space inside the slab creates a feasible region of the two conditions expressed by the hyperplanes. By taking the zone inside the slab, we choose the directions of the normal vector of the hyperplanes in opposite directions and one is pointing to the other. The solution set of a slab can be defined as follows:

$$\mathbb{S} = \{\mathbf{x} \in \mathbb{R}^n \mid c \leq \mathbf{a}^T \mathbf{x} \leq b\}. \quad (3.13)$$

The slab set form in equation 3.13 shows the opposite direction of the normal vector of the hyper-planes, where n is the dimension of the hyper-plane. Figure 3.10 depicts a 2-D slab solution of one GNSS observation, where Δ is the OIB. In real GNSS scenario the solution or the bounding zone will be the intersection of m slabs, where m is the number of observations.

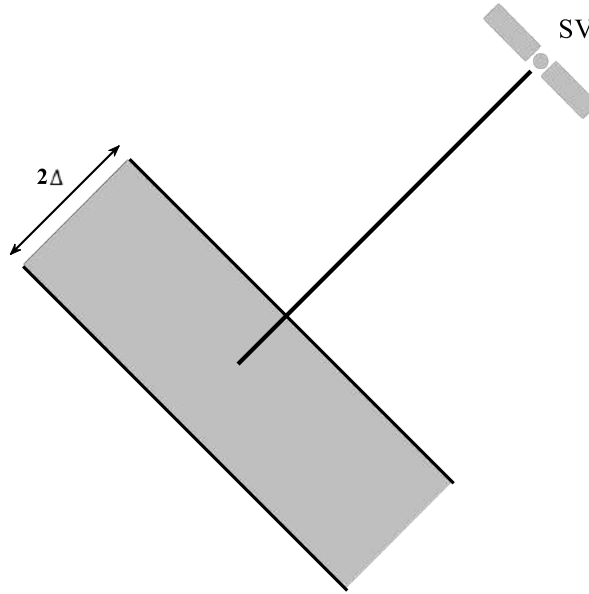


Figure 3.10: 2-D illustration of a slab feasible region (shaded area) for one GNSS observation with an observation error bound equal to an arbitrary value Δ .

3.4.2 Formulation and Methodology

The main idea is to transform the navigation problem which is defined by the system of equations (2.3) to a bounded convex system of linear equations. In order to do so, we applied interval observation bounds Δ to the OMC in both directions, so equation (2.4) reads as follows:

$$\Delta \mathbf{l} - \Delta \leq \mathbf{A} \Delta \mathbf{x} \leq \Delta \mathbf{l} + \Delta, \quad (3.14)$$

The determination of the interval radii as error bounds is explained in section 2.5. Rearranging equation (3.14), we get a system of inequalities:

$$\begin{cases} \mathbf{A} \Delta \mathbf{x} \leq \Delta \mathbf{l} + \Delta \\ -\mathbf{A} \Delta \mathbf{x} \leq -\Delta \mathbf{l} + \Delta, \end{cases} \quad (3.15)$$

which can be written as follows:

$$\mathbf{B} \Delta \mathbf{x} \leq \mathbf{b}, \quad (3.16)$$

where $\mathbf{B} = \begin{bmatrix} \mathbf{A} \\ -\mathbf{A} \end{bmatrix}$ and $\mathbf{b} = \begin{bmatrix} \Delta \mathbf{l} + \Delta \\ -\Delta \mathbf{l} + \Delta \end{bmatrix}$. This system of inequalities in equation (3.15) is the same as the definition of the slabs in equation (3.13). The above system of inequality constraints defines a convex polytope as an intersection of a finite number of half-spaces and is referred to as an H-polytope. Each inequality constraint is a half-space. To get the solution of the system of equation (3.16) in the position domain i.e., to get the vertices of the polytopal bounding zone in the coordinate system, the H-polytope has to be transformed into a V-polytope (convex hull of the polytope vertices). This transformation is the so-called vertex enumeration problem, and there exist different algorithms to solve it. In this thesis, a PDP algorithm is used to transform the H-polytope into a V-Polytope. There exist different algorithms to solve the vertex enumeration problem or PDP problem. In Avis and Fukuda (1992); Fukuda et al. (1997); Bremner et al. (1998); Fomin et al. (2008); Khachiyan et al. (2009) descriptions for the most used algorithms e.g., Backtrack and pivoting are found.

The PDP algorithm consists of three main stages. First, finding a point inside the polytope. This can be done by any estimation algorithms such as LS. Finding a point inside the polytope is a local minimization problem that is performed by applying the observations interval bounds on the observations on both sides. In principle, this should provide a polytope as a solution if the interval bounds are not violated. If the estimation LS algorithm is not able to find any local minima, the solution set is empty and an outlier in the observation is already detected.

The second stage is to check if the polytope is bounded or not. Again by applying the observations interval bounds on both sides of the observation, the solution must be a bounded polyhedron, i.e., a polytope. In this stage, the program *Qhull*¹ is used to find if the polyhedron is bounded or not. If it is not bounded the solution set is an empty set and bias is detected.

The last stage of the PDP algorithm is to find the vertices of the polytope if the first two stages are already passed. This is done by projecting the residuals on the hypercube and then shifting the projected vectors to the local minima that were computed in the first stage.

The volume of the polytope will be used later on to derive the consistency measures of the positioning problem. There is no analytical form to compute the volume of non-regular polytopes. However, there exist different methods and algorithms to derive the polytope volume numerically, as discussed in Boyd and Vandenberghe (2004); Lawrence (1991); Cohen and Hickey (1979). Contrary, the zonotope volume can be computed analytically, Ziegler (1995). In this thesis, we use the Multi-Parametric MatLab Toolbox Herceg et al. (2013) to solve the vertex enumeration problem for all cases to have consistency in the volume computation of the zonotopes and polytopes.

Figure 3.11 shows a 2D example of the transformation from H-polytope into V-polytope, where each row of the matrix \mathbf{B} represents a normal vector of the hyperplane of the H-polytope. In this example, the measurements are assumed to be error-free i.e., $\Delta \mathbf{l} = 0$ and that is why the polytope is regular with special properties (zonotope). The system of inequalities in equation (3.17) represents a zonotope. This zonotope can be interpreted as a confidence domain of the approximate position. It is the nominal polytope that can be produced by a given satellite geometry, approximate receiver position, and selection of the OIBs. Zonotopes will play a major role in the Fault Detection and Exclusion (FDE) since they represent the theoretical optimum polytope. In comparison to the FDE via statistical hypothesis testing, the zonotope is similar to the theoretical distribution that the test statistic e.g. Q_{ss} or Q_{rb} , will be checked against. In another manner, the volume of the polytope will be checked against the volume of the zonotope.

Several meters error in the initial position x_0 produces negligible errors in the zonotope volume computation due to the long distance between the satellites and the receiver, approximately 20.200 km for GPS satellites. If we do not know an approximate initial position within a 100 meters error, an iterative estimation could be performed to get a reasonable initial position.

$$\begin{cases} \mathbf{A}\Delta\mathbf{x} \leq \Delta \\ -\mathbf{A}\Delta\mathbf{x} \leq \Delta, \end{cases} \quad (3.17)$$

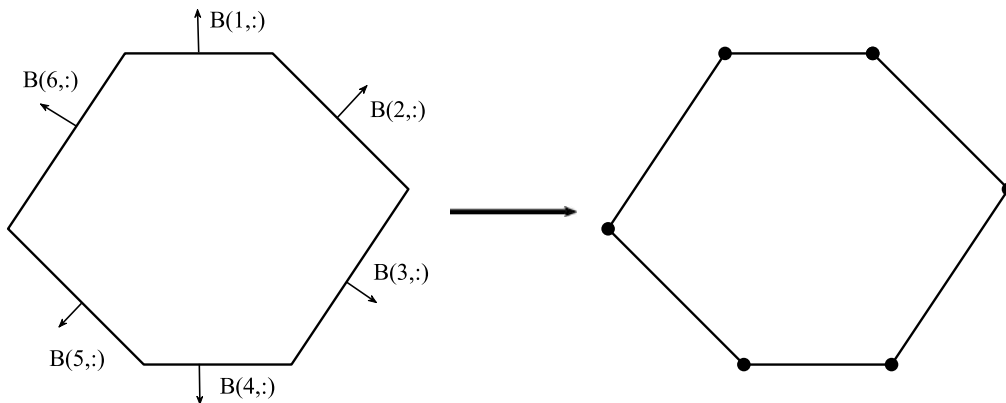


Figure 3.11: H-Polytope (left): the intersection of half-spaces determined by 6 different hyperplanes which are the rows (black normal vectors) of a matrix \mathbf{B} and its transformation into a V-polytope (right) black dots.

¹*Qhull* <http://www.qhull.org/>

3.4.3 Interpretation of Bounding Zones and Related Consistency Measures

In the following, different case studies will be analyzed for a better understanding of the shape and interpretation of the resulting polytopes. A simulation study of a moving robot in a flat world will be presented, taking into account special positioning geometries, measurement noise, and biases. We assume that the transmitters are fixed in each scenario in a known position and can communicate with the robot via electromagnetic waves as GNSS satellites and receivers. We assume further that the transmitters and the robot are synchronized so that the robot position is the only state to be estimated. We know perfectly the approximate position of the robot and moreover, the distances between the robot and the transmitters are taken very largely, an order of 20000 km. There will be different scenarios with different geometries so that the position of the transmitters is different from one scenario to another, but for each scenario, the transmitters are fixed, like we are processing one epoch of navigation problem independent of the other epochs.

The shape of the polytope depends on:

- Transmitters - receiver geometry, which can be interpreted by the GDOP.
- Applied OIBs Δ .
- Random observation errors and biases.

In order to show the impact of each factor, a separate variation is carried out.

Noise-free and Bias-free Measurements Yield Zonotope as Bounding Zone

In this section, we will discuss the impact of the navigation geometry on the polytopal bounding zone. In order to isolate the effect of the geometry on the bounding zone, the measurements are assumed to be noise-free and bias-free which fits the system of inequalities in equation (3.15). For simplicity, let's start with a very simple example with two transmitters and equal OIBs for both observations, $\Delta = 4$ m. Figure 3.12 shows an example of two transmitters where the geometry gets worsened when the position of transmitter T_{x2} changes. The black arrow indicates the direction of changes in the T_{x2} position.

At the first epoch, the bounding zone is a square since the LOS of the transmitters are perpendicular in direction of each other. When the angle between the transmitters' LOS decreases, the square becomes a parallelogram where the maximum uncertainty is at its longest diagonal. Moreover, to give some numerical values, the area of the parallelogram increases from $2 \times 4 \text{ m} \cdot 2 \times 4 \text{ m} = 4 \Delta^2 = 64 \text{ m}^2$ to 142.99 m^2 which means an increase by more than a factor of two. With the decreases in the angle between transmitters' LOS, the uncertainty is bigger. When the LOS are perpendicular, the length of the polytope edges is equal to twice the applied OIBs 2Δ . In this special case, the polytope is a square. This happens because the system is determinant, i.e, the number of observations equal to the number of states. If we add more observations, the edges will become smaller than the error bounds and as a consequence, the polytope's area will decrease. However, when LOS are not perpendicular, the edges of the polytope become larger than the applied error bounds, and eventually also the polytope's area.

In these two transmitters example, there exist two directions of maximum uncertainty. They are exactly the diagonals of the parallelogram. One is the bisector of the angle between the transmitter's LOS and the other one is in the direction perpendicular to the bisector. When the angle between transmitters LOS is acute, i.e., less than 90° the uncertainty in the bisector direction (shorter diagonal) is lower than the uncertainty in the perpendicular direction to the bisector (longer diagonal). Instead, if the angle between transmitters LOS is obtuse, i.e., between 90° and 180° , the uncertainty in the bisector direction (longer diagonal) is greater than the uncertainty in the perpendicular direction to the bisector (shorter diagonal). Figure 3.13 shows this effect, where the second transmitter T_{x2} is moving away from the first one T_{x1} which makes the angle between them an obtuse angle. When the angle between the transmitter's LOS is 90° the two diagonals are equal and have the same uncertainty.

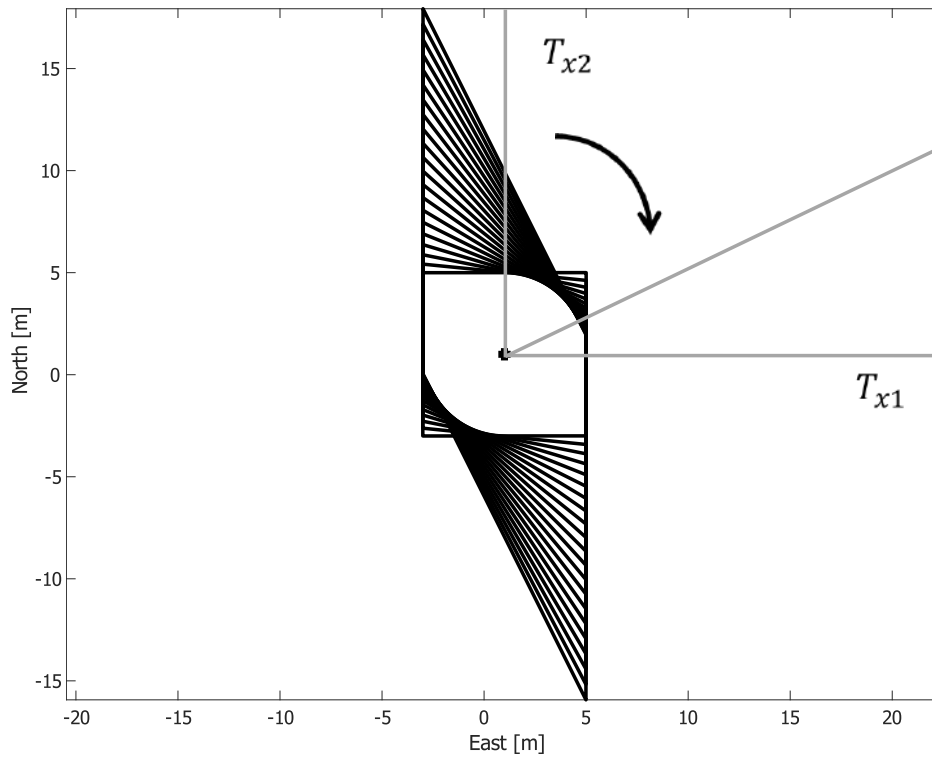


Figure 3.12: Example of the effect of geometry change onto the polytope bounding zone. In this example, T_{x2} changes its angle as indicated in by the arrow.

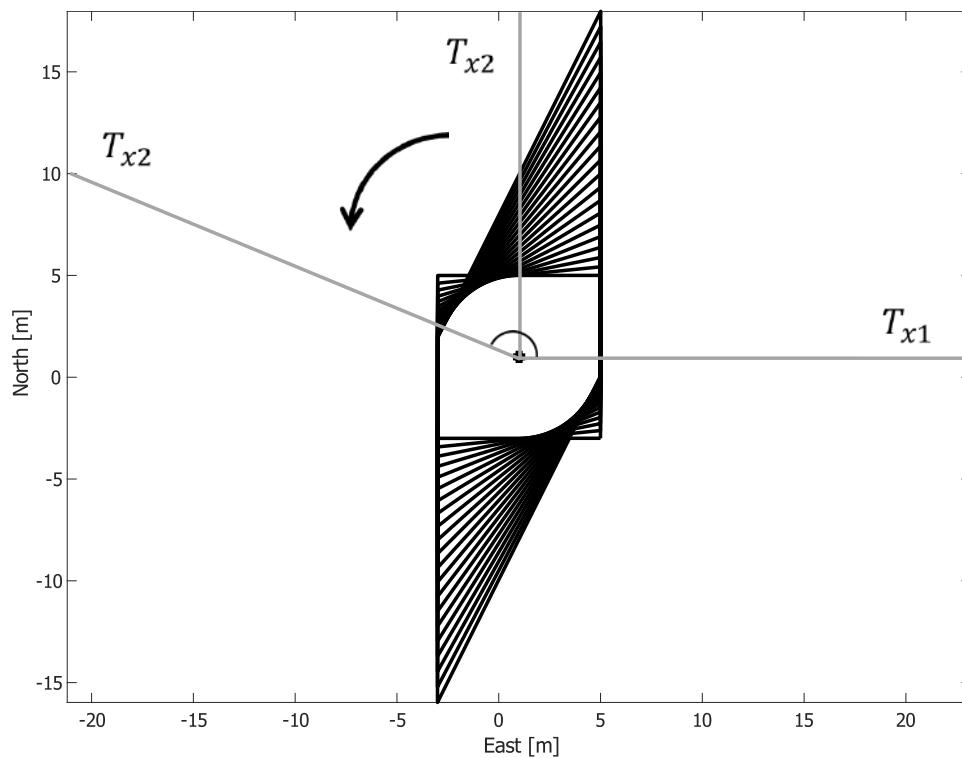


Figure 3.13: Example of the effect of geometry change onto the polytope bounding zone. In this example, T_{x2} changes its angle as indicated in by the arrow.

The general rule here is that the largest uncertainty is in the direction of the bisector of the angle between the transmitter's LOS and the other one is in the direction perpendicular to the bisector. The rule changes when one or more transmitters are added.

Figure 3.14a, expresses an example of two transmitters T_{x1} and T_{x2} with obtuse angle. Two transmitters provide two main uncertainty directions similar to the ellipse error in LS adjustment. The larger one is indicated by a black arrow while the smaller one is indicated by the grey arrow.

In order to highlight the implication of a 3rd transmitter on the uncertainty direction, we added another one to the same scenario. Figure 3.14b, shows an example with three transmitters. The addition of the 3rd transmitter makes one of the biggest directions of uncertainty (indicated by the black arrow in figure 3.14a) disappear without affecting the other big uncertainty direction (indicated by the grey arrow in figure 3.14a). The largest uncertainty direction is decomposed into two new uncertainty directions indicated both by black arrows, but one is bigger than the other due to the geometry of the transmitter. Specifically as previously explained, the angle between T_{x3} and T_{x1} is acute and the angle between T_{x3} and T_{x2} is 90° , so the uncertainty of the bounding zone between T_{x3} and T_{x1} is smaller than the uncertainty of the bounding zone between T_{x3} and T_{x2} . The remaining one is still the same as before, both are pointed out by grey arrows in figures 3.14a and 3.14b.

The new transmitter T_{x3} or in other words new observation bounds the zonotope in its directions. If the value of the new bound is smaller than the uncertainty of the previous 2-transmitters case, as in the figure 3.14b, the new observation will cut the zonotope perpendicularly to the direction of the observation. In all previous examples, the OIBs Δ are equal to each other and equal 4 meters. In this case, every new observation will have an impact on the zonotope solution. However, in real cases, the OIBs will have a different magnitude due to the different uncertainty of the observations. This is similar to the observation weights in LS adjustment. To focus on this feature, the OIB Δ_3 on the 3rd transmitter is set to values bigger than the uncertainty of the zonotope with only two transmitters. Figure 3.14c depicts this situation. Since the OIB Δ_3 is bigger than the uncertainty of the two transmitter zonotope, this new observation does not affect the zonotope, as the weight of this observation is zero in weighted LS.

To emphasize the effect of different OIBs on the zonotopes and different observation weights in weighted LS, the error ellipses of LS are added to all examples in figure 3.14. The error ellipse is explained in section 2.1.2, equation (2.11). The 2D error ellipses have a confidence level of 99.62 %, assuming the observation errors are *Gaussian* distribution which gives a χ^2 -distribution of the error ellipse. The OIB Δ is set to contain same confidence level as: $\Delta = \kappa\sigma$, where $\kappa = 2.54$ for the 99.62 % confidence interval.

Figure 3.15a and 3.15b exhibits examples of two and three transmitters, respectively, where the error ellipses orientation show very similar behavior as the zonotopes. In the two transmitters example, the error ellipse semi-major axis is a little bit smaller than the maximum uncertainty direction of the zonotope (indicated with black arrow), and the error ellipse semi-minor axis is also smaller than the second maximum uncertainty direction of the zonotope (indicated with the grey arrow). In the LOS direction which is supposed to have the smallest uncertainty, the error ellipse and the zonotope almost fit perfectly. Interestingly, in the LOS

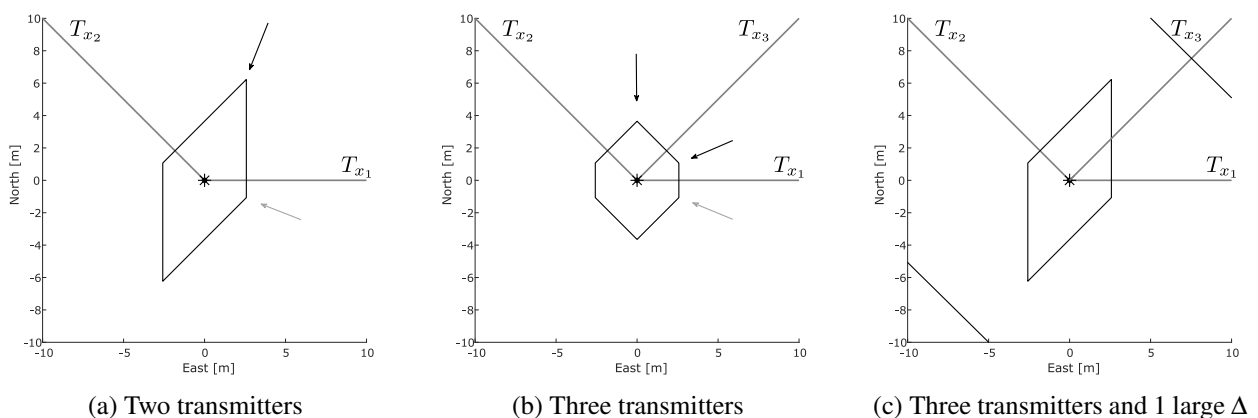


Figure 3.14: Impact of the geometry on the bounding zone. (a) Zonotope bounding zone for two transmitters with an obtuse angle, (b) Zonotope bounding zone for three transmitters, and (c) Zonotope bounding zone for two transmitters with equally OIB and 3rd transmitter with very large observation bound.

direction the zonotope represents its lower uncertainty while the error ellipse represents its lower uncertainty in the semi-minor axis direction, this means that the zonotope representing the uncertainty in a better way.

In the three transmitters example, the error ellipse and the zonotope largest and smallest uncertainty directions fit perfectly. In figure 3.15b, the semi major axis of the error ellipse is in the direction of highest uncertainty of the zonotope, while the semi minor axis which is the lowest uncertainty is in the direction perpendicular to the edge of the zonotope (T_{x_1} LOS direction) which indicate a lower uncertainty. The LOS direction of T_{x_1} is the same direction of the ellipse semi minor axis in the contrary to the two transmitter case in figure 3.15a. Moreover, for the LOS direction of transmitters T_{x_2} and T_{x_3} , the error ellipse shows intermediate uncertainty while the zonotope shows its lowest uncertainty in the LOS direction of T_{x_1} . This means the error ellipse underestimate the uncertainty in this T_{x_1} LOS direction while overestimate the uncertainty in T_{x_2} and T_{x_3} LOS directions. Figure 3.15c shows the situation when the 3rd observation has a big error bound.

In order to understand the performance of the error ellipse, different weights are applied on the 3rd observation in the LS adjustment. As the weight decreases the error ellipse increases and tilts to the right-hand side. If the weight is equal to the one we go back to the same ellipse in case b and if the weight is zero we go back to the same case a, while the zonotope is always the same. So non-proper weighting of the observation leads to the wrong representation of the uncertainty as an error ellipse. In case a large or full weight is applied on the 3rd observation, the confidence ellipse will be underestimated simultaneously as the precision declines, i.e, the area of the error ellipse will be smaller than one with a small weight and it will be tilted in the wrong direction which does not well represent the uncertainty.

The relation between the OIBs and the weight is inversely proportional. If we know that the i -th observation has a small error, we put a big weight (small variance) on it in the LS adjustment and small error bounds for the zonotope. Figure 3.16 depicts the zonotope bounding zone when the error bound Δ_3 of the 3rd observation is weighted correspondingly to the weights applied in LS adjustment in figure 3.15c. If the weight is equal to 1, i.e., full weight as the other observations, the zonotope underestimates the uncertainty in the T_{x_3} direction. Decreasing the weight to half ($w_3 = 0.5$), the zonotope almost fits the original zonotope with just 2 observations, while applied smaller weight such as $w_3 = 0.25$, constraint applied by the 3rd observation is no longer active and we get the same zonotope from the two transmitter case. This means the zonotope fits rapidly the original one when the applying weight on the bad observation while in LS the error ellipse slowly fits the original one. If we take a look to the case $w_3 = 0.25$, the error ellipse still underestimated figure 3.15c while the zonotope is fully represented, figure 3.16. Even if we apply very low weight on one observation in the LS adjustment, the confidence ellipse will be underestimated and the state estimate still is affected by that observation, see the case $w_3 = 0.1$, while in the interval-based methods it will be excluded.

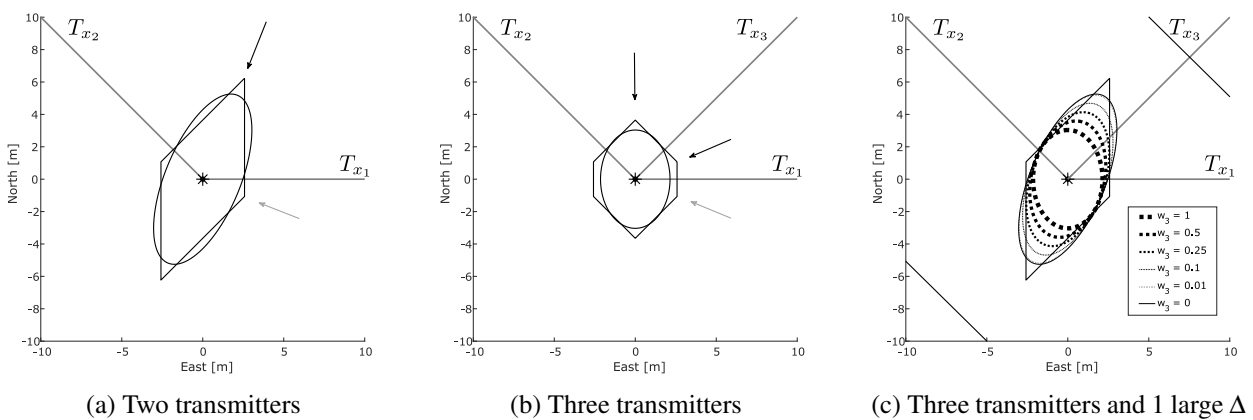


Figure 3.15: Comparison of stochastic and interval based confidence regions. Same examples from figure 3.14 with error ellipse from least-squares adjustment. In a and b the error bound is equal and the weights are equal while in c, the 3rd OIB is much larger than the others and different weight applied on the 3rd observation in LS keep the other weight equal to 1. The weight is indicated in the legends for each ellipse.

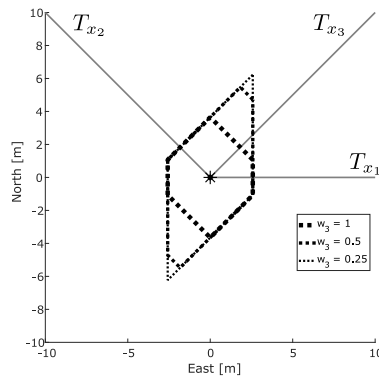


Figure 3.16: Weighting the OIB of the 3rd observation by $\Delta_3 = \frac{\Delta_3}{w_3}$.

In order to highlight the geometrical effects on the navigation problem and the uncertainty of the estimated states more simple examples are studied with three transmitters this time. Figure 3.17 shows three simulated scenarios with different transmitter geometries (transmitters are fixed in each case) thus different angles of intersection between the LOSs. The measurements are considered to be free of random errors and fit the model $\Delta l = 0$. So, we can have a better idea of the impact of the navigation geometry on the bounding zone. In all cases, the OIB is selected arbitrarily and set equal to 4 meters.

When changing the navigation geometry, i.e. going from a good, homogeneous distribution of the transmitters (case a) to a worse, more clustered one (case c), the area of the polytope increases, reflecting this situation. In this example, the area of the polytope (i.e. zonotope) is 56 m^2 , 82.3 m^2 , and 278.1 m^2 for the cases a, b, and c, respectively. This reflects the impact of the positioning geometry also presented in the Geometrical Dilution of Precision (GDOP) values ($\text{GDOP} = \sqrt{\text{trace}(\mathbf{A}^T \mathbf{A})^{-1}}$) used in navigation to characterize the strength of the navigation geometry, Langley (1999). Here, the values are $\text{GDOP} = 1.2$, 1.7 and 12.4 for case a, b and c, respectively. Utilizing the area of the polytope as an indication of the quality of the navigation geometry agrees with the GDOP indication. Sure, if we apply bigger OIBs Δ , the area of the polytope of the same geometry will increase. Then, we take the area of the polytope or volume of the polytope in a 3D case, the OIBs have to be taking into account. Correspondingly, when weights are applied on the LS adjustment, the GDOP also weighted with same weights where $\text{GDOP} = \sqrt{\text{trace}(\mathbf{A}^T \mathbf{W} \mathbf{A})^{-1}}$. As seen before, the weights and the OIBs are inversely propositional to each other. This relation makes both of them have the same effects on the quality of navigation geometry indications.

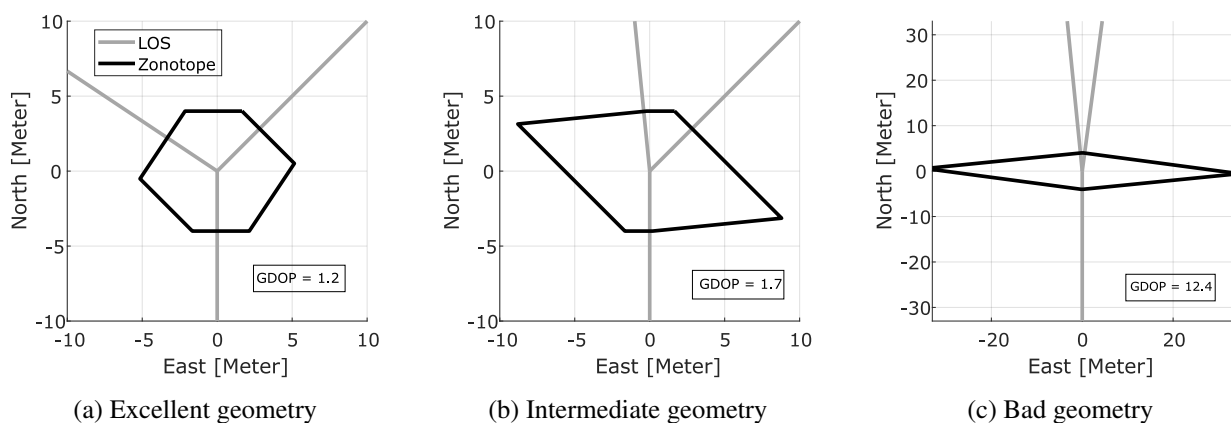


Figure 3.17: Resulting in bounding zones (black) for the error-free case. 2D simulated scenarios with error bounds equal to 4 m and 3 transmitters with different geometry (LOS). Note that, the axis scale is much larger in sub figure c in order to be able to show the whole zonotope.

The zonotope can be computed from the geometry and OIBs without any measurements so we can have information on the uncertainty directions. On the other hand, when we have real measurements, they will contain different types of errors (noise and biases) which makes the bounding zone a polytope instead of a

zonotope. The polytope is not regular and not every vertex has an opposite one. The highest uncertainty then is between opposite vertices if they exist and between vertices and their opposite hyper-plane. This will be discussed in the next section.

Impact of White Observation Noise on the Bounding Zone

Adding noise to the observations, the zonotope is deformed into a polytope, cf. Figure 3.18a. The degree of deformation depends on the ratio between the applied error bounds Δ and the standard deviation of the observations σ , i.e., the actual errors in the observations. In order to study this impact, this ratio ($\frac{\Delta}{\sigma}$) is varied while keeping the identical geometry, so the only factor affecting the polytope is this relation.

Figure 3.18b, shows the resulting bounding zones of an example with six well distributed transmitters, i.e., very good navigation geometry $\text{GDOP} = 1.1$. The colored polytopes are obtained from the same set of transmitters but from measurements experiencing additive white noise (AWN, $\sigma = 2$ m). The vector of the AWN is the same for different applied error bound Δ . Furthermore, the observation interval bound Δ is increased. As a reference, the polytopes without AWN (i.e. zonotopes) are shown in black. The big one is obtained when applying $\Delta = 16$ m while the small one for $\Delta = 4$ m. The two black zonotopes are similar and both have 12 edges perpendicular to the LOS (grey arrows). Since there is no error in the observation, the number of the edges does not change for small or big Δ , the only changes are in its area. Furthermore, the number of edges is twice the number of observations being that the applied Δ is the same for all observations. That means the cases where the observation bound could exceed the uncertainty of the zonotope in its direction as shown in figure 3.14c is impossible for the given setting.

Starting with the large zonotope, the situation changes as follows. As the size of Δ decreases, the variations due to AWN start predominating. Subsequently, the number of edges decreases since each constraint cuts the polytope from inside, cf. dashed-lined edges. The color of dashed-lined edges indicates at which magnitude of the error bound Δ that specific edge is lost. For instance, for the specific value given, edge 1 is lost from the error-free case when we add an AWN to the measurements with $\Delta = 16$ m, while edge 2 is lost when $\Delta = 4$ m, (magenta polytope). Overall, the black zonotope, blue, red, green, and magenta polytopes have 12, 11, 10, 10, and 8 edges, respectively. As the ratio $\frac{\Delta}{\sigma}$ decreases, the number of edges is reduced and the area of the polytope decreases until it becomes empty. Thus, the area or volume of the polytope Vol_P can be used to indicate the inconsistency of the observations, here generated by AWN.

The same experiments are repeated but this time with not very good geometry $\text{GDOP} = 2.4$, to see the effects of navigation geometry on the polytope while varying the ratio ($\frac{\Delta}{\sigma}$). Figure 3.19 presents same scenario presented in figure 3.18b in terms of ($\frac{\Delta}{\sigma}$) ratio with only one difference which is the transmitters geometry. Due to this specific geometry, most of the error-free polytope (i.e. zonotope) vertices are concentrated in two regions that crossing the direction of most of the LOS. The LOS directions are indicated by grey arrows. The edges between vertices in those two regions are very small. For instance, taking the blue polytope with $\Delta = 16$ m, it loses 5 vertices out of 12, keeping in mind the ratio $\frac{\Delta}{\sigma} = \frac{16}{2} = 8$ is quite large. The other polytopes with $\Delta = 12$ m, $\Delta = 8$ m, and $\Delta = 4$ m, have the same number of vertices which is 6. This is due to losses of the cluster of vertices nearby since when the edges are short it is easier to lose them due to the observation errors. Double black arrows indicate two edges emphasizing the behavior of polytope edges with regard to the $\frac{\Delta}{\sigma}$ ratio. Edge 1 increases relative to the other edges when the $\frac{\Delta}{\sigma}$ decreases, while edge 2 decreases. Somehow, the vertex between those two edges is moving right to left as $\frac{\Delta}{\sigma}$ decreases. For $\Delta = 4$ m, this vertex becomes very near to the outermost left vertex of the polytope. If we apply Δ smaller than 4 m this vertex will collide with the outermost vertex and become one vertex i.e., one of them will be lost. This behavior of edge 1, edge 2, and the vertex between them is due to the fact that the error in the observation with LOS perpendicular to edge 1 is higher than the error in the observation with LOS perpendicular to the edge 2. Also, the error in the observation with LOS perpendicular to edge 1 is larger than all the other errors, because the bigger the error in the observation gives the bigger cut in the polytope from the inner side. If the relation is reversed, i.e. error in the observation with LOS perpendicular to edge 1 is lower than the error in the observation with LOS perpendicular to edge 2. Edge 2 will increase and edge 1 will decrease as the $\frac{\Delta}{\sigma}$ ratio decreases, and the vertex between them will move from left to right.

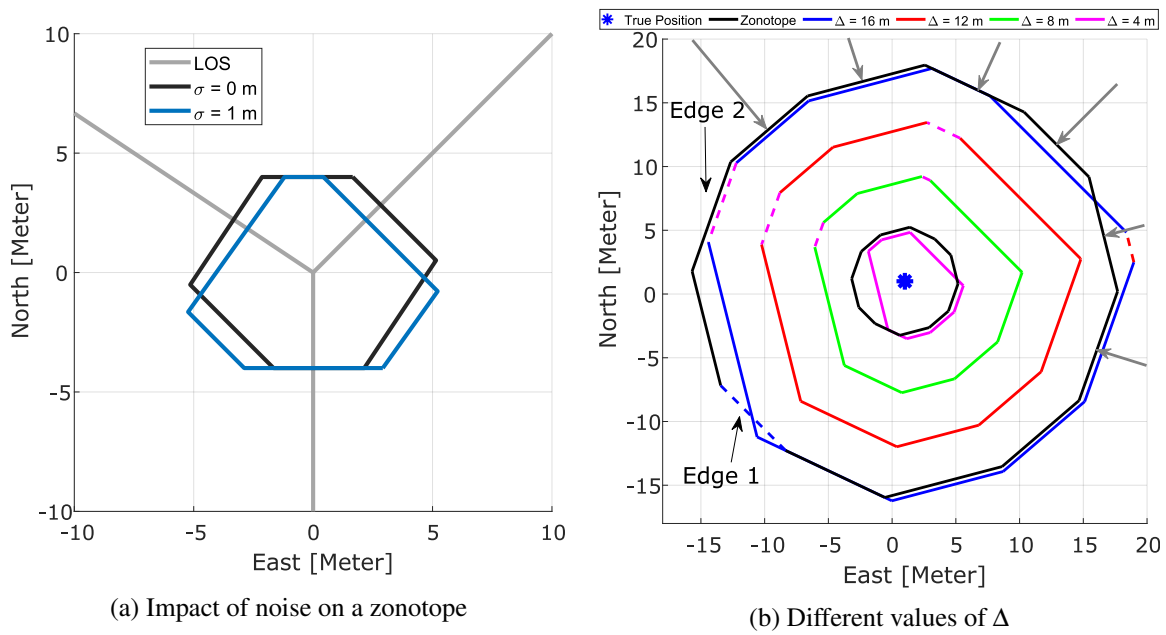


Figure 3.18: Comparison of zonotope and polytope solutions: (a) Impact of noise on a zonotope, (b) In excellent navigation geometry polytope solutions with different values for the Δ of 4 m, 8 m, 12 m, and 16 m, while keeping the same noise level. The black regular polytope (zonotope) is the solution obtained from error free measurements (big zonotope is obtained from $\Delta = 16$ m, the small one from $\Delta = 4$ m), while the colored non-regular polytopes result from measurements affected with AWN ($\sigma = 1$ m) and varying Δ . The grey lines indicate the line-of-sight directions.

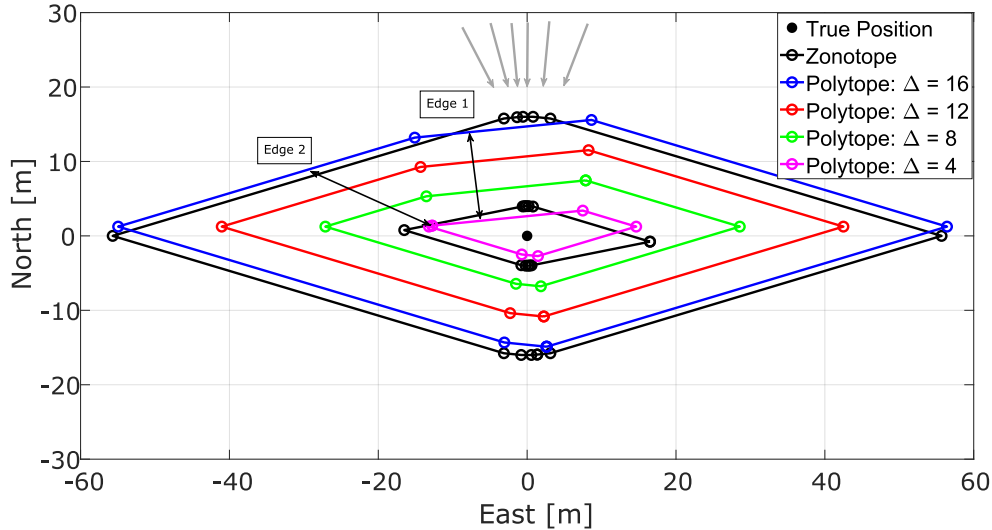


Figure 3.19: Polytope solutions with different values for the error bounds of 4 m, 8 m, 12 m, and 16 m, while keeping the same noise level with bad navigation geometry. The black regular polytope (zonotope) is the solution obtained from measurements free of random errors (big zonotope is obtained with error bound $\Delta = 16$ m, the small one is of $\Delta = 4$ m), while the colored non-regular polytopes result from measurements affected with AWN ($\sigma = 2$ m) and varying Δ . The grey lines indicate the line-of-sight directions.

The $\frac{\Delta}{\sigma}$ ratio affects the deformation of the polytope but also the geometry plays an important role in this deformation. In the same fashion, the distribution of the errors on the observation contributes to how the polytope will deform. Exchanging the error between one observation and another will deform the polytope in different ways but the area of the polytope will have a very small effect on this exchange. The area of the

polytope will not be affected too much since what the polytope loses from one observation will be gained from the other; maybe not a very equal amount but it should be close to equal.

Impact of Observation Biases on the Bounding Zone

Let us go back to the 2D example represented in Figure 3.17, and add one new fourth transmitter, so one more observation. Assuming now noise-free observations but a biased new observation, the impact of an increase in the magnitude of the bias is studied depending on the observation geometry. Figure 3.20a depicts the zonotopes for the error-free cases for three (blue) and four (green) transmitters (Tx). The new observation creates two new edges and as a consequence, the number of vertices increased by 2.

Figures 3.20b and 3.20c show the polytope solution when we introduce biases to the 4th observation with different magnitudes related to Δ . The bias acts as a half-space cut in the LOS direction (depicted in grey). As the bias increases the resulting polytope moves in the direction of the bias and shrinks down until it becomes empty at a bias $\delta = \Delta + \frac{w}{2}$, where w is the width of the blue zonotope. This formulation will be explained in section 3.4.4 and the width of the zonotope and polytope is shown in figure 3.22. When the bias is just a bit smaller than $\Delta + \frac{w}{2}$, the resulting polytope is very small, see figure 3.20c, the black triangle on the left. This underlines again the interpretation of the polytope being a consistency measure. The bigger and closer the polytope is to the zonotope, the more consistent are the observations.

To study the effect of the biased observation on the zonotope when the navigation geometry is bad, a 4th observation is added to case c from Figure 3.17. The new observation is added in the maximum uncertainty direction to highlight the extreme case. In this case, w is much bigger than the one from case a. In fact, the polytope is still non-empty for a very large bias (see black trapezoid in figure 3.21b), where a bias of $\delta = -7 \cdot \Delta = -28$ m was introduced. Thus, this underlines the strong impact of the observation geometry. The polytopes shifted away from the true position gradually with the increasing bias of the 4th observation. The area of the polytopes is still comparable to the area of the original zonotope (depicted in green) for some big biases e.g., bias = 4Δ (yellow polytope).

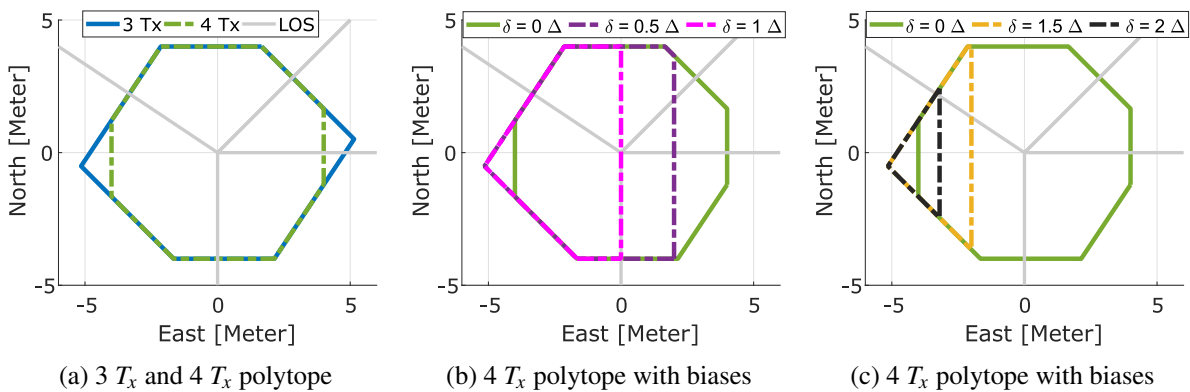


Figure 3.20: Impact of observation biases on the bounding zone in case of good geometry. (a) Introducing a range of biases to the 4th measurement in figure 3.17a, regular polytope (zonotope) before (blue) and after (green) introducing the 4th observation. (b) Biases $\delta = 0.5\Delta$ and $\delta = 1\Delta$ introduced to the 4th observation. (c) Biases $\delta = 1.5\Delta$ and $\delta = 2\Delta$ introduced to the 4th observation.

3.4.4 Minimum Detectable Bias Definition

Now, we can define a Zonotopal Minimum Detectable Bias (ZMDB) being an error in observation i so that the resulting polytope is an empty set. From geometric consideration, the ZMDB equals the sum of the error bound Δ_i and the half of the zonotope's Z_i width w_i in the LOS direction of the corresponding observation i , where the zonotope is obtained from all observations except the i -th one. The width of the zonotope is the distance between the extreme vertices of the zonotope in the LOS direction of the related observation, cf. Figure 3.22 for the geometric relations.

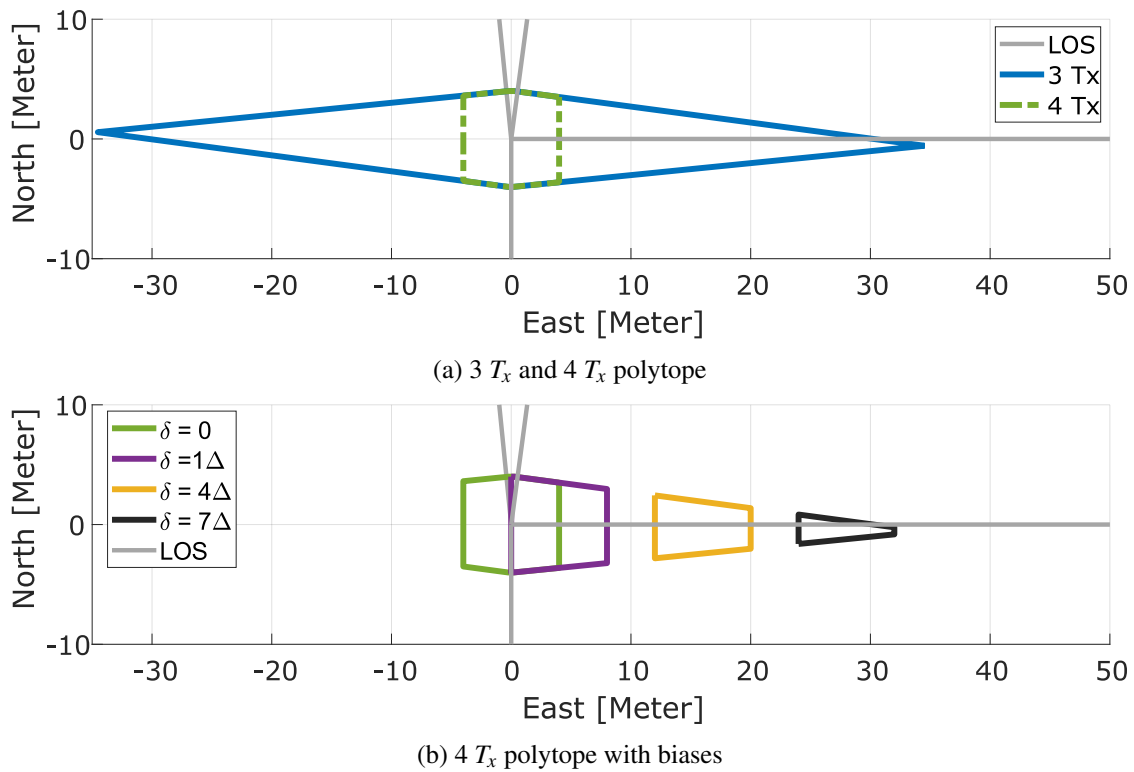


Figure 3.21: Impact of observation biases on the bounding zone in case of bad geometry. (a) introducing a 4th observation in of figure 3.17c. (b) range of biases ($\delta = 1\Delta, 4\Delta$, and 7Δ) added to the 4th observation. Zonotopes computed with only 3 observations are shown in blue and LOSs of the observations are indicated in grey.

The MDB is maximum if the LOS of the new measurement is in the direction of the maximum width of the zonotope. The big advantage is that the MDB can be computed without real measurements as a design and planning quantity. It indicates the strength of the navigation geometry to identify outliers.

Real observations however will be noisy. Thus, the resulting bounding zone is a polytope. If the actual noise contribution in each measurement is smaller than the corresponding error bound, then the true position is still contained inside the polytope but its location is unknown. The barycenter of the polytope is used to estimate the point position. Thus, only a range of Polytopal Minimum Detectable Bias (PMDB) can be computed and is given by equation (3.18), where w_{p_i} is the width of the polytope obtained with all observations except the i -th one. If the noise contribution is small w.r.t the error bounds, the polytope solution tends towards the zonotope solution. The PMDB is always greater than the OIB and smaller than the half-width of the polytope plus the observation interval bound as it is presented in equation (3.19). This is because an error less than the OIB is considered noise and not bias and an error greater than the half-width of the polytope plus the OIB provides an empty polytope.

The formula for the PMDB holds in case one observation is assumed to be biased. If this assumption does not hold and a new assumption says that more than one bias could exist at the same time, the PMDB will be underestimated and ZMDB is considered. For instance, computing the PMDB for the i -th observation while the j -th observation contain a bias that exceed the error bound Δ_j without making the polytope empty set underestimate the PMDB of the i -th observation. To be on the safe side, we use the ZMDB. On the other hand, this estimation of the PMDB could be overestimated if all the other observations are not biased and the OIBs include the true measurements. Nevertheless, any bias greater than the ZMDB will be detected since it brings an empty set as a solution. Furthermore, consistency measures that will be presented in the next section solve the problem of the underestimation and overestimation of the PMDB and it will ensure the detection of biases even less than the PMDB. We define the MDB_{Z_i} and MDB_{P_i} as follows:

$$\begin{cases} MDB_{Z_i} = \frac{w_{z_i}}{2} + \Delta_i & (a) \\ MDB_{P_i} = \frac{w_{p_i}}{2} + \Delta_i & (b) \end{cases} \quad (3.18)$$

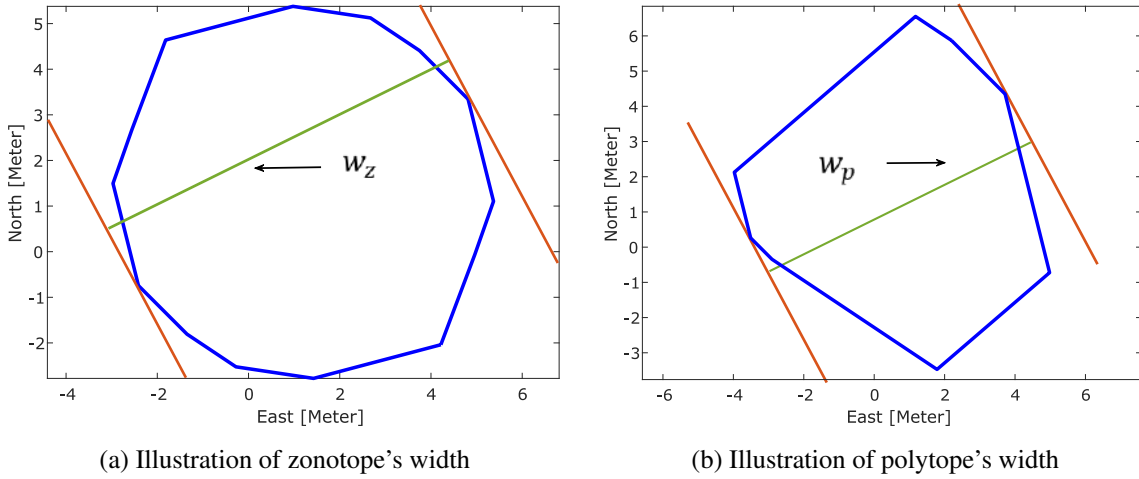


Figure 3.22: Geometry of the width of the zonotope (a) and polytope (b)

$$\Delta_i \leq MDB_{P_i} \leq \frac{w_{P_i}}{2} + \Delta_i \quad (3.19)$$

Differences Between Interval MDB and Stochastic MDB

MDB in hypothesis testing depends on the non-centrality parameter of the chi-square distribution, on the prior variance, observation weight, and on the variances of the observation residual, see equation (2.62) for SS test statistic and equation (2.49) for residual-based test statistic. The magnitude of the non-centrality parameter depends on the redundancy number which depends on the number of observations and states, and depends on the PFA and PMD, see equations (2.61) and (2.47). The redundancy number is not controllable since we can not just add more observations if they are not available. The PFA and PMD are a prior parameter which we set in advance and these parameters depend on the integrity risk for the navigation system. If we want to lower the integrity risk we have to lower the values of PFA and PMD. Lowering these two parameters means increasing the non-centrality parameter and increasing the non-centrality parameter causes increasing MDB, so we have to accept larger biases in our observations which can lead to lower accuracy in the state estimation. This is one of the main disadvantages of hypothesis test statistics.

Instead, in our approach PDP, the PMDB and its upper limit ZMDB of each observation depend on two quantities: the observation interval bound Δ_i and on the geometry of the navigation problem. Since we could not change the available geometry, the only parameter we can adjust is the observation interval bound. The observations bound can be set in different ways. This is discussed in the section *Determination of Observation Interval Bounds*. However, the idea here is when we apply smaller interval bounds on the i -th observation for an instance, the MDB of the i -th observation will be smaller without increasing the integrity risk, but it may lead to discontinuity in the navigation or positioning solution, which leads to a non-available solution. The integrity risk does not increase since there is no possible false alarm when the polytope is empty. Anyway, we need to trust our navigation system rather than having a non-reliable solution.

In case we have precise observations it makes sense to apply smaller observation bounds, so we can still trust our solution and we have smaller MDB. In case there are one or more outliers, the solution set is empty and the outlier detection is guaranteed. If we would like a higher availability, we can enlarge the observational bounds at the cost of increasing the MDB which may decrease or increase the accuracy of the estimated parameter. In the case there are no biases in the observations, i.e., the only errors are just noise, the accuracy of the PDP point positioning will increase due to the absorption of the noise in the observation intervals. The absorption of the noise means a smaller deformation of the polytope w.r.t. the nominal shape (zonotope). In this case, the number of polytope vertices increases which provides better single point position estimation. This effect can be seen in figure 3.18. Instead, if in addition to the noise, there are some small biases smaller than the MDB, the accuracy of the estimated position will deteriorate due to this NDB. In the next section 3.4.5, a fault detection and exclusion test based on the zonotope and polytope volume ratio will be

introduced which allows us to detect biases smaller than the MDB. This is one of the main advantages of our developed method w.r.t. the traditional methods that are based on hypothesis testing.

3.4.5 Integrity Measures Via Zonotopes and Polytopes

New integrity measures are developed and proposed based on zonotopes and polytopes. First, the deformation of the polytope due to the observation errors has to be tested against the nominal case, i.e. the zonotope. Somehow this is similar to the probabilistic test statistic. The polytope represents the quantity to be tested similar to the test statistic T_{rb} , T_{ff} , or T_{ss} (equations (2.43), (2.50), and (2.60)), and the zonotope represents the expected distribution of the test statistic be check against such as: theoretical χ^2 distribution of the probabilistic tests. In hypothesis testing, a computed quantity of the observations, like e.g. the residuals of the LS or the parity vector or the solution separation, is expected to have a specific distribution based on the assumption that has been made on the observation errors. Usually in GNSS the observation error is assumed to have a *Gaussian* distribution. In our case, based on the assumption made on the applied OIBs Δ , some level of polytope deformation is expected. To test this deformation, the volume of the polytope and the volume of the zonotope are used. Then, a combinatorial algorithm can be used to detect and exclude one or more faulty measurements. To complete the integrity information a zonotopal PL is derived.

Consistency Measures

As we have seen in the previous section, some biases that could not be detected just by empty sets. Figure 3.23 depicts the three main situations that can happen when an error is introduced to one of the measurements and in this case the 2nd measurement. Figure 3.23a presents the case where the error is considered as a noise and not as bias since the bounding polytope still contains the true solution. In this case, the observation interval bounds are not violated and they contain all the true observations, so the errors are less than their corresponding error bound Δ . Figure 3.23b presents the case when a detectable bias is introduced to the 2nd measurement and an empty set is the results of the intersection of bounding hyperplanes. This type of biases is greater than $\Delta + \frac{w}{2}$ detectable and they need to be isolated. The isolation process will be discussed later on, but it is worth mentioning that we do not need more observations to isolate the biased one. On the contrary, hypotheses testing need one more observation to isolate the biased one, since at least one redundant observation is needed in the tested set of observations. Figure 3.23c presents the case of the Non-Detectable Biases (NDB) which have values between Δ and $\Delta + \frac{w}{2}$. These types of non-detectable biases are dangerous because the solution set is not empty and does not contain the true solution anymore. This is especially true for a bad remaining geometry or less redundancy for a specific observation, e.g. compare case $\delta = -4 \cdot \Delta$ in figure 3.21b. What has to be done, is to detect and isolate those biases without mixing them with the small errors that are not violating the error bounds.

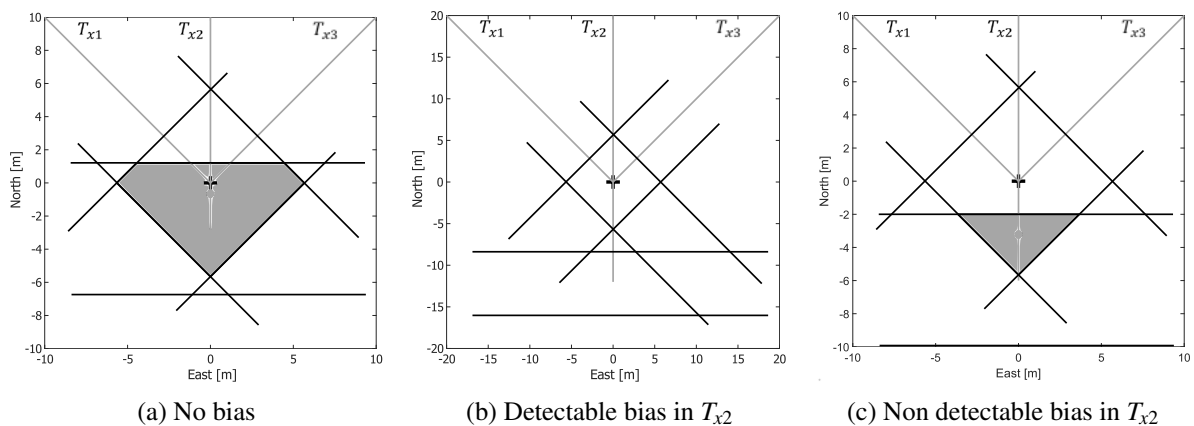


Figure 3.23: Three main situations of the biased measurement. The bias is introduced to the 2^{nd} transmitter where the black cross is the true position and the bounding zone is depicted in grey.

Fault Detection

To detect such biases we propose a new consistency measure V_{r_0} based on the relative volume between the volume of the actual polytope solution Vol_p and the error and bias-free solution (reference or nominal behavior), i.e. the zonotopal volume Vol_z :

$$V_{r_0} = \frac{Vol_z - Vol_p}{Vol_z}. \quad (3.20)$$

This is similar to the global test in the hypothesis test statistic such as equation (2.21), hence, can be called Fault Detection (FD). The consistency measure or relative volume V_{r_0} can have values between zero and one ($0 \leq V_{r_0} \leq 1$). Zero means there is no difference between the zonotope and the polytope (fully consistent) and one means empty set (inconsistent). When $V_{r_0} = 1$, i.e., empty set, a bias is detected. This bias is greater than or equal to the PMDB in equation (3.18). In GNSS application especially in urban areas, the observations will contain noise, systematic errors, and biases. Moreover, the geometry could vary from one epoch to another due to the quickly changing blockage by buildings or trees. Also, the observation interval bounds Δ , and its relation to the observation noise in terms of the standard deviation (σ), i.e. $\frac{\sigma}{\Delta}$ has a huge influence on the polytope and its corresponding zonotope. Then, all these factors together influence the consistency measures V_{r_0} . In order to understand these influences and be able to properly choose the OIB Δ and construct the Polytope Global Test (PGT), a Monte Carlo simulation will be conducted in section 4.1.

To perform the PGT, a threshold, i.e., a critical value has to be constructed and checked against the consistency measures V_{r_0} . The critical value is computed as:

$$CV_{V_{r_0}} = \kappa_p \frac{\sigma}{\Delta}, \quad (3.21)$$

where κ_p is a scalar constant similar to the constant values κ_H and κ_V in equation (2.69) and (2.70), respectively. The choice of κ_p depends on the ratio $\frac{\sigma}{\Delta}$ and the navigation system. It also depends on the desired IR. If Δ is the same for all observations then there is no problem in equation (3.21), otherwise, if each observation has a different Δ_i , then the mean value of all Δ_i can be used. The PGT is as follows:

$$T_{V_{r_0}} : \begin{cases} V_{r_0} \leq CV_{V_{r_0}} & | H_0 \\ V_{r_0} > CV_{V_{r_0}} & | H_i \end{cases} \quad (3.22)$$

The main reason for constructing the PGT is to detect biases smaller than PMDB since the consistency measures V_{r_0} can only detect biases greater than or equal to the PMDB in equation (3.18). In this way the overall MDB is decreased. How much it is decreased depends on the choice of the critical value $CV_{V_{r_0}}$, i.e. on κ_p .

Fault Exclusion

In order to identify which measurement is the faulty one, individual consistency measures have to be performed, what we call Polytope Local Test (PLT). In order to do so, the observations are arranged in combinatorial sets, where each set \mathbb{S}_i excluding the i -th tested observation, very similar to the sets in the solution separation test statistic or data snooping proposed by Baarda (1968). For instance, if we assume there exists one faulty measurement, i.e., single fault test and we want to test the i -th observation, the polytope and the zonotope with all the observations except the i -th one are computed and the following consistency measures are computed as:

$$V_{r_i} = \frac{Vol_{z_i} - Vol_{p_i}}{Vol_{z_i}}, \quad (3.23)$$

where V_{r_i} is the relative volume corresponding to set \mathbb{S}_i , and Vol_{p_i} and Vol_{z_i} are the volume of the polytope and zonotope of the set \mathbb{S}_i , respectively. Then, the PLT is performed, keeping in mind, before performing the local test, the global test has to be failed. The individual PLT can be performed on one set \mathbb{S}_i . If we suspect

only the i -th observation, then we assume that there are one faulty satellite and one alternative hypothesis H_i for the i -th observation. The individual local test can also be performed on each set \mathbb{S}_i separately, i.e., multi-hypotheses with one faulty satellite. First, a critical value for each set \mathbb{S}_i is computed as:

$$CV_{V_{r_i}} = \kappa_p \frac{\sigma}{\Delta_i}. \quad (3.24)$$

The critical value $CV_{V_{r_i}}$ is equivalent to the critical value $CV_{V_{r_0}}$ if all OIBs are equal. The $CV_{V_{r_i}}$ can be computed once and applied for all set \mathbb{S}_i . However, if the observations have different error bounds, the $CV_{V_{r_i}}$ has to be computed for each set \mathbb{S}_i by taking the mean value of all error bounds except the i -th one. The mean value of all error bounds except the i -th is different from another since the observations have different error bounds. In the case of constant error bounds for all observations, the mean value is constant and it is equal to the error bound Δ .

To test directly if the i -th observation is faulty or not, the local test is performed as:

$$T_{V_{r_i}} : \begin{cases} V_{r_i} \leq CV_{V_{r_i}} & | H_0 \\ V_{r_i} > CV_{V_{r_i}} & | H_i \end{cases} \quad (3.25)$$

In case of multiple hypotheses, the set \mathbb{S}_i which has the minimum V_{r_i} is declared faulty, i.e., the i -th observation in this case. The relative volume V_{r_i} is slightly smaller than the relative volume V_{r_0} due to the increases in volume by excluding the i -th observation. So the MIB is slightly bigger than the MDB. If the i -th observation contains no error, then $V_{r_0} = V_{r_i}$ and $MIB = MDB$.

Protection Level

The protection level of our approach is the convex hull of all the zonotopes computed from all sets \mathbb{S}_i , the so-called 1-relax zonotope. This PL is a zonotope itself centered at the barycenter of the polytope and it is guaranteed, i.e., it contains the true solution. The PL will contain the true solution no matter what biases exist in the observation. The zonotope protection level can be transformed into the cylindrical protection level as usually used in GNSS applications. To do so, the zonotope is projected to the horizontal plane and to the vertical plane and the maximum uncertainty in the horizontal zonotope will be the radius of the cylinder and the maximum uncertainty in the vertical zonotope will be the height of the cylinder. However, taking the zonotope as it is, the PL is better represented and has more than two directions. The number of directions is determined by the number of observations. Figure 3.24 depicts an example of the 3D zonotope PL and its projection on the horizontal and vertical planes where the cylindrical PL can be derived (shown in red).

To better explain the zonotope protection level, two 2D examples with three transmitters are presented in figure 3.25 and figure 3.27. The distance between the opposite vertices in the zonotopal PL contains the MDB MDB_{Z_i} in both directions, i.e., both cases of negative or positive biases will be included. In figure 3.25 the navigation geometry is quite good (transmitters LOS indicated by the grey lines), but we can easily see how the PL (red zonotope) contains all the possible biases for every observation. For instance, if there is a bias in 1st observation, \mathbb{S}_1 (depicted in yellow) which is the results of 2nd and 3rd observations, the polytope solution would move along the direction indicated by the magenta arrow which represents the distance between opposite vertices. The biased solution set could be in one of these two yellow triangles. Otherwise, it would be an empty set. The actual zonotope from all the observations (depicted in black) does not contain these two yellow triangular regions, so it may not include the true solution. The same applies to \mathbb{S}_2 (blue zonotope) and \mathbb{S}_3 (green zonotope).

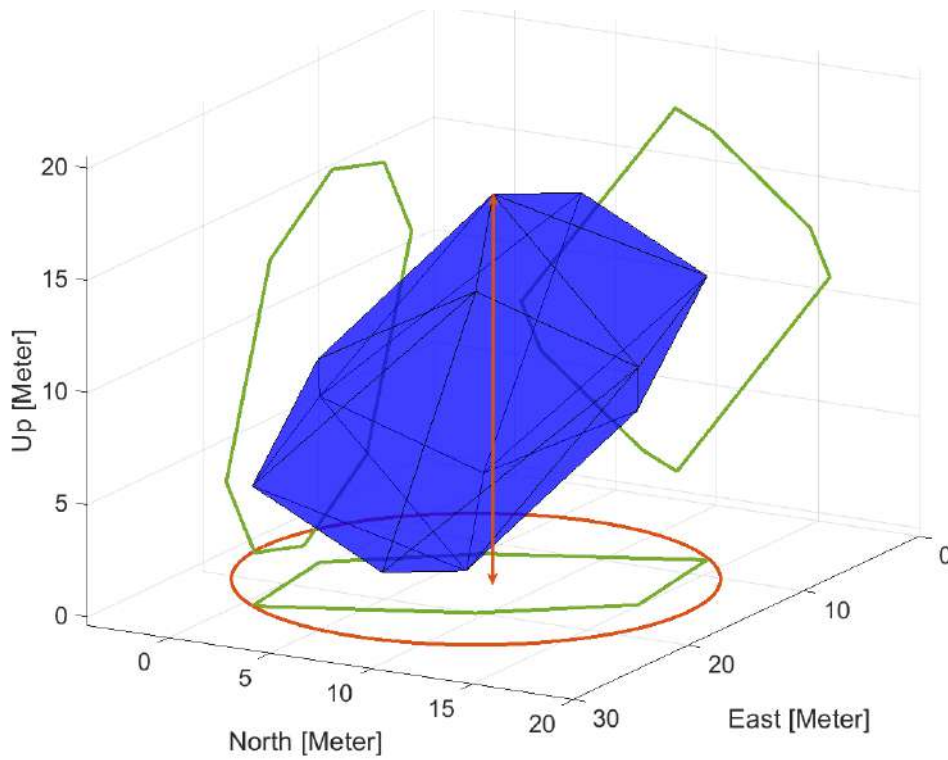


Figure 3.24: Example of zonotope protection level and its projection on the horizontal and vertical planes.

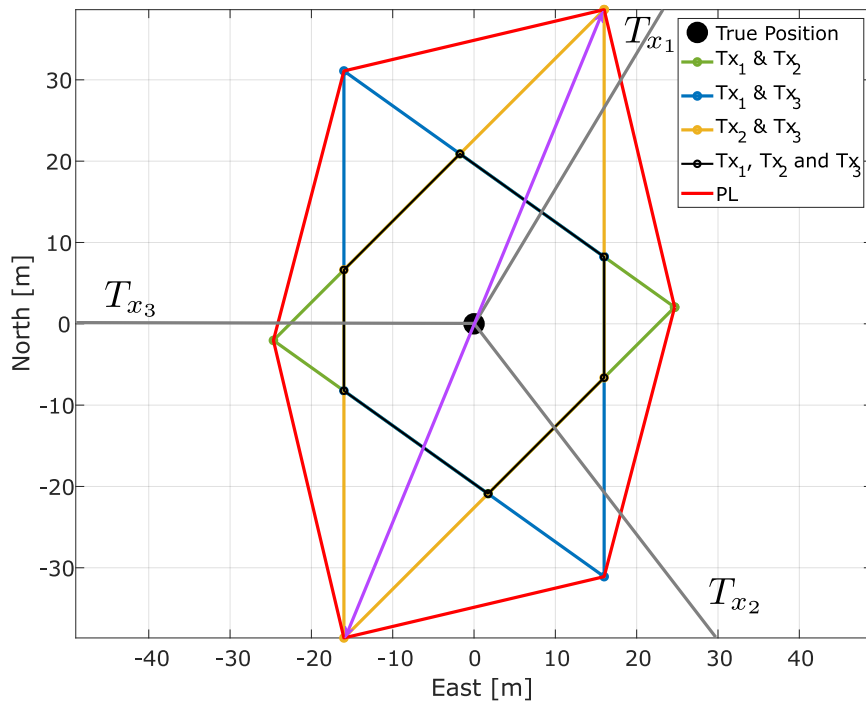


Figure 3.25: Zonotope protection level (red) for 3 transmitters scenario and zonotope solution S_0 depicted in black while the relaxed zonotopes S_1 , S_2 and S_3 are depicted in yellow, blue and green, respectively.

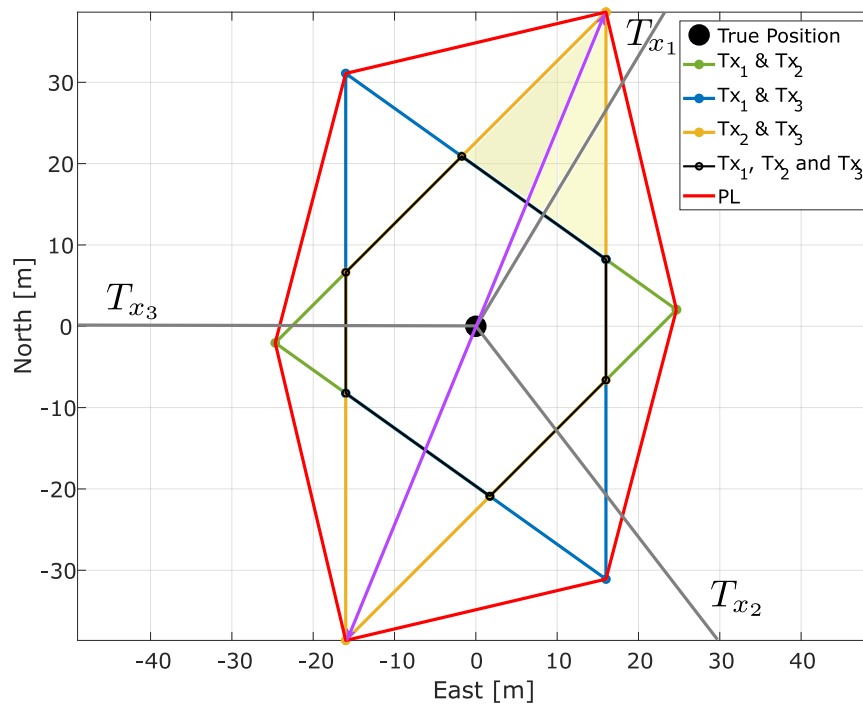
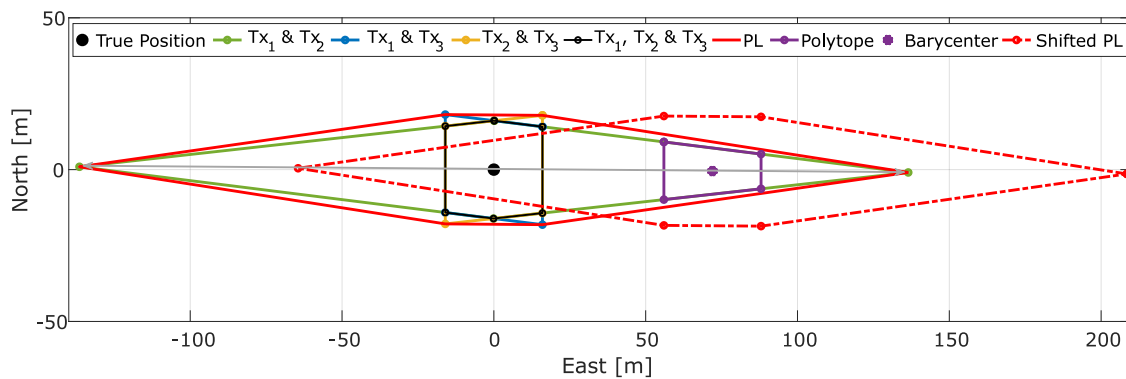
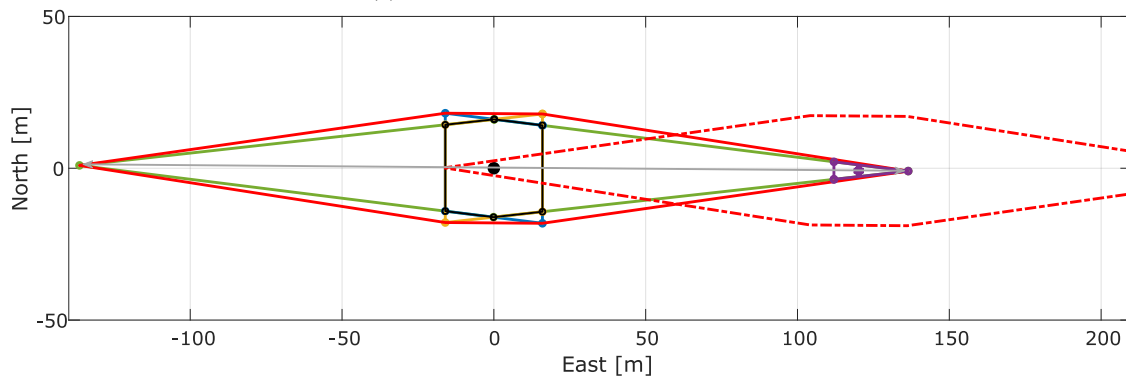


Figure 3.26: Zonotope protection level (red) for 3 transmitters scenario and zonotope solution \mathbb{S}_0 depicted in black while the relaxed zonotopes \mathbb{S}_1 , \mathbb{S}_2 and \mathbb{S}_3 are depicted in yellow, blue and green, respectively.



(a) Intermediate bias for observation 3



(b) Large bias for observation 3

Figure 3.27: Zonotope protection level (red) for 3 transmitters scenario and zonotope solution \mathbb{S}_0 depicted in black while the relaxed zonotopes \mathbb{S}_1 , \mathbb{S}_2 and \mathbb{S}_3 are depicted in yellow, blue and green, respectively. a includes the zonotope PL (dot-dashed red) and the intermediately biased polytope with its barycenter (violet), while in b, the bias is very large.

Let's go back to \mathbb{S}_1 and assume we have a NDB in the 1st observation in the upward direction. The NDB are biases smaller than the MDB so that the polytope solution is not empty and does not contain the true solution. The polytope solution will be somewhere in the upper yellow triangle, see figure 3.26. Then, the zonotope PL will be centered at the estimated position by the polytope, i.e. the barycenter of the polytope. This means the red zonotope is shifting along with the magenta diagonal and it also may shift a little bit to the right or the left due to the noise in the other observations. Since the zonotope protection level contains the PMDB, it will still contain the true solution, if it is shifting along the magenta arrow even to the upper vertex.

Figure 3.27a shows another example of the zonotope PL for a bad transmitters geometry including the shifted PL. Here a bias is added to the 3rd observation where the biased polytope \mathbb{S}_0 and its barycenter are depicted in black and violet before and after the bias is introduced, respectively. \mathbb{S}_0 is the set where all observations contribute to the polytope computation. As a result, the zonotope PL (solid red line) centered at the true position is shifted to the right by a value equal to the bias applied on the 3rd observation and it is centered at the barycenter of the polytope solution (dashed dot red line). This zonotope PL still contains the true position, even if the polytope solution is biased. If the bias increases, both the violet polytope and the zonotope PL will be shifted to the right until the polytope becomes empty, see figure 3.27b.

4 Performance Analysis of the Developed Methods by Monte Carlo Simulations

4.1 Introduction

We perform a Monte Carlo simulation to understand the behavior of the consistency measures V_{r_0} and V_{r_i} w.r.t. the satellite geometry GDOP, observation noise (σ), applied Observation Interval Bounds (OIBs), i.e. Δ , and biases δ . A second objective is to derive the critical value $CV_{V_{r_i}}$ for the polytopal tests PGT and PLT and to evaluate the minimum detectable bias.

To do so, seven different real satellite geometries (scenarios) are selected with a different number of satellites in view and geometrical dilution of precision GDOP values (Table 4.1). We simulate GPS code measurements with white noise ($\sigma = 1$ m). In each of the 1000 simulation runs (epochs), a different random vector is generated, thus given a different noise distribution. However, the sequence of random vectors is identical for all seven scenarios. In addition, eight different observation interval bounds $\Delta = 1, 2, 3, 4, 5, 6, 10, 20$ m are considered, thus changing the $\frac{\sigma}{\Delta}$ ratio. Finally, a ramp bias is introduced for all satellites (one satellite is biased in each run) starting from epoch 100 ($\delta = 0$ m) and ending at epoch 500 ($\delta = 32$ m), i.e., leading to an increase of 8 cm per epoch.

Table 4.1: GDOP and number of satellites for each scenario in the Monte Carlo simulation.

Scenario	1	2	3	4	5	6	7
Number of Satellites	9	8	6	10	7	5	6
GDOP	2.3	2.4	3.2	2.0	3.3	11.3	9

Figure 4.1 depicts the sky plot of each simulated scenario alone and the real GPS scenario (figure 4.1h) from which the simulated scenarios originate. The corresponding real GPS scenario with its real observations will be analyzed in chapter 5. We include the sky plots of the real scenario in order to show the position of each specific satellite in the simulated scenarios.

Then, the developed integrity monitoring technique based on the consistency measures, i.e., the PGT and the PLT are computed in the Monte Carlo simulated scenarios to study their performance and understand the weakness, the strength, and the robustness of our technique. In addition, RB and SS test statistics are performed on the simulated scenarios and compared to our technique.

4.2 Characterization of a Nominal Behavior

Figure 4.2 shows the consistency measures V_{r_0} of the Monte Carlo simulation for each scenario varying the observation interval bounds $\Delta = 1, 2, 3, 4, 5, 6, 10, 20$ m and keeping one common biased satellite (PRN10). Figure 4.2h depicts the ramp bias introduced to the common satellite (PRN10). So figure 4.2 shows the impact of different values Δ of the OIBs for each scenario when the same common satellite (PRN10) for all scenarios was biased. At the same time, it shows the impact of different satellite configurations on the consistency measures. A lot of information can be extracted from this figure and let us understand the behavior of the consistency measures due to different factors.

First, let us analyze the impact of the applied OIBs on the consistency measures outside the biased region (from epoch 500 to epoch 1000) to find the nominal behavior. Figure 4.2a (scenario 1) shows that, as Δ

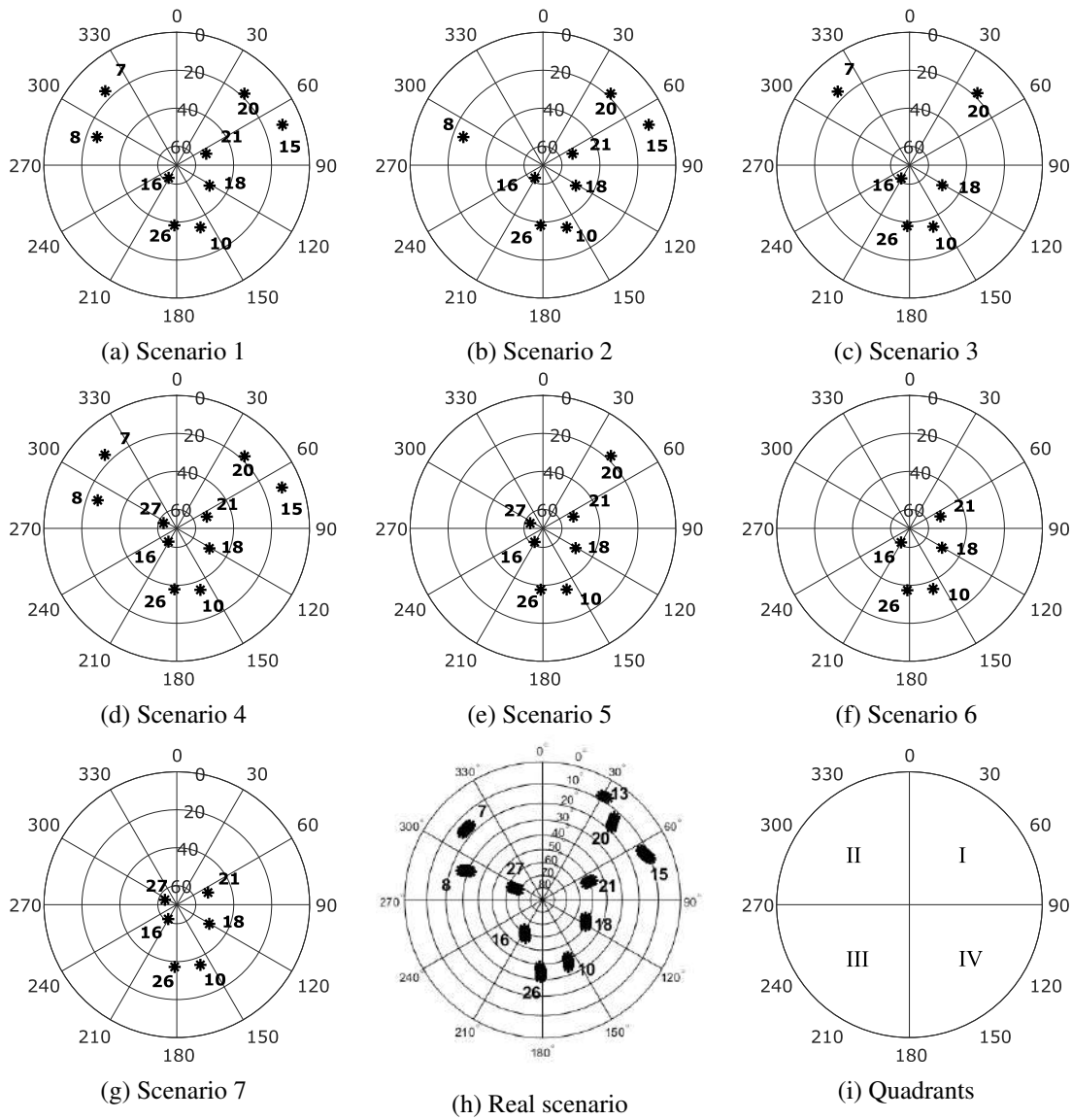


Figure 4.1: Sky plots of seven simulated scenarios taken from a real GPS data set presented in the sub-figure (h) and the quadrants numbers in sub-figure (i).

decreases from 1 m to 20 m, the scatter of the V_{r_0} increases. The standard deviation of the V_{r_0} is 0.2235, 0.0981, 0.0530, 0.0327, 0.0221, 0.0158, 0.0060, 0.0016 for $\Delta = 1, 2, 3, 4, 5, 6, 10, 20$ m, respectively. This is also related to the noise of the observations. So it is also useful to analyze the scattering of V_{r_0} w.r.t. the ratio $\frac{\sigma}{\Delta}$, which is in this case $\frac{\sigma}{\Delta} = \frac{1}{1}, \frac{1}{2}, \frac{1}{3}, \frac{1}{4}, \frac{1}{5}, \frac{1}{6}, \frac{1}{10}, \frac{1}{20}$. Figure 4.3 shows the standard deviations and the mean values of the scatter of the consistency measures as a function of the ratio $\frac{\sigma}{\Delta}$ for all scenarios. As the ratio $\frac{\sigma}{\Delta}$ increases, the standard deviation of the consistency measures increases, i.e., the volume of the polytope fluctuates w.r.t. the fixed zonotopal volume. However, the type of increase is different from one scenario to another, especially for scenario 6 which has the worst satellite geometry in terms of GDOP and the smallest number of satellites where the standard deviation is smaller than for all the others. This is because the fewer observations we have, the fewer cuts are applied on the polytope. Moreover, when the geometry is bad, the zonotope and polytope increase in volume so that observation noise has a small effect on the polytope volume (relatively) and the relative volume V_{r_0} increases slowly with the noise.

The mean value of the consistency measures, V_{r_0} , shows different behavior for different scenarios, see figure 4.3b. Scenario 4, which has the best geometry in terms of GDOP and the largest number of satellites, has the highest mean value followed by the 2nd best scenario (1) in terms of geometry, while scenario 6 with the worst geometry has the lowest mean value. Additionally, the gap between the mean values of different scenarios increases as the ratio of $\frac{\sigma}{\Delta}$ increases.

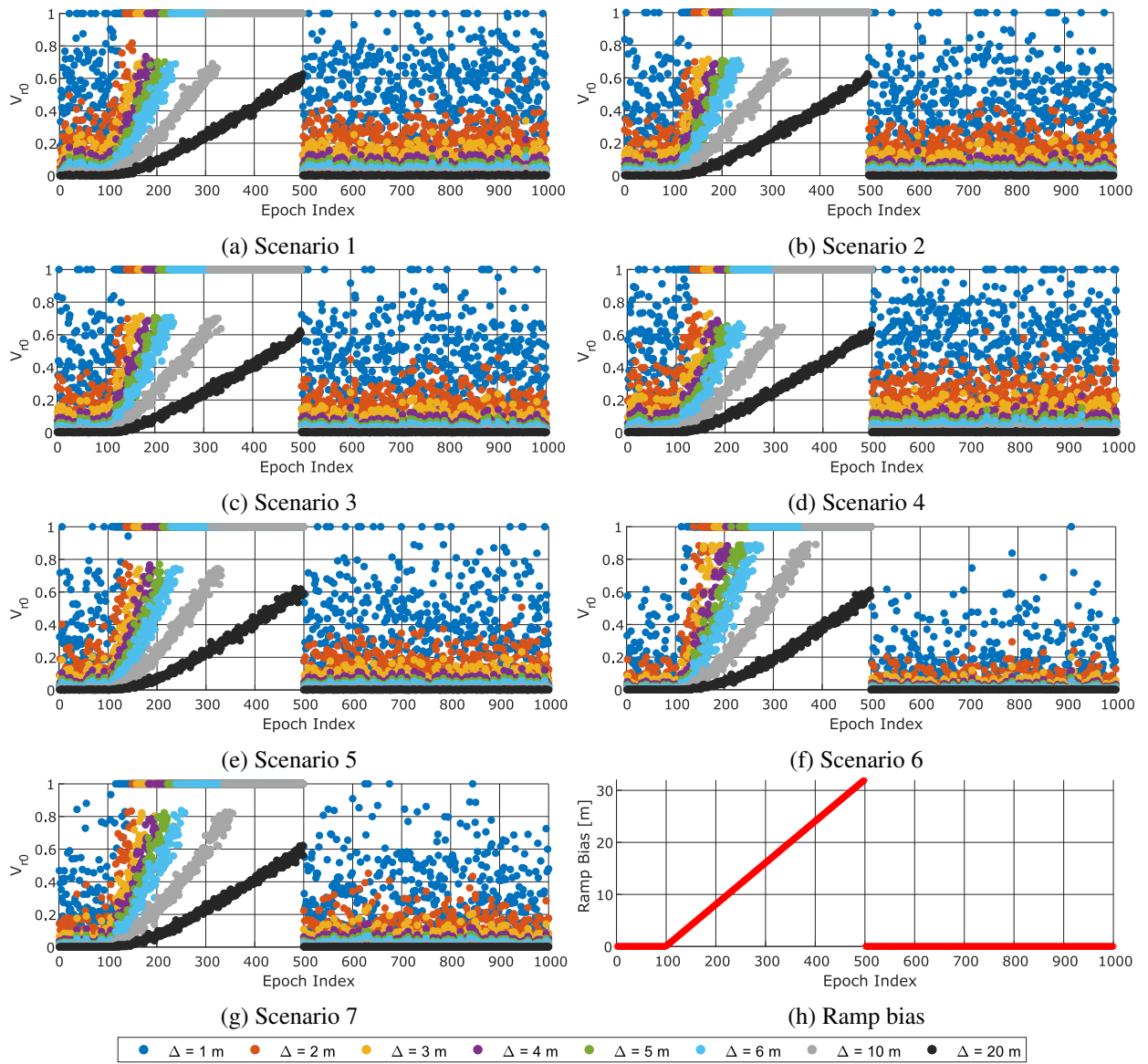


Figure 4.2: Monte Carlo simulation: The consistency measures V_{r_0} for all 7 scenarios and different applied interval bounds $\Delta = 1, 2, 3, 4, 5, 6, 10, 20$ m and observation white noise with $\sigma = 1$ m and one common ramp bias for one satellite (PRN10) between epoch 100 and 500 for all scenarios and Δ . Sub-figure (h) depicts the ramp bias applied to the biased PRN10.

That means for the same set of Δ and σ the behavior of the consistency measures with regards to its mean value and standard deviation could vary depending on the satellite geometry. They increase as the geometry enhances. This is important since in real scenarios especially in urban areas the satellite geometry could change from epoch to another due to the signal blockage by buildings or trees. For instance, the V_{r_0} mean value for scenario 4 and scenario 6, when $\Delta = \sigma$, i.e., $\frac{\sigma}{\Delta} = 1$, are 0.57 and 0.14, respectively, and their standard deviations are 0.21 and 0.16, respectively. These two scenarios take the whole spectrum (from 0 to 1) of the consistency measures V_{r_0} which makes it impossible to find suitable critical values $CV_{V_{r_0}}$ and $CV_{V_{r_i}}$ for the PGT and PLT, respectively, so that only consistency measures in terms of empty sets can be performed to find biases. Moreover, for $\Delta = \sigma$ many observations will be considered inconsistent and the consistency measures V_{r_0} would be equal to one, i.e., an empty set. Figure 4.2d which corresponds to scenario 4 shows a lot of empty sets, i.e. $V_{r_0} = 1$, when $\Delta = 1$ m, (blue dots) which degrade the continuity and availability of the navigation solution (31.73% of the epochs outside 1σ for observations with *Gaussian* noise ($\mu = 0$ m, $\sigma = 1$ m)). Contrary, setting very large OIBs Δ w.r.t. the observation noise σ , i.e. very small $\frac{\sigma}{\Delta}$ ratio gives very similar mean and standard deviation of the consistency measures V_{r_0} . For example, when $\Delta = 20$ m and $\sigma = 1$ m, i.e., $\frac{\sigma}{\Delta} = \frac{1}{20}$, the mean value and standard deviation of scenario 4 and 6 are $\mu(V_{r_0}) = 0.0025$ and $\sigma(V_{r_0}) = 0.0015$ and $\mu(V_{r_0}) = 0.00099$ and $\sigma(V_{r_0}) = 0.00098$, respectively. Since

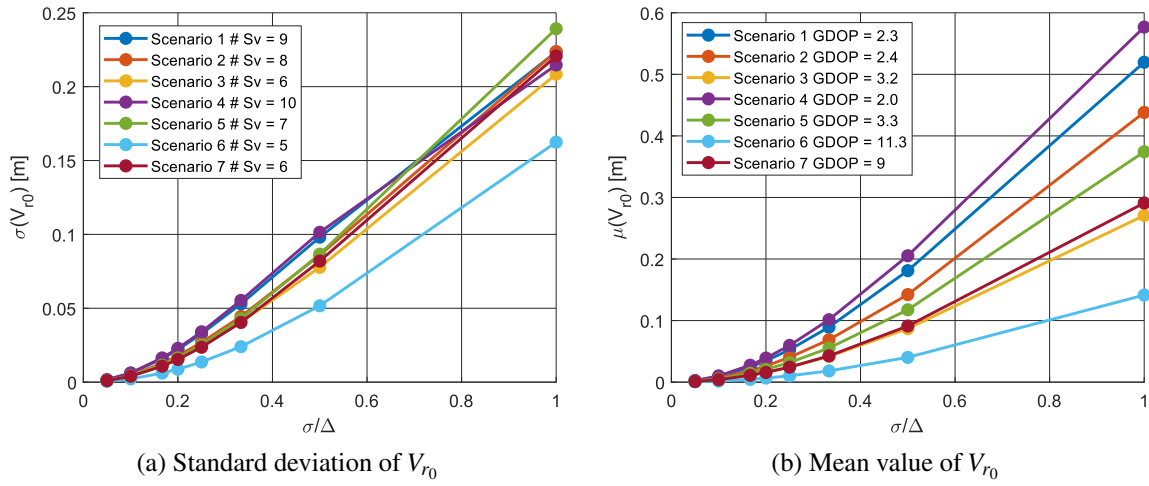


Figure 4.3: Standard deviation and mean value of the consistency measures V_{r_0} as a function of $\frac{\sigma}{\Delta}$ for all scenarios from epoch 500 to epoch 1000, i.e., non-biased epochs.

both scenarios have a very small mean value and standard deviations of the consistency measures, the critical value could be set $3 \times \sigma(V_{r_0})$ choosing the highest σ , i.e., $\sigma(V_{r_0}) = 0.0015$ of the best geometry scenario. Everything larger than the critical value can be considered a bias. However, setting a very large OIB $\Delta = 20$ m provides a very large zonotope which gives a very large PL. In this case the availability of the navigation system would be lost, since the AL usually is not that large for most of the applications.

Figure 4.4 presents the consistency measures V_{r_0} for scenario 4 (best geometry) and scenario 6 (worst geometry) for different observation interval bounds, keeping the same observation noise ($\sigma = 1$ m) and biased satellite PRN10. If we keep analyzing the second half of the Monte Carlo run (from epoch 500 to 1000), the scatter of V_{r_0} decreases as Δ increases. Moreover, the difference between the two scenarios decreases as Δ increases until they become very similar for $\Delta = 20$ m. These two scenarios are taken from a small test drive in urban areas, so this kind of geometry variation could happen at any moment in real scenarios.

The valuable information we learn from this Monte Carlo simulation until now is as follows:

- In order to construct a test quantity, OIBs should be chosen in a way to keep the differences between the mean values of V_{r_0} of different scenarios quite small so that the test is independent of the geometry.
- A small scatter of V_{r_0} is needed, i.e. a small standard deviation of V_{r_0} , so it is easier to differentiate between noise and biases when the PGT and PLT are performed.
- Good navigation geometry is affected more than bad navigation geometry in terms of mean value and standard deviation of the consistency measures.
- The mean and the variance $\mu(V_{r_0})$ and $\sigma(V_{r_0})$ increase as geometry gets better, but the incremental rate depends on the observation interval bound Δ .
- Small OIBs (Δ) w.r.t. observation noise σ are not suitable for the PGT and PLT and cause a loss of continuity and availability. The scatter of V_{r_0} goes all over the consistency area (from 0 to 1) and no critical value can be applied and only empty sets can be detected as biases.
- Very large OIBs Δ w.r.t. observation noise σ are also not suitable for the PGT and PLT and cause a loss of availability since the protection level will be very large. But the PGT and PLT can be conducted and they will perform very well due to the small scatter of V_{r_0} in the nominal region.
- The power of the test increases when Δ increases at the cost of larger MDB.
- The power of the test is reduced when Δ decreases but smaller biases can be detected.
- In order to set proper critical values for the PGT and PLT information about the variance and mean of the scatter of V_{r_0} w.r.t. $\frac{\sigma}{\Delta}$ ratio as well as information on the navigation geometry is needed.

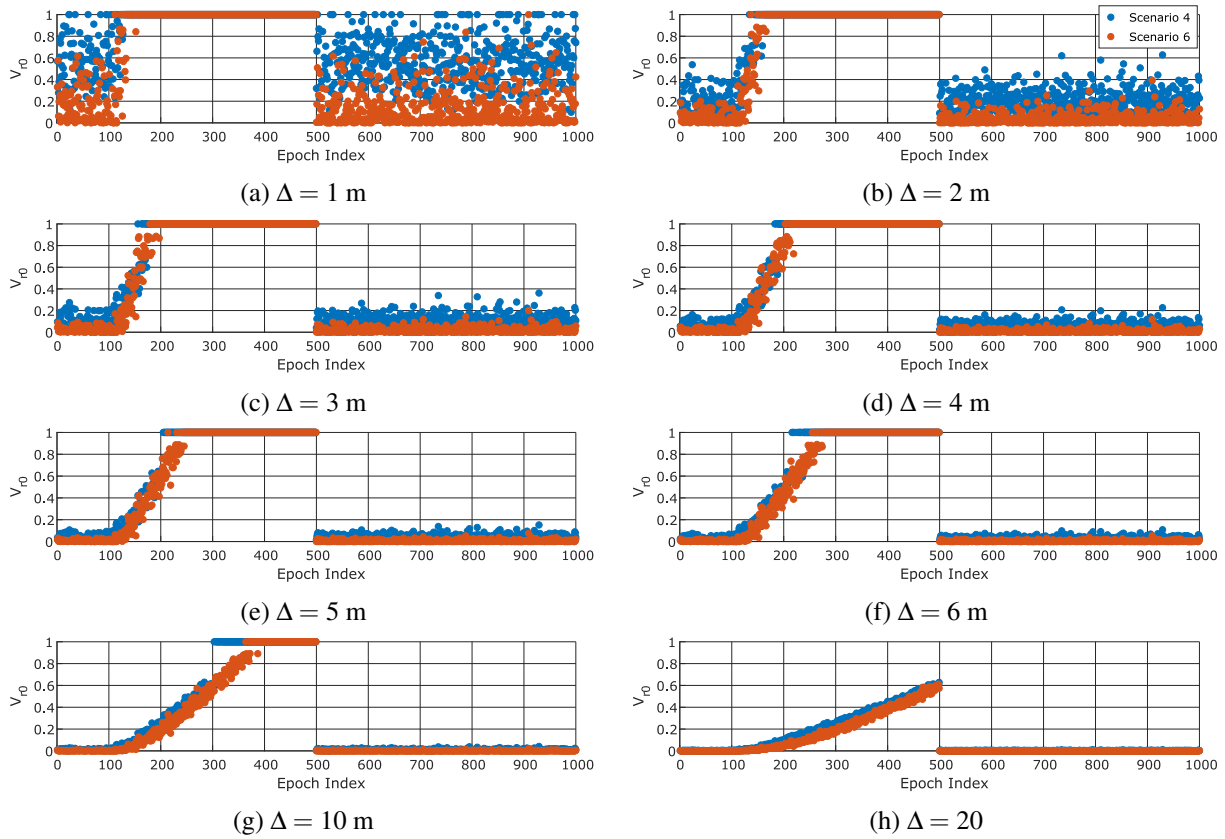


Figure 4.4: Monte Carlo simulation: The consistency measures V_{r_0} for scenario 4 and 6 and different interval bounds $\Delta = 1, 2, 3, 4, 5, 6, 10, 20$ m and observation white noise with $\sigma = 1$ m and one common ramp bias for one satellite (PRN10) between epoch 100 and 500 for both scenarios and all Δ .

4.3 Proposal to Select the Critical Value of the Polytope Tests

For observations with *Gaussian* noise ($\mu = 0$, $\sigma = 1$ m) a suitable OIB Δ could vary between 3 m and 6 m, i.e., $\frac{1}{3} \leq \frac{\sigma}{\Delta} \leq \frac{1}{6}$. Figure (4.3) shows a small variation of the standard deviation and mean value of V_{r_0} for all scenarios when $\frac{1}{3} \leq \frac{\sigma}{\Delta} \leq \frac{1}{6}$, for instance, when $\frac{\sigma}{\Delta} = \frac{1}{3}$ the highest mean value is equal to 0.1 for scenario 4 and the highest scatter is $\sigma = 0.05$ also for scenario 4. For 99.73% of the epochs the critical values in equation (3.21) and equation (3.24) should be equal to $3 \times \sigma(V_{r_0}) + \mu(V_{r_0}) = 0.25$ to be consistent with the OIBs Δ . In this case, the scale parameter $\kappa_p = CV_{V_{r_0}} \times \frac{\Delta}{\sigma} = 0.25 \times \frac{3}{1} = 0.75$. While for 99.999998% of the epochs, the critical value $CV_{V_{r_0}} = 0.43$, i.e., $\kappa_p = 1.29$.

When $\frac{\sigma}{\Delta} = \frac{1}{6}$, the highest mean value is 0.039, the highest scatter is $\sigma = 0.0163$ for all scenarios. Then, for 99.73% and 99.999998% of the epochs to be consistent with the OIBs Δ , the critical values are $CV_{V_{r_0}} = 0.0879$ and $CV_{V_{r_0}} = 0.136$, respectively. This leads to the scale parameters $\kappa_p = 0.527$ and $\kappa_p = 0.816$ for 99.73% and 99.999998%, respectively.

However, in the real applications, κ_p has to be set in advance, so it is possible to compute the critical value. Before we choose κ_p , some knowledge of the navigation system has to be available, or at least a good assumption has to be made. The type of noise in the observations, especially its standard deviation or variance, has to be known or assumed even if it is not *Gaussian*. The κ_p depends also on the IR specified for the navigation system and on the acceptable gross errors in the observations. To do so, we need to understand the behavior of the consistency measures V_{r_0} in the presence of biases under different circumstances, i.e., different satellite distribution, OIB, and different biased satellites with different rates.

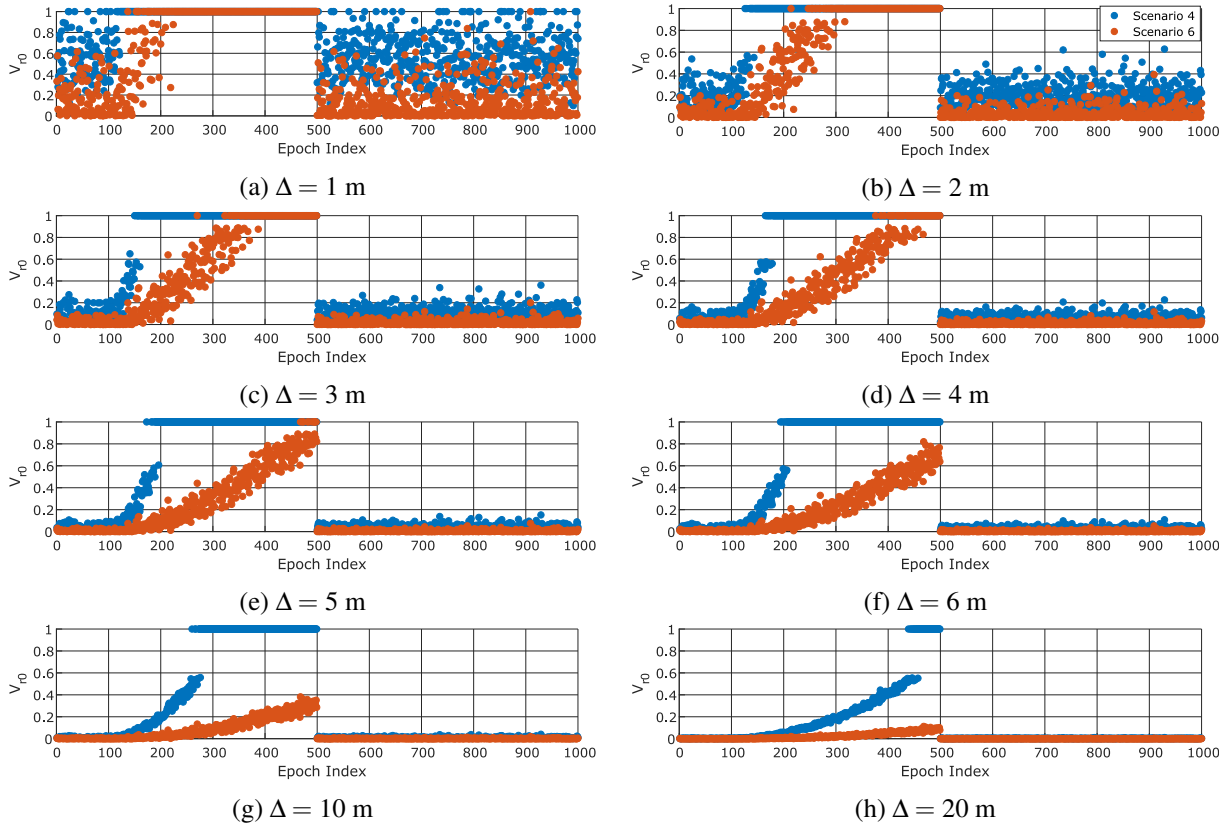


Figure 4.5: Monte Carlo simulation: The consistency measures V_{r_0} for scenario 4 and 6 and different interval bounds $\Delta = 1, 2, 3, 4, 5, 6, 10, 20$ m and observation white noise with $\sigma = 1$ m and one common ramp bias for one satellite (PRN16) between epoch 100 and 500 for both scenarios and all Δ .

4.4 Impact of Biases

4.4.1 Introductory Example

Now, we analyze the behavior of the consistency measures in cases of biases, focusing on the biased region in figure 4.2, i.e., from epoch 100 to epoch 500 where a ramp biases has been introduced to one satellite (i.d. PRN10) with 0.08 m increments per epoch. The bias increases from 0 m at epoch 100 to 32 m at epoch 500. The ramp bias is presented in figure 4.2h, so the reader can relate graphically the bias to the change in V_{r_0} . For an OIB $\Delta = 1$ m almost for all scenarios the resulting polytope is empty, i.e. $V_{r_0} = 1$. Except for scenario 6 the first few epochs are still not empty. This is because the PMDB of the consistency measures V_{r_0} in equation (3.18) depends on Δ and on the geometry. The PMDB is directly proportional to Δ and the quality of the navigation geometry, i.e. width of the polytope. As Δ increases, the consistency measures in the biased region decreases and the polytope start to get empty at larger biases for larger Δ , e.g., in scenario 1, V_{r_0} starts to provide empty sets at epoch $\simeq 229$, i.e., a bias $\delta = 10.32$ m for $\Delta = 6$ and V_{r_0} starts to be 1 (empty polytope) at epoch $\simeq 305$, i.e. $\delta = 16.4$ m for $\Delta = 10$ m. However, the consistency measures increase linearly in the biased region at different rates for different Δ until it becomes empty. For $\Delta = 20$ m the polytope never becomes empty due to increase in the PMDB which becomes larger than the applied bias.

One other feature is the incremental rate of V_{r_0} in the biased region. It gets lower as Δ increases. Looking at scenario 4 and scenario 6 the best and worst scenarios in terms of GDOP, respectively, with an observation interval bound $\Delta = 10$ m (grey plots in figure 4.2), the consistency measures V_{r_0} start to be 1 (empty polytope) at different biases. Scenario 4 start to have empty polytope at epoch 303 ($\delta = 16.42$ m) while scenario 6 starts to have empty polytopes at epoch 364 ($\delta = 21.12$ m). This is due to the polytope width w_{p_i} in equation (3.18).

4.4.2 Impact of Different Biased Satellites and Observation Interval Bounds

To better illustrate the effect of different OIBs Δ and different biased satellites with the same geometries, the same analysis done in figure (4.2) is performed again. This time for biased satellite PRN16, figure 4.6. Scenario 1 and 2 show a very similar behavior for both biased satellite (PRN10 figure 4.2 and PRN16 figure 4.6) for all Δ s except for $\Delta = 20$ m. The consistency measures in the biased region increase almost quadratically for PRN16, while it increases quite linearly for PRN10, but still quite similar in terms of magnitude. Contrary to the other scenarios, V_{r_0} shows different behavior for PRN16 in the biased region, especially for scenario 6. For the biased PRN16 in scenario 6, V_{r_0} has smaller values than the case PRN10 is biased. For example, in scenario 6, $\Delta = 6$ m the consistency measure for biased satellite PRN16 has no values 1 at all, i.e. no empty polytopes, while for biased satellite PRN10 the empty polytopes started at epoch 255, i.e. $\delta = 12.4$ m. Similarly, for $\Delta = 10$ m the consistency measure for biased satellite PRN16 has no empty sets at all while for biased satellite PRN10 the empty sets started at epoch 364, i.e. $\delta = 21.1$ m.

Furthermore, the scatter of the consistency measures in the biased region is different for different applied OIBs. This can be easily seen in scenario 6 in figure (4.4). As Δ increases the scatter decreases, similarly to the non-biased region (epoch 500 to 1000) but with a different order of magnitude. I assess this analysis visually since it is not possible to compute the scatter in the biased region without performing fitting to the consistency measures, i.e. removing the bias and drift from the V_{r_0} data. The scatter in the non-biased region decreases significantly while in the biased region it decreases moderately. For example, in scenario 6 when $\Delta = 6$ m the scatter in the biased region in V_{r_0} is higher than the scatter of V_{r_0} in the non-biased region, see third panel, right sub-figure in figure 4.4.

Since the effect of a biased satellite (PRN10) looks similar for all scenarios, we analyze another biased common satellite (PRN16). Figure (4.5) depict the consistency measures V_{r_0} for scenario 4 and 6, different applied interval bounds $\Delta = 1, 2, 3, 4, 5, 6, 10, 20$ m, observation white noise with $\sigma = 1$ m and a one common ramp bias for one satellite (PRN16) between epoch 100 and 500 for all scenarios and all Δ . In this figure, we show only two scenarios (best and worse in terms of geometry) in order to have a clear image of the consistency measure behavior. Here, the difference in the scatter of the consistency measures for different observation interval bounds in the biased region is quite obvious, especially for scenario 6. As the OIB increases the scatter of V_{r_0} decreases, similar to the non-biased region. On the contrary, it is clear that the scatter in scenario 6 is larger than the scatter of scenario 4 for the same OIB (in the biased region), while in the non-biased region the scatter of scenario 4 is larger than the scatter of scenario 6, e.g. ($\Delta = 5$ m and $\Delta = 6$ m), see figure 4.5e and figure 4.5f.

Also, for the same Δ and same scenario but a different biased satellite, the scatter of the consistency measures changes. For example, the scatter of the consistency measures is much larger in case of the biased satellite PRN16 than the biased satellite PRN10 for any Δ , compare corresponding subplots in figure (4.4) and figure (4.5). In section (4.4.3) the effect of biased satellites on the consistency measures will be studied in more detail.

4.4.3 Impact of Different Biased Satellites and Satellite Geometry

To better illustrate the effect of different biased satellites on the consistency measures (1 biased PRN each run), superimposed consistency measures of all biased PRN are plotted together for each scenario for $\Delta = 3$ m and $\Delta = 6$ m in figure 4.7 and figure 4.8, respectively. In the case of $\Delta = 3$ m, scenario 1 and 4 show very comparable behavior which is expected due to the number of satellites in these scenarios and the low GDOP values. For scenario 1 the polytopes get empty for biases larger than 8.24 m, i.e. at epoch 203. Also, there are many empty polytopes between epoch 137 and 203, i.e., $\delta = 2.96$ m and $\delta = 8.24$ m. Since the PMDB is equal to the OIB plus the half width of the polytope (3.18), in this case the half width $\frac{w_{pi}}{2}$ is comparable to the OIB due to the bounding from all directions.

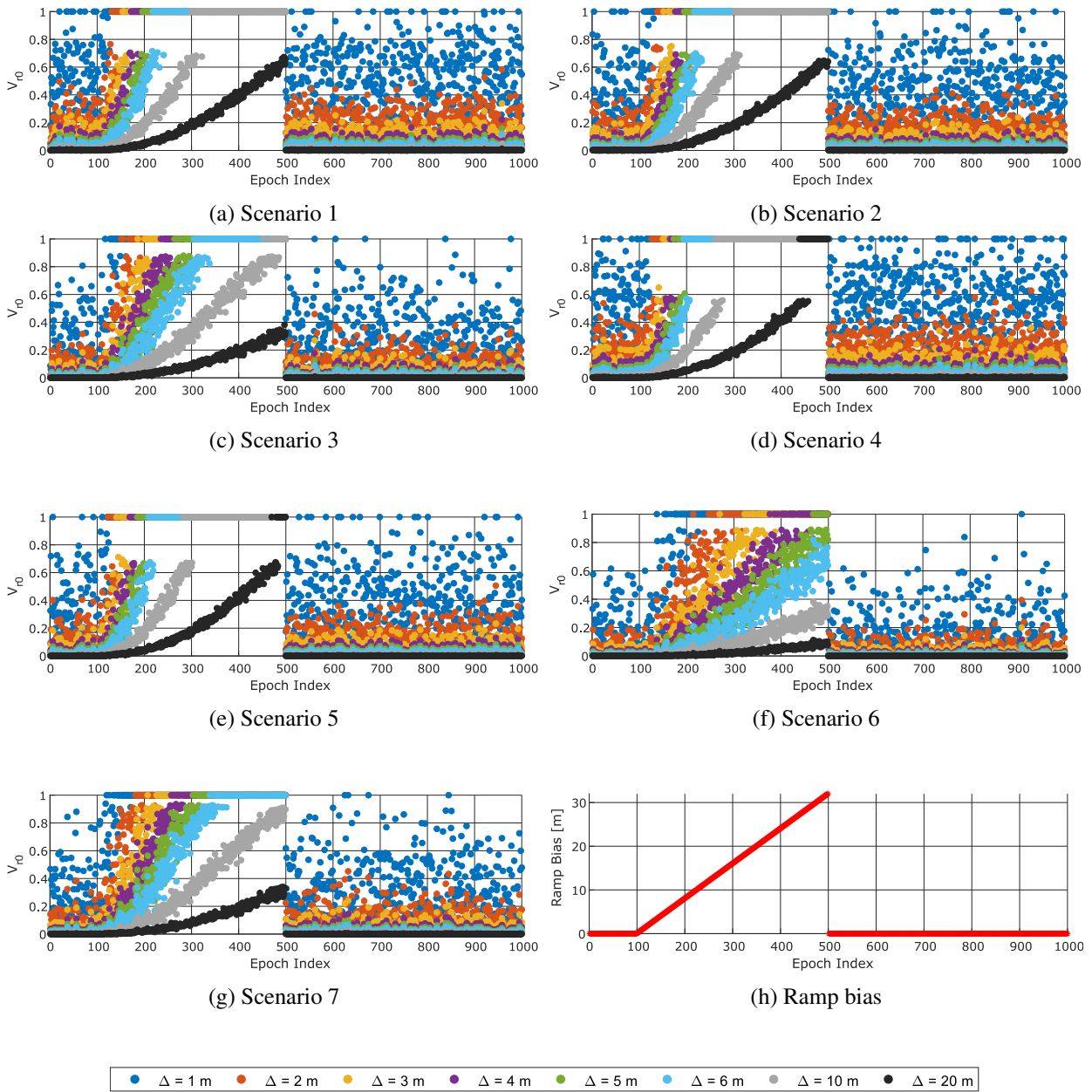


Figure 4.6: Monte Carlo simulation: Polytope global test V_{r_0} for all 7 scenarios and different applied error bounds $\Delta = 1, 2, 3, 4, 5, 6, 10, 20$ m (indicated by the legend) and observation white noise with $\sigma = 1$ m and a one common ramp bias for one satellite (PRN16) between epoch 100 and 500 for all scenarios and Δ . The last subplot depicts the ramp bias applied to the biased PRN16.

In scenarios 2 and 3, different biased satellites have slightly different effects on the consistency measures. In scenario 3, satellite PRN07 and PRN20 start providing empty polytopes at larger biases than the other satellites. To speculate why this happens for those 2 satellites and not the other, we can have a look at the skyplot of this scenario, figure 4.1c. In scenario 3, six satellites are in view, four of them are in the southern section of the sky (two satellites in quadrant III and two satellites in quadrant IV) and the other two satellites (PRN07 and PRN20) are in the northern section (quadrant II and quadrant I, respectively). Since the PMDB for i -th observation depends on the geometry of all other satellites except the i -th observation, the polytope gets blown up in the direction of PRN07 and PRN20 when they are excluded. So the PMDB of those satellites is larger than the other. For instance, excluding PRN07 there will be no remaining satellites in the quadrant II while excluding one of the satellites at quadrant III or quadrant IV, e.g., PRN18, the polytope is still bounded by the other satellite (PRN10, PRN26, and PRN16) at those quadrants.

In scenario 5, seven satellites are in view, but they are not very well distributed. There are one satellite PRN27 at quadrant II and high elevation angle, and two satellites (PRN20 at low elevation angle and PRN21

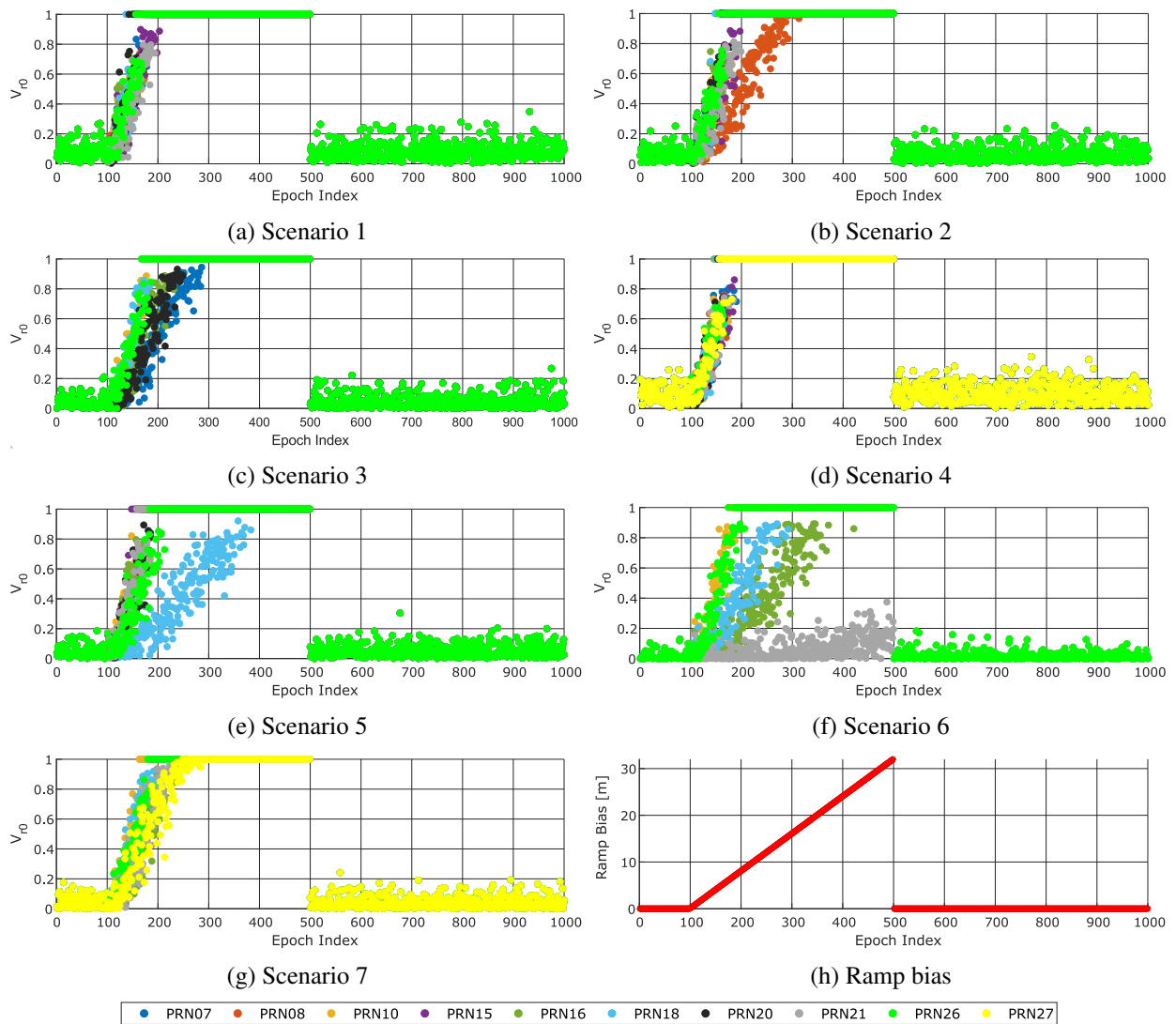


Figure 4.7: Monte Carlo simulation: Consistency measures V_{r_0} for all scenarios with $\Delta = 3$ m and $\sigma = 1$ m for different biased satellites indicated by the legend.

at high elevation angle) at quadrant I. Excluding one of these two satellites or one of the other four satellites in quadrant II and IV does not affect the polytope too much and still bounds it almost in the same way. Contrary to this, excluding PRN20, the polytope is not bounded anymore from quadrant I and II at low elevations. This makes the PMDB of PRN20 larger than the others and this is clear in the V_{r_0} for these satellites, scenario 5 in figure 4.7.

Scenario 6 which has the worst satellite geometry and the smallest number of satellites (five satellites in view) shows much lower values of V_{r_0} than all the other scenarios. Moreover, when PRN21 is the biased satellite, the consistency measures have very low values compared to the non-biased epochs with a slightly larger scatter. In this case, the PMDB of PRN21 is much higher than the one of the other satellites. This behavior is expected for such a bad geometry scenario and a low number of satellites. Regardless of the bad geometry in general, let us have a look at the skyplot of scenario 6, figure 4.1. PRN21 is located at quadrant I at high elevation, while all other satellites are located at quadrant III and IV. So, the polytope solution of all satellites except PRN21 is expected to have every large uncertainty in the direction of the upper quadrants, i.e quadrant I and II, and as a consequence, a very large PMDB of PRN21. This is an extreme example of bad geometry similar to what is explained in figure 3.21.

Now we perform a similar analysis but with a larger OIB. Figure 4.8 depicts the same analysis as in figure 4.7 except that now the OIB is equal to 6 m. For larger OIBs, the effect of the geometry on the biased region and each biased satellite is more distinct. In the very good geometry cases such as scenario 1 and scenario 4,

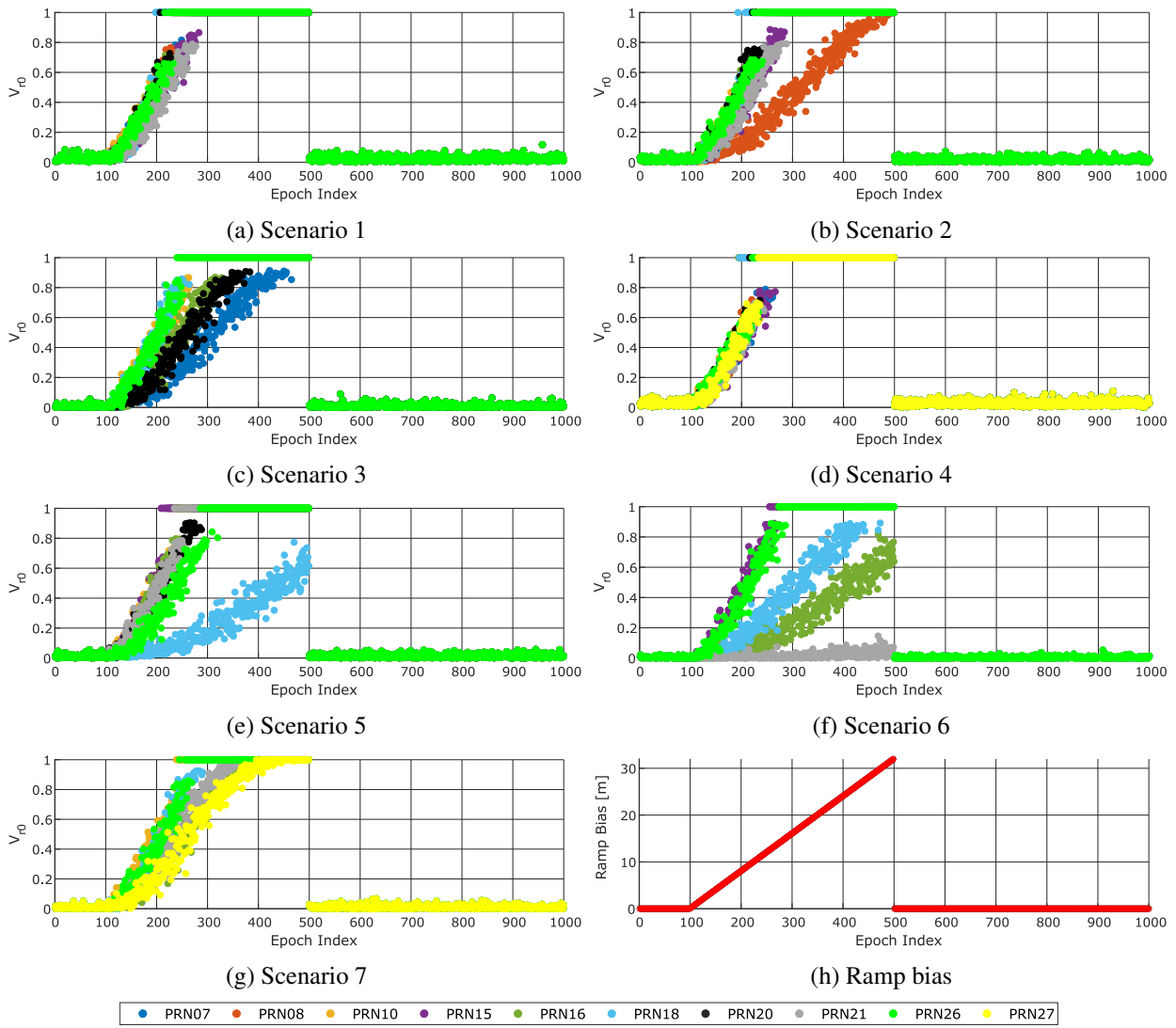


Figure 4.8: Monte Carlo simulation: Consistency measures V_{r0} for all scenarios with $\Delta = 6$ m and $\sigma = 1$ m for different biased satellites indicated by the legend.

the results are still the same and all satellites have almost equivalent behavior. The only difference from the case $\Delta = 3$ m is that the PMDB is larger due to the larger Δ . Contrary to this, for scenarios with intermediate geometry (scenarios 2, 3, and 5) and bad geometry (scenario 6), the difference of the consistency measures V_{r0} for different biased satellites becomes larger because one part of PMDB depends on Δ itself and the other part depends on the effect of Δ on the polytope in bad geometry. So, the width of the polytope w_{p_i} increases with more than one factor when Δ increases with one factor.

To better explain this effect we look back on figure 3.18b and figure 3.19. To illustrate the effects of the OIBs and geometric effects without taking into account the observation noise, we compare the black zonotope in figure 3.18b (good geometry) and figure 3.19 (bad geometry). In a good geometry case, the two black zonotopes, one with $\Delta = 4$ m and the other with $\Delta = 16$ m have the polytope width w_{p_i} very comparable to $2 \cdot \Delta$ in all directions and in both cases $\Delta = 4$ m and $\Delta = 12$ m. Instead, in the bad geometry case i.e., figure 3.19, the two black zonotopes have different width in different directions. In the north direction the width is comparable to $2 \cdot \Delta$ in both cases $\Delta = 4$ and $\Delta = 16$, i.e. $w_{p_i} \simeq 2 \cdot \Delta$, while in the east direction the polytope width is much bigger than $2 \cdot \Delta$, i.e. $w_{p_i} \simeq 8 \cdot \Delta$. So increasing Δ in a very good geometry has one as scale factor on the polytope width, while in bad geometry case it has a scale larger than factor one. The effect different OIBs on the polytope width and volume will be discussed in more details in section 4.8.

Scenario 7 has a bad geometry in terms of the number of satellites and $\text{GDOP} = 9$. However, it shows better consistency measures than the scenario 2, 3, and 5 with $\text{GDOP} = 2.4, 3.2$ and 3.3 , respectively. The

consistency measures V_{r_0} of scenario 7 is better than the one of scenarios 2, 3, and 5 in the non-biased region, which means that it has a lower scatter than the other scenarios. In the biased region, V_{r_0} of scenario 7 increases faster than the other scenarios. This happens because in scenario 7 all satellites in view are at high elevations, while in the other scenarios the satellites are distributed at high and low elevations. Having all satellites at a high elevation makes the polytope well bounded in the up direction and the opposite in the horizontal direction. So the cutting of the polytopes is always happening in the up direction and not in the horizontal one. So the effect of high uncertainty in the horizontal direction does not affect the consistency measures. If one satellite appears at a low elevation angle then the horizontal uncertainty will have the highest effect on the consistency measures. This simulation concludes that the GDOP is a good measure of uncertainty, but it is not always a good measure for consistency measures.

4.5 Analysis of the Polytope Global and Local Tests

4.5.1 General Proceeding

The polytope global test PGT is performed on the consistency measures V_{r_0} . In order to perform the global test on the consistency measures, a critical value has to be set on the V_{r_0} , see equation (3.21). The critical value depends on the observation interval bound Δ , the standard deviation of the observation noise σ , and on a scale parameter κ_p . As we have seen in section 4.2, κ_p depends on many factors and the optimum value could vary between 0.5 to 1.5. For the first analysis $\kappa_p = 1.5$ will be used. Figure 4.9 depicts the superimposed consistency measures V_{r_0} and V_{r_i} for scenario 1, applying an OIB of $\Delta = 3$ m to all biased satellites. Each subplot represents a different biased satellite. The consistency measures V_{r_0} , i.e., the whole set of observations (\mathbb{S}_0) without excluding any observation, shows higher values in the biased region than the consistency measures V_{r_i} for set (\mathbb{S}_i), i.e., excluding i -th observation. At the beginning of the biased region, all the consistency measures increase until the polytopes become empty, i.e., $V_{r_0} = 1$. The consistency measures of \mathbb{S}_i show the same behavior as the non-biased region, i.e. a noisy pattern. For instance, in figure 4.9a, PRN07 is the biased satellite. As we can see, all the consistency measures start increasing when the bias is introduced to PNR07 except the consistency measures $V_{r-PRN07}$ (orange dots), since the polytope computation $V_{r-PRN07}$ excludes the observation to PRN07 which is the only biased observation in this case. When different satellites are biased, similar results are achieved: only the non-biased consistency measures show nominal behavior (of an unbiased case) in the biased region (see other subplots and relate the color in the legend).

Figure 4.10 depicts the results of the PGT and PLT of scenario 1 for two different OIBs $\Delta = 3$ m and $\Delta = 6$ m. First, the PGT is performed for $\kappa_p = 1.5$ then the PLT is performed on the failed epochs with the same κ_p , i.e., $CV_{V_{r_0}} = CV_{V_{r_i}}$. It's clear that for $\Delta = 3$ m the detection starts at smaller biases than for $\Delta = 6$ m since the MDB depends on OIBs. However, for $\Delta = 3$ m there was one false detection when PRN07 and PRN08 were biased. For the rest of biased satellites, there is no false detection and the isolation processes succeed 100 %. On the other hand, for $\Delta = 6$ m the isolation process succeeds 100 % for every biased satellites. So at the cost of higher MDB, perfect isolation can be achieved. The reason why at lower OIBs false identification or isolation occurred, is that for smaller Δ the scatter of the consistency measures is higher.

To better highlight the effect of different OIBs, $\Delta = 3, 4, 5, 6, 10, 20$ m is applied on scenario 1 for the case PRN08 is biased. Figure (4.11) depict the consistency measures V_{r_0} for scenario 1 at different OIBs superimposed with critical value $CV_{V_{r_0}}$ for each Δ and also superimposed with fault detection decision (in arbitrary scale) for each Δ . The double arrows indicate the region where the PGT failed, i.e. a fault is detected and the polytopes are not empty, i.e $V_{r_0} < 1$. The critical value is smaller for larger Δ but it intersects with V_{r_0} at higher bias values, i.e. the detection starts at higher bias values. For instance, when $\Delta = 3$ m the MDB is $\delta = 3.52$ m, while for $\Delta = 10$ m and $\Delta = 3$ 20 m the MDB is $\delta = 5.12$ m and $\delta = 7.44$ m, respectively. In addition, after the first detected bias in all cases, not all biased epoch are detected.

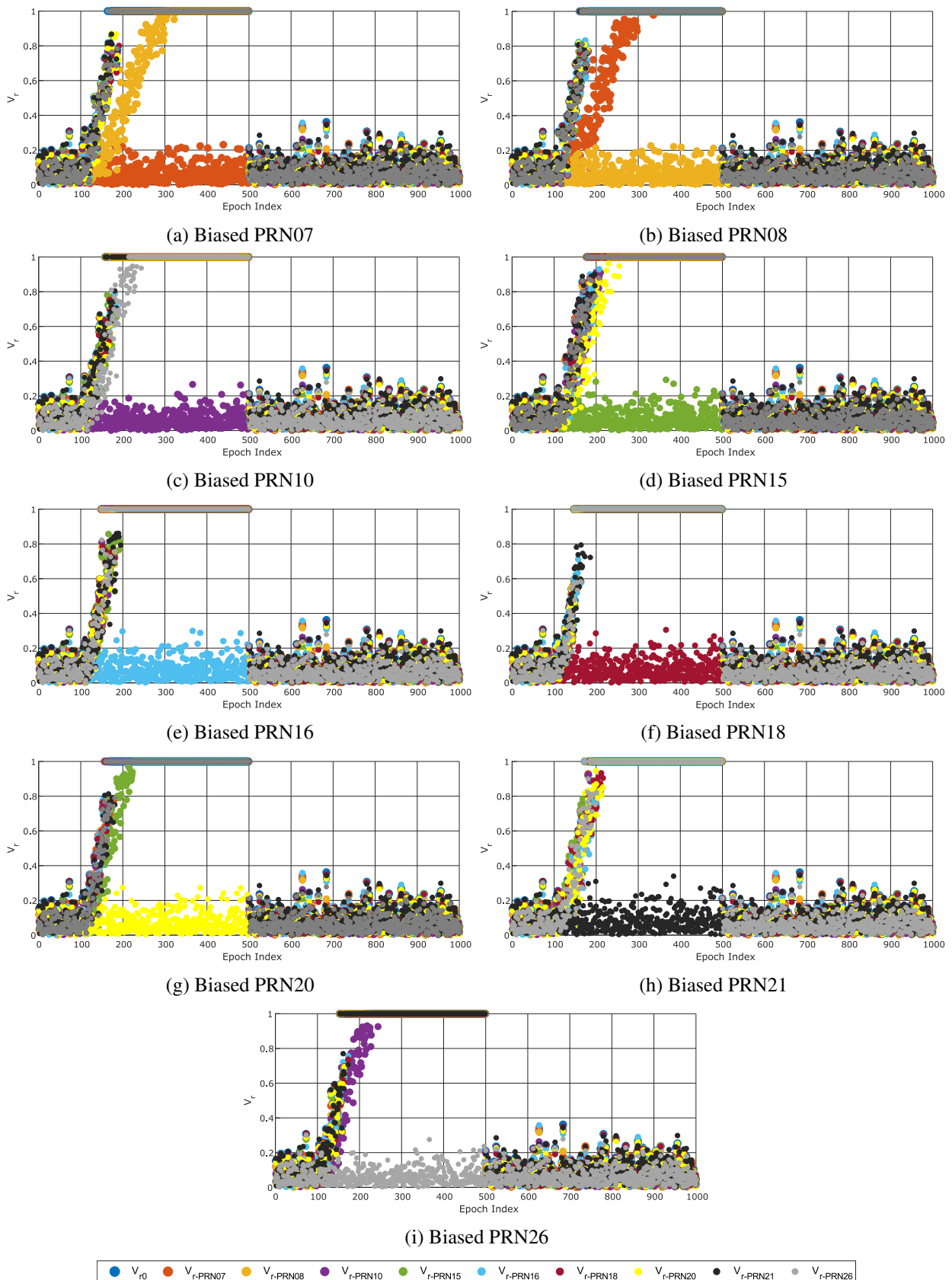


Figure 4.9: Superimposed consistency measures V_{r0} and V_{ri} for scenario 1, $\Delta = 3$ m, $\sigma = 1$ m for different biased satellites.

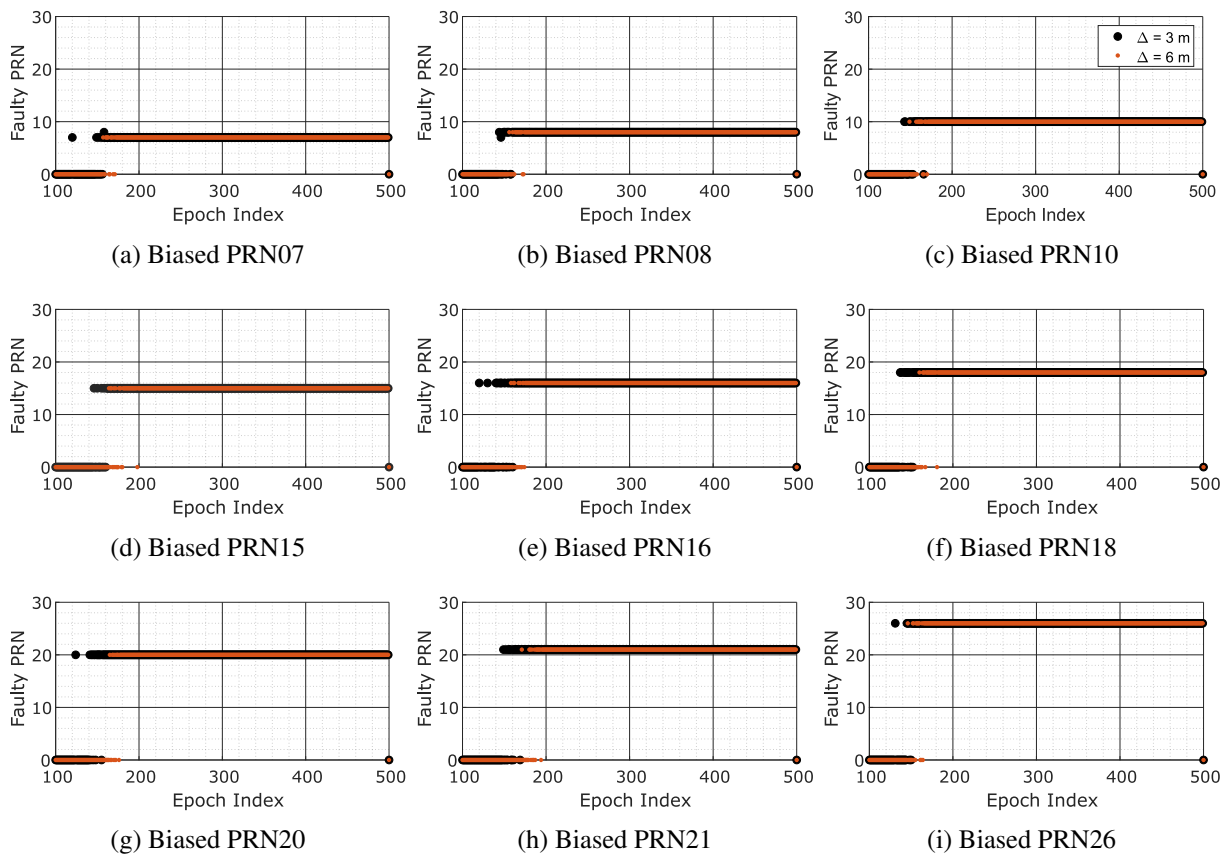


Figure 4.10: Polytope hypothesis test on V_{r_0} and V_{r_i} for scenario 1, $\Delta = 3$ m and $\Delta = 6$ m, $\sigma = 1$ m for different biased satellites. Zero indicates that no bias was detected, i.e. PGT is passed.

There is a region after the first detected bias where some epochs are detected as faults and other epochs passed the PGT. After this region, all biased epochs failed the PGT. For instance, when $\Delta = 10$ the region of intersection starts at epoch 155 and ends at epoch 187 ($\delta = 4.4$ m to 6.96 m) while for $\Delta = 20$ the region of intersection is from epoch 190 to epoch 212 ($\delta = 7.2$ m to 8.96 m). Moreover the intersection region is larger for smaller Δ , e.g. $\Delta = 10$ has 2.56 m ramp bias (32 epochs) while $\Delta = 20$ has 1.76 m ramp bias (22 epochs). This is due to the higher scatter in V_{r_0} for lower Δ , i.e. the MDB becomes smaller.

In addition to that, figure (4.11) gives a clear idea of how the minimum detectable bias decreases from just considering empty sets as criteria of detected bias to the application of PGT as criteria, especially for larger OIBs. As an illustration, for $\Delta = 20$ there is no empty polytope at all and just taking the empty set as detection criteria, no bias can be detected in the range of 0 to 32 m, while when applying PGT all biases greater than 8.96 m are detected and the biases between 7.2 m and 8.96 m are partially detected. Biases smaller than 7.2 meter are not detected at all for $\Delta = 20$. Taking another example such as $\Delta = 10$ m, the polytope starts showing empty sets at epoch 325, i.e. $\delta = 18$ m, while the smallest detected bias by polytope global test PGT is $\delta 5.12$ m. So, the MDB is decreased by 13.6 m. The same holds for smaller observation interval bounds, but the decrease in the minimum detectable bias is smaller since for smaller Δ the polytope gets empty at smaller biases.

Table 4.2 depicts the smallest detected bias in each PRN of scenario 1 for $\Delta = 3$ m and $\Delta = 6$ m, i.e., the simulation from figure (4.16). The theoretical PMDB and its upper bound ZMDB are the MDB of the consistency measures V_{r_0} , while the smallest detected bias in Table 4.2 is the actual detected bias by the PGT and PLT which is always smaller than the PMDB. In some cases the polytope detection and isolation algorithm is able to detect biases even smaller than the OIB, e.g., for $\Delta = 3$, the smallest detected biases in PRN16, PRN20, and PRN26 are 1.6 m, 1.92 m, and 2.48 m, respectively.

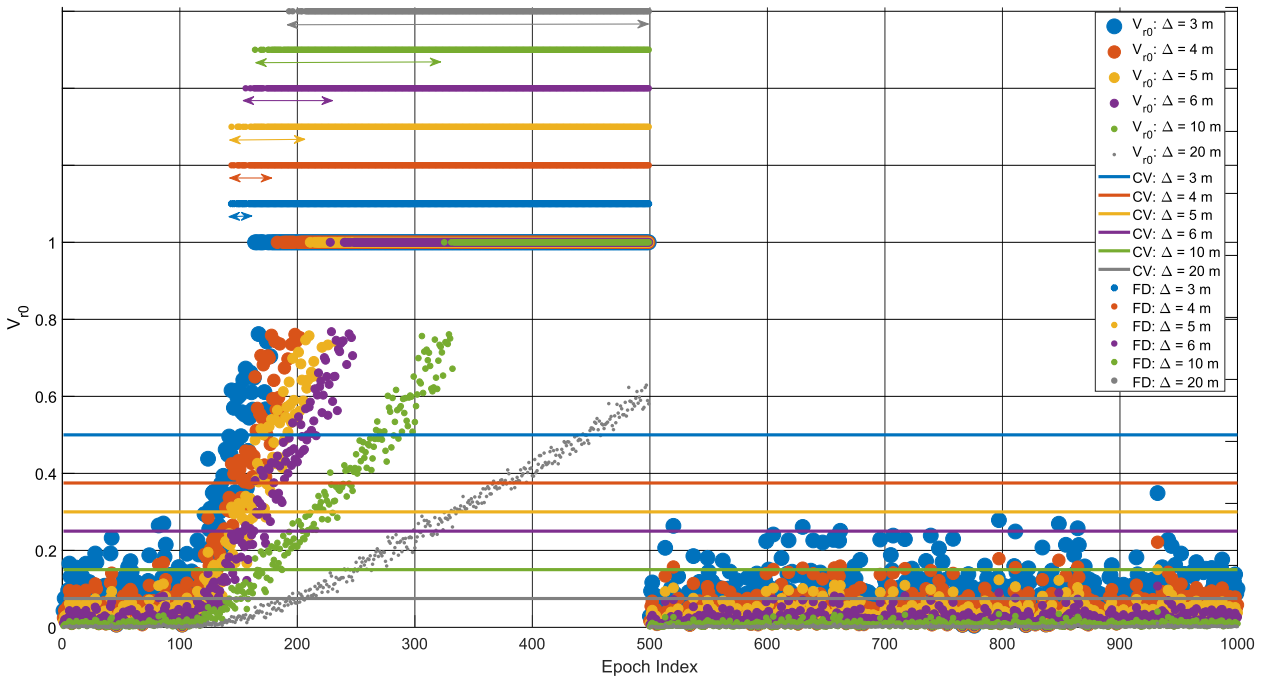


Figure 4.11: Polytope global test PGT on V_{r_0} for scenario 1 for biased satellite PRN08, the observation interval bound is $\Delta = 3, 4, 5, 6, 10, 20$ m, and the observation noise $\sigma = 1$ m. The fault detection decision and critical value for each Δ are indicated by asterisk and solid lines, respectively. The double arrows indicate the region where PLT is failed while the polytope is not empty.

Table 4.2: Smallest detected bias δ_{min} in meters for each PRN in scenario 1 for $\Delta = 3$ m and $\Delta = 6$ m.

Biased PRN	PRN07	PRN08	PRN10	PRN15	PRN16	PRN18	PRN20	PRN21	PRN26
MDB $\Delta = 3$ m	3.92	3.52	3.44	3.68	1.60	2.96	1.92	3.92	2.48
MDB $\Delta = 6$ m	4.56	3.68	3.92	5.12	4.64	4.80	5.20	5.68	3.68
ZMDB $\Delta = 3$ m	9.86	7.72	14.25	13.40	11.60	8.97	8.42	19.34	7.94
ZMDB $\Delta = 6$ m	19.73	15.45	28.50	16.81	23.20	17.95	16.84	38.68	15.88

Figure 4.12 depicts the superimposed consistency measures V_{r_0} and V_{r_i} for scenario 4, observation interval bound $\Delta = 3$ m and all biased satellites, i.e. the same analysis from figure 4.9 but for a different scenario. Scenario 4 is slightly better than scenario 1 in terms of geometry and the number of satellites. Also, here the result is very similar to scenario 1 where V_{r_0} and V_{r_i} start increasing with the bias except one of the sets without the biased satellite. For instance, let us have a look at figure 4.12j where all sets contain the biased satellite PRN27 except the set indicated by magenta color. The last set $V_{r_{PRN27}}$ shows the same behavior for all epochs as expected while all the other sets start to change their behaviors when the bias is introduced until they become empty at some point. The other subplots, i.e. the cases with different biased satellites show also the same behaviors as the case PRN27 is biased. Only the set without a biased satellite shows a nominal behavior in the biased region (see other subplots and relate to the color in the legend).

Figure 4.13 depicts the results of the PGT and PLT of scenario 4 for two different OIBs $\Delta = 3$ m and $\Delta = 6$ m. First, PGT is performed for $\kappa_p = 1.5$, then the PLT is performed on the failed epochs with the same κ_p , i.e. $CV_{V_{r_0}} = CV_{V_{r_i}}$. Also, here in scenario 1, for $\Delta = 3$ m the detection starts at smaller biases than for $\Delta = 6$ m. In this specific scenario, there was no false detection at all and the isolation processes succeed 100 % for both cases $\Delta = 3$ m and $\Delta = 6$ m.

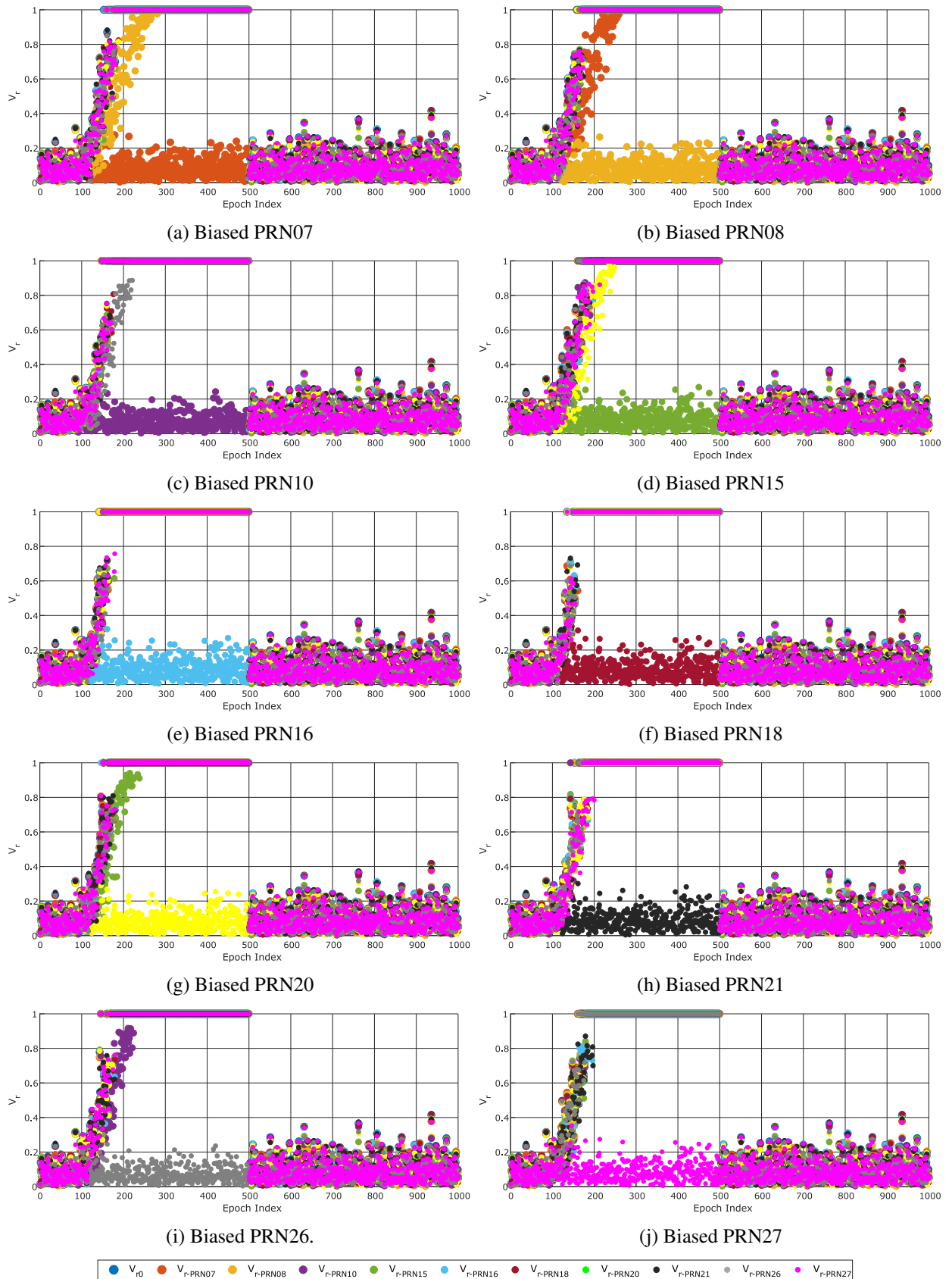


Figure 4.12: Superimposed consistency measures V_{r0} and V_{r_i} for scenario 4, $\Delta = 3$ m, $\sigma = 1$ m for different biased satellites.

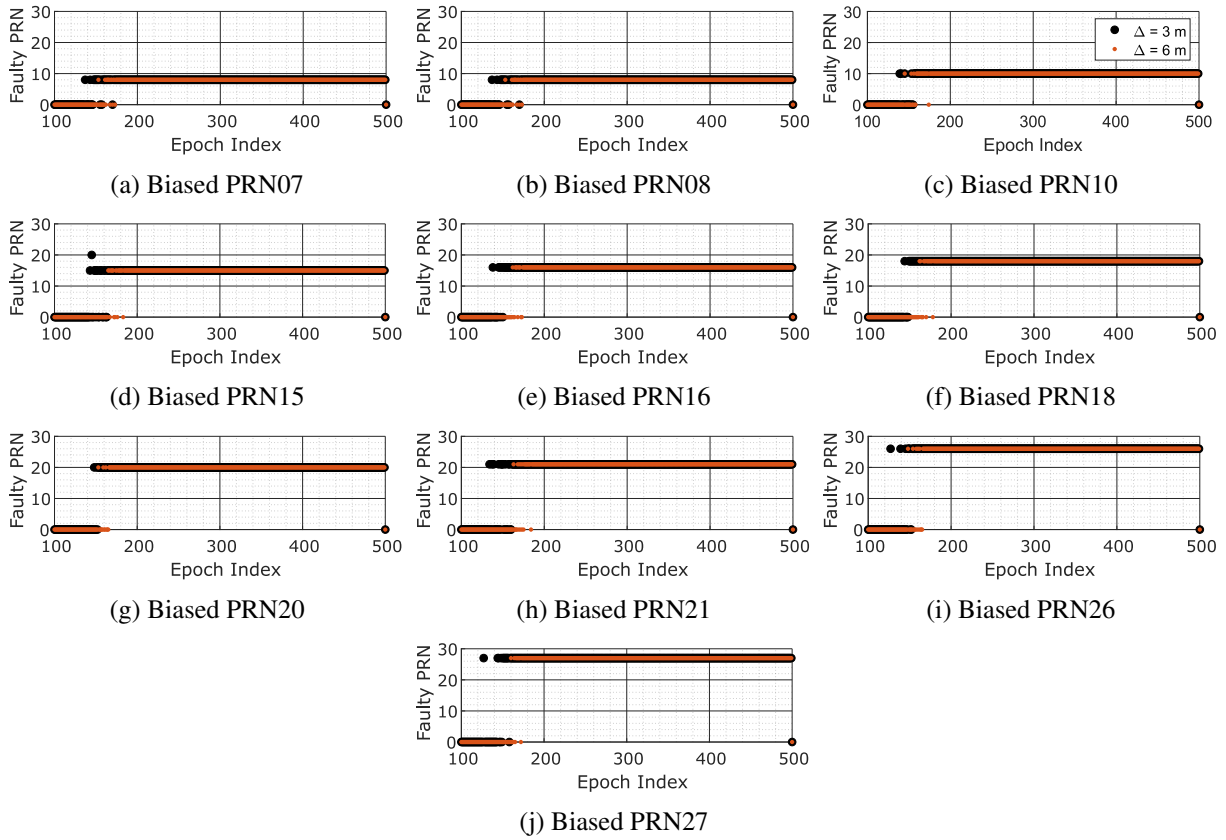


Figure 4.13: Polytope hypothesis test on V_{r_0} and V_{r_i} for scenario 4, $\Delta = 3$ m and $\Delta = 6$ m, $\sigma = 1$ m for different biased satellites. Zero indicates that no bias was detected, i.e. PGT is passed.

4.5.2 Critical Detection Scenarios - Correlated Satellites

Again the same analysis of the polytope global test PGT and polytope local test PLT is done on scenario 3 where the geometry is considered good in terms of GDOP but the number of satellites in view is quite low with 6 satellites. First, let us have a look at the consistency measures V_{r_0} and V_{r_i} . Figure 4.14 depicts the consistency measures for different biased satellites, where the observation interval bound is $\Delta = 3$ m. For different biased satellites the consistency measures V_{r_0} shows similar behavior since the geometry is the same and the only change is the biased satellite. So, the polytope global test PGT is expected to work well.

Going back to figure 4.7c, the consistency measures V_{r_0} of the cases PRN07 and PRN20 are biased and show slightly lower values than the other cases in the biased region. This indicates that these two satellites could be more difficult to be detected than the others.

In figure 4.14a where the biased satellite is PRN07, the consistency measures $V_{r_{PRN07}}$ and $V_{r_{PRN20}}$ show similar values of the consistency measures in the biased region, while the consistency measures of the other satellites show the expected behavior. This makes it difficult to isolate one from the other (PRN07 and PRN20), so false detection is expected. The consistency measures $V_{r_{PRN07}}$ are expected to show low values in the biased region since the biased satellite PRN07 is excluded for the polytope computation, while the consistency measures $V_{r_{PRN20}}$ are expected to increase with increasing the bias in PRN07 since in this case PRN07 is included in the computation. The consistency measures $V_{r_{PRN20}}$ need a bias in PRN07 larger than 32 m to get an empty set. This is due to the geometry of the satellites of the set (\mathbb{S}_{PRN07}) which contains 4 satellites in quadrant III and IV, only PRN20 in quadrant I and no satellite in quadrant II. So the uncertainty of the polytope of this set is very large in the PRN20 LOS direction. The same issue happens to the set (\mathbb{S}_{PRN20}), i.e. all satellites except PRN20. The uncertainty in the PRN07 LOS direction is very large since it is the only satellite in quadrant II. Indeed, $V_{r_{PRN07}}$ and $V_{r_{PRN20}}$ show also similar behavior for set (\mathbb{S}_{PRN20}), i.e., when PRN20 is biased, see figure 4.14d. Moreover, in the first 150 biased epochs approximately, i.e. the bias

between $\delta = 0.08$ m and $\delta = 12$ m, the consistency measures V_{r_i} for all cases shows low values, so in this region, it is not easy to isolate the real biased satellite.

Analyzing the other biased satellite cases, the correlation between different satellites can be identified. As we just have seen, PRN07 and PRN20 are correlated due to their positions and geometry of the rest of the satellites. Also, PRN16 and PRN18 show a similar correlation but at a lower level than PRN07 and PRN20. When PRN16 and PRN18 have biases, the small values of the consistency measures in the biased region are in both cases $V_{r_{PRN16}}$ and $V_{r_{PRN18}}$ while the other V_{r_i} shows larger values. Similar behavior is also shown in PRN10 and PRN26. To understand why these specific satellites are correlated we look back to the sky plot in figure 4.1. PRN07 and PRN20 are the only satellites located at quadrant II and quadrant I, respectively. So it is easy to see the correlation between them in terms of polytope computation and related consistency measures. PRN16 and PRN18 are located at quadrant III and quadrant IV, respectively, and both are at high elevations. The same applies to PRN10 and PRN26. Therefore, the satellites located at the adjacent quadrant at a similar elevation have a higher correlation between each other than the rest of the satellites. Definitely, the overall correlation depends on the whole satellite geometry. For instance, PRN07 and PRN20 have a higher correlation than the other couple of satellites since they are the only satellites at quadrant I and II, while for another couple of satellites there are still other satellites at quadrant III and quadrant IV.

Figure 4.15 shows the polytope global and local test applied to scenario 6 for two different OIBs $\Delta = 3$ m and $\Delta = 6$ m. If the faulty PRN is flagged zero, it means that the polytope global test is passed and no local test is applied, otherwise the faulty PRN is indicated. First analyzing the case $\Delta = 3$ m, i.e., the tests were applied on the results in figure 4.14. As expected from the consistency measures, the isolation between different pairs of satellites was not successful. For example, when PRN07 is biased, at the beginning of the biased region two PRN were wrongly detected: PRN20 and PRN18. After a few epochs in the biased region, the wrong isolation was only between PRN07 and PRN20. Correspondingly, when PRN20 is biased, there is wrong isolation between PRN20 and PRN07 for the whole biased region and only a few wrong isolation with PRN10 at the beginning of the biased region. In the same fashion, for the cases PRN10 and PRN26 are biased, there is wrong isolation between them, but in this case, only a few epochs were wrongly isolated for small biases, less than 12.4 m. For biases greater than 12.4 m, the isolation was successful. Furthermore, there was no wrong isolation with other satellites. In like manner, when PRN16 and PRN 18 are biased, there is wrong isolation between them for a large number of epochs, especially for small biases. In case PRN18 is the biased satellite, there are few wrong isolation with PNR20 at the beginning of the biased region as well, while in the case PRN16 is biased the only wrong isolation was with PRN18.

Applying larger OIBs, i.e. $\Delta = 6$ m, the detection process degrades, while the isolation process is enhanced. That the detection is degraded means that the detection starts at slightly larger biases for all cases (red ($\Delta = 6$ m) plot has more zeros than the black plot ($\Delta = 3$ m)). The isolation process is enhanced in a way that only the correlated pairs of satellites are involved, where missed isolation happened, except at one epoch when PRN18 is biased where the wrong isolation is between PRN18 and PRN16 and at one epoch where the faulty satellite was PRN20. For the other two correlated pairs of satellites, i.e., (PRN07, PRN20) and (PRN10, PRN26), the wrong isolation was only between the corresponding correlated satellite.

The isolation or identification of the biased satellites is done by taking the minimum V_{r_i} of the satellites that did not pass the test since the hypothesis is to have only one faulty satellite. However, when the wrong isolation occurs, not only the isolated satellite failed the polytope local test, also the truly biased satellite failed the local test, but its consistency measures are slightly larger than the other failed satellite. For instance, when $\Delta = 6$ m and PRN07 is biased, for all the wrong isolation epochs, i.e, PRN20 declared faulty, also PRN07 failed the local test but $V_{r_{PRN07}} > V_{r_{PRN20}}$ so the identified faulty satellite is PRN20. The isolation can be programmed in a way that every satellite that fails the local test is considered a faulty one and not only the minimum V_{r_i} . In this particular case, i.e., scenario 2, $\Delta = 6$ m, and biased PRN07, there will be more than one faulty satellite. One will be the truly biased satellite and the other will be the correlated one. So, we will have true identification all the time and also the wrong detection, but not only wrong detections.

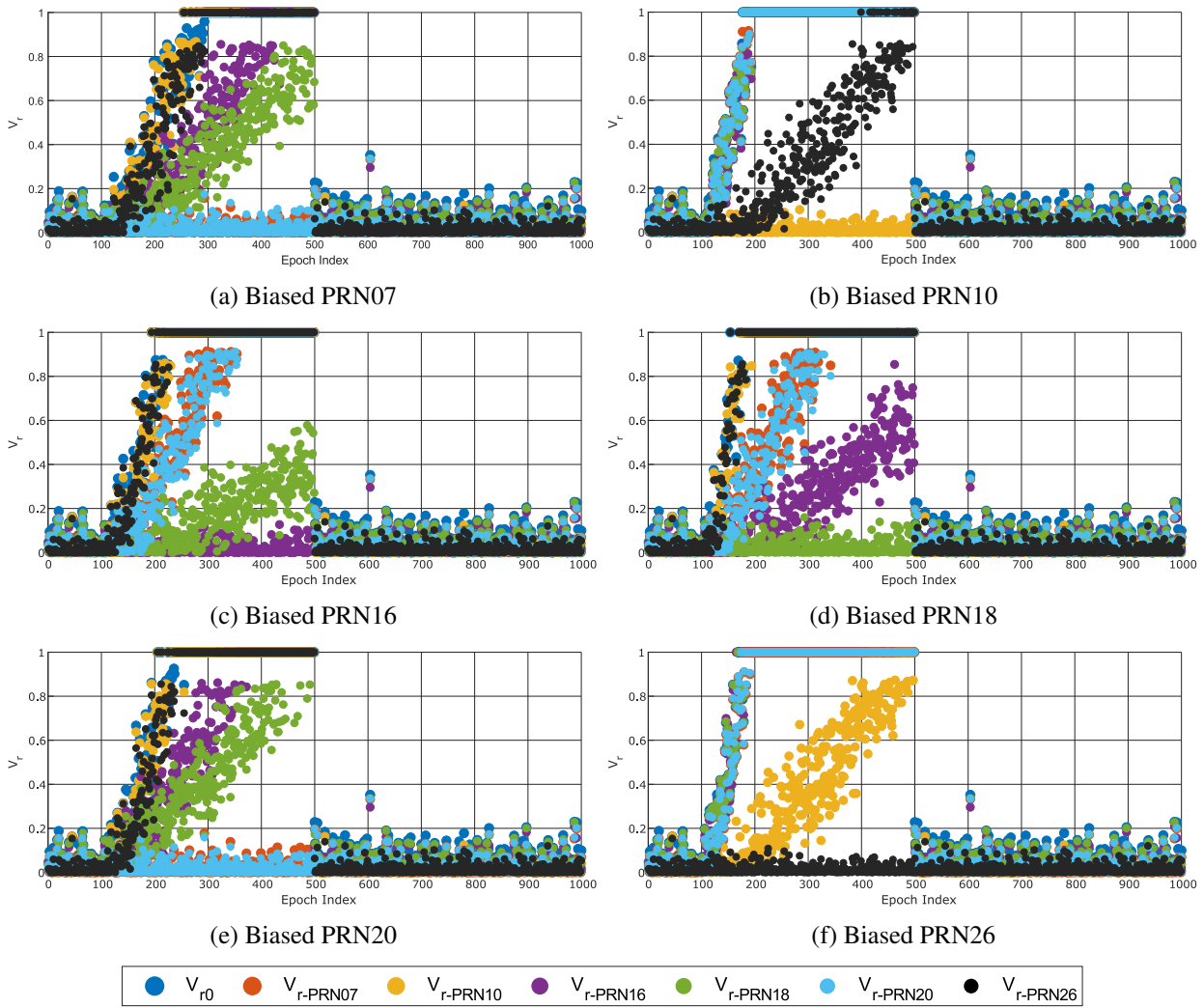


Figure 4.14: Superimposed consistency measures V_{r0} and V_{ri} for scenario 3, $\Delta = 3$ m, $\sigma = 1$ m for different biased satellites.

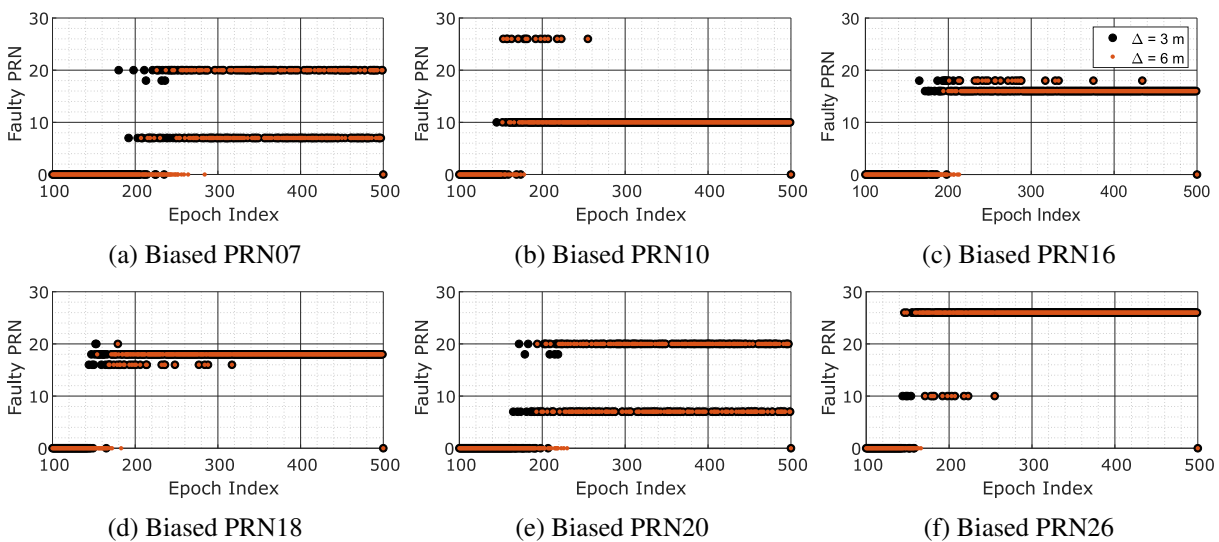


Figure 4.15: Polytope hypothesis test on V_{r0} and V_{ri} for scenario 3, $\Delta = 3$ m and $\Delta = 6$ m, $\sigma = 1$ m for different biased satellites. Zero indicates that no bias was detected, i.e. PGT is passed.

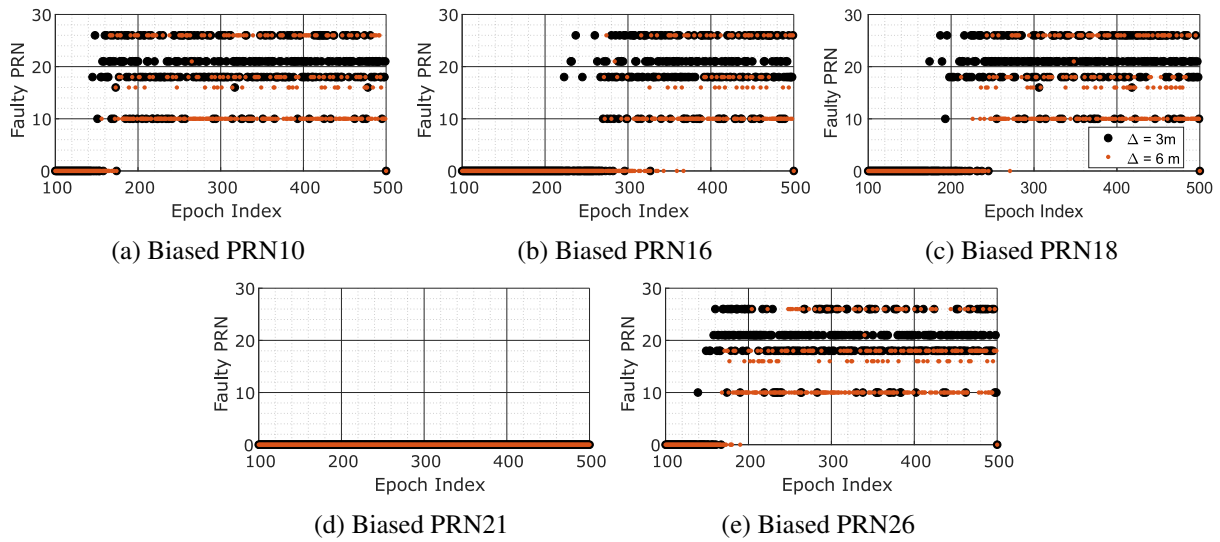


Figure 4.16: Polytope hypothesis test on V_{r_0} and V_{r_i} for scenario 6, $\Delta = 3$ m and $\Delta = 6$ m, $\sigma = 1$ m for different biased satellites. Zero indicates that no bias was detected, i.e. PGT is passed.

4.5.3 Critical Detection Scenarios - Bad Geometry

Now, we perform the polytope global test PGT and polytope local test PLT on scenario 6 which has only five satellites in view. Figure 4.16 depicts the test for two cases, $\Delta = 3$ m and $\Delta = 6$ m. This time, the polytope global test still performs well and it is able to detect quite small biases in all cases except when PRN21 is biased, see figure 4.16d. Looking back to figure 4.7f, i.e. consistency measures V_{r_0} of scenario 6 for different biased satellites, we can see that the consistency measures V_{r_0} for the set \mathbb{S}_{PRN21} (grey dots) have low values in the biased region. As explained in section 4.4.3, the PMDB of PRN21 is large due to the specific geometry of scenario 6 and specifically, due to the location of PRN21 w.r.t. the other satellites. So, it is expected to not detect any bias in case PRN21 is the biased satellite. If biases larger than the PMDB are applied to the observation of PRN21, it will be detected via polytope global test PGT. On the other hand, the polytope local test PLT did not perform well, where almost half of the time when the PGT failed, the detected satellite is the wrong one. This is due to the increasing polytope volume when it is computed with only four satellites in view. The consistency measures V_{r_i} will have low values for all sets and it is almost impossible to identify which one is the biased observation. However, in the probabilistic approaches the local test, i.e. the identification of faulty observation cannot be performed since it needs at least 2 as a degree of freedom.

Scenarios 2, 5, and 7 have been not included in this analysis, however, they show similar results. Scenarios 2 and 5 show results like scenarios 3 and 4, almost no wrong isolation, while scenario 7 shows results like scenario 3: excellent detection with many wrong isolation cases.

4.6 Probabilistic Test Statistic Results

In this section, the same Monte Carlo simulation that was performed on the polytopic and zonotopic integrity approach is conducted on the probabilistic approaches, namely residual-based RAIM and the solution separation RAIM.

4.6.1 Results of Probabilistic Test Statistics

Figure 4.17 depicts the RB test statistic with two different PFA $\alpha = 0.001$, $\alpha = 0.00001$ while PMD is fixed to $\beta = 0.001$ for scenario 1. The performance of the RB test is very good in general. However, for $\alpha = 0.001$ there are two false identifications, one when the biased satellite is PRN07 and the other one is for biased satellites PRN08.

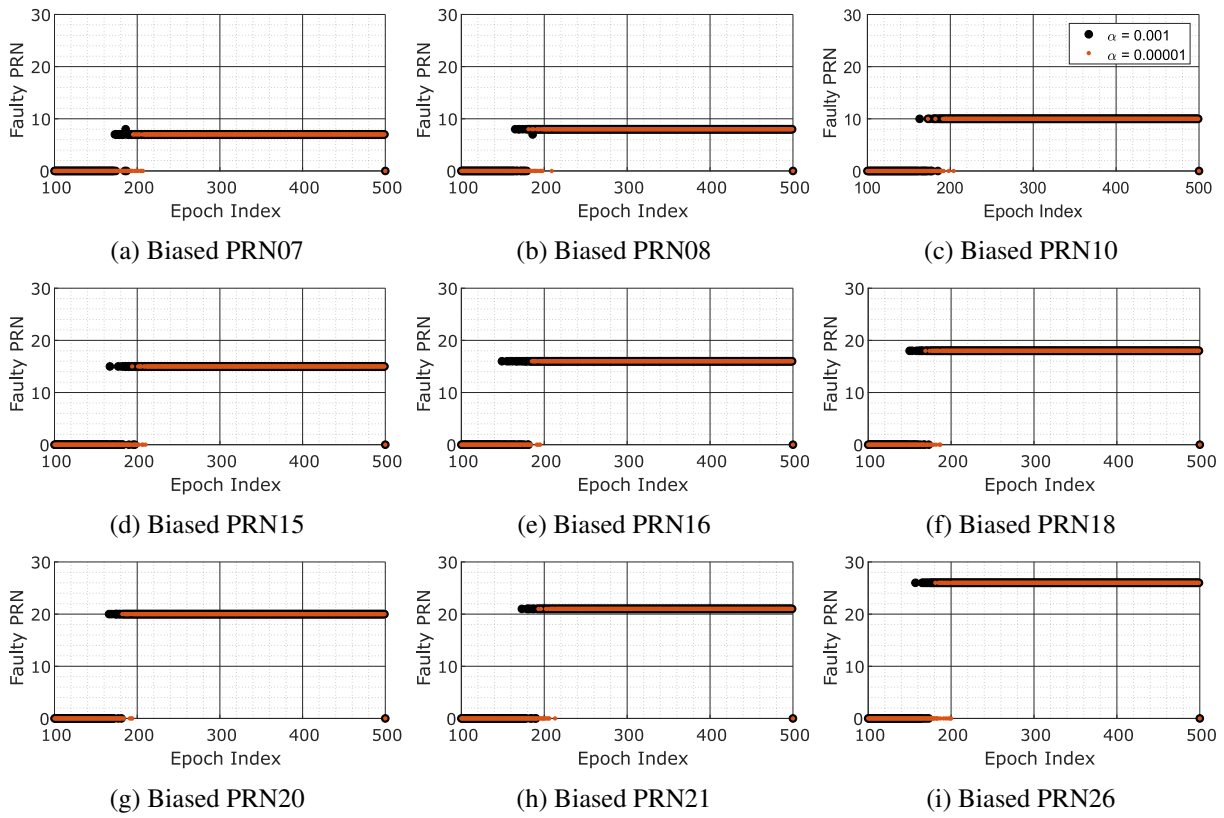


Figure 4.17: Residual-based test statistics for scenario 1 when $\alpha = 0.001$, $\alpha = 0.00001$, and $\beta = 0.001$. Zero indicates that no bias was detected, i.e. RB test is passed.

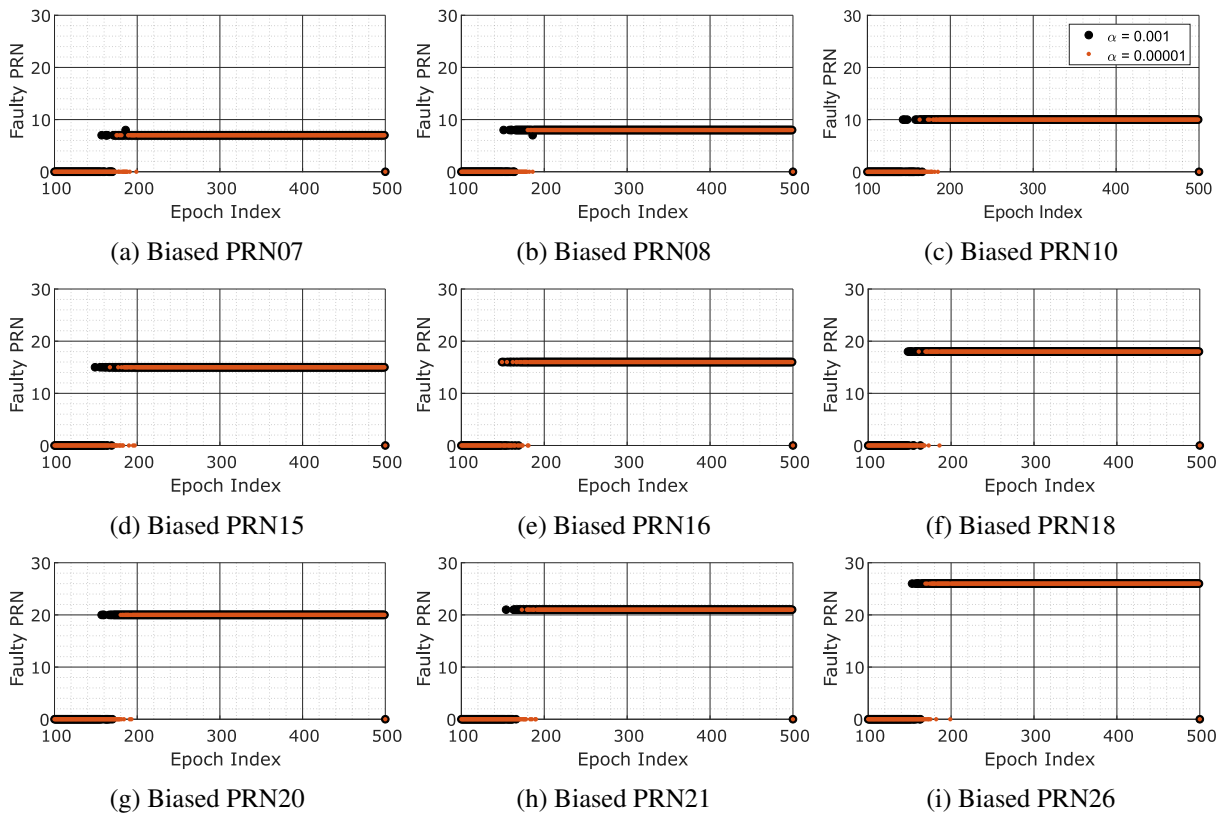


Figure 4.18: Solution separation test statistics for scenario 1 when $\alpha = 0.001$, $\alpha = 0.00001$, and $\beta = 0.001$. Zero indicates that no bias was detected, i.e. SS test is passed.

On the other hand, for $\alpha = 0.00001$ all the detection and exclusion processes are 100 % correct but the detection starts at higher values of the bias than for $\alpha = 0.001$, since the MDB depends on selected PFA value and it increases as α decreases as we have seen in section 2.3.4. For instance, in the case PRN07 is the biased satellite, the fault detection starts at bias $\delta = 5.84$ m and $\delta = 7.6$ m for $\alpha = 0.001$ and $\alpha = 0.00001$, respectively.

Figure 4.18 depicts the SS test statistic with two different PFA $\alpha = 0.001$, $\alpha = 0.00001$ while PMD is fixed to $\beta = 0.001$ for scenario 1. Similarly to the RB test statistic, there are only two false identifications of the biased satellite in case $\alpha = 0.001$: one when the biased satellite is PRN07 and the other one is for the biased satellite PRN08. There is no false identification in the case $\alpha = 0.00001$. However, the main difference from the RB test is the MDB, where the SS test detects smaller biases than RB for different biased satellites and for both cases $\alpha = 0.001$ and $\alpha = 0.00001$. When PRN07 is biased, the MDB of SS test is $\delta = 4.56$ m and $\delta = 6$ m for $\alpha = 0.001$ and $\alpha = 0.00001$, respectively.

4.7 Comparison Between Probabilistic Tests and Polytopal Test

4.7.1 Good Satellite Geometry

Comparing RB and SS tests to the PGT in scenario 1, PGT has also the same performance in terms of detection and identification processes where also in this case two false identifications occur. Regardless, PGT is able to detect biases smaller than the detected biases in both probabilistic test statistics RB and SS. For a fair comparison between all tests, the OIBs $\Delta = 3$ and $\Delta = 6$ with $\kappa_p = 1.5$ of the PGT test were set which corresponds to the probabilistic tests with $\alpha = 0.001$ and $\alpha = 0.00001$, respectively. The MDB for the polytope test in scenario 1 and biased satellite PRN07 is 2.56 m and 4.56 m for $\Delta = 3$ and $\Delta = 6$, respectively. These values are even smaller than the one of the SS test statistic.

To have an overview for different biased satellites in scenario 1, the MDBs of all tests are shown in figure 4.19. The MDB of PGT is smaller than the MDB of the SS test and the one of SS test is smaller than the the MDB of RB test. However, for some specific biased satellites the MDB of PGT and SS have the same values, e.g., $\Delta = 3$ m and $\alpha = 0.001$ for biased satellites PRN10 and PRN15 and $\Delta = 6$ m and $\alpha = 0.00001$ for biased satellites PRN15, PRN16 and PRN18. The same findings are true for RB and SS tests: they have equal MDB when $\alpha = 0.001$ and the biased satellite is PRN16. The overall analysis of MDB in terms of its mean value for different biased satellites is 5.0 m, 4.09 m, and 3.22 m when $\Delta = 3$ m and $\alpha = 0.001$ and 6.69 m, 5.48 m, and 4.56.2 m when $\Delta = 6$ m and $\alpha = 0.00001$ for RB, SS, and PGT, respectively. The PGT increases the performance in terms of MDB by 22 % and 35 % for SS and RB tests, respectively.

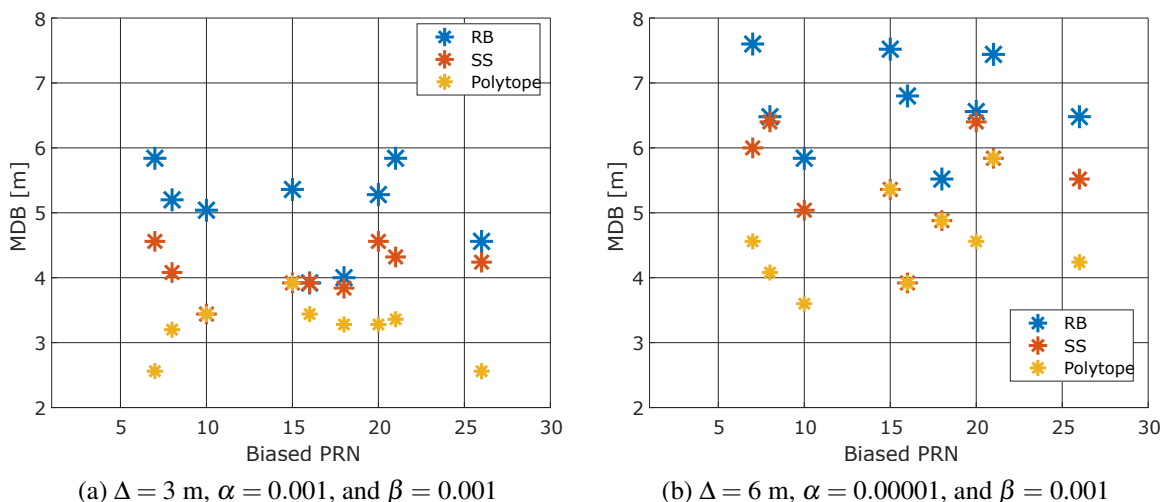


Figure 4.19: MDB of RB, SS, and PGT for different biased satellites for scenario 1.

4.7.2 Bad Satellite Geometry

Now the same analysis of the tests PLT, SS and RB is performed for scenario 3 where the geometry is considered intermediate with only 6 satellites in view. Figure (4.20) depicts the RB test statistic for different biased satellites at a time and figure (4.21) depicts SS test statistic. Also here, 2 values of PFA are applied $\alpha = 0.001$ and $\alpha = 0.00001$ while the PMD is kept the same $\beta = 0.001$. In this scenario there are many wrong identifications of the biased satellite in both tests with very similar results, i.e. both tests have the same wrong identification when it happens. However, the RB has less wrong identifications than the SS test, especially when PRN16 is the biased satellite.

Comparing the probabilistic FDE to the PLT, the RB is very similar to the PLT and when there is a wrong identification, most of the time both methods have the same wrong identified PRN, see figure (4.15).

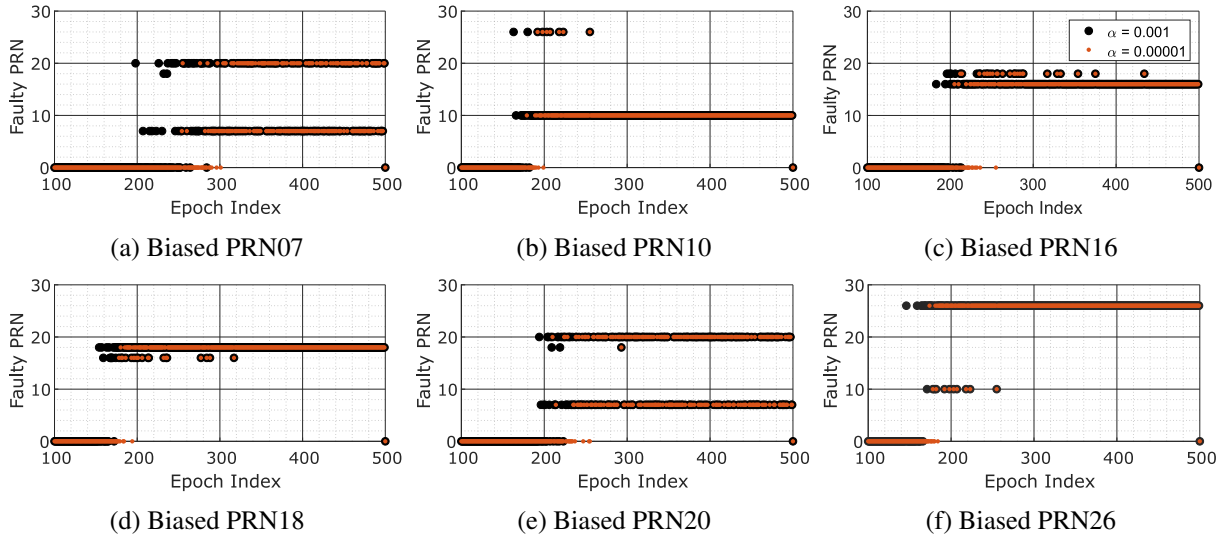


Figure 4.20: Residual-based test statistics for scenario 3 when $\alpha = 0.001$, $\alpha = 0.00001$, and $\beta = 0.001$.

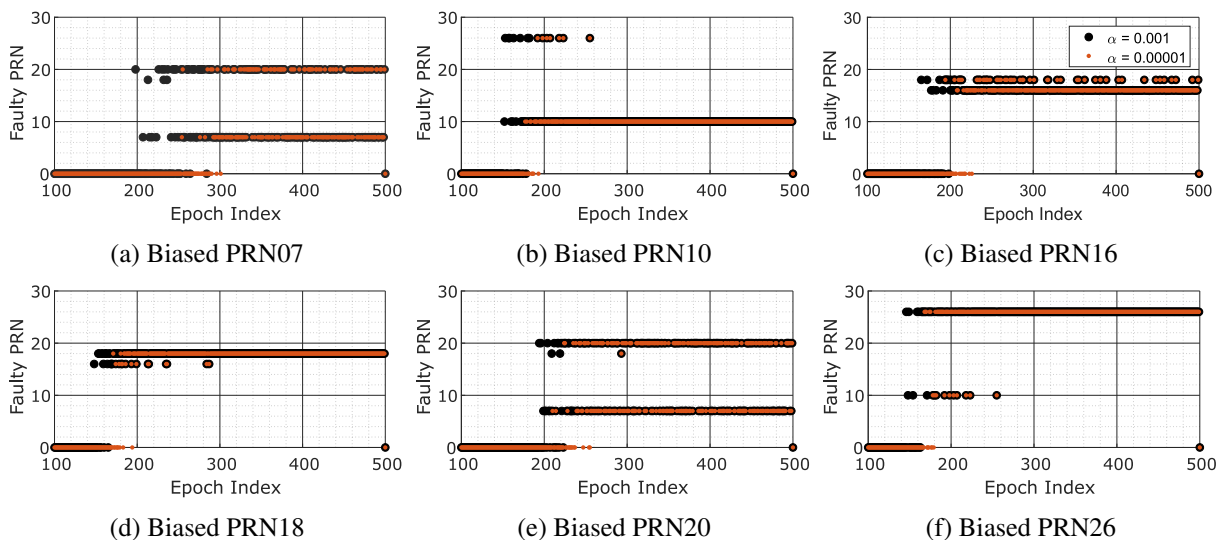


Figure 4.21: Solution separation test statistics for scenario 3 when $\alpha = 0.001$, $\alpha = 0.00001$, and $\beta = 0.001$.

To have a better quantitative analysis of scenario 3 for all tests, the number of detected faulty epochs and the number of the true identifications of the faulty epochs are reported in table 4.3, and the number of the wrong identification are reported in table (4.4) with test parameters: $\alpha = 0.001$, $\beta = 0.001$, $\Delta = 3$, and $\kappa_p = 1.5$. As expected, PGT detects more faults than the probabilistic approaches while the SS test detects more faults than the RB test. This is due to the fact that the MDB of PGT is smaller than the MDB of the SS test and the

MDB of the SS test is smaller than the MDB of the RB test as already shown in figure 4.19. The number of true identifications is also higher for the PLT except when PRN18 is biased. Then the SS test has the higher value of true identification, but PLT still has more true detections than the RB test.

In the wrong identifications, PLT has higher values than the other methods and this can be explained by the fact that PLT has a higher rate of detection than the other methods. Also, it starts the detection at smaller biases where wrong identifications are more likely to happen. However, for biased satellite PRN16 PLT has lower wrong identifications than the SS test. Also, the difference in the wrong identification between the PLT and the other tests is very small. On the other hand, depending on the biased satellite, SS could have smaller or higher wrong identifications than RB test. For example, when PRN07 is biased SS test has less wrong identifications than RB test and when PRN10 is biased SS test has more wrong identification than RB test. Figure 4.22 depicts the results of table 4.3 and table 4.4 for better visualization.

Table 4.3: Number of detected faults and number of true identification for RB, SS, and PDP local and global tests for scenario 3 with test parameters: $\alpha = 0.001$, $\beta = 0.001$, $\Delta = 3$, and $\kappa_p = 1.5$.

Biased PRN	RB-GT	RB-LT	SS-GT	SS-LT	PDP-GT	PDP-LT
	Detection	True Idn	Detection	True Idn	Detection	True Idn
PRN07	260	141	262	150	291	159
PRN10	327	318	335	321	344	329
PRN16	300	270	313	251	320	288
PRN18	337	313	344	325	352	319
PRN20	295	158	295	149	316	165
PRN26	337	326	342	329	349	334

(GL) denotes global test, (LT) denotes local test and (Idn) denotes identification.

Table 4.4: Number of detected faults and number of wrong identification for RB, SS, and PDP local and global tests for scenario 3 with test parameters: $\alpha = 0.001$, $\beta = 0.001$, $\Delta = 3$, and $\kappa_p = 1.5$.

Biased PRN	RB-GT	RB-LT	SS-GT	SS-LT	PDP-GT	PDP-LT
	Detection	wrong Idn	Detection	wrong Idn	Detection	wrong Idn
PRN07	260	119	262	112	291	132
PRN10	327	9	335	14	344	15
PRN16	300	30	313	62	320	32
PRN18	337	24	344	19	352	33
PRN20	295	137	295	146	316	151
PRN26	337	11	342	13	349	15

(GL) denotes global test, (LT) denotes local test and (Idn) denotes identification.

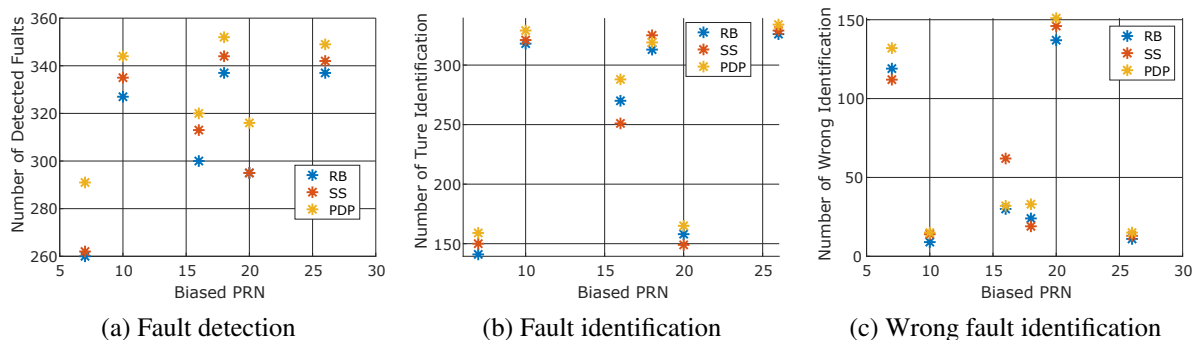


Figure 4.22: Number of fault detection and exclusion for RB, SS, and PDP local and global tests for scenario 3 with test parameters: $\alpha = 0.001$, $\beta = 0.001$, $\Delta = 3$, and $\kappa_p = 1.5$

4.8 Analysis of Protection Levels

To complete the integrity analysis of the Monte Carlo simulation, analysis of the protection level PL for all simulated scenarios and all methods is carried out in terms of simplified Stanford diagrams. We mean by simplified Stanford diagram, the diagram is shown without assigning any alert limit AL, since the AL is different from one application to another. However, before analyzing the protection level by means of a Stanford diagram, let us study the behavior of the polytopal protection level for different geometry and observation interval bounds.

4.8.1 Zonotopal Horizontal and Vertical Protection Levels

Figure 4.23 depicts the zonotopal HPL and VPL as a function of OIBs Δ for all seven simulated scenarios. Since the zonotope protection level depends only on the geometry and the observation interval bounds, one epoch of each scenario is enough to analyze the protection level for a different Δ . Both, the HPL and VPL increase linearly with the Δ for all scenarios. However, the increasing rate is different from one scenario to another, which depends on the quality of the geometry, i.e. the number of satellites in view and LOS. Note that the axes are not the same in figure 4.23. Scenario 4 has the lowest increasing rate, i.e. the lowest slope, which is expected since it has the best geometry in terms of GDOP values and number of satellites in view. Moreover, in scenario 4 the HPL is the lowest possible protection level that can be achieved since it is double the observation interval bound Δ . On the other hand, scenario 6 has the highest increasing rate with a very steep slope which is also expected due to the poor geometry.

For better visualization and comparison of the polytope PL of different scenarios, the superimposed HPL are depicted in figure 4.24a, and its zoom in the direction of HPL is depicted in figure 4.24b. Some scenarios have a very similar slope value of the HPL line while others have higher slopes. The ascending order of the slope of the HPL line is the same as the GDOP values, where scenarios 4, and 1 have quite identical slopes, scenarios 2 and 3 also have almost identical slopes, scenarios 5 and 7 have different slopes and greater than the first 4 scenarios, and the scenario 6 has a very large slope w.r.t. the others. In conclusion, having a GDOP value less than 3 provides a tight zonotopal protection level.

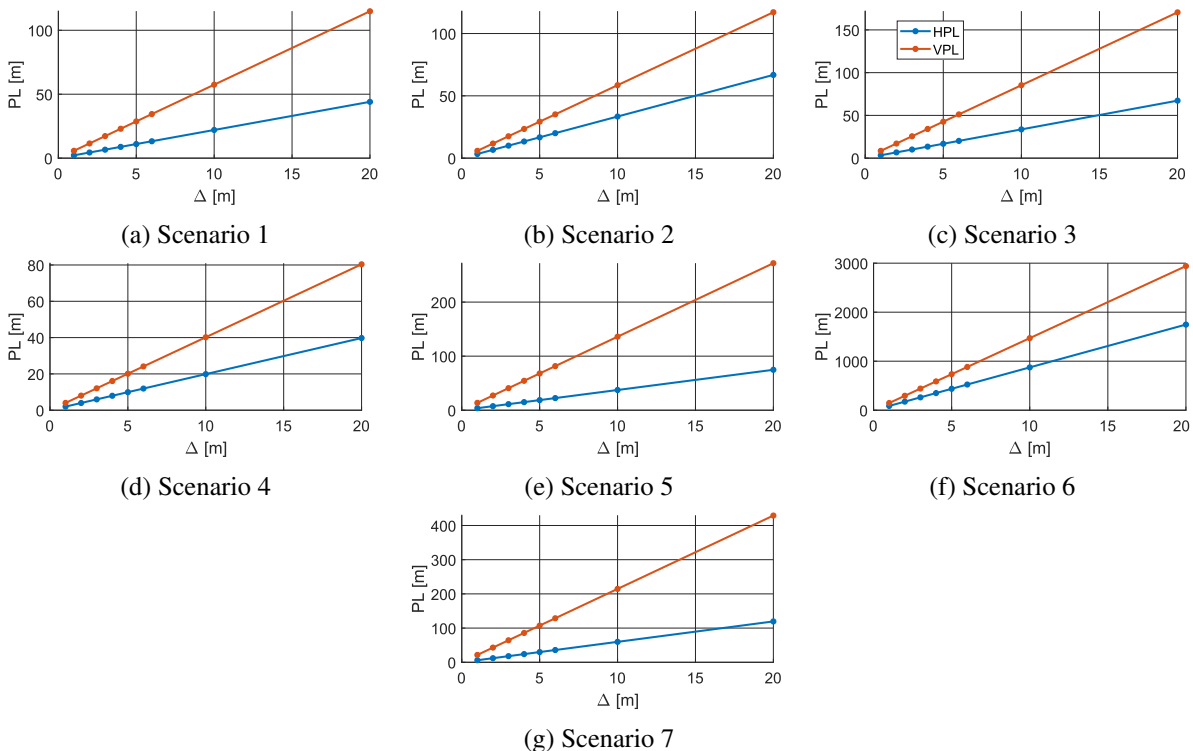


Figure 4.23: Polytopal horizontal and vertical protection level as a function of observation interval bound Δ for all scenarios.

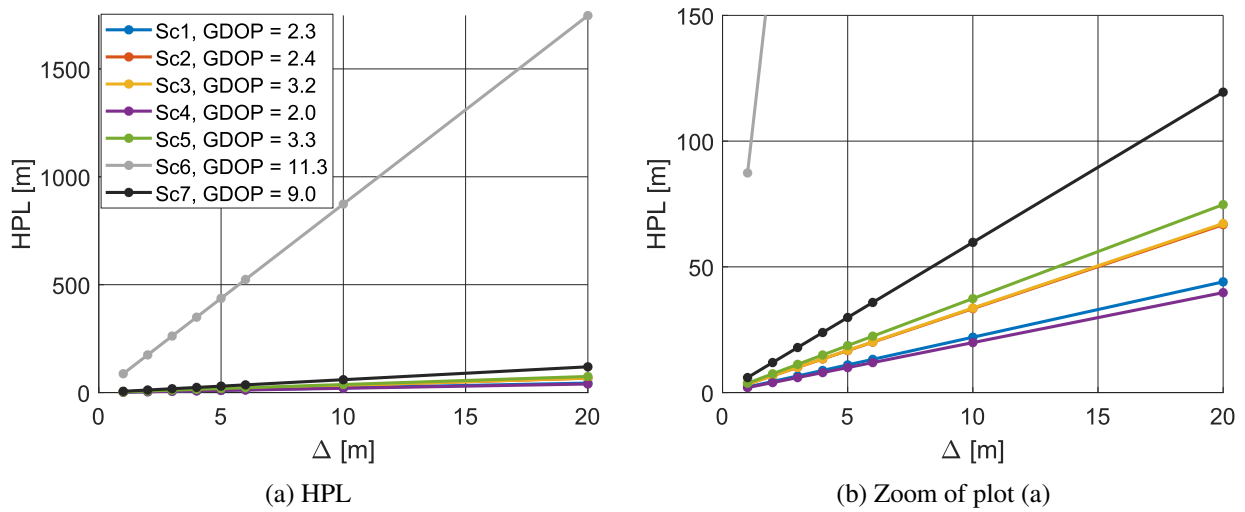


Figure 4.24: Superimposed polytopal horizontal protection level as a function of observation interval bound Δ for all scenarios.

Figure 4.25 depicts the simplified Stanford diagrams of the zonotopal protection level HPL and VPL of all simulated scenarios for biased satellites PRN10 and $\Delta = 3$ m. Note that the axes of the plots of different scenarios are not the same due to quite large differences from one scenario to another, e.g., scenario 4 has very low PL compared to scenario 6. We choose PRN10 to be the biased satellite since it is a common satellite for all scenarios. The values of HPL and VPL for each scenario does not change from epoch to another since the geometry and OIBs are the same.

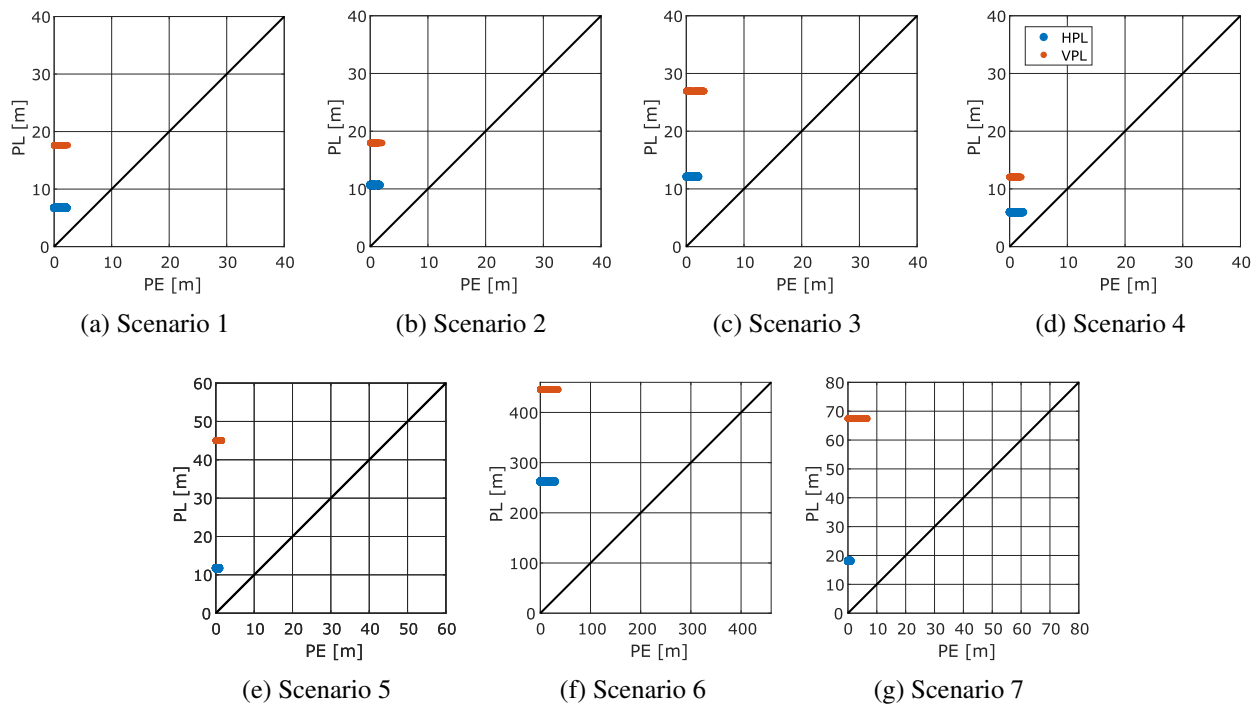


Figure 4.25: Stanford diagram: horizontal and vertical protection level of PDP and PLT test for all scenarios with biased PRN10 and with test parameters $\Delta = 3$ m and $\kappa_p = 1.5$.

For all scenarios, the protection level does not surpass the line $PL = PE$ which guarantees that the solution will never be in the misleading operation or hazardous misleading operation regions. If we would like lower values for the protection level, the only parameter that can be changed here is the OIB. In very good positioning geometry, the protection level could be equal or slightly bigger than twice the OIB, e.g. scenario 4. The minimum value of the zonotopal protection level is twice Δ and the maximum value depends on the

geometry of the satellite. In addition, in any detection and exclusion processes, i.e. no matter if the detection and exclusion are wrong or not, the protection level will never be below the straight-line $PL = PE$.

Applying smaller interval bounds provides a smaller protection level might lead to more empty sets depending on the quality of the observation, so the continuity will be lower. However, depending on the alert limit, having lower protection levels, the continuity and availability could be higher. So, it seems that applying small observation interval bounds is better for the integrity of the navigation system. Nevertheless, the values of the observation interval bounds should be consistent with observations, otherwise, the solution set will be empty most of the time. So we are restricted to the quality of the observations.

4.8.2 Statistical Based Horizontal and Vertical Protection Level

Figure (4.26) depicts the Stanford diagrams of the HPL and VPL of the RB test with test parameters $\alpha = 0.001$, $\beta = 0.001$, $\kappa_H = 6$, and $\kappa_V = 5.33$. $\alpha = 0.001$ and $\beta = 0.001$ are not involved in the computation of the PL and the RB test is only performed to exclude the faulty observation so that this protection level can be computed even if the RB test is not performed as the PDP protection level can be computed without performing PGT and PLT. The factors $\kappa_H = 6$, and $\kappa_V = 5.33$ are kept constant as recommended by, RTCA (2006). So, the only factor that changes the protection level is the geometry of the navigation problem and since the geometry for each scenario does not change, the protection level also does not change. Both HPL and VPL have quite small values, especially w.r.t. the polytope protection levels. However, in scenario 6 and scenario 7 the HPL is quite large due to the bad geometry in those scenarios. In addition, there are no weights applied on the observation in the LS which makes the co-factor matrix depend only on the geometry, otherwise the protection level would be quite different.

Also here, the protection level never surpasses the straight line $PL = PE$ due to the perfect situation with the assumption of having only one faulty satellite and the assumption of having *Gaussian* noise in the residuals hold. So, at least the global test can easily detect faults in case they exist. On the other hand, the position error is quite higher than the position error in the PDP approach, especially the vertical position error in scenarios 3 and 7.

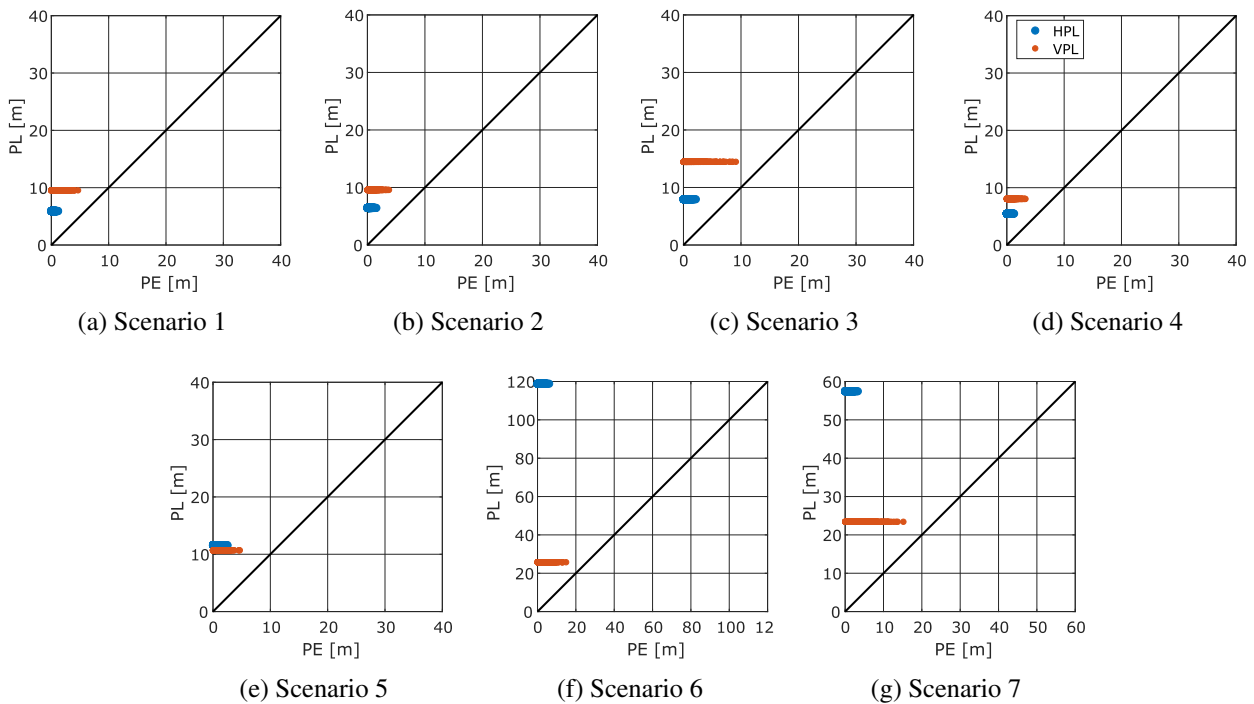


Figure 4.26: Stanford diagram: horizontal and vertical protection level of the RB test for all scenarios with biased PRN10 and with test parameters $\alpha = 0.001$ and $\beta = 0.001$.

On the contrary of RB and PDP, the protection level derived from the SS test cannot be computed without performing the test. The SS protection level depends on the critical value of the test and on the matrix \mathbf{x}_{SS} .

The vector \mathbf{x}_{ss} changes according to the errors in the state estimation and depends on the geometry since the geometry reflects the precision of the estimation. The critical value also changes from the solution set to another, which depends on the rank deficiency in the SS covariance matrix \mathbf{Q}_{ss} .

Figure (4.27) depicts the Stanford diagram of the SS test for all simulated scenario with the test parameters $\alpha = 0.001$, $\beta = 0.001$ and biased satellites PRN10. The protection level is not constant for the same scenario as previously explained. Both the HPL and VPL show high values w.r.t. the other methods RB and PDP. Nevertheless, all the solutions lie on the upper part of the diagram and never surpass the line $PL = PE$. In addition, the SS test incorporates the error in the solution separation and the critical value to the protection level. Also here, the solution of scenario 4 is the best in terms of position error and protection level since it has the best geometry. Contrary, the solution of scenario 6 is the worst in terms of position error and protection level.

To have a more insightful analysis of the protection level of all three methods and to have a better comparison, the superimposed HPL time series of all methods are presented in figure (4.28). The HPL is plotted for all epochs including the ones where the test fails. For the first four scenarios, the RB protection level is always smaller than the PDP protection level and both are smaller than the SS protection level. However, the SS protection level reflects the observation error and increases as the bias increases in PRN10. In scenario 5 the RB and PDP horizontal protection level coincides and in scenario 6 the HPL of SS test has lower values in the non-biased region. That means that the SS test depends more on the observation errors while RB and PDP horizontal protection levels depend more on the satellites' geometry.

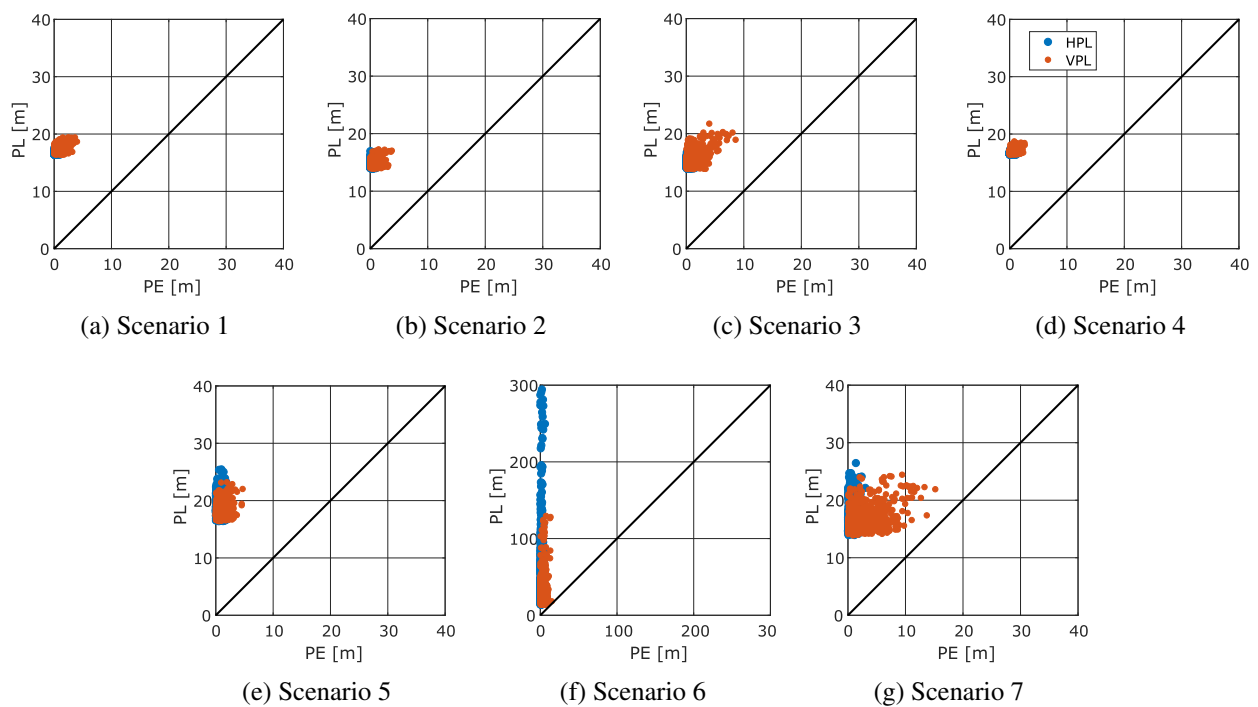


Figure 4.27: Stanford diagram: horizontal and vertical protection level of the SS test for all scenarios with biased PRN10 and with test parameters $\alpha = 0.001$ and $\beta = 0.001$.

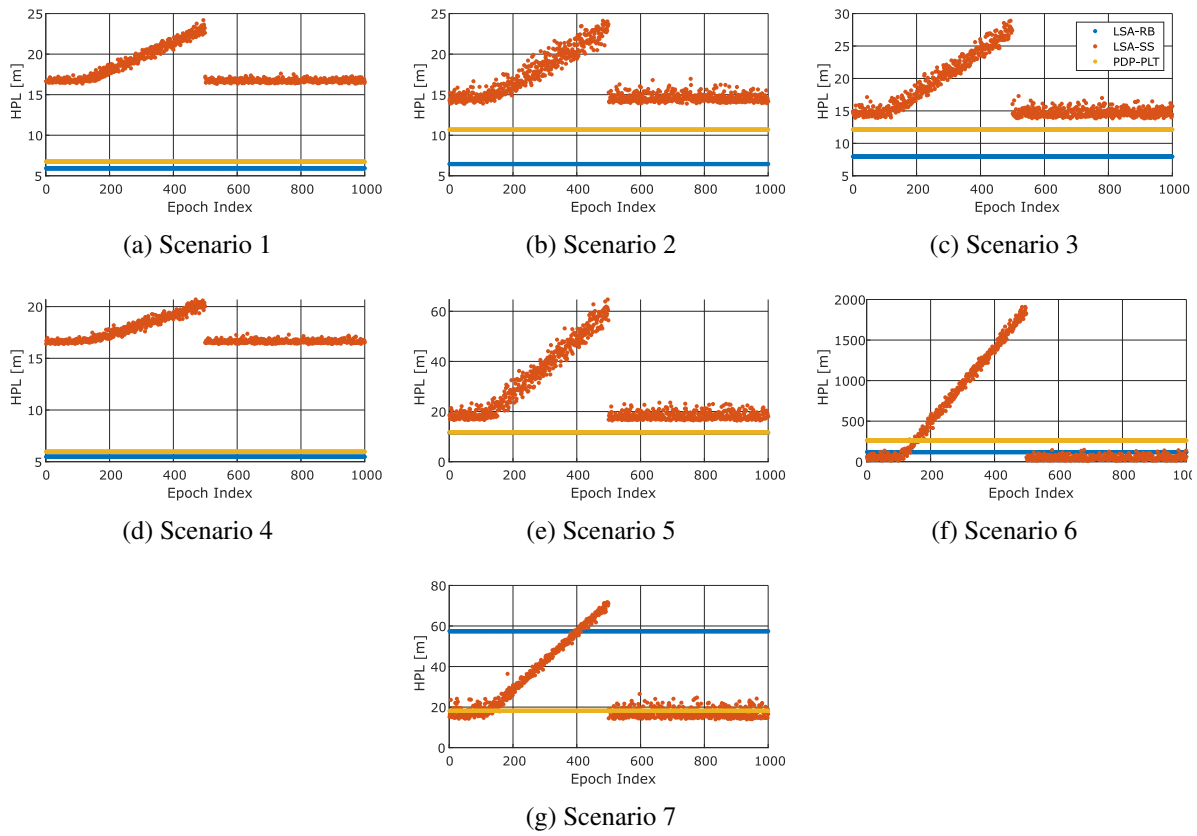


Figure 4.28: Superimposed time series horizontal protection level of RB, SS, and PLT tests for all scenarios with biased PRN10 and with test parameters $\alpha = 0.001$, $\beta = 0.001$, $\Delta = 3$ m and $\kappa_p = 1.5$.

5 Real Data Analysis

5.1 Introduction

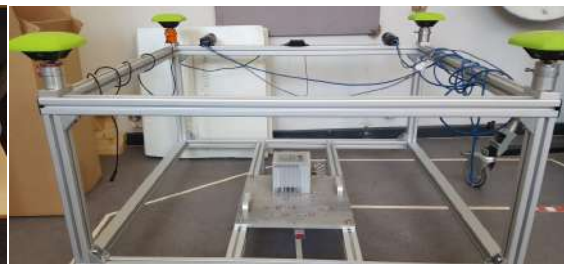
Intensive test drives have been done within the scope of DFG funded research training group “I.C.SENS”, Schön et al. (2018). Three vehicles are utilized in the measurement campaign equipped with different types of sensors, Figure 5.1. Vehicle 1 on the left top view is the one we collect data for this thesis. Vehicle 1 is equipped with *Javad* QUA-G3D Sigma receiver which can collect data from four antennas, and a *Novatel* SPAN system consisting of a dual-frequency GNSS receiver NovAtel (2012) connected to two of the *Javad* antennas and an iMAR FSAS, IMU iMAR IMU (2016). The equipment is depicted in figure 5.1b. In addition to that, a *Microstrain* IMU and pair of stereo cameras were mounted on the platform. However, in this thesis, the data is taken only from the *Javad* and the Span system. To combine measurements from different GNSS antennas and the IMU, the lever arm is determined in a geodetic laboratory using a laser tracker (Leica Absolute Tracker AT960) with an accuracy better than 1 mm.



(a) Vehicles



(b) GNSS equipment



(c) Set up

Figure 5.1: Three vehicles used in the kinematic test drive and the GNSS equipment for vehicle 1 and the platform set up for vehicle 1.

In this study, we will present 2 of those test drives. The chosen test drives were recorded in the city of Hanover, Germany. A first drive was recorded in a GNSS denied urban area, Figure 5.2bb. The ground truth is provided by the post-processing software TerraPos, Kjörsvik and Brøste (2009), where the very precise carrier phase observations of 2 GNSS antennas were tightly coupled with the iMAR IMU measurements. Moreover, the trajectory which looks like an eight-shape is repeated four times, i.e., one trajectory consists of four rounds. Scenario 2 is also recorded with the same equipment, but this time in a GNSS semi-denied

urban area where small houses and trees are located near the street, see figure 5.6.b. Also, scenario 2 consists of six rounds of the same trajectory.

GPS L1 code measurements (C/A) are used in the computation of all different solutions with different methods except the reference solution where dual-frequency carrier phase measurements are used. The *Klobuchar* ionospheric model is applied for the ionospheric corrections and the *Saastamoinen* tropospheric model is applied for the tropospheric corrections, Klobuchar (1987); Saastamoinen (1972, 1973). The frequency of the recorded data was 10 Hz for the reference solution while the other solutions are preprocessed at a frequency of 1 Hz. In the following, different solutions of the two chosen scenarios will be analyzed in terms of precision, accuracy, reliability, and integrity. The point position obtained from least-squares is named LSA-SPP and the point position of the primal-dual polytopes is named PDP-SPP. The interval boxes computed from SIVIA will be compared to the polytopes in scenario 2, while the rest of the analysis is made on the LSA with and without RB and SS test statistics and the PDP with and without the PGT and PLT.

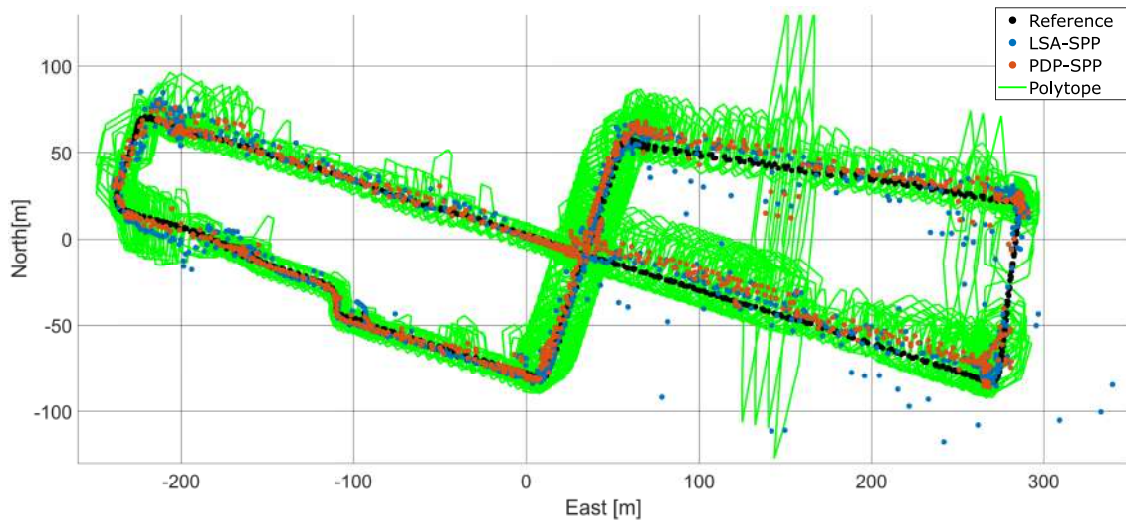
5.2 Positioning Analysis

5.2.1 Results from Scenario 1 - Urban Area

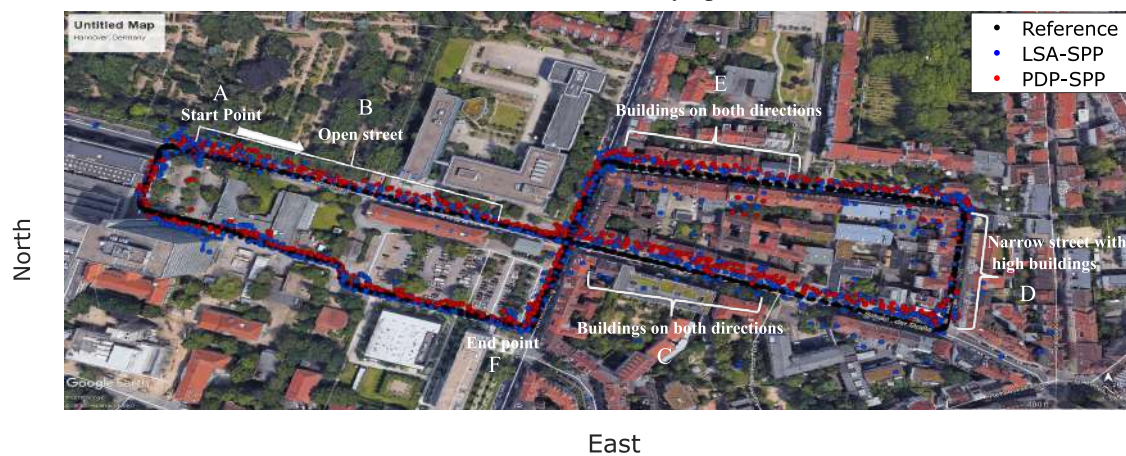
In this section, the LSA-SPP and PDP-SPP are analyzed in terms of precision and accuracy in a local topocentric ENU coordinate system. We consider the barycenter of the polytope as its point position. Figure 5.2a, depicts the reference solution (black solid line), the least-squares adjustment single point position LSA-SPP (blue dot), the polytope barycenter from PDP as single point position (red dot), and the computed polytope (green) for scenario 1. In the LSA, the prior variance factor is set to $\sigma_0^2 = 1$ and for the polytopes the OIB is set to $\Delta = 6 \text{ m}$ for all observations.

In this scenario, there are a lot of high buildings and a small tunnel where most of the GPS signals are blocked or experience multi-path reflections. Figure 5.2b depicts the Google earth map, where the starting point (A) is indicated by a white arrow followed by quite an open street (B). Then areas with high buildings and narrow streets (C), (D), and (E) are highlighted. It is evident that the LSA-SPP is sparse and there are a lot of solutions far away from the reference solution, especially on the east side of the trajectory (point D), where that area contains high buildings on both sides of a narrow street. On the other hand, the PDP-SPP is less scattered than the LSA-SPP solution, where most of the scattered positions are not presented anymore. This is due to the fact that when large biases are present in the measurements, we get an empty polytope and thus no solution. In this case, we lose the continuity of having a positioning solution but at least we do not have a very bad positioning. In addition, the polytope always contains the reference position which is assumed to be the true solution except for three epochs which will be analyzed next. However, some of the polytopes are very large. This is due to the blockage of the GPS signals in the lateral directions. In the area of points C and E where the very large polytopes prevail, there are high buildings on both sides of the street, so only satellites at high elevation angles are visible. Under this condition, the polytopes have tight bounds in the up direction and wide bounds in the horizontal direction.

Figure 5.3 depicts each round of scenario 1 alone, so it is easier to see what is happening in each round and how similar the polytopes are. The last round is not complete. At the starting point (zone B), where the sky is quite open, the polytopes are rather small and very well bounded for all rounds. In zone C, with high buildings on both sides (north and south) of the street, the polytopes get larger than the one in zone B for all rounds. Moreover, few empty polytopes occurred in zone C. This is more visible in the last round. In zone D, with high buildings on both sides (east and west) and a very narrow street, the polytopes are empty most of the time for all rounds. In zone E, the polytopes are very similar during the first two rounds. Most of the polytopes are biased a bit in the northeast direction w.r.t. the reference solution. In addition, the polytopes get empty for few epochs in those regions. In the 3rd round in zone E, most of the polytopes are similar to the polytopes in the 1st and 2nd rounds. However, in the 3rd round, there are three biased and relatively small polytopes that do not contain the reference solution and the other three biased and relatively large polytopes which include the reference solution. These three large polytopes correspond to empty polytopes in the 2nd round. In the last round, the same three large polytopes occurred again with the three large polytopes at the



(a) Point Position and Polytopes



(b) Google Earth

Figure 5.2: Results of scenario 1: (a) polytopes and its PDP-SPP superimposed with LSA-SPP for $\Delta = 6$ m. (b) Google earth screen-shot of the SPP.

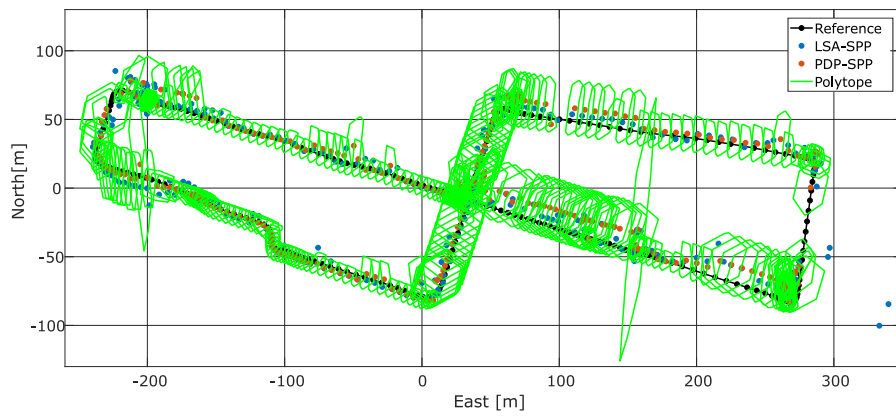
northeast corner. There are some empty polytopes in the last round corresponding to the biased polytopes from 3rd round that does not contain the reference solution near zone E.

From point F to point A, there is an open sky area (parking lot, see figure 5.2b) so the polytopes become small again due to good navigation geometry in all four rounds. Before arriving at the starting point, there is the highest building in the area, where the polytopes become large again especially in the northern direction.

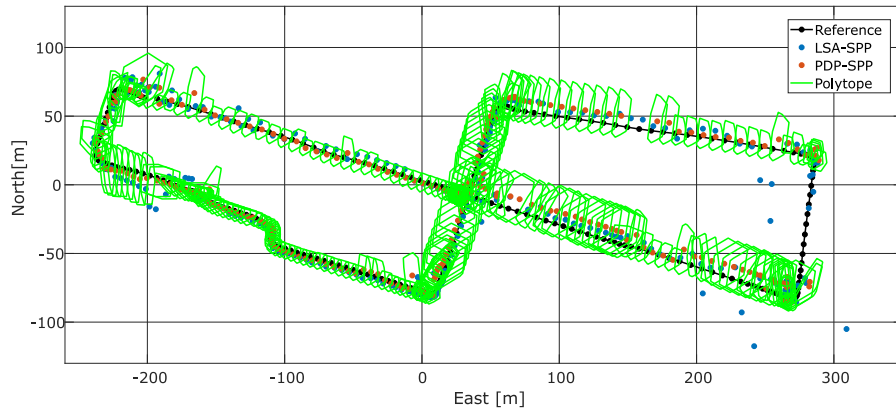
Figure 5.4.a is a zoom of round 3 at zone C depicting only the three biased polytopes which do not include the reference solution. Figure 5.4b depicts the 1-relaxed zonotope which we consider as a guaranteed protection level. All three 1-relaxed zonotopes contain the reference solution.

To have a closer look at the point position error, the relative cumulative histogram of the 3D position error is performed for scenario 1 for all methods, figure 5.5. In this scenario, the result of the LSA is enhanced after applying the test statistic RB and SS. Probably this is due to large biases in the observations since this scenario is located in a GPS denied area and some observations could have multiple reflections. At 60 % of the epochs, LSA without any test and with RB and SS tests have 15.25 m, 14.88 m, and 13.11 m 3D position error, respectively, while PDP without and with PLT have 14.08 m and 11.06 m 3D position error, respectively.

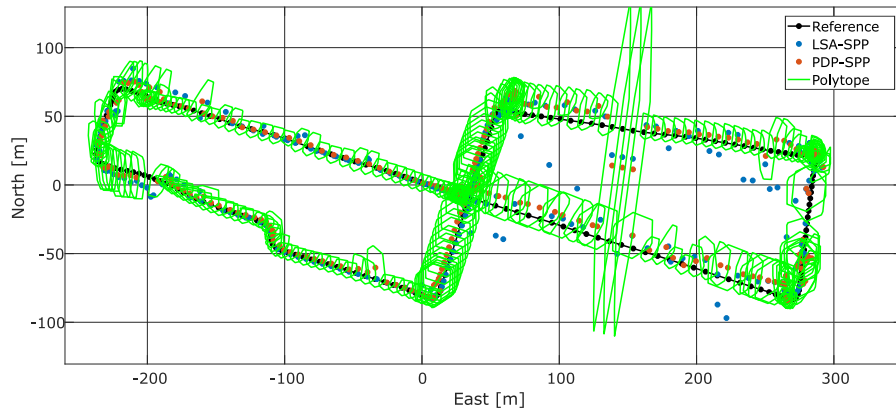
The overall root mean squares errors of the 3D positioning error of LS, LS with RB test, LS with SS test, PDP, and PDP with PLT are 14.0 m, 13.2 m, 12.5 m, 12.8 m, and 10.2 m, respectively.



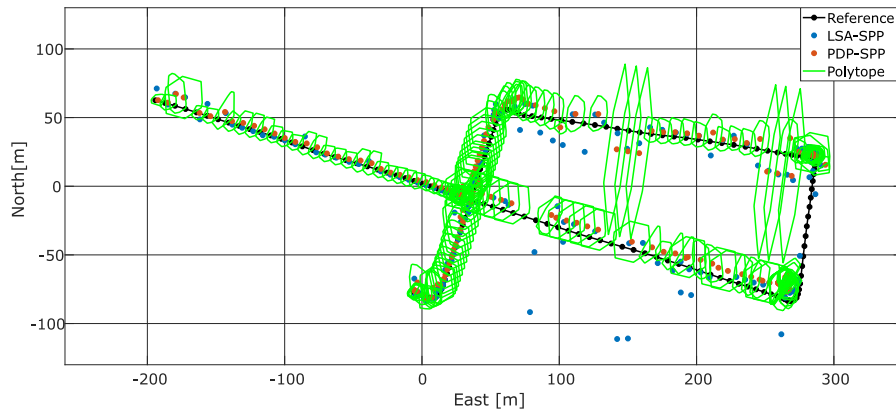
(a) First round



(b) Second round



(c) Third round



(d) Fourth round

Figure 5.3: Results of scenario 1 divided into 4 rounds.

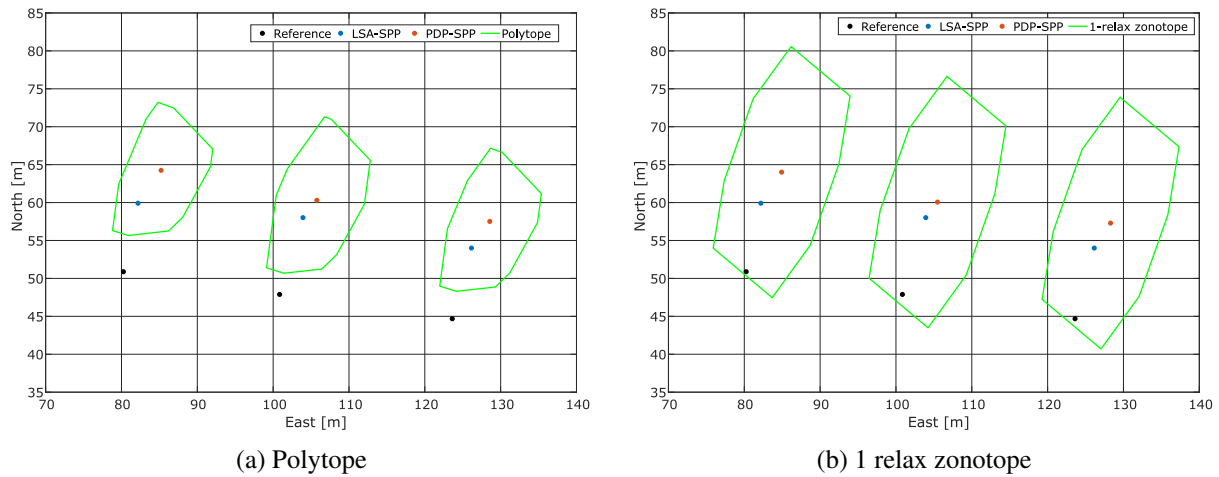


Figure 5.4: Zoom on figure 5.3c, where some polytopes do not contain the true position.

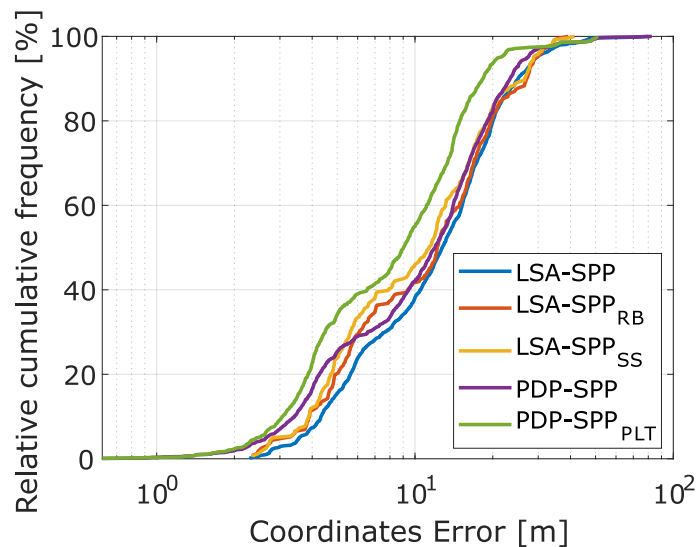


Figure 5.5: Relative cumulative frequency of the 3D position error of scenario 1 with and without applying RB test, SS test and PLT where the test parameters are $\alpha = 0.00001$, $\beta = 0.001$, for RB and SS, and $\Delta = 6 m$ and $\kappa = 1.5$ for PLT.

PDP combined with PLT outperforms all the other methods. However, the enhancement in accuracy, reliability, and integrity is at the cost of continuity. So our method provides high integrity measures but in order to have a continuous navigation solution a good observation quality is needed. In addition, in such GNSS denied areas and using only GPS code observation it is impossible to have a continuous navigation solution regardless of the estimation and FDE methods.

5.2.2 Results from Scenario 2 - Semi-Urban Area

Now, we analyze the positioning performance of the 2nd scenario. Figure 5.6b illustrates the Google Earth map of scenario 2 including the LSA-SPP (blue), PDP-SPP (red), and the reference solution (black). The starting point of the test drive is at point A, and the direction of the drive is indicated by the white arrow. The trajectory consists of 6 rounds. But first we will analyze the bounding zone from SIVIA and PDP. We dedicate this small section to have a comparison between interval-based algorithms. Figure 5.6a depicts the solution sets of the polytope (blue), SIVIA bounding boxes (red), and the reference trajectory (black) of scenario 2. The same type of GPS observations as in scenario 1 are used here. Both bounding zones (polytopes and SIVIA interval boxes) contain the true solution overall the trajectory. This is checked with *belong* functions that can check if a point belongs to a polytope or interval box. However, SIVIA interval boxes are

larger than the PDP polytopes, where the polytopes are located inside the interval boxes. In addition, the interval boxes do not well represent the uncertainty since their edges are always parallel to the coordinate axes while the polytope represents the uncertainty in all directions and their edges are perpendicular to the satellites LOS. In figure 5.6a we show the bounding zones provided by the polytopes and the SIVIA interval boxes to express the differences between the two bounding methods. In addition, there is no test performed on the SIVIA interval boxes, so there is no fair comparison to further investigate.

In this scenario, both LSA and PDP single point positioning show quite good precision and accuracy compared to the SPP in scenario 1. This is due to the fact that the area where scenario 2 is recorded contains low buildings and trees, while the area of scenario 1 contains very high buildings and obstructions. Table 5.1 depicts the mean values and the standard deviations of the LSA-SPP and PDP-SPP w.r.t. ground truth for scenario 1 and 2. The difference between the two scenarios is higher in terms of standard deviation where scenario 1 has a very large standard deviation compared to scenario 2 in both methods.

Table 5.1: Mean value μ and standard deviation σ of LSA-SPP and PDP-SPP of scenarios 1 and 2.

	Scenario 1				Scenario 2			
	LSA-SPP		PDP-SPP		LSA-SPP		PDP-SPP	
	$\mu[m]$	$\sigma[m]$	$\mu[m]$	$\sigma[m]$	$\mu[m]$	$\sigma[m]$	$\mu[m]$	$\sigma[m]$
East	1.2	7.9	1.5	7.9	3.3	1.3	2.4	1.7
North	5.0	7.1	3.3	6.9	-0.2	1.2	0.8	1.8
Up	6.6	9.8	3.5	9.2	7.9	4.1	6.1	6.1

To further investigate the SPP of both methods, the time series of the horizontal and vertical position errors in the local topocentric ENU coordinate system of scenario 2 are plotted in figure 5.7b and figure 5.7c, respectively. In addition to that, the number of satellites in view, Horizontal Dilution of Precision (HDOP), and Vertical Dilution of Precision (VDOP) are presented in figure 5.7a separating each round by a vertical black line. The starting epoch of each round is depicted by a black bar in the time series of the number of satellites in view, the HDOP, and VDOP.

This way, specific epochs can be investigated in terms of the number of satellites in view, HDOP, and VDOP, i.e., in terms of positioning geometry. Figure 5.7b and 5.7c depict the horizontal and vertical position errors of the LSA, PDP, and PDP combined with its global test PGT as explained in section 3.4.5. The position error analysis of LSA combined with RB and SS test statistics will be investigated later on. Analyzing the area for scenario 2 for each round, the geometry in terms of the number of satellites in view and DOP values is quite good at the starting point (A), while it worsens at the middle of the trajectory, especially around point B (see figure 5.6.b) and then gets better when it is reaching the starting point again. Note that the time of each round is different from one round to another. Around point B there are very large trees and a few high buildings. The test drive was recorded on June 12, 2017, so the trees are in full leaves.

Let us first look at the positioning errors of the LSA (blue) and PDP (red) without the PGT in figures 5.7b and 5.7c. At most epochs, they have comparable errors with slightly smaller values for the PDP method. However, the PDP position error has a lot of peaks especially when the positioning geometry is getting worse. We can relate the peaks of PDP position errors, especially visible in the vertical position error to the peaks in the HDOP and VDOP. Some of these peaks are indicated by the black arrows in figure 5.7c, where there are peaks in both PDP horizontal and vertical position errors and in HDOP and VDOP. This concludes that PDP is sensitive to the bad positioning geometry and in this case, the theoretical ZMDB and PMDB get very large and biases smaller. ZMDB could not be simply detected by only having empty sets as we have seen in section (3.4.3) and section (3.4.4). A proper test is needed to detect this type of biases. Also, the position error from LSA has peaks at those bad geometry epochs, but with lower values than the errors in PDP. So we can say that PDP is more sensitive to the positioning geometry than LSA if there is no test applied on both methods. On the other hand, when the positioning geometry is quite good, PDP performed better than LSA and in the presence of biases, the LSA solution is degraded while PDP solutions get empty, i.e., the bias is detected without performing any tests. For instance, around the epochs indicated by grey arrows which are related to a good geometry in terms of HDOP, VDOP and number of satellites, the LSA

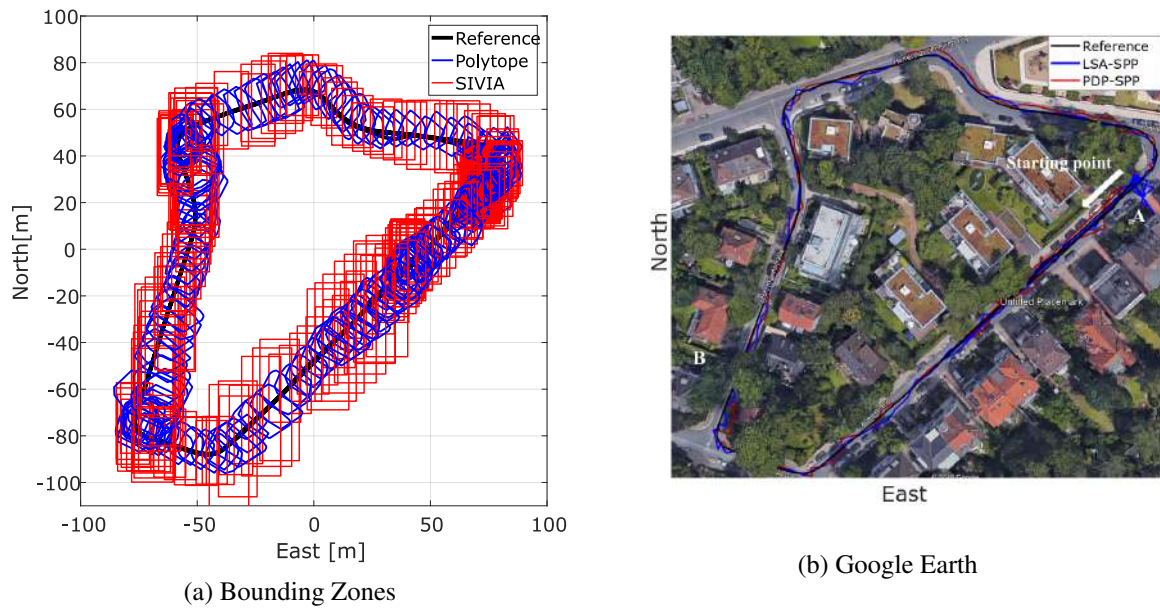


Figure 5.6: Scenario 2:a, polytope and SIVIA interval boxes for $\Delta = 6$ m. b, Google earth screen-shot of the polytope and LS SPP.

position error shows peaks (high values) in both horizontal and vertical directions while PDP has empty sets. So the PDP shows high integrity in this case at the cost of the continuity, i.e., it is possible to know that there is a problem in the navigation solution and an alarm could be raised. So, our newly developed methods provide integrity measures even without performing any test. This measure depends on satellite geometry and the observation interval bounds. Any bias greater than ZMDB is guaranteed to be detected.

Moreover, the horizontal and vertical position error of PDP with the PGT are plotted (yellow) in figure 5.7c and 5.7, respectively. Most of the epochs with bad geometry (indicated by black arrows) where there are peaks in the PDP without test solutions are now detected. In this analysis, we assign an empty set to the polytope when the test has failed. It is possible to perform PLT to exclude the biased satellite. But in this urban area, most of the satellites experience multi-pathing, and excluding one of them is not going to enhance the positioning. Especially in the case of bad geometry and the low number of satellites in view where it becomes difficult to identify the biased satellite. At least, in this analysis, we can see the power of the PGT which enhances the reliability and integrity of the positioning system.

To have an overview on the positioning error, a relative cumulative histogram of the 3D positioning analysis is performed, figure 5.8. Figure 5.8a depicts the cumulative frequency of the 3D position error for LSA and PDP SPP without applying any test on both methods, while figure 5.8b depicts the cumulative frequency of the 3D position error for LSA without any test (blue), LSA with RB test (red), LSA with SS test (yellow), PDP without any test (violet) and PDP with PLT. Analyzing both methods LSA and PDP without any test, it is visible that PDP outperforms LSA in 92.4 % of the cases, i.e., errors less than 15.2 m, but still PDP underperforms LSA for 7.6 % i.e., at error values greater than 15.2 m. This is due to the high positioning errors of PDP with bad geometry condition, since polytopes do not get empty for biases less than the theoretical PMDB.

In addition, the barycenter as a point position is not suitable in this case, because when we have a large cut of the polytope in one direction, the barycenter will be shifted to the other direction where there are more vertices. One possibility to get a better point position for the polytope is to find a correction of the observation that makes the polytope fit the theoretical zonotope. This will be one of the problems to be solved in the future.

If PLT is applied to the PDP methods, it outperforms 100 % the LSA with RB and SS test statistics, see figure 5.8.b. In this analysis, $\Delta = 6$ m is applied to the observations and $\kappa = 1.5$ to the critical value CV_{V_0} for PLT, while $\alpha = 0.00001$, $\beta = 0.001$ are applied to the RB and SS tests. There is a small enhancement in the LSA 3D positioning errors after applying the RB and SS test. Probably this is due to multiple small biases

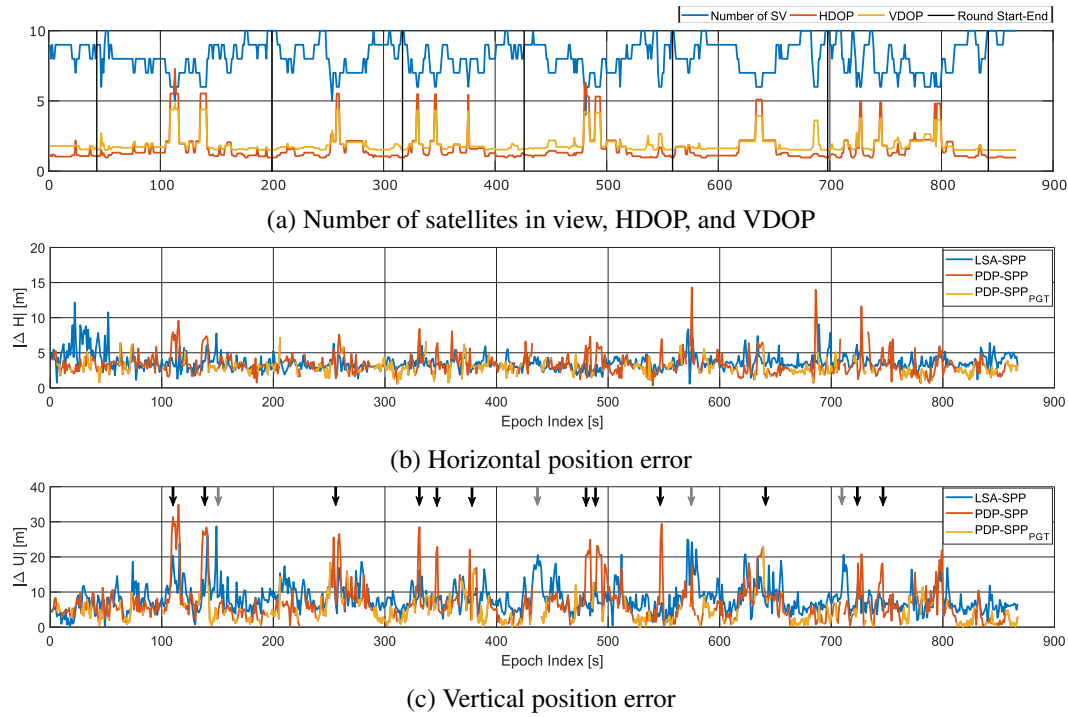


Figure 5.7: Time series horizontal and vertical position error of LS, PDP, and PDP combined with PGT for scenario 2 with $\Delta = 6$ m.

in the observation since scenario 2 is located in a GPS semi-urban area which makes it difficult to detect faulty measurements. On the other hand, multiple small biases in the observation decrease the volume of the polytope where each bias cuts a portion from the original polytope, so the PGT is able to detect biases while it is still difficult to identify the biased satellite. Also, if we identify one biased satellite, there is a high probability to have more than one bias, and the PDP-SPP will not enhance by excluding only one bias. So in this analysis, we set the polytope to an empty set when biases are detected and we also exclude the solution of LSA when a fault is detected in both tests RB and SS. So a fair comparison is done. The identification of the biased observation and the statistics of the detected and excluded faults will be analyzed in the next section.

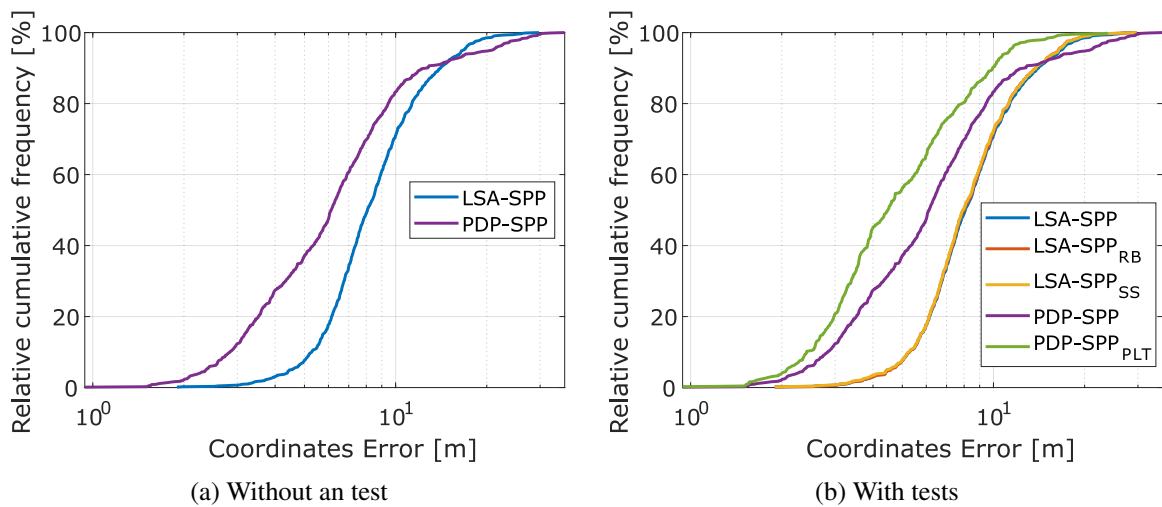


Figure 5.8: Relative cumulative frequency of the 3D position error of scenario 2 with and without applying RB test, SS test and PLT where the test parameters are $\alpha = 0.00001$, $\alpha = 0.001$, for RB and SS, and $\Delta = 6$ m and $\kappa = 1.5$ for PLT.

To have more solid comparison of the 3D error analysis, we provide the 3D position error at 60 % of the epochs of the cumulative frequency errors and they are 8.9 m for LSA, 8.87 m for LSA with RB test, and 8.82 m for LSA with SS test, while 6.91 m for PDP without any test and 5.48 m for PDP with PLT.

5.3 Fault Detection and Exclusion

In this section, the analysis of the FDE for RB, SS, and PLT is performed on scenario 2. Figure 5.9 depicts the identified faulty PRN satellites for all test with different parameters. Figure 5.9a shows the results from PLT with three different observation interval bound $\Delta = 3$ m, 6 m, and 9 m, while $\kappa_p = 1.5$ kept constant for all cases. As expected, increasing the OIBs, less satellites are detected since the PMDB depends on the applied observation intervals. All faulty satellites detected when $\Delta = 9$ m are also detected when $\Delta = 6$ m and $\Delta = 3$ m. Similarly, all detected faults for $\Delta = 6$ m are also detected when $\Delta = 3$ m. Figure 5.9b and 5.9c depict the results when applying RB and SS tests, respectively, with three different applied PFA on the hypothesis test statistic $\alpha = 0.001$, 0.00001, and 0.0000001 and PMD $\beta = 0.001$ kept constant. As expected for both probabilistic tests decreasing the PFA, i.e., having lower integrity risk, decreases the number of detected faulty satellites. The integrity risk is lower in this case because smaller PFA provides bigger PL. So the risk is lower but this could come at the cost of the continuity since increasing the protection level could surpass the AL and then the solution is not available any more.

Both, RB and SS tests show a very similar behavior to each other, however at some epochs different satellites are detected or some satellites are detected by one method and not detected by the other. To have better visualization and comparison, all methods plotted in the same plot with corresponding test parameters, i.e., $\Delta = 3$ m, 6 m, and 9 m for PGT correspond to $\alpha = 0.001$, 0.00001 and 0.0000001 for RB and SS tests in figure 5.10a, 5.10a, and 5.10a, respectively. The PLT detects all the faults that have been detected by both tests RB and SS and it is able to detect more faults than both of them. However, for few epochs the identified faulty satellite by SS and / or RB has different identifications by PLT. For $\Delta = 3$ m and $\alpha = 0.001$ there are 7 epochs where the identification is different from PLT to SS and the epochs are: 182, 266, 375, 392, 544, 548, and 708. The Same epochs are detected by the RB test and SS except the epoch 375 RB did not detect any fault. There are some other epochs where PDP detect a faulty satellite and only one of the probabilistic tests detect the same faulty satellite, e.g., at epoch 665, 668, and 674 only PLT and RB identifies PRN06 as faulty, while the SS test passes. Similar situations happen for $\Delta = 6$ m and $\Delta = 9$ m.

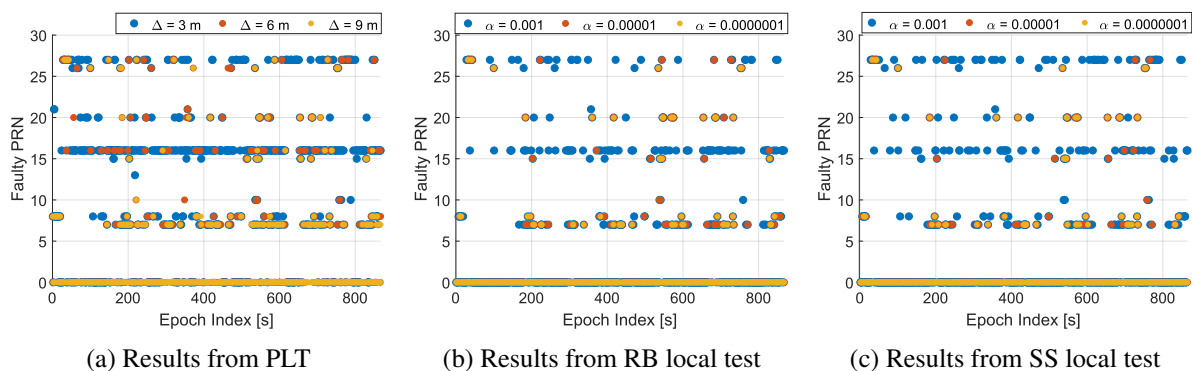


Figure 5.9: Fault detection and exclusion performed on GPS code measurements of scenario 2 for 3 different observation interval bounds $\Delta = 3$ m, 6 m, and 9 m with $\kappa_p = 1.5$ corresponding to the probabilistic tests significant level $\alpha = 0.001$, 0.00001, and 0.0000001 with $\beta = 0.001$. The vertical axes indicates the PRN number flagged as faulty and zero means no fault detected.

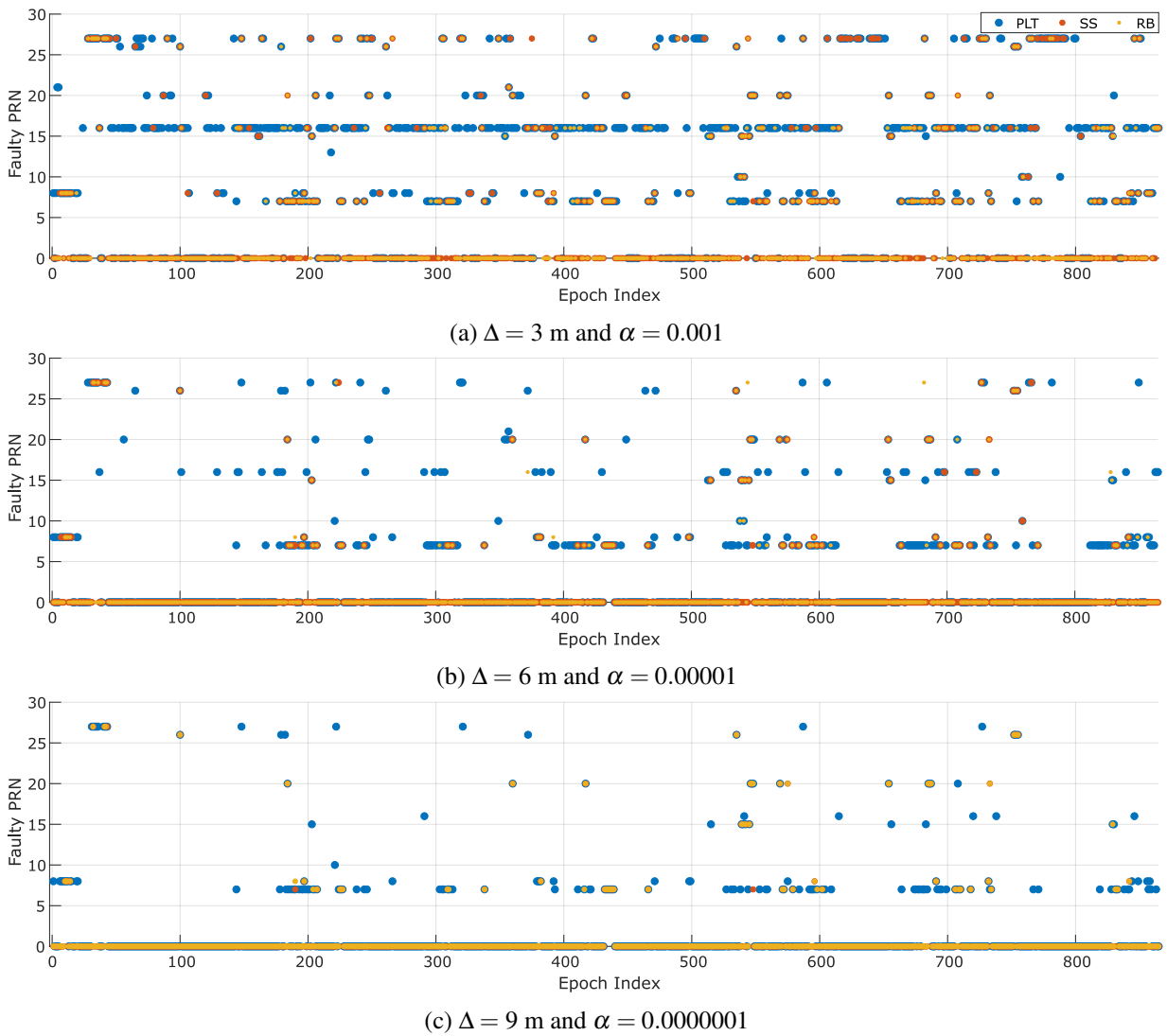


Figure 5.10: Superimposed fault detection and exclusion performed on GPS code measurements of scenario 2 for 3 different observation interval bounds $\Delta = 3 \text{ m}$, 6 m , and 9 m corresponding to the probabilistic tests significant level $\alpha = 0.001, 0.00001$ and 0.0000001 .

Let us now have a quantitative analysis of all FDE methods. Table 5.2 reports the number of detected and excluded faults for all tests with different test parameters. The detection capability of the PGT is much higher than the probabilistic test statistic SS and RB. From the Monte Carlo simulation, we have seen that the PGT can detect more biases than both probabilistic approaches but in a comparable way. This was explained by the controlled simulated observation, where we are sure that there is only one faulty PRN and we know its identity. In real data, especially in urban areas, multiple biases are expected with a low number of satellites in view which makes it difficult for the probabilistic approaches to detect biases, while for the PGT, the multiple biases accumulate as one bias, i.e., each small bias takes away a small portion of the polytope so that multiple biases produce a small or even empty polytope volume w.r.t. the zonotope volume. In this way, the PGT, can detect a high number of outliers, but the PLT will not be able to differentiate between different biases. The PLT could be programmed to detect multi-faults, where more sets have to be analyzed and more than one satellite has to be excluded from the polytope computation. For example, if we assume two faults could occur at the same time, all sets with one excluded observation and all sets with two excluded observations have to be checked. However, in this thesis, we are focusing on single-fault cases, even though for GPS real data in an urban environment there is a high probability for multi-faults to happen.

Table 5.2: Number of detected and excluded faults for PLT, SS, and RB tests for different test parameters.

	PLT	SS	RB
$\Delta = 3 \text{ m}, \alpha = 0.001$	706	292	294
$\Delta = 6 \text{ m}, \alpha = 0.00001$	334	97	111
$\Delta = 9 \text{ m}, \alpha = 0.0000001$	182	62	69

5.4 Minimum Detectable Bias

In this section, the MDB of RB, SS, and V_{r_0} will be investigated. For V_{r_0} , the ZMDB and PMDB are defined in equation (3.18) where MDB_{Z_i} is the upper limit of MDB_{P_i} . This is the bias that provides an empty polytope. In the PGT, a critical value $CV_{V_{r_0}}$ is assigned on the consistency measures V_{r_0} in order to detect biases smaller than MDB_{P_i} , i.e., the polytope is not empty but biased. However, an analytical formulation of the MDB of the PGT is still not developed. For the probabilistic tests RB and SS the MDB are the one defined in equation (2.49) and equation(2.62), respectively.

Figure 5.11 depicts the PMDB of all satellites in view with the applied observation interval bound $\Delta = 6 \text{ m}$ and figure 5.12 depicts its upper limit, i.e., ZMDB. Most of the PMDB lie between 10 m and 30 m, while the ZMDB lie between 13 m and 30 m. This range of values is related to the observation interval bound Δ and the geometry of the navigation system. The minimum value of ZMDB is twice the observation interval bound (2Δ) if the geometry is perfect, while the PMDB could have values lower than 2Δ due to the multiple errors in all observations. The peaks in the PMDB and ZMDB are related to bad satellites geometry. We can see that these peaks occur when we have peaks in the HDOP and VDOP, see figure 5.7a.

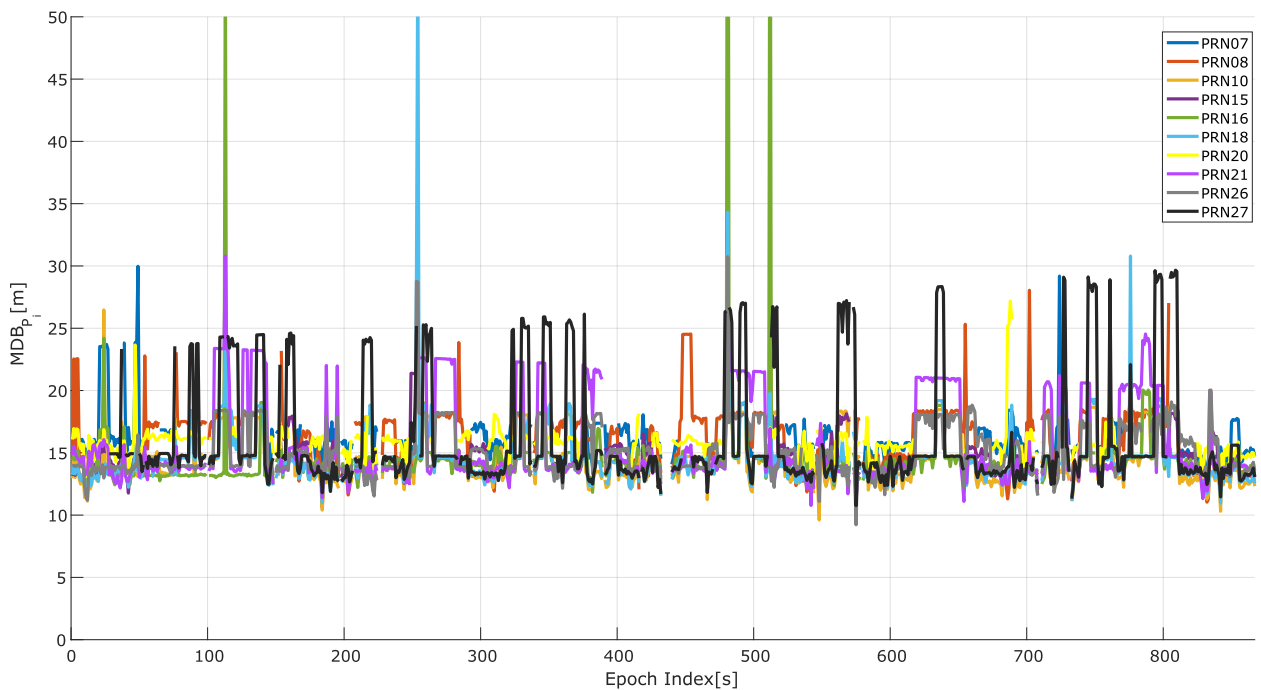
Figure 5.11: PMDB of the consistency measures V_{r_0} with $\Delta = 6 \text{ m}$.

Figure 5.13 depicts the MDB of the RB test with $\alpha = 0.00001$ and $\beta = 0.001$ for scenario 2. In the RB test, each satellite has its behavior and it depends mostly on its elevation angle since the observations are weighted by the elevation angle in the LSA. The variation of the individual MDB along the time series is quite stable. When some of the satellites are blocked by obstacles and the number of satellites is reduced, i.e., the overall geometry of the navigation system is degraded, the remaining satellites in view show small

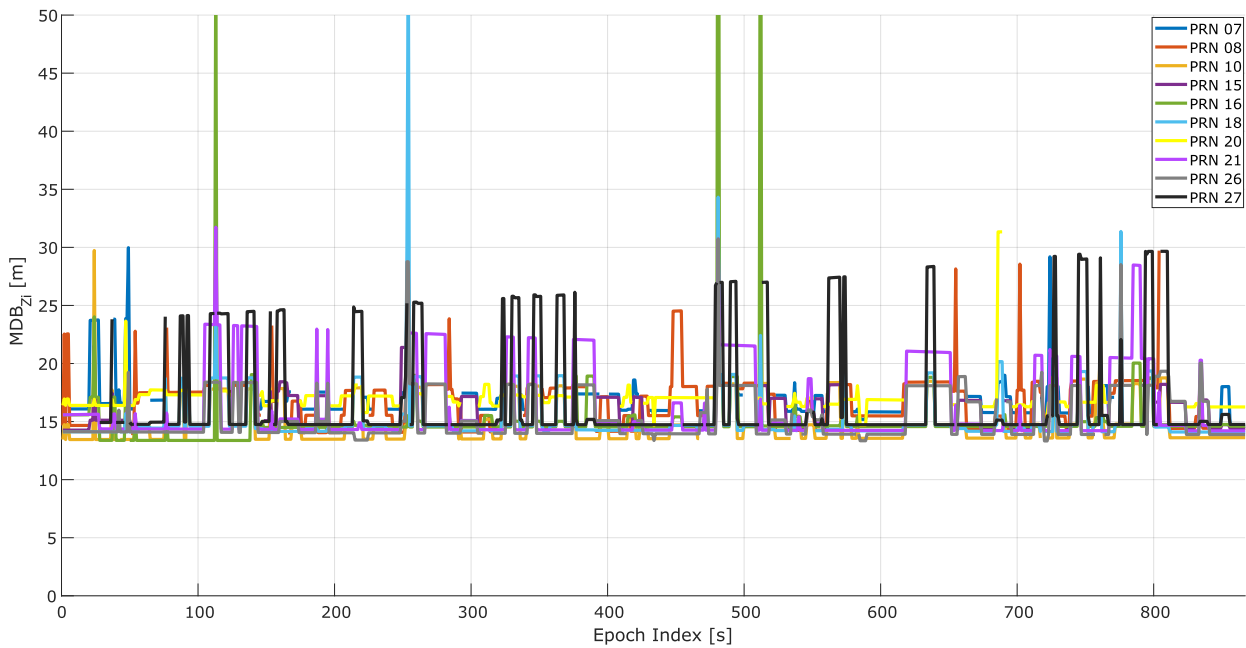


Figure 5.12: ZMDB of the consistency measures V_{r_0} with $\Delta = 6$ m.

peaks in their MDB. For example, around epoch 110, PRN07, PRN08, PRN15, and PRN20 are not visible anymore, and peaks rise in the MDB of PRN16, PRN18, PRN21, and PRN27.

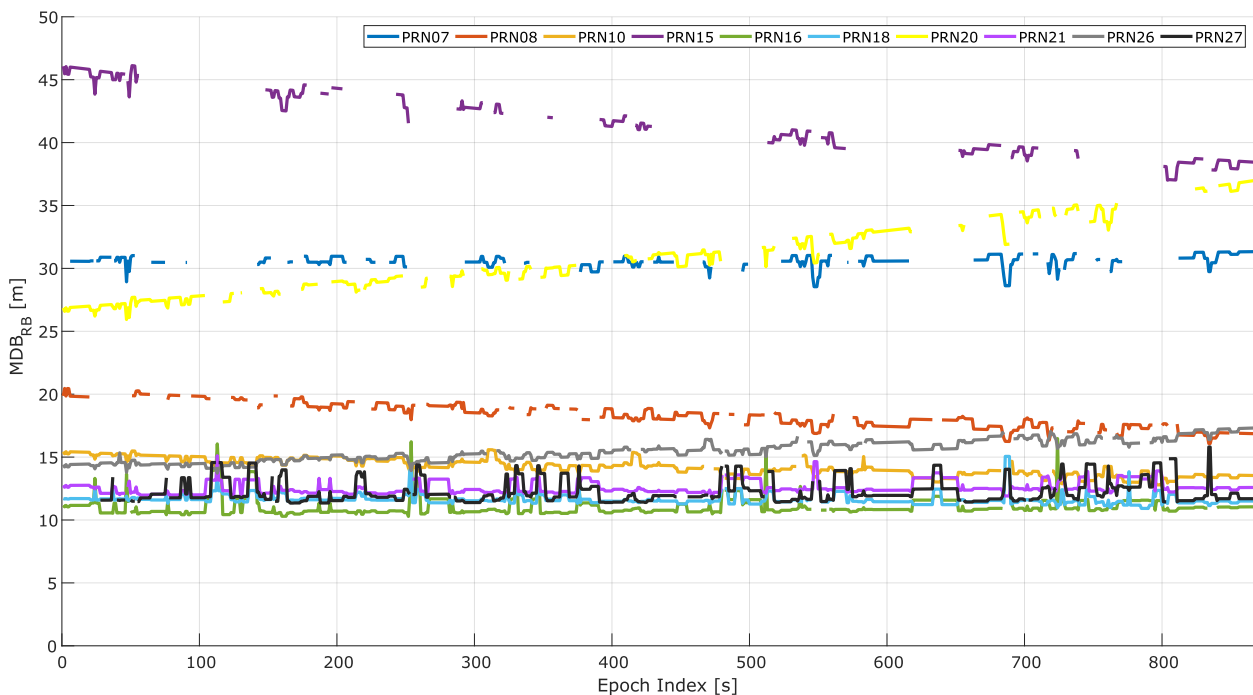


Figure 5.13: MDB of the consistency measures RB test statistic with $\alpha = 0.00001$ and $\beta = 0.001$.

Figure 5.14 depicts the MDB of the SS test with $\alpha = 0.00001$ and $\beta = 0.001$ for scenario 2. Contrary to the RB test statistic, MDB of the SS for different satellites has similar behavior with slightly different values. There is no big difference between the MDB of one satellite and another even if we use elevation dependent weights in the observations. This is due to the fact that the SS test is performed in the parameter domain and not in the measurement domain like the RB test. The overall values of the MDB of SS test is smaller than the RB test, but the fault vectors of the SS test are smaller than the fault vector of the RB test as we have seen in section 2.3.4 and in figure 2.4, where for the SS test we have a set of fault vectors in parity space while the RB test has only one fault vector in the parity space. So the magnitude of the MDB is somehow related

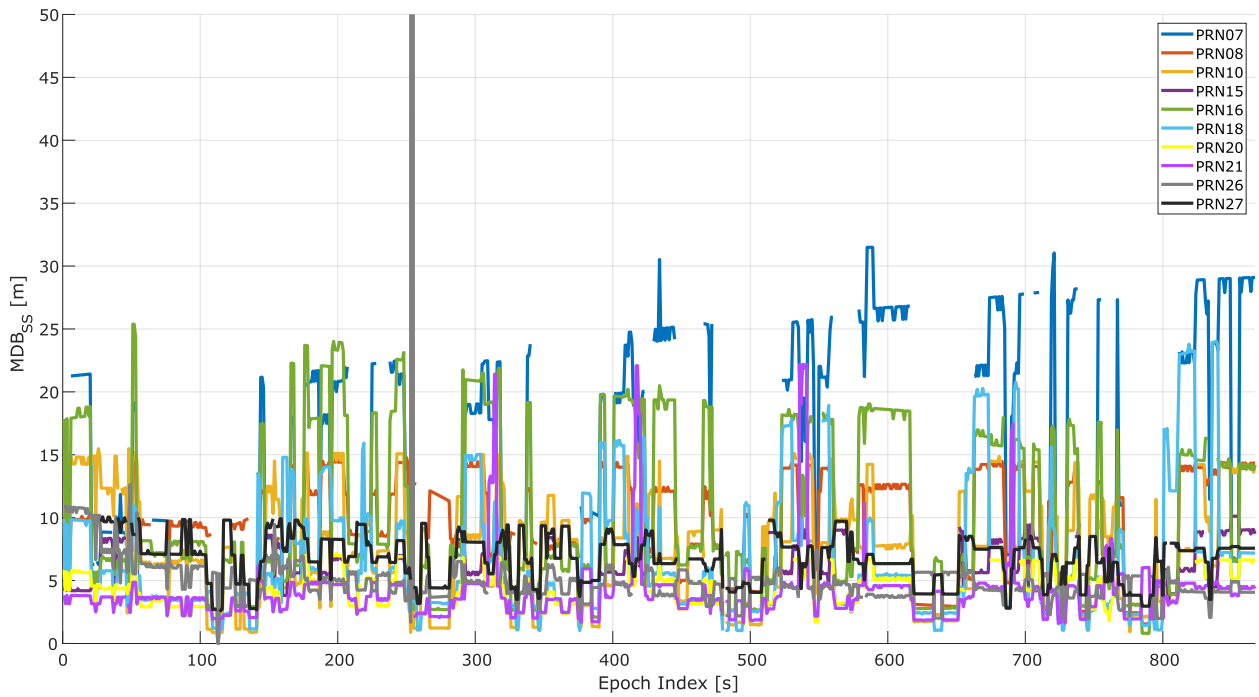


Figure 5.14: MDB of the consistency measures SS test statistic with $\alpha = 0.00001$ and $\beta = 0.001$.

to the fault vector of each probabilistic method. Comparing the MDB of the SS to the PMDB, we found that they are much smaller. But the actual MDB of the PGT and PLT are much smaller than the theoretical PMDB and that is why we have more detection in the PGT than the probabilistic approaches.

5.5 Protection Level

The protection level is one of the most important parameters in the integrity monitoring process, and it can determine if the navigation solution is valid or not, i.e., if the navigation solution is available. In this section, a comparison is performed between the protection level derived from PDP polytope, i.e. the 1-relaxed polytope, before and after performing the PLT and the LSA with RB and SS tests. In the LS framework, the HPL and VPL in equation (2.69) and equation (2.70), respectively, can be computed before and after applying the RB test. Instead, in the SS, the protection level is derived from the test itself as in equation (2.76). First, we will analyze the HPL and VPL of scenario 1 of PDP and LS without any test. For PL of LSA the scale factors used are $\kappa_H = 6$ for HPL and $\kappa_V = 5.33$ for the VPL. The scale factor $\kappa_H = 6$ is computed from the integrity requirement of the en-route, terminal, and lateral navigation phases of flight, and $\kappa_V = 5.33$ is computed for localization performance with vertical guidance instrument procedures which are defined by RTCA (2006). For the PDP, we use $\Delta = 6$ m. Figure 5.15a and figure 5.15c depict the HPL and VPL of PDP, respectively. Also figure 5.15b and figure 5.15d depict the HPL and VPL of LSA, respectively.

Both horizontal and vertical zonotopal protection levels lie above the line $PL = PE$, so they do not have any value in the misleading information regions and hazardous operation regions. For this reason, we call our protection level is guaranteed. The Stanford diagram here does not contain any AL since it depends on applications. If the PL surpasses the AL the system will be unavailable, but we will never be in the hazardous operation region. Moreover, it is visible that the zonotopal HPL has bigger values than zonotopal VPL which should not be the case in an open area scenario where the up direction has bigger errors than the horizontal error. However, in scenario 1, there are a lot of tall buildings, and only satellites at high elevation angles are visible, so the polytope is bounded in up direction by the observation interval bound while in the horizontal direction there are no interval bounds. So the polytope gets large in that direction. On the other hand, the HPL and VPL of the LSA show smaller values w.r.t. the polytope one, but the LSA protection level have some values below the line $PL = PE$ which belong to the misleading and hazardous misleading regions. This happened when the protection level is underestimated w.r.t. the position error.

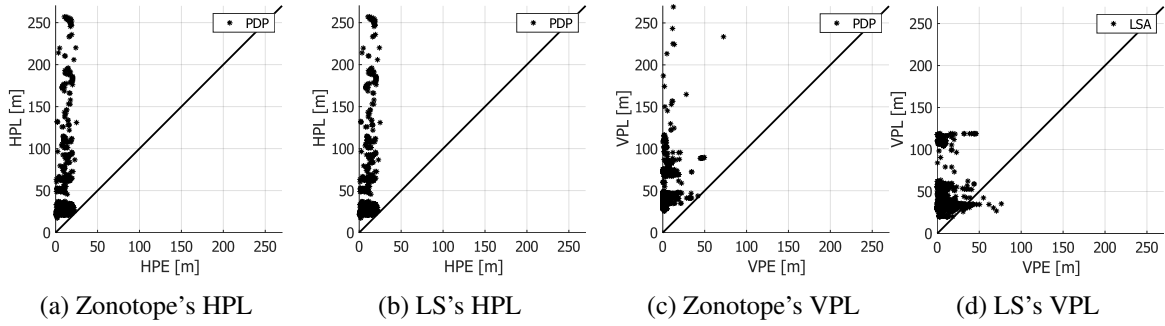


Figure 5.15: Stanford diagram without applying outlier screening: HPL and VPL of the zonotope and LS of scenario 1. For the zonotope the observation interval bound is $\Delta = 6$ m and for the LSA $\kappa_H = 6$ and $\kappa_V = 5.33$.

The zonotopal protection level provides guaranteed integrity measures and sometimes it could be at the cost of continuity and availability of the navigation system, but at least we are on the safe side and no hazardous situations could ever occur. On the contrary, in the case of the probabilistic protection levels, there is the probability of being in the hazardous operational regions without knowing it.

The PL analysis in scenario 1 is also done after performing PLT on PDP and RB and SS tests on LSA with the same parameters as before, i.e., $\Delta = 6$ m and $\kappa_P = 1.5$ for PDP and for the LS $\kappa_V = 5.33$ with $\alpha = 0.00001$ and $\beta = 0.001$ for the RB and SS tests. Figure 5.16a depicts the HPL of PDP combined with PLT, figure 5.16b depicts the HPL of LSA combined with RB, and figure 5.16c depicts the HPL of LSA combined with the SS test. The zonotopal HPL shows better performance than the one without the test and most of the epochs with high HPL have been detected and eliminated by the PLT. The RB test did not show visible improvement w.r.t. the solution without testing in figure 5.15b, while the SS test shows improvements w.r.t. the solution without test in figure 5.15b where less epochs are present below the line $PL = PE$. However, other epochs got a bigger protection level than before since with the SS test many epochs are around 100 m of HPL.

Figure 5.17 depicts the VPL of all methods with the same parameters as in figure 5.16. The zonotopal VPL is also improved by performing PLT where most of the epochs with very large values of the VPL have been detected and eliminated. On the other hand, the RB test has very little improvement w.r.t. the LSA solution without any test while the SS test shows slightly better improvement than the RB test. Also here in the VPL, the epochs below the line $PL = PE$ have been reduced by the SS test at the cost of having more epochs with larger VPL values. This is due to the elimination of one observation so the navigation geometry is degraded.

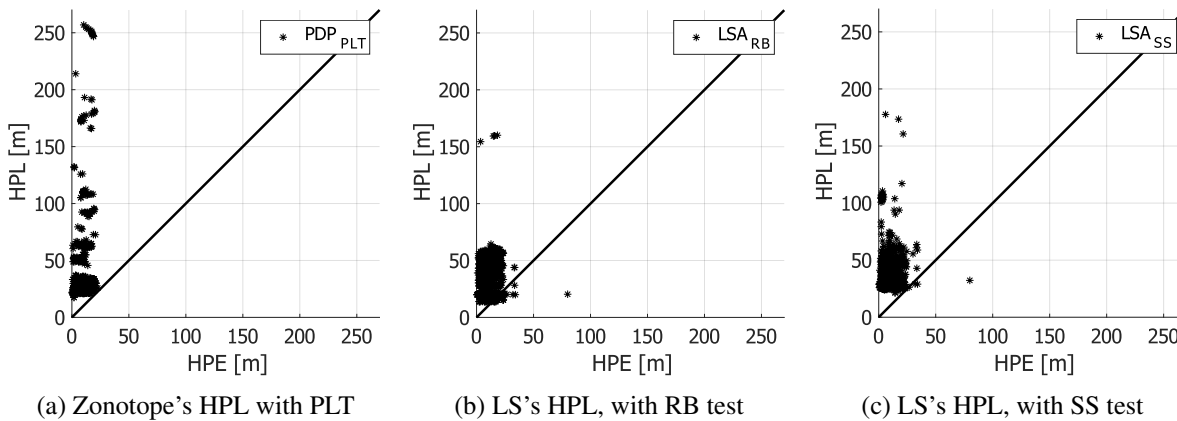


Figure 5.16: Stanford diagram after outlier screening: For zonotope the observation interval bound is $\Delta = 6$ m and $\kappa_P = 1.5$ and for the LS $\kappa_H = 6$ with $\alpha = 0.00001$ and $\beta = 0.001$ for the RB and SS tests.

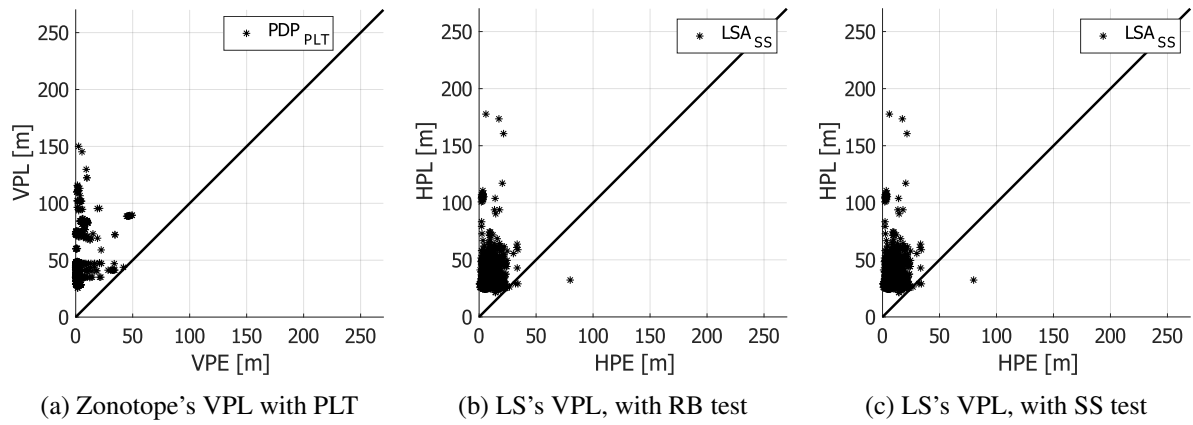


Figure 5.17: Stanford diagram after outlier screening: For the zonotope the observation interval bound is $\Delta = 6$ m and $\kappa_P = 1.5$ and for the LS $\kappa_V = 5.33$ with $\alpha = 0.00001$ and $\beta = 0.001$ for the RB and SS tests.

6 Conclusions and Outlook

The integrity of the navigation system is of great interest in today's navigation applications, especially for liability and safety-critical applications. Satellite-based augmentation systems and ground-based augmentation systems can provide high-integrity measures in many areas of navigation, especially in aviation. However, these are complex systems and very expensive to maintain. In the last three decades, more interest has focused on monitoring the integrity inside a Global Navigation Satellite Systems (GNSSs) receiver itself, the so-called Receiver Autonomous Integrity Monitoring (RAIM). First, it was intended for soft integrity requirements such as en-route navigation operation, where the quality of GNSS observations is in its best condition. In the last decades, autonomous integrity monitoring has gained a high interest in automated applications, particularly autonomous driving cars where the navigation condition can change from one epoch to another. Due to the probabilistic nature of most of the parameter estimation processes used in navigation applications (mainly LSA and Kalman filtering), most of the RAIM approaches are based on the probabilistic hypothesis testing. Moreover, the probabilistic theory is very well developed. In addition to the probabilistic approaches, interval-based integrity monitoring started to emerge in the last decade due to the rigorous and robust nature of interval computations. The interval-based methods are quite new and need more development and validations.

The goal of this thesis was to develop alternative integrity monitoring techniques based on interval analysis and set theory that can provide guaranteed information. In addition, the goal is also to analyze the already existing integrity monitoring techniques that are mostly applied to GNSS observations, investigate each technique and assess the respective advantages and disadvantages of each technique. Since, the main goal is to develop a new concept of the integrity monitoring technique,

The focus is on the basic algorithm with a single fault which can be extended to multi-faults. The two most used single fault probabilistic approaches, namely residual-based and solution separation RAIM, have been investigated to compare them to the newly developed method. Besides, the existing interval-based approaches have been investigated but they still do not contain a full integrity monitoring. Least-squares via interval analysis provide only a confidence domain using interval box or zonotope, while set inversion via interval analysis provides a feasible region of the positioning utilizing interval box which is guaranteed to contain the true solution if the assumption holds that has been made on the observation interval bounds (OIBs). Nevertheless, the two interval-based algorithms do not provide full integrity monitoring as the probabilistic RAIMs do.

The purpose of integrity monitoring is to meet a predefined integrity measure depending on the intended application such as Integrity Risk (IR), alert limit (AL), time to alert (TTA), and protection level (PL). Since almost every integrity parameter is defined by a probability that has to be assigned in the test statistic i.e., probability of false alarm and probability of missed detection, it is not straightforward to assign integrity measures by means of intervals. When intervals are applied to an observation, every point inside the interval is treated equally and there is no distribution inside that interval. In addition, the test performance of any test statistic, which is the core of RAIM is defined by its ability to detect and identify faults in the observation. On top of that, the test statistic must provide a PL that meets the integrity and continuity requirements.

In this thesis, a new method of integrity monitoring is developed based on interval analysis and set theory. The navigation problem is transformed into a convex problem by introducing OIBs to the observations. The solution set is the polytope bounding zone for the new convex navigation problem computed by a Primal-Dual Polytope (PDP) algorithm. The polytope bounding zone is a set of all feasible solutions for the navigation problem, i.e. any point inside the polytope is a possible solution. The barycenter of the polytope is considered the point position. The error-free observations provide a symmetrical polytope as a bounding zone which is a zonotope. The zonotope is the nominal solution of the convex navigation problem which

I interpret as a confidence bounding zone. The nominal zonotope can be computed from the OIBs and Line-of-sights without using the observations.

In this thesis, a set of different simple but didactic examples are presented to explain the behavior of the zonotopes and polytopes bounding zones. So, I have studied the impact of navigation geometry on the zonotope bounding zone. I found out that the better the navigation geometry is, i.e. decreasing the geometrical delusion of precision (GDOP), the smaller and better bounded the zonotope and polytope get. The volume of the bounding zones increases linearly with the OIBs. Nevertheless, the quality of navigation geometry has the biggest effect on the volume of the bounding zone. The zonotope is compared to its counterpart from the probabilistic approach, i.e., the confidence error ellipse of least square adjustment. The zonotope shows a better representation of the confidence domain, especially when the observations have different weights. Afterward, the impact of the observation noise on the polytopal bounding zone is examined both in good and bad navigation geometry. Additionally, the impact of the relation between the observation noise (variance) and the OIBs on the polytope bounding zone is addressed, where lower $\frac{\Delta}{\sigma}$ ratio induced more deformation to the polytope. Eventually, the impact of biased observation on the bound zone is investigated for different geometrical situations where the worse the navigation geometry is, the bigger the minimum detectable bias (MDB) is. I found out that, if there are no systematic errors and biases, the barycenter is quite a good estimation of the point position, especially for large $\frac{\Delta}{\sigma}$ ratio. However, if one non-detected bias is present in the observation, a big cut on the polytope happens in the direction of the biased observation, which degrades the accuracy of the barycenter as a point position. This happens especially in a bad geometry where the non-detected bias could be quite large with respect to the OIB. The MDB is the bias that provides an empty set. At this point, we proposed a new method to derive the MDB for the positioning bounding zone. The derivation of the MDB is proposed PMDB on the actual polytope and an upper bound on the PMDB called ZMDB. Later on, in the newly developed test, the actual MDB will be even lower than PMDB. The newly developed PMDB is guaranteed and any bias greater than the PMDB will provide an empty set and will be 100% detected.

On top of that, consistency check, fault detection, and fault identification, as well as protection level are proposed based on the newly developed method. The new integrity monitoring method or new RAIM is based on the relative volume between the nominal polytope, i.e. the zonotope and the actual polytope. First, the normalized relative volume between the polytope and the zonotope represents a consistency measure of the observations w.r.t. the OIBs. In comparison to the probabilistic approaches, the zonotope represents the theoretical distribution against which the polytope has to be checked. Then, a polytopal global test (PGT) is developed on the consistency measures taking into account all observations. A critical value has to be assigned for the PGT which depends on the observation noise, OIBs, and a scaling factor. The scaling factor plays an important role in the reliability performance of the test, i.e. the value of the MDB. Then, a polytopal local test (PLT) was developed on the separate sets of observations to identify the faulty observation. So, the PGT is the fault detection and the PLT is the fault identification. The PLT was developed in a way that one fault can occur at a time. However, it is a multi-test where each set has its local test. It can be easily extended to multi-faults taking into account more sets of observations by excluding more than one observation from the set at a time. As for the PGT, we have to assign a critical value for the PLT which also depends on the observation noise, OIBs, and a scaling factor. The critical value of the PLT determines the minimum identifiable bias (MIB). Finally, a zonotopal protection level based on a 1-relaxed zonotope is proposed and it is guaranteed to contain the true solution even if multi-biases are presented in the observations.

To understand the behaviors of the newly developed integrity monitoring technique in different navigation situations and to compare it to the already existing probabilistic approaches, a Monte Carlo simulation is conducted and presented. Seven different real satellite geometries, i.e. 7 scenarios are selected with different numbers of satellites in view and GDOP. Random white noise is introduced to the observation with a linear drift to the clock offset. In addition to the white noise, a ramp bias is introduced to all observations and all scenarios in separate cases. First, we analyze the impact of the OIB on consistency measures. I found out, that the scatter of the consistency measure and its mean value decreases when the OIB increases. This means that the assignment of the critical value of the PGT and PLT has to take into account the relation between the observation noise and the OIB. In addition, the increasing rate depends also on the navigation geometry where the scatter and the mean value of the consistency measures have a higher incremental rate for better navigation geometry. I also found out, when one of the observations is biased, the scatter of V_{r_0}

is smaller than if no bias is present. Similarly to the non-biased region, the scatter in the biased region changes with the geometry. Analyzing the impact of the bias on the consistency measure in terms of OIB and navigation geometry, I found out that the incremental rate of V_{r0} in the biased region gets slower as OIB increases. Moreover, as OIB increases, the consistency measures in the biased region decrease and the polytope starts to be empty at larger bias for larger OIB. We also realize that different biased satellites have different effects on the inconsistency measures. This also depends on the overall geometry. In good geometry scenarios, different biased satellites have very similar effects on the consistency measures, i.e. they have very comparable MDB. In bad geometry, the different biased satellites have different effects on the consistency measures and eventually have different MDB from the others. In addition, the MDB depends on the correlation between the satellites. Satellites in different quadrants are more correlated than satellites in the same quadrant. For instance, a satellite in quadrant I has the highest correlation with the satellites in quadrant III. Moreover, if a quadrant has only one satellite in view, the uncertainty and the MDB of that satellite observation is big relative to the other observations.

The assessment of the PGT and PLT critical values is investigated. Since the critical values depend on the observation noise, OIBs, and the scaling factor κ_p , it is not straightforward to select proper critical values. Before we set the critical value, some knowledge of the navigation system has to be available, or at least a good assumption has to be made. Moreover, OIBs and κ_p depend on the specified IR and on the acceptable gross errors in the observations. A full relation between the IR and critical value, i.e. OIBs and κ_p together is still not clear and needs further investigation. Presently, the OIBs with specified IR have been determined. This is only valid for the polytope solution, i.e. the polytope will contain the true solution with the specified IR under the assumption of the observation noise. However, introducing the PGT and PLT enhances the integrity of the navigation solution, but the link between the critical values and the IR is still not fully developed. For this reason, I assign constant critical values for the polytopal tests when I compare them to the stochastic-based tests.

Comparing the MDB of the polytopal tests to the SS and RB test, I found out that the PLT has smaller MDB than the other tests in all different scenarios and all different biased satellites. Sometimes PLT and SS have the same MDB in a good geometry scenario for some satellites but for other satellites the MDB of PLT is still smaller. Comparing the RB to SS, we found out the MDB of SS is smaller than RB and eventually more biases can be detected.

In good geometry scenarios e.g., simulated scenarios 1 and 4, all tests RB, SS, and PLT perform very well. In bad geometry scenarios, e.g., simulated scenario 3, all tests have a lot of wrong identifications, however PLT test has less wrong identification than SS and SS has less wrong identification than RB. One last main difference between polytopal tests, PGT and PLT w.r.t. the probabilistic test is that the PGT needs only 4 satellites in view to be performed and PLT needs at least 5 satellites in view to be performed, while for both probabilistic tests we need 5 satellites in view for the global test and 6 satellites in view for the local test. This is a big advantage, especially in urban areas.

Analyzing the PL of all tests, we learn that the zonotopal and the RB PL do not change their values since they depend only on the predefined parameters. Moreover, the RB protection level is quite smaller than the zonotopal protection level. On the other hand, the PL of the SS test changes when observation errors change, even if the geometry and the test parameters are fixed, which makes it more realistic than the others. However, most of the time the SS protection level is larger than the other, i.e., RB and the zonotopal PL.

In this simulation, since everything is under control, all the PLs for all tests stay on the upper part (above the line $PL = PE$) of the Stanford diagram, i.e., the solution is never in the hazardous misleading operation or the hazardous operation regions. In a real scenario where the observation may contain random noise, systematic errors, and biases, the protection level of the probabilistic approach can enter the lower part region of the Stanford diagram while the zonotopal protection level will never be in the lower part region. Last but not least, the time series of the PLs shows that the PL of the SS has a very similar reaction to the consistency measures of the polytope which raises a question about the relation between these two different methods and the possibility to derive different PL from the consistency measures of the polytope and its related tests.

Finally, a car test drive to collect real data is conducted to analyze all methods in terms of precision, accuracy, reliability, integrity, and continuity. Two test drives, one in a GNSS denied area, and another in a suburban

area is studied. In both scenarios, the PDP point position shows better accuracy and precision than LSA before and after applying the tests. However, we learn that the PDP is more sensitive to the navigation geometry, and in the bad geometry its solution is worse than the LSA solution. In terms of reliability, PDP tests show better results than the probabilistic test in terms of MDB. In terms of fault detection PLT has a much higher detection rate than the probabilistic tests. However, when we compare the interval-based test and the probabilistic test we assign the OIB $\delta = 3$ m with $\kappa_p = 1.5$ corresponding to the PFA $\alpha = 0.001$ and PMD $\beta = 0.001$. This assignment of the test parameter may not be the best choice to compare interval methods to probabilistic methods which show the need for more studies in this field in the future. Last but not least, the zonotope's protection level shows much better results than both SS and RB as expected, as in the Stanford diagram it is always above the line $PL = PE$ while with both probabilistic tests for some epoch, the PL goes below the line $PL = PE$ which reaches the level of misleading information or even hazardous misleading information. We know that in these urban areas a lot of multi-pathing could happen where the assumption of one bias is not valid anymore, but even in this case, the zonotopal protection level is guaranteed to contain the true solution.

In this work, we have developed a new and alternative method based on interval analysis and set theory for GNSS positioning with uncertainty, consistency, reliability, and integrity measures. Fault detection and exclusion have been proposed and validated in simulation and real data scenarios. A guaranteed protection level for the point position is developed and validated as well. This new method is highly recommended to be used in open areas such as en-route aviation operations. It is also recommended to be used in urban areas since it provides a guaranteed PL, and especially with multi-sensor systems. It is also recommended to integrate ranging sensors to the GNSSs receiver since the OIBs acts as a geometrical constraint. In addition to the multi-sensor systems, a digital elevation map is a perfect match to be integrated to the GNSS observations.

Regardless of the development of GNSS alternative integrity measures based on interval analysis and set theory and the validation of the newly developed method, many open questions remain for improvements and finalization of the integrity monitoring. The GNSS integrity parameters and requirements are defined in a probabilistic way, and converting all the requirements to intervals and sets is not straightforward. First, the parameters of the polytopal method especially the OIBs and the global and local test critical values still need to be investigated to be properly allocated to the probabilistic requirements of the integrity requirements. Once this is done, a more legitimate comparison between the polytopal method and the probabilistic methods can be done. Moreover, the polytopal methods can then be applied in real-life applications. This also brings us back to the OIBs and the best way to determine them. In the sensitivity analysis, we have investigated only two correction models and other models need to be investigated.

Another open area of research is the type of observation. In this thesis, we only used simulated observations and GPS code observation. The question is whether we can use Doppler and carrier phase observations. What type of biases we will have to deal with and how will the polytope behave to the cycle slip in the carrier phase observations?

The PDP algorithm in the thesis is an epoch-wise estimation. This can be transferred to sequential and filtering techniques. In that case, what are the benefits and the shortcomings, and how can the fault detection and identifications be performed? In addition, the GNSS measurements can be coupled with other sensors and in the best case to a range measurement sensors. Laser scanners could be very good candidates for this purpose, especially in the GNSS denied area. The laser scanner can bound the polytopes in the horizontal directions in the urban areas where we have buildings on both sides. This would be very useful since when we have buildings on both sides and only GNSS measurements are used, the polytope blows up in the horizontal directions where there is no observation to bound it. However, using a laser scanner is somehow complicated and in the best case, it needs map elements with a known position. Otherwise, simultaneous localization and mapping have to be performed. Also, GNSS observation could be coupled with a digital elevation map, if available, where a tight bound on the up direction could be applied. This is useful in open areas where the horizontal positioning is more accurate than the vertical one. So, coupling other observations with GNSS is a wide area of research to be investigated.

Moreover, the barycenter is not the best choice as a point position in the presence of non-detectable biases. Research in this direction needs to be conducted and one idea is to find observation corrections by fitting the

polytope into the nominal zonotope. In this way, the observations get better accuracy and as a consequence, the PDP point position gets better accuracy, reliability, and integrity.

We have already provided a guaranteed PL. However, it represents the OIBs and the navigation geometry without taking into account the actual observation. It is useful to have a guaranteed PL, but when it gets too big we lose the continuity. The question is if it is possible to find a smaller guaranteed PL than the one already proposed incorporating the observations. The idea here is to use something similar to the consistency measures that we have developed, but evaluation of the relative volume should be computed between the zonotope and polytope without normalization.

One last thing to study is a multi-GNSS constellation and the effects of the inter-system biases on the polytope estimation. Moreover, the so-called clock receiver modeling could be used to eliminate the clock offset from the estimations where the external stable clock has to be connected to the GNSS receiver. Having only three position parameters to be estimated will reduce the polytope computation time and make the estimation more geometrically dependent.

Bibliography

- Alefeld, G. and Herzberger, J., 1983. *Introduction to interval computation*. Vol. 1, Academic Press.
- Ashokaraj, I., Tsourdos, A., Silson, P. and White, B., 2004. Sensor based robot localisation and navigation: Using interval analysis and extended Kalman filter. In: *5th Asian Control Conference IEEE*, Vol. 2, IEEE, pp. 1086–1093.
- Avis, D. and Fukuda, K., 1992. A pivoting algorithm for convex hulls and vertex enumeration of arrangements and polyhedra. *Discrete & Computational Geometry* 8(3), pp. 295–313.
- Baarda, W., 1967. *Statistical concepts in geodesy*. Vol. 2 Number 4, Rijkscommissie voor Geodesie, Netherlands: Netherlands Geodetic Commission, Delft, Netherlands.
- Baarda, W., 1968. *A Testing Procedure for Use in Geodetic Networks*. Vol. 2 Number 5, Computing Centre of the Delft Geodetic Institute, Publications on Geodesy, Delft, Netherlands.
- Bakker, P. F., Marel, H. and Teunissen, P., 2009. The minimal detectable bias for GNSS observations with a single receiver setup and a geometry-free model. In: *European Navigation Conference - ENC-GNSS*, pp. 1–12.
- Beidleman, S. W., 2005. GPS vs Galileo: balancing for position in space. *Astropolitics* 3(2), pp. 117–161.
- Belabbas, B. and Gass, F., 2005. RAIM algorithms analysis for a combined GPS/Galileo constellation. In: *18th International Technical Meeting of the Satellite Division of The Institute of Navigation*, pp. 1781–1788.
- Berardo, M., Manfredini, E. G., Dovis, F. and Lo Presti, L. L., 2016. A spoofing mitigation technique for dynamic applications. In: *8th ESA Workshop on Satellite Navigation Technologies and European Workshop on GNSS Signals and Signal Processing (NAVITEC)*, IEEE, pp. 1–7.
- Binjammaz, T., Al-Bayatti, A. and Al-Hargan, A., 2013. GPS integrity monitoring for an intelligent transport system. In: *10th Workshop on Positioning Navigation and Communication (WPNC)*, pp. 1–6.
- Blanch, J., Choi, M. J., Walter, T., Enge, P. and Suzuki, K., 2010a. Prototyping advanced RAIM for vertical guidance. In: *23rd International Technical Meeting of the Satellite Division of The Institute of Navigation*, pp. 285–291.
- Blanch, J., Ene, A., Walter, T. and Enge, P., 2007. An optimized multiple hypothesis RAIM algorithm for vertical guidance. In: *20th International Technical Meeting of the Satellite Division of The Institute of Navigation*, pp. 2924–2933.
- Blanch, J., Walter, T. and Enge, P., 2010b. RAIM with optimal integrity and continuity allocations under multiple failures. *IEEE Transactions on Aerospace and Electronic Systems* 46(3), pp. 1235–1247.
- Blanch, J., Walter, T. and Enge, P., 2013. Optimal positioning for advanced raim. *Journal of The Institute of Navigation* 60(4), pp. 279–289.
- Blanch, J., Walter, T., Enge, P., Pervan, B., Joerger, M., Khanafseh, S., Burns, J., Alexander, K., Boyero, J. P., Lee, Y. et al., 2014. Architectures for advanced RAIM: Offline and online. In: *27th International Technical Meeting of the Satellite Division of The Institute of Navigation*, pp. 787–804.

- Blesa, J., Puig, V. and Saludes, J., 2011. Identification for passive robust fault detection using zonotope-based set-membership approaches. *International Journal of Adaptive Control and Signal Processing* 25(9), pp. 788–812.
- Borio, D., Dosis, F., Kuusniemi, H. and Lo Presti, L., 2016. Impact and detection of GNSS jammers on consumer grade satellite navigation receivers. *Proceedings of the IEEE* 104(6), pp. 1233–1245.
- Boyd, S. and Vandenberghe, L., 2004. *Convex optimization*. Cambridge university press, California.
- Bremner, D., Fukuda, K. and Marzetta, A., 1998. Primal—dual methods for vertex and facet enumeration. *Discrete & Computational Geometry* 20(3), pp. 333–357.
- Brenner, M., 1996. Integrated GPS/inertial fault detection availability. *Journal of The Institute of Navigation* 43(2), pp. 111–130.
- Brown, R. G., 1992. A baseline GPS RAIM scheme and a note on the equivalence of three RAIM methods. *Journal of The Institute of Navigation* 39(3), pp. 301–316.
- Brown, R. G., 1997. Solution of the two-failure GPS RAIM problem under worst-case bias conditions: parity space approach. *Journal of The Institute of Navigation* 44(4), pp. 425–431.
- Brown, R. G. and McBurney, P. W., 1988. Self-contained GPS integrity check using maximum solution separation. *Journal of The Institute of Navigation* 35(1), pp. 41–53.
- Chabert, G. and Jaulin, L., 2009. Contractor programming. *Artificial Intelligence* 173, pp. 1079–1100.
- Chen, G., Wang, J. and Shieh, L. S., 1997. Interval Kalman filtering. *IEEE Transactions on Aerospace and electronic Systems* 33(1), pp. 250–259.
- CODE, 2017. Code - analysis center. <https://www.aiub.unibe.ch/>.
- Cohen, J. and Hickey, T., 1979. Two algorithms for determining volumes of convex polyhedra. *Journal of the ACM (JACM)* 26(3), pp. 401–414.
- Crutzen, P. J. and Zimmermann, P. H., 1991. The changing photochemistry of the troposphere. *Tellus A: Dynamic Meteorology and Oceanography* 43(4), pp. 136–151.
- Dach, R. and Jean, Y., 2013. International GNSS service. Technical report, Astronomical Institute, University of Bern.
- Dbouk, H. and Schön, S., 2018. Comparison of different bounding methods for providing GPS integrity information. In: *IEEE/ION Position, Location and Navigation Symposium (PLANS) of The Institute of Navigation*, IEEE, pp. 355–366.
- Dbouk, H. and Schön, S., 2019. Reliability and integrity measures of GPS positioning via geometrical constraints. In: *International Technical Meeting of The Institute of Navigation*, pp. 730–743.
- Dbouk, H. and Schön, S., 2020. Reliable bounding zones and inconsistency measures for GPS positioning using geometrical constraints. *Acta Cybernetica* 24(3), pp. 573–591.
- De Jong, K. and Teunissen, P. J. G., 2000. Minimal detectable biases of GPS observations for a weighted ionosphere. *Earth, Planets and Space* 52(10), pp. 857–862.
- Deif, A., 1991. The interval eigenvalue problem. *ZAMM-Journal of Applied Mathematics and Mechanics/Zeitschrift für Angewandte Mathematik und Mechanik* 71(1), pp. 61–64.
- Deif, A., 2012. *Sensitivity analysis in linear systems*. Springer-Verlag Berlin Heidelberg New York.
- Directorate, G., 2019. Interface control document ICD-GPS-240D.
- DoD/DHS, 2008. Federal radionavigation plan. Technical report, National Technical Information Service, Springfield. Virginia.

- DoD/DHS, 2020. Global positioning system standard positioning service performance standard.
- Drevelle, V. and Bonnifait, P., 2009. High integrity GNSS location zone characterization using interval analysis. In: *22nd International Technical Meeting of the Satellite Division of The Institute of Navigation*, pp. 2178–2187.
- Drevelle, V. and Bonnifait, P., 2011. A set-membership approach for high integrity height-aided satellite positioning. *GPS solutions* 15(4), pp. 357–368.
- Drevelle, V. and Bonnifait, P., 2013. Reliable positioning domain computation for urban navigation. *IEEE Intelligent Transportation Systems Magazine* 5(3), pp. 21–29.
- EGSA, 2015. Report on the performance and level of integrity for safety and liability critical multi-applications. Technical report, EUROPEAN GNSS AGENCY.
- EGSA, 2020. Galileo constellation. <https://www.gsc-europa.eu/system-service-status/constellation-information>.
- Engel, P. K. and Van Dierendonck, A. J., 1996. *Global Positioning System: Theory and Applications Volume II*. American Institute of Aeronautics and Astronautics, chapter 4, pp. 117–142.
- Eppstein, D., 1995. Zonohedra and zonotopes. Technical Report 95-53, Donald Bren School of Information and Computer Sciences (ICS).
- European-Union, 2018. Galileo open service signal in space interface control document.
- FAA, 2008. Global positioning system wide area augmentation system (WAAS) performance standard. Department of Transportation and Federal Aviation Administration (FAA). Washington, DC, USA.
- Felux, M., Dautermann, T. and Becker, H., 2013. GBAS landing system–precision approach guidance after ILS. *Aircraft Engineering and Aerospace Technology* 85(5), pp. 382–388.
- Feng, S., Ochieng, W., Moore, T., Hill, C. and Hide, C., 2009. Carrier phase-based integrity monitoring for high-accuracy positioning. *GPS solutions* 13(1), pp. 13–22.
- Fomin, F. V., Gaspers, S., Pyatkin, A. V. and Razgon, I., 2008. On the minimum feedback vertex set problem: Exact and enumeration algorithms. *Algorithmica* 52(2), pp. 293–307.
- Fukuda, K., Liebling, T. M. and Margot, F., 1997. Analysis of backtrack algorithms for listing all vertices and all faces of a convex polyhedron. *Computational Geometry* 8(1), pp. 1–12.
- GEAS, F., 2010. Phase II of the GNSS evolutionary architecture study.
- Georgiadou, P., and Kleusberg, A., 1988. On carrier signal multipath effects in relative GPS positioning. *Journal of Geodesy, Manuscripta geodetica* 13(3), pp. 172–179.
- Gratton, L., Joerger, M. and Pervan, B., 2010. Carrier phase relative RAIM algorithms and protection level derivation. *The Journal of Navigation* 63(2), pp. 215–231.
- Griffiths, J., 2019. Combined orbits and clocks from IGS second reprocessing. *Journal of Geodesy* 93, pp. 177–195.
- Griffiths, J. and Ray, J. R., 2009. On the precision and accuracy of IGS orbits. *Journal of Geodesy* 83, pp. 277–287.
- Herceg, M., Kvasnica, M., Jones, C. N. and Morari, M., 2013. Multi-parametric toolbox 3.0. In: *European Control Conference (ECC), 2013*, IEEE, pp. 502–510.
- Hewitson, S. and Wang, J., 2010. Extended receiver autonomous integrity monitoring (E RAIM) for GNSS/INS integration. *Journal of Surveying Engineering* 136(1), pp. 13–22.

- Hofmann-Wellenhof, B., Lichtenegger, H. and Wasle, E., 2008. *GNSS – Global Navigation Satellite Systems*. SpringerWienNewYork, chapter 5, pp. 105–160.
- Hopfield, H., 1969. Two-quartic tropospheric refractivity profile for correcting satellite data. *Journal of Geophysical research* 74(18), pp. 4487–4499.
- Hopfield, H. S., 1971. Tropospheric effect on electromagnetically measured range: Prediction from surface weather data. *Radio science* 6(3), pp. 357–367.
- Humphreys, T. E., Ledvina, B. M., Psiaki, M. L., O’Hanlon, B. W. and Kintner, P. M., 2008. Assessing the spoofing threat: Development of a portable GPS civilian spoofer. In: *Radionavigation laboratory conference proceedings*.
- IACPNT, 2020. Beidou constellation status. <https://www.glonass-iac.ru/en/BEIDOU/>.
- ICAO, 2006. Aeronautical telecommunications: International standards and recommended practices and procedures for air navigation services: Annex 10 to the convention on international civil aviation.
- ICD, 2019. Interface control document ICD-GPS-870D.
- iMAR IMU, 2016. <https://www.novatel.com/assets/documents/papers/fsas.pdf>.
- Imparato, D., Teunissen, P. and Tiberius, C., 2019. Minimal detectable and identifiable biases for quality control. *Survey review* 51(367), pp. 289–299.
- Jaulin, L., 2009. Robust set-membership state estimation; application to underwater robotics. *Automatica* 45(1), pp. 202–206.
- Jaulin, L. and Walter, E., 1993a. Guaranteed nonlinear parameter estimation from bounded-error data via interval analysis. *Mathematics and computers in simulation* 35(2), pp. 123–137.
- Jaulin, L. and Walter, E., 1993b. Set inversion via interval analysis for nonlinear bounded-error estimation. *Automatica* 29(4), pp. 1053–1064.
- Jaulin, L., Kieffer, M., Didrit, O. and Walter, E., 2001. *Applied Interval Analysis*. Springer-Verlag London.
- Jaulin, L., Walter, E. and Didrit, O., 1996. Guaranteed robust nonlinear parameter bounding. In: *CESA IMA CS multiconference (symposium on modelling, analysis and simulation)*, Vol. 96, pp. 1156–1161.
- Jaulin, L., Walter, E., Lévêque, O. and Meizel, D., 2000. Set inversion for χ -algorithms, with application to guaranteed robot localization. *Mathematics and Computers in Simulation* 52(3-4), pp. 197–210.
- Jiang, C., Zhang, S. and Zhang, Q., 2016. A novel robust interval Kalman filter algorithm for GPS/INS integrated navigation. *Journal of Sensors*.
- Joerger, M. and Pervan, B., 2014. Solution separation and chi-squared ARAIM for fault detection and exclusion. In: *IEEE/ION Position, Location and Navigation Symposium (PLANS) of The Institute of Navigation*, IEEE, pp. 294–307.
- Joerger, M. and Pervan, B., 2016. Fault detection and exclusion using solution separation and chi-squared ARAIM. *IEEE Transactions on Aerospace and Electronic Systems* 52(2), pp. 726–742.
- Joerger, M. and Spenko, M., 2017. Toward navigation safety for autonomous car. *InsideGNSS* pp. 40–49.
- Joerger, M., Chan, F. C. and Pervan, B., 2014. Solution separation versus residual-based RAIM. *Journal of The Institute of Navigation* 61(4), pp. 273–291.
- Joerger, M., Chan, F. C., Langel, S. E. and Pervan, B., 2012. RAIM detector and estimator design to minimize the integrity risk. In: *25th International Technical Meeting of the Satellite Division of The Institute of Navigation*, pp. 2785–2807.

- Joerger, M., Langel, S. and Pervan, B., 2016a. Integrity risk minimisation in RAIM part 2: optimal estimator design. *The Journal of Navigation* 69(4), pp. 709–728.
- Joerger, M., Stevanovic, S., Chan, F.-C., Langel, S. and Pervan, B., 2013. Integrity risk and continuity risk for fault detection and exclusion using solution separation ARAIM. In: *Proceedings of the 26th International Technical Meeting of the Satellite Division of The Institute of Navigation (ION GNSS+)*, pp. 2702–2722.
- Joerger, M., Stevanovic, S., Langel, S. and Pervan, B., 2016b. Integrity risk minimisation in RAIM part 1: optimal detector design. *The Journal of Navigation* 69(3), pp. 449–467.
- Jokinen, A., Feng, S., Ochieng, W., Hide, C., Moore, T. and Hill, C., 2012. Fixed ambiguity precise point positioning (ppp) with FDE RAIM. In: *IEEE/ION Position, Location and Navigation Symposium (PLANS) of The Institute of Navigation*, IEEE, pp. 643–658.
- Kalman, R. E., 1960. A new approach to linear filtering and prediction problems. *Journal of Basic Engineering* 82(1), pp. 35–45.
- Khachiyan, L., Boros, E., Borys, K., Gurvich, V. and Elbassioni, K., 2009. Generating all vertices of a polyhedron is hard. In: *Twentieth Anniversary Volume*, Springer, pp. 1–17.
- Kieffer, M., Braems, I., Walter, E. and Jaulin, L., 2001. Guaranteed set computation with subpavings. In: *Scientific Computing, Validated Numerics, Interval Methods*, Springer, pp. 167–178.
- Kjørsvik, N. S. and Brøste, E., 2009. Using TerraPOS for efficient and accurate marine positioning. White paper, TerraTec AS, Lysaker, Norway.
- Klobuchar, J. A., 1987. Ionospheric time-delay algorithm for single-frequency GPS users. *IEEE Transactions on aerospace and electronic systems* 23(3), pp. 325–331.
- Koch, K., 1999. *Parameter Estimation and Hypothesis Testing in Linear Models*. Springer-Verlag Berlin Heidelberg.
- Kühn, W., 1998. Zonotope dynamics in numerical quality control. In: *Mathematical Visualization*, Springer, Berlin, Heidelberg, pp. 125–134.
- Kutterer, H., 1994. *Intermediate mathematical treatment of finite blur "a linear adjustment models*. Beck.
- Langley, B. L., 2011. Innovation: GNSS and the ionosphere. *GPS World*.
- Langley, R., 1999. Dilution of precision. *GPS world* 10(5), pp. 52–59.
- Lawrence, J., 1991. Polytope volume computation. *Mathematics of Computation* 57(195), pp. 259–271.
- Le Bars, F., Antonio, E., Cervantes, J., De La Cruz, C. and Jaulin, L., 2018. Estimating the trajectory of low-cost autonomous robots using interval analysis: Application to the eurathlon competition. In: *Marine Robotics and Applications*, Springer, pp. 51–68.
- Lee, Y. C., 1986. Analysis of range and position comparison methods as a means to provide gps integrity in the user receiver. In: *42nd Annual Meeting of the Institute of Navigation*, pp. 1–4.
- Lee, Y. C., 2007. Two new RAIM methods based on the optimally weighted average solution (owas) concept. *Journal of The Institute of Navigation* 54(4), pp. 333–345.
- Lee, Y. C., 2011. A position domain relative RAIM method. *IEEE Transactions on Aerospace and Electronic Systems* 47(1), pp. 85–97.
- Lehmann, R. and Scheffler, T., 2011. Monte Carlo-based data snooping with application to a geodetic network. *Journal of Applied Geodesy* 5(3–4), pp. 123–134.
- Li, W., 2016. Directions 2017: Beidou's road to global service. *GPS world* 27, pp. 24–25.

- Liu, J., Gu, D., Ju, B., Yao, J., Duan, X. and Yi, D., 2014. Basic performance of BeiDou-2 navigation satellite system used in LEO satellites precise orbit determination. *Chinese Journal of Aeronautics* 27(5), pp. 1251–1258.
- Luenberger, D. G., Ye, Y. et al., 1984. *Linear and nonlinear programming*. International Series in Operations Research & Management Science, Vol. 2, Springer.
- Luo, X., Mayer, M., Heck, B. and Awange, J. L., 2014. A realistic and easy-to-implement weighting model for GPS phase observations. *IEEE Transactions on Geoscience and Remote Sensing* 52(10), pp. 6110–6118.
- Mahato, N. R., Jaulin, L., Chakraverty, S. and Dezert, J., 2020. Validated enclosure of uncertain nonlinear equations using SIVIA Monte Carlo. In: *Recent Trends in Wave Mechanics and Vibrations*, Springer, pp. 455–468.
- Martineau, A., Macabiau, C. and Mabillean, M., 2009. GNSS RAIM assumptions for vertically guided approaches. In: *22nd International Technical Meeting of the Satellite Division of The Institute of Navigation*.
- Meurer, M. and Antreich, F., 2017. *Signals and Modulation*. Springer, Cham, chapter 4, pp. 91–119.
- Mingyu, K. and Jeongrae, K., 2015. A long-term analysis of the GPS broadcast orbit and clock error variations. *Procedia Engineering* 99, pp. 654–658.
- Mink, M., 2016. Performance of receiver autonomous integrity monitoring (RAIM) for maritime operations. PhD thesis, Karlsruher Institut für Technologie (KIT).
- Misra, P. and Enge, P., 2011. *Global Positioning System: Signals, Measurements and Performance Revised Second Edition*. Ganga-Jamuna Press.
- Montenbruck, O. and Hauschild, A., 2013. Code biases in Multi-GNSS point positioning. In: *International Technical Meeting of The Institute of Navigation*, pp. 616–628.
- Moore, R. E., 1966. *Interval analysis*. Vol. 4, Prentice-Hall Englewood Cliffs.
- Moore, R. E., Kearfott, R. B. and Cloud, M. J., 2009. *Introduction to interval analysis*. Society for Industrial and Applied Mathematics, Philadelphia.
- Motella, B., Pini, M., Fantino, M., Mulassano, P., Nicola, M., Fortuny-Guasch, J., Wildemeersch, M. and Symeonidis, D., 2010. Performance assessment of low cost GPS receivers under civilian spoofing attacks. In: *5th ESA Workshop on Satellite Navigation Technologies and European Workshop on GNSS Signals and Signal Processing (NAVITEC)*, IEEE, pp. 1–8.
- Murphy, T. and Harris, M., 2008. RAIM performance in the post SA era. In: *21st International Technical Meeting of the Satellite Division of The Institute of Navigation*, pp. 139–150.
- Nava, B., Coisson, P. and Radicella, S. M., 2008. A new version of the NeQuick ionosphere electron density model. *Journal of Atmospheric and Solar-Terrestrial Physics* 70(15), pp. 1856–1862.
- Nicola, J. and Jaulin, L., 2018. Comparison of Kalman and interval approaches for the simultaneous localization and mapping of an underwater vehicle. In: *Marine Robotics and Applications*, Springer, pp. 117–136.
- Nicola, M., Musumeci, L., Pini, M., Fantino, M. and Mulassano, P., 2010. Design of a gnss spoofing device based on a GPS/Galileo software receiver for the development of robust countermeasures. In: *European Navigation Conference on Global Navigation Satellite Systems - ENC GNSS*.
- NovAtel, 2012. <https://www.novatel.com/assets/documents/manuals/om-20000124.pdf>.

- Ochieng, W. Y., Sauer, K., Walsh, D., Brodin, G., Griffin, S. and Denney, M., 2003. GPS integrity and potential impact on aviation safety. *The Journal of Navigation* 56(1), pp. 51–65.
- Odiijk, D., 2003. Ionosphere-free phase combinations for modernized GPS. *Journal of surveying engineering* 129(4), pp. 165–173.
- Parkinson, B. W. and Axelrad, P., 1987. A basis for the development of operational algorithms for simplified GPS integrity checking. In: *1st Technical Meeting of the satellite Division of the Institute of Navigation*, pp. 269–276.
- Parkinson, B. W. and Axelrad, P., 1988. Autonomous GPS integrity monitoring using the pseudorange residual. *Journal of The Institute of Navigation* 35(2), pp. 255–274.
- Parkinson, B. W. and Enge, P., 1996. *Global Positioning System: Theory and Applications Volume II*. Vol. 2, American Institute of Aeronautics and Astronautics, chapter 1, pp. 3–50.
- Parkinson, B. W., Enge, P., Axelrad, P., Spilker, J. and James, J., 1996. *Global Positioning system: Theory and applications, Volume II*. American Institute of Aeronautics and Astronautics.
- Porretta, M., Banos, D. J., Crisci, M., Solari, G. and Fiumara, A., 2016. GNSS evolutions for maritime: An incremental approach. *Inside GNSS* pp. 54–62.
- Potter, J. and Suman, M., 1977. Thresholdless redundancy management with arrays of skewed instruments. *Integrity in Electron Flight Control Systems* AGARDOGRAPH-224(80A0018789), pp. 11–15.
- Rakipi, A., Kamo, B., Cakaj, S., Kolici, V., Lala, A., Shinko, I. et al., 2015. Integrity monitoring in navigation systems: Fault detection and exclusion raim algorithm implementation. *Journal of Computer and Communications* 3(06), pp. 25.
- Rauh, A., Kletting, M., Aschemann, H. and Hofer, E. P., 2006. Interval methods for simulation of dynamical systems with state-dependent switching characteristics. In: *IEEE Conference on Computer Aided Control System Design, International Conference on Control Applications, International Symposium on Intelligent Control*, IEEE, pp. 355–360.
- Rauh, A., Senkel, L. and Aschemann, H., 2015. Interval-based sliding mode control design for solid oxide fuel cells with state and actuator constraints. *IEEE Transactions on Industrial Electronics* 62(8), pp. 5208–5217.
- Reid, T. G. R., Houts, S. E., Cammarata, R., Mills, G., Agarwal, S., Vora, A. and Pandey, G., 2019. Localization requirements for autonomous vehicles. *International Journal of Connected and Automated* pp. 173–190.
- Renfro, B. A., Stein, M., Boeker, N. and Terry, A., 2018. An analysis of global positioning system (gps) standard positioning service (sps) performance for 2017. Technical report, Space and Geophysics Laboratory, Applied Research Laboratories, The University of Texas at Austin.
- Ries, L., Legrand, F., Lestarguit, L., Vigneau, W. and Issler, J. L., 2003. Tracking and multipath performance assessments of BOC signals using a bit-level signal processing simulator. In: *16th International Technical Meeting of the Satellite Division of The Institute of Navigation*, Institute fo Navigation, Oregon Convention Center Portland, OR, pp. 1996–2010.
- RTCA, 2006. Minimum operational performance standards for global positioning system/wide area augmentation system airborne equipment. document SC-159, RTCA/DO-229D,, RTCA.
- Russian Space Systems, J., 2016. GLONASS interface control document.
- Saastamoinen, J., 1972. Contributions to the theory of atmospheric refraction. *Bulletin Géodésique* 105(1), pp. 279–298.

- Saastamoinen, J., 1973. Contributions to the theory of atmospheric refraction. *Bulletin Géodésique* 107(1), pp. 13–34.
- Salós, D., Martineau, A., Macabiau, C., Bonhoure, B. and Kubrak, D., 2013. Receiver autonomous integrity monitoring of GNSS signals for electronic toll collection. *IEEE transactions on intelligent transportation systems* 15(1), pp. 94–103.
- Schmitt, G., 1977. Some considerations using interval analysis in adjustment calculations. In: *16th General Assembly of the International Union of Geodesy (IUGG)*, pp. 87–97.
- Schön, S., 2002. Using zonotopes for overestimation-free interval least-squares—some geodetic applications. In: *10th GAMM-IMACS International Symposium on Scientific Computing, Computer Arithmetic, and Validated Numerics*.
- Schön, S., 2016. Interval-based reliability and integrity measures. In: *8th European Space Agency (ESA) Workshop on Satellite Navigation Technologies and European Workshop on GNSS Signals and Signal Processing NAVITEC*, pp. 14–16.
- Schön, S. and Kutterer, H., 2001. Optimal design of geodetic monitoring networks by means of interval mathematics. In: *10th FIG International Symposium on Deformation Analysis, Orange California*, pp. 362–371.
- Schön, S. and Kutterer, H., 2003. Imprecision in geodetic observations case study GPS monitoring network. In: *11th FIG Symposium on Deformation Measurements*, Vol. 11, Santorini, Greece, pp. 471–478.
- Schön, S. and Kutterer, H., 2005a. Realistic uncertainty measures for GPS observations. In: *A Window on the Future of Geodesy*, Springer, pp. 54–59.
- Schön, S. and Kutterer, H., 2005b. Using zonotopes for overestimation-free interval least-squares—some geodetic applications. *Reliable Computing* 11(2), pp. 137–155.
- Schön, S. and Kutterer, H., 2006. Uncertainty in GPS networks due to remaining systematic errors: the interval approach. *Journal of Geodesy* 80(3), pp. 150–162.
- Schön, S., Brenner, C., Alkhatib, H., Coenen, M., Dbouk, H., Garcia-Fernandez, N., Fischer, C., Heipke, C., Lohmann, K., Neumann, I. et al., 2018. Integrity and collaboration in dynamic sensor networks. *Sensors* 18(7), pp. 2400.
- SEA, 2018. Taxonomy and definitions for terms related to driving automation systems for on-road motor vehicles. J3016 standard.
- Speidel, J., Tossaint, M., Wallner, S. and Angel Avila-Rodriguez, J., 2013. Integrity for aviation: Comparing future concepts. *Inside GNSS* 8(4), pp. 54–64.
- Spilker, J., James, J., Penina, A., Parkinson, B. W. and Enge, P., 1996. *Global positioning system: Theory and applications, Volume I*. American Institute of Aeronautics and Astronautics.
- Stallo, C., Neri, A., Salvatori, P., Capua, R. and Rispoli, F., 2019. GNSS integrity monitoring for rail applications: Two-tiers method. *IEEE Transactions on Aerospace and Electronic Systems* 55(4), pp. 1850–1863.
- Sturza, M. A., 1988. Navigation system integrity monitoring using redundant measurements. *Journal of The Institute of Navigation* 35(4), pp. 483–501.
- Sturza, M. and Brown, A., 1990. Comparison of fixed and variable threshold RAIM algorithms. In: *Proceedings of the 3rd International Technical Meeting of the Satellite Division of The Institute of Navigation (ION GPS)*, pp. 437–443.
- Tay, S. and Marais, J., 2013. Weighting models for GPS pseudorange observations for land transportation in urban canyons. In: *6th European Workshop on GNSS Signals and Signal Processing*.

- Teunissen, P., 1995. The least-squares ambiguity decorrelation adjustment: a method for fast GPS integer ambiguity estimation. *Journal of Geodesy* 70, pp. 65–82.
- Teunissen, P., 1998. Minimal detectable biases of GPS data. *Journal of Geodesy* 72(4), pp. 236–244.
- Teunissen, P., 2006. *Testing theory: an introduction*. Delft university press, VSSD.
- Teunissen, P. and Kleusberg, A., 1998. *GPS for Geodesy*. Springer-Verlag Berlin Heidelberg.
- Teunissen, P. and Montenbruck, O. (eds), 2017. *Springer Handbook of Global Navigation Satellite Systems*. Springer, Cham.
- Teunissen, P. J. G., 1985. Quality control in geodetic networks. In: *Grafarend, E.W., Sansó F. (eds) Optimization and Design of Geodetic Networks*, Springer, Berlin, Heidelberg, pp. 526–547.
- Tossaint, M., Samson, J., Soran, F., Ventura-Traveset, J., Hernandez-Pajares, M., Juan, J. M., Sanz, J. and Ramos-bosch, P., 2014. The stanford - ESA integrity diagram: A new tool for the user domain SBAS integrity assessment. *Journal of the Institute of Navigation* 54(2), pp. 153–162.
- Tossaint, M., Samson, J., Toran, F., Ventura-Traveset, J., Sanz, J., Hernandez-Pajares, M. and Juan, J., 2006. The Stanford–ESA integrity diagram: Focusing on SBAS integrity. In: *19th international technical meeting of the satellite division of the institute of navigation*, pp. 26–29.
- Tranquilla, J. M. and Carr, J. P., 1990. GPS multipath field observations at land and water sites. *Journal of The Institute of Navigation* 37(4), pp. 393–414.
- Tucker, W., 2011. *Validated numerics: a short introduction to rigorous computations*. Vol. 1, Princeton University Press.
- Van Der Marel, H. and De Bakker, P., 2012. Single versus dual frequency precise point positioning. *InsideGNSS* 7(4), pp. 30–35.
- Van Nee, R. D. J., 1992. Multipath effects on GPS code phase measurements. *Journal of The Institute of Navigation* 39(2), pp. 177–190.
- Ventura-Traveset, J., Gauthier, L., Toran, F., Michel, P., Solari, G., Salabert, F., Flament, D. and Auroy, J. nad Beaugnon, D., 2006. *EGNOS the European geostationary navigation overlay system*. Vol. 1303, ESA.
- Voges, R. and Wagner, B., 2018. Timestamp offset calibration for an IMU-Camera system under interval uncertainty. In: *IEEE/RSJ International Conference on Intelligent Robots and Systems (IROS)*, IEEE, pp. 377–384.
- Wells, D., Beck, N., Kleusberg, A., Krakiwsky, E. J., Lachapelle, G., Langley, R. B., Schwarz, K., Tranquilla, J. M., Vanicek, P. and Delikaraoglou, D., 1987. Guide to GPS positioning. In: *Canadian GPS Associates*.
- Witold, R., 2012. The precision of humidity in GNSS tomography. *Atmospheric research* 107, pp. 69–75.
- Wörner, M., Schuster, F., Dölitzscher, F., Keller, C. G., Haueis, M. and Dietmayer, K., 2016. Integrity for autonomous driving: A survey. In: *IEEE/ION Position, Location and Navigation Symposium (PLANS) of The Institute of Navigation*, pp. 666–671.
- Wu, W., Guo, F. and Zheng, J., 2020. Analysis of Galileo signal-in-space range error and positioning performance during 2015–2018. *Satellite Navigation* 1(6), pp. 1–13.
- Young, R. C., 1931. The algebra of many-valued quantities. *Mathematische Annalen* 104(1), pp. 260–290.
- Zalewski, P., 2019. GNSS integrity concepts for maritime users. In: *European Navigation Conference (ENC)*, IEEE, IEEE, Warsaw, Poland, pp. 1–10.

- Zhu, N., Marais, J., Bétaille, D. and Berbineau, M., 2018. GNSS position integrity in urban environments: A review of literature. *IEEE Transactions on Intelligent Transportation Systems* 19(9), pp. 2762–2778.
- Ziegler, G. M., 1995. *Lectures on Polytopes*. Graduate Texts in Mathematics, Vol. 152, Springer-Verlag New York, Berlin, Heidelberg.

Acknowledgments

This work was supported by the German Research Foundation (DFG) as a part of the Research Training Group i.c.sens (GRK2159) during my employment at the Institut für Erdmessung (IfE) at Leibniz Universität Hannover.

First of all, I would like to thank my supervisor Prof. Dr.-Ing. Steffen Schön for his support and guidance during the development of this dissertation. Without his instructions and motivation, this work would not be possible to be achieved. Also, I would like to thank my co-reviewers, Prof. Dr.-Ing. Claus Brenner and Prof. Dr. Mathieu Joerger for taking the time to review this dissertation and for providing valuable advice and constructive criticism.

I am thankful to my colleagues at IfE and i.c.sens for their help and support during my time at the institute and the GRK group, especially Petra Heldt-Bertrand, Max Mehlretter, Nicolas Garcia Fernandez, Thomas Krawinkel, and Tobias Kersten.

A special thanks to my family for their emotional and mental support during these long years. Finally, I would like to thank my beloved Giulia Tirelli for her supports, encouragement, and being present all the time. Grazie di Cuore!

Hani Dbouk
October 2020

Curriculum Vitae

Personal Information

Name Hani Dbouk
Date of Birth March 08, 1984
Place of Birth Deir Ames, Lebanon

Course of Education

09/2002–07/2003 Baccalaureate in General Science, Hussein Ali Nasser High School, Beirut, Lebanon.
10/2004–06/2011 Bachelor of Science in General Physics, Lebanese University, Hadath, Lebanon.
10/2011–12/2014 Master of Science in Nanotechnologies for ICTs (Electronic Engineering Degree–Level of Bologna Process), Polytechnic of Turin, Italy.
10/2015–09/2016 Second Level Specializing Master in Navigation and Related Application, Polytechnic of Turin, Italy.

Work Experience

09/2009 – 07/2011 Physics and Mathematics Teacher, Friends College, Beirut, Lebanon.
Since 01/2017 Research Assistant, Institut für Erdmessung, Leibniz Universität Hannover

